Small-Signal Dynamics in Converter-Permeated Power Systems: Multi-Machine Interactions, Probabilistic Analysis, and Variability Quantification

PhD Thesis

Luke Ian Benedetti

Advanced Electrical Systems

Department of Electronic & Electrical Engineering

University of Strathclyde, Glasgow

August 2, 2025

This thesis is the result of the author's original research. It has been composed by the author and has not been previously submitted for examination which has led to the award of a degree.

Signed: 

Date: August 2, 2025

Abstract

Novel emerging dynamic interactions in converter-permeated power systems are in urgent need of thorough investigation. Their potential for causing deterioration of power system stability and the introduction of previously unseen oscillations can lead to problems such as damage or tripping of equipment, load shedding measures, or even cascading failures leading to blackouts. The result of this is the stagnation of the critical uptake of renewable energy-sourced generation and the unwillingness to decommission fossil-fuelled synchronous generators.

The wide-bandwidth control of converters-interfaced generators bring unconventional dynamics and the potential for interaction with other power system elements from electromechanical to electromagnetic timescales. A further consequence of this is the requirement for more detailed models of power system components such as dynamic representation of the electromagnetic elements of the network. It is well understood that traditional grid-following converter control approaches, which track the voltage angle at the connection point and output the specified power accordingly, will introduce significant challenges when they constitute high penetrations of the generation mixture of a power system. As such, grid-forming converter control is expected to be utilised to ensure the formation and maintenance of the grid voltage phasor in converter-permeated bulk power systems. In addition to this, the flexibility of converter control results in a plethora of possible implementations, especially for the grid-forming converters whose application to bulk power systems are less mature.

Furthermore, the variability of the renewable energy sources driving the converter-interfaced generation magnifies the uncertainty and potential range of system operating points. Even greater complexity is compounded by the more distributed nature of

converter-interfaced generation compared to traditional synchronous generators.

Ultimately, we find a huge range of operating points, system layouts, converter control philosophies, realisations, architectures, and tunings, all of which increase the complexity of the system dynamics and obscure the pre-existing intuition of power system engineers, especially with regards to multi-machine (or multi-element) interactions. This is the reason for the focus in this thesis on investigative studies of multi-machine interactions and the development of analysis methodologies which take into account the complexity of converter-permeated systems. Furthermore, caused in part by this increased dependence on the converter controllers, traditional static grid strength metrics such as the short circuit ratio (SCR) are becoming less valid.

In this context, small-signal modelling and analysis is utilised for interaction identification and characterisation studies in power systems, revealing the potential impact of the integration of converters for a range of system conditions and controller variations. Additionally, a framework is developed to enable characterisation of dynamic interactions in the context of probabilistic small-signal analysis. This offers an approach to understand any given system in terms of both the stability and involved elements for specific interactions across the full operating range. Finally, in response to the decreasing validity of static grid strength metrics as converters proliferate, a modal contribution metric is introduced which enables observation of the small-signal variability of voltage magnitude and/or frequency at different locations in response to standard disturbances. In theme with the rest of the work in this thesis, the corresponding approach also allows for the further investigation of the interactive characteristics of the specific modes contributing most to said small-signal variability.

Ultimately, the investigations performed and analysis methodologies developed will help in the ongoing process of comprehending the dynamics of modern and future converter-permeated bulk power systems with a particular focus on small-signal multi-machine interactions.

Contents

List of Figures

List of Figures

List of Tables

List of Abbreviations

AEMO	Australian Energy Market Operator.
APC	active power control.
AVR	automatic voltage regulator.
BESS	battery energy storage system.
BPS	bulk power system.
CCM	component connection method.
CIG	converter-interfaced generator.
DACVC	direct AC voltage control.
DDSSO	device-dependent subsynchronous oscillation.
DILC	double inner loop control.
DLC	double loop control.
ECDF	empirical cumulative distribution function.
EMT	electromagnetic transient.
EV	electric vehicle.
FACTS	flexible AC transmission system.
FFR	fast frequency response.
GFL	grid-following.
GFM	grid-forming.
HVDC	high voltage direct current.
ICC	inner current control.
ICCr	inner current controller-related.

IEEE	Institute of Electrical and Electronic Engineers.
IVC	inner voltage control.
IVCr	inner voltage controller-related.
LCC	linear correlation coefficient.
LPF	low pass filter.
MAMC	maximum absolute modal contribution.
MF&Dr	measurement filter- & delay-related.
MIMO	multiple-input multiple-output.
MMC	modular multilevel converter.
NESO	National Energy System Operator.
NGESO	National Grid Electricity System Operator.
OMIB	one machine-infinite bus.
OPF	optimal power flow.
P-F	active power-frequency.
PCC	point of common coupling.
PF	participation factor.
PI	proportional-integral.
PLL	phase-locked loop.
PSS	power system stabiliser.
PSSA	probabilistic small-signal analysis.
PV	photovoltaic.
PWM	pulse width modulation.
Q-V	reactive power-voltage.
RES	renewable energy source.
RFT	reference frame transformation.
RMS	root-mean-square.
RPC	reactive power control.

S^{2}SO	sub-/super-synchronous oscillation.
SCR	short-circuit ratio.
SG	synchronous generator.
SILC	single inner loop control.
SLC	single loop control.
SRF	synchronous reference frame.
SSCI	subsynchronous control interaction.
SSM	small-signal model.
SSO	sub-synchronous oscillation.
SWPI	stability weighted participation index.
TDRMD	time-domain response maximum deviation.
VMC	voltage magnitude control.
VSC	voltage-sourced converter.
VSM	virtual synchronous machine.
WCSS	within-clusters sum of squares.
WSCC	Western System Coordinating Council.

Acknowledgements

I would like to start by offering my sincerest thanks and gratitude to my supervisors Dr Panagiotis Papadopoulos and Prof Agustí Egea-Àlvarez, both for sharing their wealth of expertise, offering constant guidance when I inevitably got lost, and of course, for the pastoral care! I have also been very lucky to have benefitted from the collaboration with, and the advice of, several incredible engineers including Dr Alexandros Paspatis and Dr Robin Preece.

I absolutely could not have completed this PhD without the help, encouragement and support of the wonderful Sophie Coffey. You keep me happy even when the journey gets tough, not to mention that it is quite useful to have such an intelligent engineer as a partner!

To mum and dad, I want to thank you for all the love and support, not just during the course of my PhD but for everything leading up to this point. I never do, and never will, take it for granted. That of course extends to the rest of my family as well, with special mentions to Grandma for providing entertainment on Sunday evenings and to Tia for the sisterly friendship which means so much to me.

A final mention to my friends at Strathclyde, without whom the PhD journey would have been a lot less fun!

This work was funded by an Engineering and Physical Sciences Research Council (EPSRC) Student Excellence Award Studentship (2437798). Further acknowledgement is given to the UK Research and Innovation (UKRI) Future Leaders Fellowship (MR/S034420/1 and MR/Y00390X/1) awarded to Dr Panagiotis N. Papadopolous, the primary supervisor of this PhD.

Chapter 1

Introduction

1.1 Motivation

As variable renewable energy sources (RESs) and their grid-interfacing converters proliferate, the dynamics of the power system quickly diverge from the well studied and understood dynamics of the synchronous generator (SG)-dominated past. This is further compounded by the growing influence of other power electronics-interfaced devices such as battery energy storage systems (BESSs), high voltage direct current (HVDC) interconnectors, and electric vehicles (EVs). The resultant complexity, resource uncertainty, and relative infancy of the academic literature introduces unsolved, and potentially even as of yet unidentified challenges, halting the urgently necessary uptake of RES-based devices and phasing out of fossil-fuelled generation. However, the use of investigative studies into emerging small-signal dynamic interactions and the development of new analysis methodologies can help to enable better understanding of dynamics to ensure stable, secure operation of power systems with RES-based converter-interfaced generators (CIGs). Ultimately, this helps to illuminate the path towards the mitigation of the devastating effects of climate change[1]. This is illustrated in Fig. 1.1 which provides a summary of the high-level motivations driving the work in this thesis. In particular, the uptake of RESs is evidenced by statistics from the International Energy Agency (IEA) [4], which forecasts

[1]The devastation of climate change, including the multitude of resultant environmental and social catastrophes, is well-established with some further reading found in [1–3].

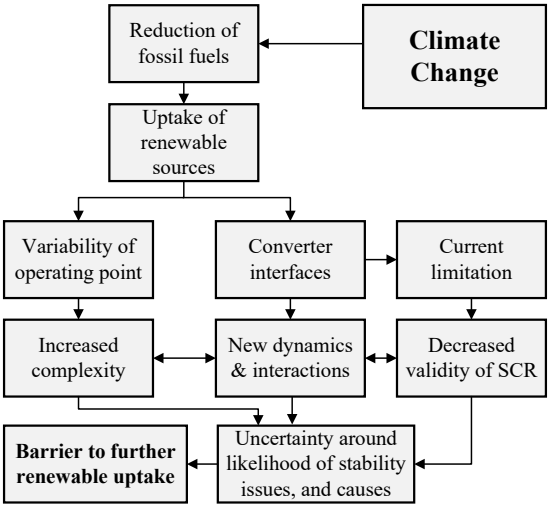

Figure 1.1: Illustration of the high-level motivations.

a global increase of almost 90% by 2030 compared to 2023 levels. Visualisation of this forecast, along with the breakdown of RESs by technology is seen in Fig. 1.2.

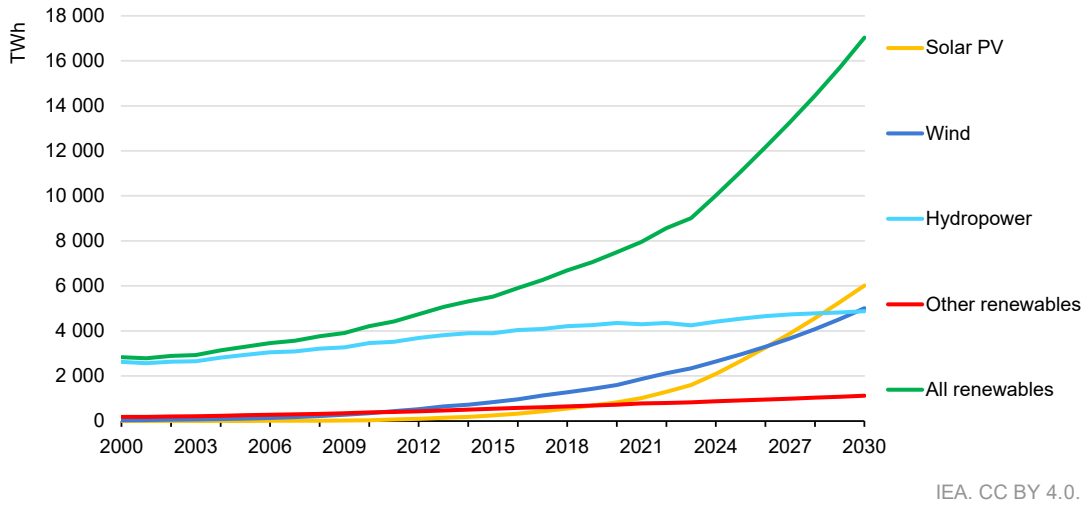

Figure 1.2: Global electricity generation by technology, forecast by the International Energy Agency (IEA) [4].

It is not necessarily the case that the influx of CIGs will deteriorate the dynamic response and stability of the power system. In fact, there is potential for improved power system dynamic response through manipulation of the flexible, digitally implemented control schemes. For example, it is known that as the penetration

of CIGs increases, traditional grid-following (GFL) control will be susceptible to instabilities [5] but the inclusion of grid-forming (GFM) control can often maintain stability of the voltage-sourced system [6] in such circumstances. However, this understanding is based on the fundamental concepts of GFL and GFM control (see Section 1.2.2 for more information), while actual control implementation can be more complex and might introduce unexpected dynamics and interactions under different operating conditions. Furthermore, novel control-based stability mechanisms–which were previously impossible due to the rigidity of the SG dynamics–are made possible in CIG-permeated systems. For example, fast frequency response (FFR) [7] or impedance shaping [8, 9], amongst others. Ultimately, the range of possible control implementations, and hence dynamics, on the power system can aid or deteriorate the system response, but either way the complexity is escalated.

In this context, the research in this thesis follows two primary intertwining goals. The first is towards the shedding of light on novel power system small-signal dynamics and interactions resulting from the vast uptake of CIGs, with a particular interest in the use of GFM control. While the second proposes methodologies for better understanding small-signal dynamics in power systems with CIGs from a probabilistic and then an output variability perspective.

Small-signal studies make use of the linear approximation around the power system operating point, enabling associated analysis techniques [10–14]. It is utilised in this work for extracting the eigenvalue decomposed dynamics of power systems with CIGs, offering insights into novel emerging interactions and their behavioural characteristics and potential for mitigation. This is a common study approach in power system engineering but the relative unfamiliarity of CIG-permeated systems necessitates further case studies with regards to different control philosophies (e.g., GFL and GFM), architectures (i.e., cascaded structures), implementations (e.g., virtual synchronous machine vs. droop control [15]), and tunings, in addition to different power system layouts, operating points, generation mixtures, amongst other aspects, to ensure a comprehensive understanding of how future power systems will respond to the small-disturbances which they are continually subjected to.

Moreover, as a result of the increasing uptake of variable RESs and the concomitant uncertainty of operating point, probabilistic methods are becoming increasingly necessary in CIG-permeated bulk power systems (BPSs) [16,17]. However, when executing probabilistic small-signal analysis (PSSA), practitioners are generally restricted to worst-case stability index-based assessments with the majority of the detail obscured by the plethora of data [18–23], even for modern machine-learning-enhanced approaches [24, 25]. Therefore, we suggest a framework for the PSSA of power systems with CIG which enables the characterisation and behavioural analysis of specific dynamic interactions across the full operating range. This should theoretically provide a comprehensive overview of interactions of which to be vigilant as well as greater confidence for the system operator with regards to the (small-signal) stable operation of any given system despite likely operating point variations.

Another ongoing research area is associated with the limitations of short-circuit ratio (SCR)–and similar traditional static grid strength metrics–in CIG-permeated BPSs. The SCR has been used as a proxy measure for grid strength since it reflects the impedance coupling from an ideal voltage source [26]. However, CIG current limitation to protect the power electronic switches means that it will not provide the same level of short-circuit current, even if using GFM control approaches. Furthermore, such metrics focus on fundamental frequency dynamics and do not capture the wide bandwidth interactions that might be seen in CIG-permeated power systems. Recent attempts at grid strength quantification have proved better at reflecting the influence of CIGs [26–29], however, these are either based on small-signal stability margins and/or are not able to reflect the decoupling of voltage and frequency strength in modern power systems [15, 30, 31]. Whereas, in this thesis we suggest an alternative viewpoint for *small-signal grid strength* through a perspective of *small-signal variability* (related to time-domain amplitude deviations)–rather than small-signal stability margin–which can capture the decoupling of voltage magnitude and frequency strength, as well as the impact of different small-signal disturbance locations on the variability of the system. From this, a quantification metric and analysis methodology is derived based on the modal superposition concept. By adopting a modal contribution perspective, the

influence of particular dynamic modes/eigenvalues (which might represent interactions between power system elements) on the small-signal variability of the output time-domain response can be investigated. The approach is also shown to enable the analysis of small-signal variability, including the influence of different dynamic modes, on different timescales.

Ultimately, the work in this thesis is expected to benefit electrical engineers in both academia and industry through progression of the knowledge of the emerging power system dynamic landscape with respect to multi-machine interactions involving CIGs, while providing tools to better analyse such systems from a small-signal perspective.

The technical motivations of the thesis goals are explored more thoroughly in the discussions of the technical background in Section 1.2, before the contributions and publications are outlined in Section 1.3 and Section 1.4, respectively. The outline of the thesis is detailed in Section 1.5.

1.2 Background

With the high-level motivation justified, this section provides further general technical context and hence reasoning for the targeted studies throughout the thesis[2]. This includes an overview of the changes occurring within the power system dynamic landscape, the underlying concepts associated with the GFL and GFM control philosophies, the need for more detailed power system models, and the basics of small-signal modelling and analysis.

1.2.1 The Changing Dynamic Landscape

The power system dynamic transition is characterised by an increasing dependence on converter control and variable RESs. This causes drastic change for steady-state, small-signal, and large-signal stability[3].

[2] A literature review is provided at the start of each technical chapter in this thesis (Chapters 3 to 6 and Appendix B) to contextualise the specific contributions and novelty with respect to the state-of-the-art.

[3] Note, small- or large-signal phraseology is often replaced with small- or large-disturbance in the literature.

Power System Stability Classifications

Epitomising the scale of the undergoing changes is the recent revision and extension of the power system stability classifications by a Task Force set up by the Institute of Electrical and Electronic Engineers (IEEE) Power System Dynamic Performance Committee, as reported in [32] (summarised in [33]). It is explained how the introduction of CIGs may influence traditional stability categories, and in particular how "CIGs can impact a wide range of dynamic phenomena, ranging from electromagnetic transients to voltage stability, and across both small- and large-disturbance stability." For example, it is stated that CIGs can affect electromechanical modal characteristics such as damping, frequency and observability, thereby influencing small-signal rotor angle stability. Similarly, large-signal rotor angle stability can be influenced by reduced system inertia and non-swing-equation-based dynamic behaviour resulting from CIG controls. With regards to voltage stability, the emergence of active distribution networks with significant penetrations of CIGs can influence the reactive power flows and hence voltage dynamics of the larger system. Finally, it is described that CIGs can be a detriment to frequency stability if they reduce inertia provision or are limited in supply due to RES intermittency, but the flexibility of control can also enable FFR [7] provided sufficient active power headroom and over-sizing of electrical components. In general, it is repeatedly mentioned that the inclusion of CIGs can have positive or negative impact on different stability categories dependent on a wide range of factors–including choice of control, system operating point, system layout, etc.–and hence there is often no consensus on the overall dynamic understanding and best practices with regards to the choice of location, controller architecture, and controller tuning of CIGs. This is the basis for the investigative studies in this thesis, whereby we have aimed to increase the depth of knowledge within the literature relating to small-signal interactions in power systems with CIGs. This includes participation factor (PF)-based analysis for better understanding the underlying mechanisms of novel multi-machine interactions, in addition to parametric sensitivity studies and the influence of different controller architecture choices.

In addition to the influence of CIGs on existing stability phenomena, there is the

introduction of two completely new classifications: resonance stability and converter-driven stability. The full resultant framework is found in the hierarchical diagram of Fig. 1.3. The resonance stability phenomena incorporates torsional resonance and electrical resonance. These are both primarily due to interactions involving series compensation, with the former involving the mechanical turbine-governor shaft and the latter with the electrical aspects of the (usually induction) generator. The control of CIGs–or other converter-interfaced devices such as HVDC connections, flexible AC transmission system (FACTS) devices, EVs, amongst others–acting in the timescales of such sub-synchronous phenomena can influence their characteristics. When considering torsional resonance, this is termed device-dependent subsynchronous oscillation (DDSSO) and for electrical resonance it is termed subsynchronous control interaction (SSCI) [34]. Note, DDSSO may also refer to interactions with non converter-interfaced controllers such as power system stabilisers (PSSs). It is highlighted that the influence of control in DDSSO can be both beneficial or detrimental, whereas discussions of SSCI are usually related to circumstances whereby the control of the doubly-fed induction generator's converter is the catalyst for the negative damping characteristic resulting in instability. However, they emphasise the fact that the underlying phenomena related to the resonance stability is not dependent on the CIG control.

Contrastingly, as the name suggests, converter-driven stability is directly caused by power electronic converters and their controllers. As a result of the wide-bandwidth of converter control, interactions from electromechanical to electromagnetic timescales can occur. To address this, the converter-driven stability has been split into fast interaction and slow interaction categories. The former applying to dynamics approximately 10 Hz or less and the latter covering everything above this, up to the kHz range.

Despite the unarguable usefulness of the classification framework presented in [32, 33] and Fig. 1.3, an alternative approach has been proposed by Shair et al. in [35] which aims to maintain consistency with respect to the categories of the original classification developed in 2004 [36]. They argue that the resonance and converter-driven stability categories do not fall into the system variable, disturbance size, and time scale layers of the original framework, spurring their alternative classification

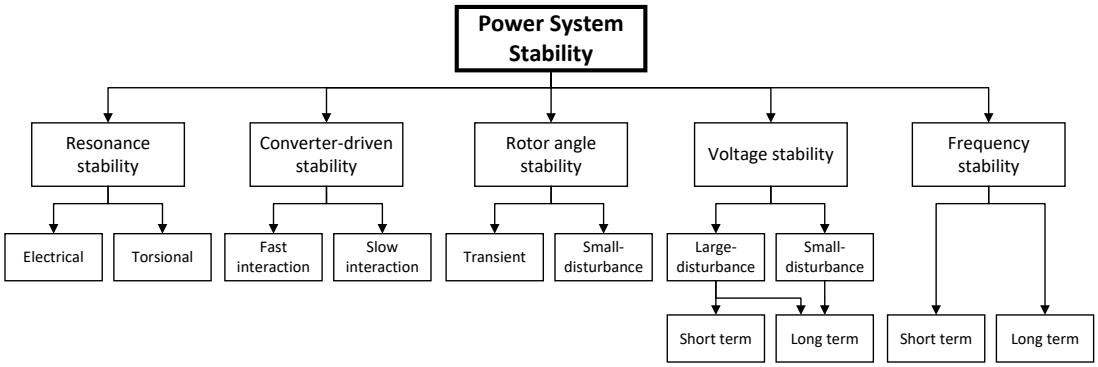

Figure 1.3: Power system stability classification framework developed by the IEEE Power System Dynamic Performance Committee Task Force in [32].

structure as displayed in Fig. 1.4. An example of the potential ambiguity they have attempted to circumvent is the use of the term converter-driven stability since we have seen that resonance stability could be primarily converter-driven and stability issues may arise due to converter control with respect to rotor angle stability, voltage stability, and frequency stability, for small- and large-disturbances and in both the short and long term. To address the identified issues, they have added another level of categorisation which is dependent on the frequency range of the dynamic phenomena. This allows for the separation of dynamics near the fundamental frequency–which are the focus of the original classification and the quasi-static phasor/root-mean-square (RMS) modelling approximation (see Section 1.2.3)–and the wide-bandwidth dynamics and potential stability issues which are more prevalent in CIG-permeated systems [30]. Additionally, rotor angle stability is renamed angle/synchronous stability to reflect the fact that this can encompass control-based synchronisation such as with the phase-locked loop (PLL) of the GFL or a range of synchronisation approaches for the GFM (which will be returned to in Section 1.2.2). An additional point to note is the inclusion of sub-/super-synchronous oscillations (S^2SOs) which was not highlighted by [32] despite having been seen in real-world scenarios. This phenomena results from observing sub-synchronous oscillations (SSOs) from the electromagnetic perspective, i.e., when observing the voltage and/or current signals an SSO will cause two sidebands around the fundamental frequency. E.g., an apparently induction generator effect-

induced event occurred in the Guyuan area system in China on the 19th of March, 2013, with strongly coupled 8.1 Hz and 91.9 Hz oscillations [37]. Note, these equate to sideband oscillations of 50 Hz $\pm$ 41.9 Hz. It is suggested in [35] to refer to such situations as S^{2}SOs but to revert to the terminology of SSO if the coupled super-synchronous oscillation is not obvious. Finally, the intermediate and high frequency categories account for interactions between the wide-bandwidth control of CIGs, also with the potential for contribution from passive network elements such as transmission lines, series compensation, and CIG output filters [35].

The work in this thesis is focused on the potential for CIGs to interact with each other and existing power system elements from a small-signal perspective. As such, this may come under the converter-driven stability, resonance stability, or small-disturbance rotor angle and voltage stability if considering the framework presented in Fig. 1.3. However, if using the framework in Fig. 1.4, the work comes under small-disturbance stability, across all frequency ranges, stability variables (excepting frequency stability since this is not considered to have a small-disturbance aspect), and timescales (dependent on what has been modelled).

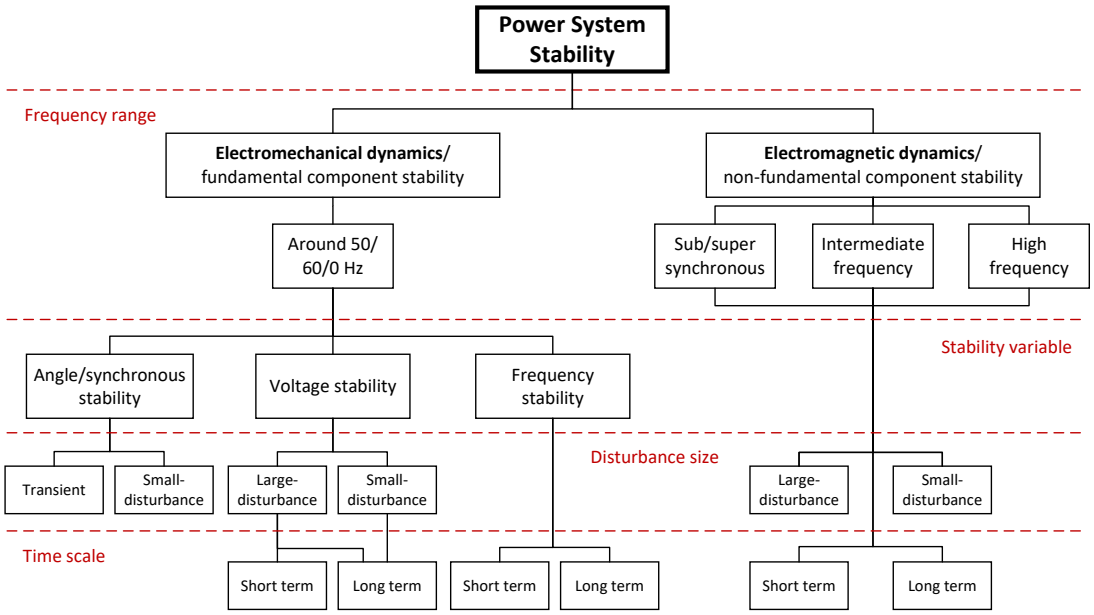

Figure 1.4: Alternative power system stability classification framework suggested by Shair et al. in [35].

Further discussions of power system stability (and its classifications) in modern CIG-permeated BPSs can be found throughout the literature with some examples being found in [38–42].

Real-World Examples

Regardless of how the emerging dynamic phenomena is ultimately categorised, the attempt to understand the fundamental causes of converter related interactions is an ongoing process. As an example, an approximately 8 Hz oscillation appeared on two separate occasions in the wind power heavy North of Scotland on the 24$^{\text{th}}$ of August, 2021 [43]. On this occasion, the oscillations were suppressed through the connection of more synchronous generation. However, similar events occurred again on five days in June and July of 2023. The UK National Grid Electricity System Operator (NGESO)[4] subsequently performed model-based investigations to identify the source of the issue and instruct the appropriate equipment owner to adjust their control settings. This ostensibly solved the issue. NGESO reported these events in their ESO Operational Transparency Forum on the 8$^{\text{th}}$ of November, 2023 [44] and in the annual Operability Strategy Report [45]. This is an example of a situation in which model-based interaction analysis was able to provide vital information with regards to oscillation source detection and subsequent mitigation through updating control settings. Note, it is not actually revealed if the changes were made to the control of a CIG specifically but the usefulness of such studies and the infancy of the identification and mitigation of converter-driven oscillations is clear from this example. Strengthening this idea is the fact that NGESO have recently introduced guidance notes for a series of small-signal studies, including the eigenvalue method, expected to be performed as part of the connection compliance process for CIGs [46]. Similarly, small-signal studies are highlighted throughout the Australian Energy Market Operator (AEMO) Power System Stability Guidelines [47].

Some instances of converter interactions have been investigated and presented more thoroughly in the literature, such as the Guyuan example mentioned earlier [37],

[4]NGESO have recently become National Energy System Operator (NESO), however, the familiar name of NGESO is still used throughout this thesis where relevant.

amongst others [35, 43, 48–53]. However, the flexibility and lack of standardisation of converter control brings a plethora of possible controller realisations, in particular for GFMs, with potential for differing interaction mechanisms that need to be understood prior to more widespread adoption of CIG technologies. Some attempts have been made in this direction, mostly relating to GFLs. For example, [50] highlights the potential for approximately 20 Hz SSOs–similar to the 20 Hz Hydro One event [54], the AEMO 19 Hz event on 20$^{\text{th}}$ August 2020 [55], and the 22 Hz Dominion Energy oscillations [56]–due to slow current control, insufficient damping of the PLL, or interactions between the PLL and shunt compensation. This is aside from the vast array of influencing factors on small-signal dynamic stability and interactions more generally, as discussed in both [32] and [35].

Variability of Renewable Energy Sources

It is well known that the variability of RESs, and concomitant variation of system operating point, can have a significant impact on small-signal dynamics [57]. The power that can be extracted by wind turbines and photovoltaic (PV) panels is of course influenced by the wind speed and solar irradiance, respectively. From a system operator perspective, this can impact the variability of generation when considering large transmission-scale wind farms or PV solar farms. However, it can also impact the demand due to the unmetered wind and solar connected at the distribution level. To exemplify such variability (notwithstanding the forecast uncertainty), Fig. 1.5 displays the forecast embedded wind and solar generation in the UK on the 8$^{\text{th}}$ of August 2024, normalised by the estimated installed capacity[5]. This forecast was obtained from the "Embedded Solar and Wind Forecast" dataset from the National Grid Data Portal [58], accessed on 7$^{\text{th}}$ of August 2024. Note, this displays the variability in a single day, never mind the variability across a full week, month, or even year.

The work in this thesis is focused on small-signal modelling and analysis (Section 1.2.4) which is valid only in small-regions around the linearisation (or operating) point. With increased variability of generator dispatch, and hence operating point, due to

[5]Note, the combined estimated wind and solar generation is normalised against the combined wind and solar installed capacity.

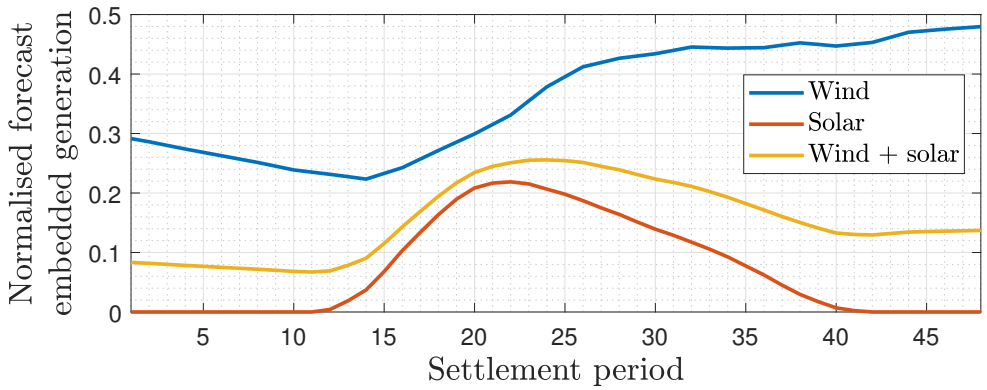

Figure 1.5: Normalised forecast embedded wind and solar generation in the UK for the 8$^{\text{th}}$ of August 2024 [58].

the variable RESs comes the reduction of generalisability of single operating-point deterministic power system small-signal analysis studies. Such variability will not only affect the small-signal stability margins of the power system but also the particular interactions that are occurring (e.g., in terms of modal participation factors, Section 1.2.4). This is the motivation behind the proposed probabilistic small-signal interaction analysis framework in Chapter 5.

1.2.2 Grid-Following and Grid-Forming Converters

This subsection reviews the fundamental concepts of GFL and GFM generation sources. The discussion is framed within the context of their behaviour within BPSs and the associated benefits and drawbacks of each approach. The specific control structures that are adopted throughout this thesis are further discussed in Chapter 2.

As alluded to previously, controlling CIGs in a GFL nature–whereby the voltage angle at the point of common coupling (PCC) is measured and the desired active and reactive power is exchanged with the grid accordingly[6]–has been the go-to approach in BPSs to date. However, as the penetration of CIGs increases, there are fundamental limitations with the GFL control philosophy. Primarily, the lack of GFM source means that the voltage across the (voltage-source-based) power system is insufficiently maintained. The resultant lack of strict voltage-sourced behaviour is

[6]This description highlights the "current-source" nature of GFL-controlled CIGs [6].

typically referred to as a weak grid, in which issues arise related to high variability of frequency and voltage signals, a common (but not the only) example being the destabilising interactions between the highly variable grid voltage and the PLL-based synchronisation mechanism of the GFL control [5, 59].

Consequently, the use of GFM control approaches–which have historically been restricted to micro-grid applications [60]–for CIGs connected to BPSs has attracted huge interest in the research community [61–65] and, increasingly, practical applications in industry [66, 67]. This control philosophy is the opposite of GFL, in that the GFM controller actively generates the voltage phasor at the PCC[7].

The definitions of GFM and GFL sources have been discussed extensively in the literature, from a range of perspectives including control topologies, functional specifications, and impedance characteristics, amongst others [6, 9, 38, 62, 68–74]. We will discuss here only the basic concepts of GFM and GFL control and typical supplementary functionalities when connected to BPSs to help contextualise the choice of particular control topologies outlined in Chapter 2. For more information with regards to the mathematical concepts and underlying dynamical characteristics, the reader is referred to the references populated throughout this subsection.

From a theoretical perspective, a GFL and a GFM can be considered to be a controlled current source and a controlled voltage source [6], respectively, with a wide spectrum of additional ancillary services and control functionalities (sometimes referred to as grid-supporting [60]) between these two bounds. These concepts are further explored in [60] (which refers to GFL as "grid-feeding"), from which the (adapted) Fig. 1.6 is taken. Practically, a GFL converter is not an ideal current source and a GFM converter is not an ideal voltage source. Furthermore, for BPS applications, there are some functionalities which are indispensable and are therefore often considered in the practical definitions of GFM control such as the need for power sharing between, and self-synchronisation with other devices on the system. An example is the commonly cited definition provided by North American Electric Reliability Corporation (NERC) [69]:

[7]The specific location actually depends on the particular control structure used. For more information, see Section 2.5.5.

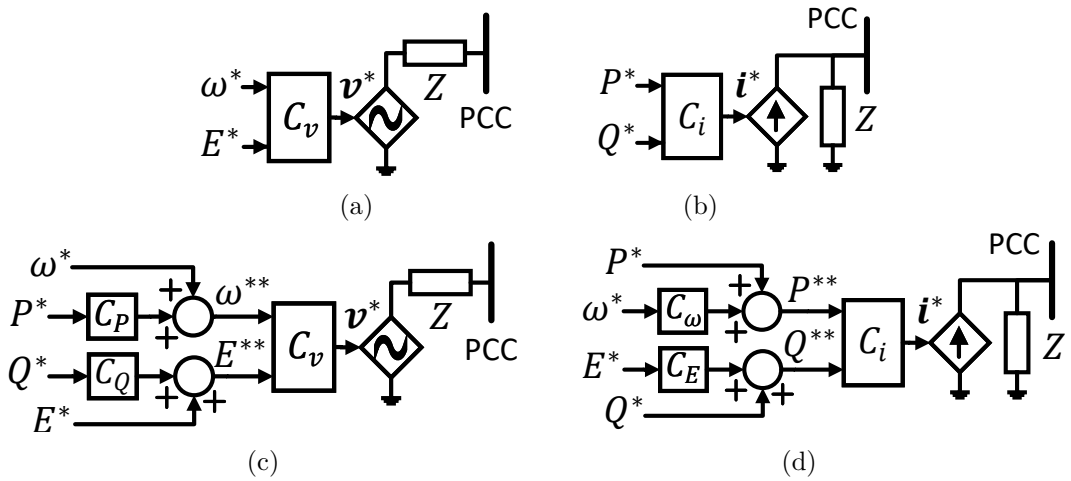

Figure 1.6: Adapted from [60]. Simplified representation of bulk power system-connected CIGs. (a) grid-forming, (b) grid-feeding (grid-following), (c) voltage-source-based grid-supporting, and (d) current-source-based grid-supporting.

> The primary objective of GFM control for BPS-connected IBRs [inverter-based resources] is to maintain an internal voltage phasor that is constant or nearly constant in the sub-transient to transient time frame. This allows the IBR to immediately respond to changes in the external system and maintain IBR control stability during challenging network conditions. The voltage phasor must be controlled to maintain synchronism with other devices in the grid and must also regulate active and reactive power appropriately to support the grid.

It is not just variations of the GFL (or current-forming-voltage-following [6]) and GFM (or voltage-forming-current-following) concepts that are possible, but direct combinations of these philosophies with regards to the partial-forming or, similarly, cross-forming concepts [31, 75–77]. This is where the formation of the voltage (and/or current) magnitude and angle are considered separately, enabling useful functionality such as the choice of different combinations of controlled and measured variables [31, 76, 77], and even saturation-informed current limitation [75, 76] for avoiding the deficiencies of current limitation in purely-GFM-based control approaches[8] [78, 79].

Distinguishing between GFLs and GFMs via functional specifications is suggested

[8] Discussion on the research area of CIG current limitation is largely out of the scope of this thesis.

in [68] and expanded on in [80]. For example, Table 1.1 which is taken from [80] outlines key functional specifications in the context of BESSs.

Table 1.1: Functional specifications of GFL and GFM BESS, taken from [80].

Capability	**Grid-forming**	**Grid-following**
Sub-cycle Voltage and Frequency Support	✓	
Phase Jump Resistance	✓	
System Strength Support	✓	
Ability to Stably Operate with Loss of Last Synchronous Machine	✓	
Dispatchability	✓	✓
Steady-state Voltage Control	✓	✓
Dynamic Reactive Power Support	✓	✓
Active-Power Frequency Control	✓	✓
Disturbance Ride-Through Performance	✓	✓
Fault Current and Negative Sequence Current Contribution	✓	✓
Cyber and Physical Security	✓	✓

The brief discussion in this subsection is to provide context with regards to the state-of-the-art CIG control philosophies which have informed the particular implementations utilised for the work in this thesis, as described further in Chapter 2.

1.2.3 The Need for Detailed Models

It has been found that the inclusion of power electronics-interfaced devices reduces the validity of the quasi-static modelling assumption, partly due to interactions involving the wide-bandwidth control of the converters and potentially the electromagnetic dynamics of the network [81–85]. Although there have been several attempts at determining conditions under which quasi-static modelling approaches are sufficient, even with the inclusion of converters [86–94], in the majority of cases it is not so clear whether the assumptions are valid unless some kind of formal procedure is performed such as with the singular perturbation theory (SPT) [95]. Furthermore, in some cases, these studies suggest parameter conditions under which the quasi-static assumption can be used for accurate power system studies. However, the ability to adopt quasi-static phasor modelling would therefore be reliant on specific controller architecture/tuning

choices which would not necessarily provide the most optimal response (not to mention that, for BPS studies, this would require enforcement of such parameter conditions for all CIG owners on the system). However, if a quasi-static model is deemed appropriate, it can be used for the investigation of a more limited range of dynamic phenomena. More specifically, the classical fundamental frequency power system stability categories [35]. Out of the range of capability are higher frequency phenomena associated with fast converter control and electromagnetic dynamics as well as sub-synchronous resonance, as discussed earlier in Section 1.2.1.

The importance of including the network dynamics in small-signal studies, in particular, is highlighted in [96]. They display examples of systems whereby the linear quasi-static model fails to predict instability when the linear electromagnetic transient (EMT) model (in the dq0-frame) shows that there actually is instability occurring. This happens even when the system eigenvalues have frequencies much lower than the nominal synchronous frequency. This paper also provides a potential criterion for determining when the quasi-static model is appropriate. It notes that the main reasons for the failings are the constant frequency assumption and the omission of the high frequency effects in the performed studies. Similarly, [97] models a droop-controlled CIG-based microgrid and compares a reduced order small-signal model to a small-signal model derived from dynamic phasors (i.e., with a higher level of modelling detail including the network dynamics). It is found that the reduced order small-signal model is unable to predict small-signal instabilities that occur. The dynamic phasor based small-signal model does predict these small-signal instabilities. These studies show the inability of reduced-order models in identifying small-signal instability, and hence the need for higher fidelity detailed models. This is not even to mention the potential lack of ability to capture novel dynamic interactions involving different elements of CIG control. An example of this is found in [98] whereby eigenvalue analysis was performed on a 118-bus network with CIGs. From the small-signal analysis of the large system, it is revealed that there are scenarios in which unstable SSOs (approximately 30 Hz in this case) can occur, which the EMT-level model exhibits but the quasi-static model does not capture.

The concept of hybrid modelling has also emerged in an attempt to ensure the relevant network dynamics are represented while achieving some reduction in complexity of the system model [83, 99, 100] (if possible). This involves dynamic modelling of the network but only in the regions around CIGs or other power electronics-interfaced devices.

As has already been touched on in this subsection, the discussion of sufficiency in power system modelling is often focused around the question of quasi-static/quasi-steady/quasi-stationary phasor/RMS vs. EMT models and, relatedly, solvers. Alternative modelling approaches such as the dynamic phasor concept can also be used, offering a trade off in terms of model order reduction and representation of the necessary dynamics in CIG-permeated systems. For more detailed information on different modelling approaches, see [30, 81, 101]. As will be discussed in more detail in Chapter 2, the studies in this thesis utilise detailed models including network dynamics, 8^{th} order SGs, and detailed representation of CIG control in terms of the cascaded control structures. This modelling is completed with dq0 representation (including for the network dynamics) which, when paired with common modelling assumptions such as the neglection of converter switching transients [102], can achieve improvement in computational efficiency[9] for balanced three-phase systems compared to instantaneous abc representation without loss of accuracy [101]. Such high detailed models may in some cases be referred to as EMT. EMT modelling, as the name suggests, maintains detail regarding the electromagnetic dynamics of electrical systems. When the EMT approach is mentioned within the literature, it is sometimes alluding to the instantaneous (abc/waveform) representation of the power system signals (voltages and currents). This is termed "electromagnetic transient" because of the inclusion of the namesake's faster dynamics in the modelling, and to distinguish from the quasi-

[9]The increase in computational efficiency arises from the increase in time-step resulting from the baseband nature of the dynamic phenomena [101]. Even if somewhat higher frequency phenomena such as SSOs are present, increase in time-step can be achieved for large segments of the simulations by pairing the dq0 representation with variable time-step solvers. Note, these benefits are not necessary for the majority of the work in this thesis since it focuses on small-signal eigenvalue analysis rather than time-domain simulations. However, the use of dq0 transformed signals for the representation of the network might also simplify the interconnection with machines which are typically modelled in this frame: for SGs this is to remove the time-dependent inductive elements related to the flux linkage [10, 11] and for CIGs this is because the dq0 transform simplifies the control design [103].

static/RMS approach which neglects these dynamics. However, the definition based on inclusion of network/electromagnetic dynamics means that, in the literature, EMT may be a broader heading encompassing abc/waveform models, detailed dynamic phasors, and dq0 transformed models, amongst others [81, 101]. Note, the dq0 representation is obtained from the abc representation via transformation without simplification [101]. In this thesis, when referring to EMT, we mean inclusion of the network dynamics and not the instantaneous abc representation of the network and signals.

1.2.4 Small-Signal Analysis

Linearisation of a power system dynamic model enables the utilisation of linear analysis techniques, which can offer insights into the nature of power system dynamics that are not achievable through non-linear time-domain simulations alone [13, 14, 104–106].

Eigenvalue analysis is the foundation on which the small-signal interaction analyses are performed (Chapter 3 and Chapter 4), and the advanced analysis methodologies are developed (Chapter 5 and Chapter 6) in this thesis. More information on the mathematics of eigenvalue analysis, including the calculation of PFs, can be found in Section 2.1.2.

The eigenvalues of the linear power system dynamic model represent the inherent oscillatory and/or non-oscillatory dynamics [40]. The time-domain trajectory of any state or output of the system in response to an input disturbance can be determined by a superposition of the individual *modal* responses whose behaviour is described by the corresponding eigenvalue and its eigenvectors [10]. This idea of modal superposition is further investigated in Chapter 6. The eigenvalues themselves provide information regarding the damping and oscillation frequency of these eigenvalue-described dynamics, and, as the name suggests, the PFs provide detail on the states which participate in the eigenvalues/modes. These PFs are related to the right and left eigenvectors, the former of which provides information regarding the observability of modes on each state, and the latter provides information on the controllability of each mode with respect to each state [10].

Therefore, the eigendecomposition of the linear dynamic power system model can

aid in the identification of potential novel oscillations–or even non-oscillatory dynamics which have been shown in academic literature to have the potential to cause instabilities in CIG-permeated systems (although to the best of my knowledge this has not yet been seen in practice) [59]–while, using the PFs, illuminating the participating system states. This latter point thereby facilitates the identification of novel interactions between different elements in CIG-permeated BPSs, hence the adoption of small-signal analysis for the studies in this thesis.

1.3 Contributions

As has been motivated and contextualised, there are two primary intertwining themes of the work in this thesis: novel small-signal interaction identification and characterisation, and small-signal analysis methodologies for power systems with CIGs. Such focus is adopted to address the research gaps outlined previously regarding the need for investigative studies of novel small-signal multi-machine interactions in detailed power system models with consideration of the complex (and varied) controller dynamics, the increasing range and uncertainty of system operating point, and the reducing validity of static grid strength quantification metrics.

The particular scientific contributions can be summarised as follows:

- Identification and characterisation, of multi-machine interactions in a transmission-scale multi-machine power system with SGs and bandwidth-restricted GFMs. Furthermore, the parametric sensitivity analysis of such identified interactions with respect to key control parameters.

- Detailed comparative study of different combinations of GFL and GFM controller architectures (in terms of cascaded control structures) in multi-machine systems with SGs, GFLs and GFMs. Including further interaction characterisation in addition to eigenvalue and stability margin trajectories corresponding to variation of key system parameters.

- A framework is proposed for detailed probabilistic analysis and characterisation of

the behaviour of new types of interactions in converter-permeated power systems. In relation to this framework are the following contributions:

  - A systematic characterisation method for detailed dynamic interaction analysis across the operating range.
  - The application of clustering to decompose the full range of modes across the operating range into key distinct interactions based on their PFs.
  - The introduction of a stability weighted participation index (SWPI) for characterising interactions (clusters of modes with similar PFs) with a (real part of eigenvalue) weighted average of PFs.
  - Application of the proposed PSSA framework to a multi-machine system with detailed high-order models of SGs, GFLs, and GFMs to study the behaviour of new types of interactions. This includes a thorough investigation of novel small-signal dynamics across the operating range in CIG-permeated systems, including the highlighting of potential SSOs related primarily to the inner voltage controls (IVCs) of GFMs.

- A method is proposed for the analysis of output small-signal variability (related to amplitude deviations of the time-domain response, which is used as a proxy for small-signal grid strength). In particular, it is suggested for quantification of voltage magnitude and frequency variability at different bus locations. The specific contributions associated with this method are:

  - An alternative viewpoint for small-signal system strength from the perspective of small-signal variability, providing a more direct quantification of output signal (e.g., voltage and frequency) amplitude deviations.
  - The introduction of a metric to quantify small-signal variability based on modal superposition. This is named maximum absolute modal contribution (MAMC) and it allows to take into account detailed aspects related to system dynamics and interactions, contrary to conventional system strength metrics.
  - A clear link between the contribution of any given mode/interaction to the

variability of any given output through the analytical calculation of the maximum deviation of the decoupled modal response.

- The capability to extract distinct variability trends across different timescales and the respective fast or slow dynamic modes that contribute.
- Using the proposed method and metric, the impact of the introduction of both GFLs and GFMs on the locational small-signal variability of a multi-machine system is investigated. For example, replacing SGs with GFLs in a given area is seen to increase both the voltage and frequency variability in said area.

- Finally, a significant proportion of the work completed throughout this PhD was the development of an automatic and modular power system small-signal modelling tool. The approach was developed in MATLAB 2021b [107] and it is hoped that the detailed description within this thesis along with access to the open source script files that are made publicly available (including examples) at [108] will benefit engineers looking to perform small-signal investigations into power systems containing CIGs. See Chapter 2 for further details regarding the power system modelling approach and the repository of linearised dynamic models that have been developed.

1.4 Publications

Provided here is a list of publications that have been developed over the course of this PhD degree. When the work that lead to a publication is described within this thesis, specific mention is given in the chapter introduction.

Journal Papers - Leading Author:

Published:

- **L. Benedetti**, P. N. Papadopoulos and A. Egea-Àlvarez, "A modal contribution metric for quantifying small-signal variability in power systems with converter-

interfaced generation," *IEEE Transactions on Power Systems*, vol. 40, no. 3, 2025. doi:10.1109/TPWRS.2024.3500786.

- **L. Benedetti**, A. Paspatis, P. N. Papadopoulos, A. Egea-Àlvarez and N. Hatziargyriou, "Investigation of grid-forming and grid-following converter multi-machine interactions under different control architectures," *Electric Power Systems Research*, vol. 234, article no. 110813, 2024. doi:10.1016/j.epsr.2024.110813.

Submitted for publication:

- **L. Benedetti**, A. Egea-Àlvarez, R. Preece and P. N. Papadopoulos "Enabling characterisation of dynamic interactions with probabilistic small-signal analysis in converter-interfaced power systems," *IEEE Transactions on Power Systems*, under review.

Journal Papers - Co-author:

- Y. Chen, **L. Benedetti**, R. Preece, P. N. Papadopoulos, M. Barnes and A. Egea-Àlvarez, "Investigating small-disturbance stability in power systems with grid-following and grid-forming VSCs using hybrid modelling approaches," *Electric Power Systems Research*, vol. 211, article no. 108448, 2022. doi:10.1016/j.epsr.2022.108448.

Conference Papers - Leading Author:

- **L. Benedetti**, P. N. Papadopoulos and A. Egea-Àlvarez, "Small signal study of grid-forming converters and impact of different control structures and parameters," *2022 IEEE PES Innovative Smart Grid Technologies Conference Europe (ISGT-Europe)*, Novi Sad, Serbia, 2022. doi:10.1109/ISGT-Europe54678.2022.9960644.

- **L. Benedetti**, P. N. Papadopoulos and A. Egea-Àlvarez, "Small signal interactions involving a synchronous machine and a grid forming

converter", *2021 IEEE Madrid PowerTech*, Madrid, Spain, 2021. doi:10.1109/PowerTech46648.2021.9494923.

1.5 Thesis Outline

The content and organisation of the remaining chapters are described hereafter. A literature review is provided at the start of each technical chapter in this thesis (Chapters 3 to 6 and Appendix B) to contextualise the specific contributions and novelty with respect to the state-of-the-art.

Chapter 2 details the power system modelling that has been utilised in this work. This includes the specific dynamic models that have been adopted and linearised for each power system component as well as the automatic and modular initialisation and compilation procedure that has been implemented.

Chapter 3 investigates potential small-signal interactions between GFM sources, i.e., SGs and GFM converters in a transmission-scale multi-machine power system (a modified version of the IEEE 39-bus network). Detailed models are utilised including 8^{th} order SGs and multi-loop controlled, bandwidth-restricted GFMs. PF analysis is used to identify the key types of interactions present on the system, which are further investigated through parametric sweeps, offering insights into their potential for destabilising effects under different system and control parameters. In particular, the identified key interactions are split into three categories: electromechanical, inner current control (ICC)-related, and IVC-related.

Chapter 4 performs a comparative small-signal analysis of different combinations of CIG controllers in systems with SGs, GFLs, and GFMs. In particular, the impact of different cascaded control structures for both the GFMs and GFLs are considered. For the 2-machine and IEEE 9-bus (3-machine) systems studied, the different types of multi-machine interactions that can exist for the different combinations are investigated through PF analysis. Furthermore, the eigenvalue trajectories (and therefore system stability margins) under variations of key system parameters are compared for the different architecture combinations.

Chapter 5 proposes a framework for PSSA in power systems incorporating CIGs. A

systematic characterisation procedure is suggested, which includes clustering of modes based on their PF-based characteristics, as well as the introduction of the SWPI. This index enables characterisation of groups (or clusters) of modes, aiding in identifying the key interactions across the whole operating range. This approach enables analysis both in terms of probabilistic behaviour (e.g., probability of instability) and the contribution of particular categories (such as generators or power system dynamic phenomena) to the identified interactions on the system. The proposed framework is applied to a modified IEEE 68-bus system to gain insights into potential interactions involving SGs, GFLs, and GFMs across the full range of operating points, and their probabilistic behaviour.

Chapter 6 addresses the issue of the reducing validity of static grid strength metrics such as the SCR. From an alternative viewpoint of small-signal variability, a methodology and accompanying metric, named the MAMC, are introduced. This enables quantification of locational small-signal variability as well as tractability with regards to the specific interactions contributing most to variability of any given output/location (in particular, we focus on the voltage magnitudes and frequencies at each bus). The Kundur 2-area system is adopted to display the capabilities of the metric. Further case studies are performed to highlight the impact that the introduction of GFLs or GFMs have on the small-signal variability of the system as well as to highlight the capability of quantifying the variability, and identifying the most contributing interactions, at different timescales.

Chapter 7 summarises the conclusions of the thesis, also providing a summary of the different dynamic phenomena and interactions observed throughout the thesis. Furthermore, a discussion of directions for the continuation of the work is included.

Appendix A details the validation of the small-signal models of Chapter 2.

Appendix B discusses a preliminary investigation into interactions between SGs and GFMs from an electromechanical perspective with simplified generator models.

Chapter 2

Power System Small-Signal Modelling

This chapter details the mathematical small-signal modelling of the power system and the implementation approach developed in MATLAB 2021b [107]. Since the small-signal models have been developed by the author of this thesis, please refer to Appendix A for the validation against corresponding non-linear Simulink [109] models using the Simscape Electrical Specialized Power Systems library (version 7.6) [110] and the Julia [111] open-source Sienna modelling framework by National Renewable Energy Laboratory (NREL) [112]. A repository has been made available which includes the MATLAB scripts for creation of power system small-signal models as used for the work in this thesis [108]. This also includes metadata and examples to aid in the use of the small-signal modelling tool. Note, included in this chapter are descriptions of the power system elements that have been modelled (in particular, Sections 2.4 to 2.6), but certain variations on these models are used throughout the different chapters of this thesis. As such, explicit mention of what has been implemented for every case study is specified when relevant.

Vectors are denoted by boldface lowercase letters (unless stated otherwise) and matrices are denoted by boldface uppercase letters.

2.1 Small-Signal State Space Modelling

A non-linear dynamical system can be represented in the state space as a series of differential and algebraic equations [10, 11, 104] of the form

$$\begin{aligned} \dot{\boldsymbol{x}} &= \boldsymbol{f}\left(\boldsymbol{x}, \boldsymbol{u}\right), \\ \boldsymbol{y} &= \boldsymbol{g}\left(\boldsymbol{x}, \boldsymbol{u}\right), \end{aligned} \tag{2.1}$$

where $\boldsymbol{x}_{N\times 1}$ is the vector of states, $\boldsymbol{u}_{N_i\times 1}$ is the vector of inputs, and $\boldsymbol{y}_{N_o\times 1}$ is the vector of outputs. The dot operator represents differentiation with respect to time.

In small-signal modelling and analysis, we are interested in the small region around the operating point in which the dynamics of the system are approximately linear. As such, we can define the model in (2.1) as a perturbation around the operating point as

$$\begin{aligned} \dot{\boldsymbol{x}} = \dot{\boldsymbol{x_0}} + \Delta\dot{\boldsymbol{x}} &= f\left[(\boldsymbol{x_0} + \Delta\boldsymbol{x}), (\boldsymbol{u_0} + \Delta\boldsymbol{u})\right] \\ \boldsymbol{y} = \boldsymbol{y_0} + \Delta\boldsymbol{y} &= g\left[(\boldsymbol{x_0} + \Delta\boldsymbol{x}), (\boldsymbol{u_0} + \Delta\boldsymbol{u})\right], \end{aligned} \tag{2.2}$$

where the subscript 0 indicates the initial value and the prefix Δ refers to a small deviation. The Taylor series expansion can then be used on the small deviation terms and by neglecting all terms above first order, we extract the linear model. For state i this is

$$\begin{aligned} \dot{x}_i = \dot{x}_{i,0} + \Delta\dot{x}_i &= f_i\left[(\boldsymbol{x}_0 + \Delta\boldsymbol{x}), (\boldsymbol{u}_0 + \Delta\boldsymbol{u})\right] \\ &= f_i(\boldsymbol{x_0}, \boldsymbol{u_0}) + \left[\frac{\delta f_i}{\delta x_1}\Delta x_1 + \cdots + \frac{\delta f_i}{\delta x_n}\Delta x_n + \cdots + \frac{\delta f_i}{\delta x_N}\Delta x_N \right. \\ &\qquad \left. + \frac{\delta f_i}{\delta u_1}\Delta u_1 + \cdots + \frac{\delta f_i}{\delta u_r}\Delta u_r + \cdots + \frac{\delta f_i}{\delta u_{N_i}}\Delta u_{N_i}\right], \end{aligned} \tag{2.3}$$

where the $f_i(\boldsymbol{x_0}, \boldsymbol{u_0})$ term will disappear since it is the rate of change at the steady-state operating point, and hence equivalent to zero, and $\delta f_i/\delta x_n$ is the partial derivative of the non-linear function f_i with respect to state x_n, evaluated at the operating point.

A similar process is applied to the output function resulting in

$$\Delta y_j = \frac{\delta g_j}{\delta x_1}\Delta x_1 + \cdots + \frac{\delta g_j}{\delta x_n}\Delta x_n + \cdots + \frac{\delta g_j}{\delta x_N}\Delta x_N \tag{2.4}$$

$$+ \frac{\delta g_j}{\delta u_1}\Delta u_1 + \cdots + \frac{\delta g_j}{\delta u_r}\Delta u_r + \cdots + \frac{\delta g_j}{\delta u_{N_i}}\Delta u_{N_i} \tag{2.5}$$

for the j^{th} output.

The standard format for the linearised model in the state space is

$$\begin{aligned} \dot{\Delta \boldsymbol{x}} &= \boldsymbol{A}\Delta\boldsymbol{x} + \boldsymbol{B}\Delta\boldsymbol{u} \\ \Delta\boldsymbol{y} &= \boldsymbol{C}\Delta\boldsymbol{x} + \boldsymbol{D}\Delta\boldsymbol{u}, \end{aligned} \tag{2.6}$$

where the matrices $\boldsymbol{A}_{N\times N}$, $\boldsymbol{B}_{N\times N_i}$, $\boldsymbol{C}_{N_o\times N}$ and $\boldsymbol{D}_{N_o\times N_i}$ correspond to the state matrix, input matrix, output matrix and feed-forward matrix, respectively [10]. The particular approach in this thesis to obtain the model described in (2.6)–including the MATLAB functions that are utilised–is discussed further in Section 2.2.

2.1.1 Determination of Operating Point

There are typically two stages to the initialisation of a power system model. The first is to perform a power flow analysis which, as the name suggests, determines the static power flows on the network. This makes use of network data including the transmission line and load impedances, generator output, and relevant constraints. If it is an optimal power flow (OPF) then the cost functions for each generator are also required. For further information with regards to the inputs, outputs, and data for performing power flow analyses, see [12, 113]. In this work, the MATLAB add-on package of MATPOWER [113] is used to perform power flow and OPF.

The second stage is to initialise the individual dynamic components. This is achieved by considering that the system is at steady-state and hence the differential terms in (2.1) are zero. The result of this is a set of non-linear simultaneous equations of the form

$$0 = \boldsymbol{f}\left(\boldsymbol{x_0}, \boldsymbol{u_0}\right), \tag{2.7}$$

where, for an individual component such as a generator, the inputs will include the voltage at the connection point and the output complex power, as determined through the power flow analysis. Further inputs will include any input control references to the machine or, e.g., the mechanical input power of the generator shaft, amongst others. The application of this stage is completed in this work through the development of a repository of initialisation functions. These functions take in the inputs as previously described along with the dynamic parameters, and output the initial states of the component which is solved using the `solve()` function from the MATLAB Symbolic Math Toolbox [114]. There is a function for each power system element (excepting passive network components[1]) including the SG, GFL, and GFM models.

2.1.2 Eigenvalues, Eigenvectors, and Participation Factors

Eigenvalue analysis is commonly utilised in power system small-signal analyses due to its multiple-input multiple-output (MIMO) capabilities suiting the complex large-scale MIMO nature of BPSs [10,11,14]. It also suits the typical objective of identification of multi-machine interactions through the eigendecomposition of the system dynamics.

The eigenvalues (also referred to as modes) of the system–which correspond to the poles in typical control theory terminology–can be found through the calculation of

$$\det(\boldsymbol{A} - \boldsymbol{\Lambda}\boldsymbol{I}) = 0, \tag{2.8}$$

where det() is the determinant operator and $\boldsymbol{I}_{N\times N}$ is the identity matrix. The matrix $\boldsymbol{\Lambda}_{N\times N}$ has diagonal elements which are the eigenvalues, $\{\lambda_1, \lambda_2, \ldots, \lambda_N\}$, and non-diagonal elements of zero.

The eigenvalues can be either real-valued (non-oscillatory) representing an exponential decay (or increase) or a complex conjugate pair representing a damped oscillation. For eigenvalue k, the frequency of the oscillation, ω_k and the damping time constant, $1/\sigma_k$, can be determined directly from the real, $\Re$, and imaginary, $\Im$, parts

[1]Network elements do not require initial states to create the small deviation linearised model due to their passive nature. However, if the initial states are required (e.g., to display the absolute value of the output) they can be taken directly from the power flow.

as

$$\lambda_k = \sigma_k \pm j\omega_k. \tag{2.9}$$

Whether the response corresponding to an individual eigenvalue exponentially converges to, or diverges from, the new operating point after a disturbance depends on the sign of the real part, σ_k, with stability being achieved only if $\Re(\lambda_k) = \sigma_k \leq 0$. If an oscillatory mode has zero real part then there will be a sustained sinusoid.

Further information can be gathered through the eigenvectors associated with each eigenvalue. The matrices whose columns are the right eigenvectors, $\boldsymbol{\phi}$, and left eigenvectors, $\boldsymbol{\psi}$, are calculated with (2.10) and (2.11), respectively.

$$\boldsymbol{A}\boldsymbol{\phi} = \boldsymbol{\phi}\boldsymbol{\Lambda} \tag{2.10}$$

$$\boldsymbol{\psi}^{\mathsf{T}}\boldsymbol{A} = \boldsymbol{\Lambda}\boldsymbol{\psi}^{\mathsf{T}} \tag{2.11}$$

The entry of the right eigenvector, $\phi_{i,k}$, describes the observability[2] of eigenvalue k on state i and the entry of the left eigenvector, $\psi_{i,k}$, describes the how much eigenvalue k will be excited in response to variations of state i. This can be understood further by the relation between the free response of a system state and the superposition of eigenvalues [10], a concept which is returned to in Chapter 6. A measure of the relation between eigenvalue and state, considering both the right and left eigenvector entries, is the PF. There are several possible PF calculations but in this thesis the approach in [11] is adopted which ensures real valued vector entries and applies an ℓ_1 normalisation. The calculation is

$$p_{i,k} = \frac{|\phi_{i,k}|\,|\psi_{i,k}|}{\sum_{i=1}^{N}|\phi_{i,k}|\,|\psi_{i,k}|}. \tag{2.12}$$

PF analysis opens a new avenue of dynamic characterisation, allowing engineers to understand the states of the system most related to any undesirable modes, determining if they constitute multi-machine interactions and guiding towards mitigation approaches. In conventional SG-based power systems, PFs have been

[2]This can be leveraged to differentiate local and inter-area oscillations whereby the rotor speed states of groups of generators oscillate in phase with each other or out of phase against each other, respectively [10].

used to identify generators contributing most to electromechanical oscillations, thereby enabling optimal location choice for PSSs [115]. Furthermore, through understanding which states contribute most to the oscillation, an appropriate input signal to the PSS can be selected.

For the calculation of eigenvalues and eigenvectors in this thesis, the `eig()` function in MATLAB is used [107]. When only the $\boldsymbol{A}$ matrix is provided (i.e., the linear eigenvalue problem), the QZ algorithm (generalized Schur decomposition) is utilised. For more information with regards to methods for the computation of eigenvalues and eigenvectors, as well as theoretical discussions regarding the linear eigenvalue problem and generalised eigenvalue problem, see [116].

2.2 Modularity and Automatic Compilation

This subsection details the implementation of the MATLAB tool which generates the small-signal model of the form in (2.6). The high-level flow of the adopted modelling procedure is illustrated in Fig. 2.1. The required input information is summarised as follows:

- *Power flow case file:* containing branch (transmission line and transformer), bus, and generator information. Branch data includes sending and receiving end bus locations, resistance, inductive reactance, and shunt capacitive reactance, as well as tap ratios for transformers. Bus data includes active and reactive power consumption, bus type (i.e., swing, PV, or PQ [12]), and shunt conductance and susceptance. Generator data includes the bus connection location, the requested real and reactive power output, minimum and maximum output active and reactive power, terminal voltage references, and OPF costs (if required). For this work, the MATPOWER [113] format is adopted.

- *Dynamic parameters file:* containing parameter information for the dynamic models of the generators and associated controllers (including bus location identifiers). If it was to be included, dynamic data for load models could also be included here. More information regarding the particular models used in this

thesis and associated parameters are found throughout this chapter.

- *Model initialisation repository:* consisting of functions which take relevant inputs (including power flow output data and model dynamic parameters) and return the resultant initial states as described further in Section 2.1.1.

- *Small-signal model (SSM) repository:* which consists of functions to convert input data of initial states, dynamic parameters, and location identifiers to SSM objects. The SSM objects are data containers with the state space matrices (see Section 2.1), input names, output names, state names, and any other relevant metadata. The `ss()` function from the MATLAB Control System Toolbox [117] is used to generate these SSM objects. Note, the bus connections are also encoded as a SSM object, whereby the $\boldsymbol{D}$ matrix, i.e., from (2.6), acts as a connection matrix linking the inputs and outputs of the rest of the SSM object modules of the system.

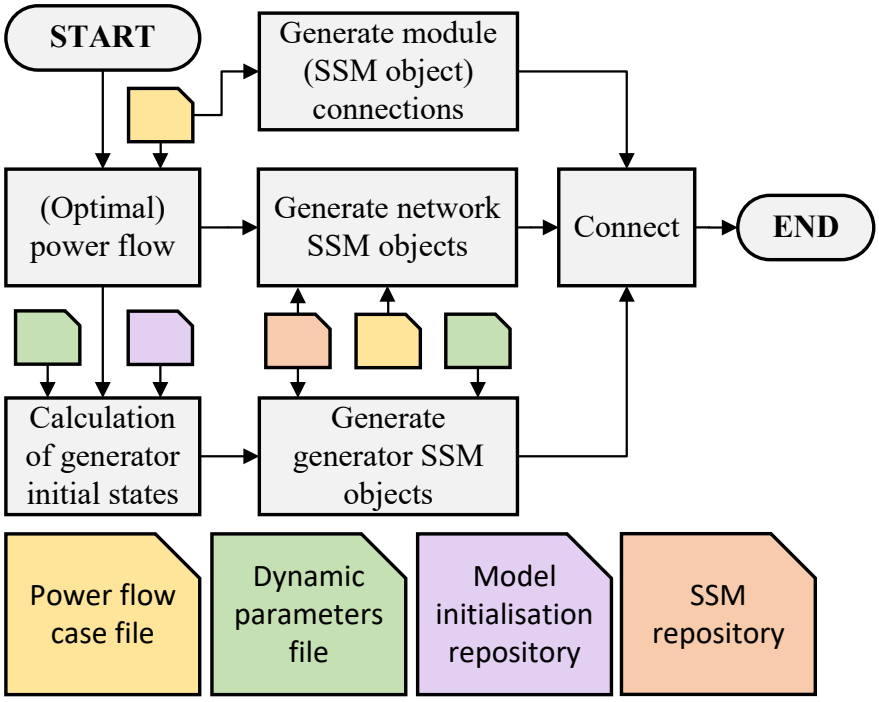

Figure 2.1: Automatic and modular compilation procedure flowchart.
SSM = small-signal model.

The first step required to generate the power system SSM is to determine the

operating point of interest. This is achieved through running a power flow, or OPF if desired. MATPOWER is utilised for this purpose as described in Section 2.1.1. Provided the power flow converges, the process can continue to the calculation of initial states for the individual components (in our case this is only generators), which has also been described further in Section 2.1.1. With the full system initial operating point and states determined, the models of each component can be generated. This is achieved using the SSM repository.

With each element modelled individually as its own module, there requires a process whereby the power system model is connected. To ease the procedure and facilitate scalability, an automatic procedure is performed. The connection is made at each bus considering Kirchhoff's current law, with generators, loads and transmission branch currents being combined to determine the total value applied to the amalgamated capacitance at the bus of interest. The voltage across the capacitance can then be determined and applied to the previously described elements. This process is visualised in Fig. 2.2. These connections are applied using the `connect()` function in the MATLAB Control System Toolbox [117] which requires the names of the inputs and outputs being connected between the modules (e.g., the terminal voltage of a generator, V_t, may be "connected" to the bus voltage magnitude V_{bus}). These input and output names have been created automatically in the MATLAB scripts and functions with consistency of convention used when setting up the SSM objects with the `ss()` function (also from the Control System Toolbox). This allows for a fully automated procedure to be performed provided the data regarding parameters, initial states, and bus locations of all elements are provided. This approach whereby separate dynamic linear models are developed along with a model representing the component interconnections is akin to the component connection method (CCM) [118, 119].

Note, this requires at least one shunt at each bus. If this is not the case then a modelling artefact can be added with very large impedance so as to draw very limited current and avoid influencing the dynamic characteristics of the system [120].

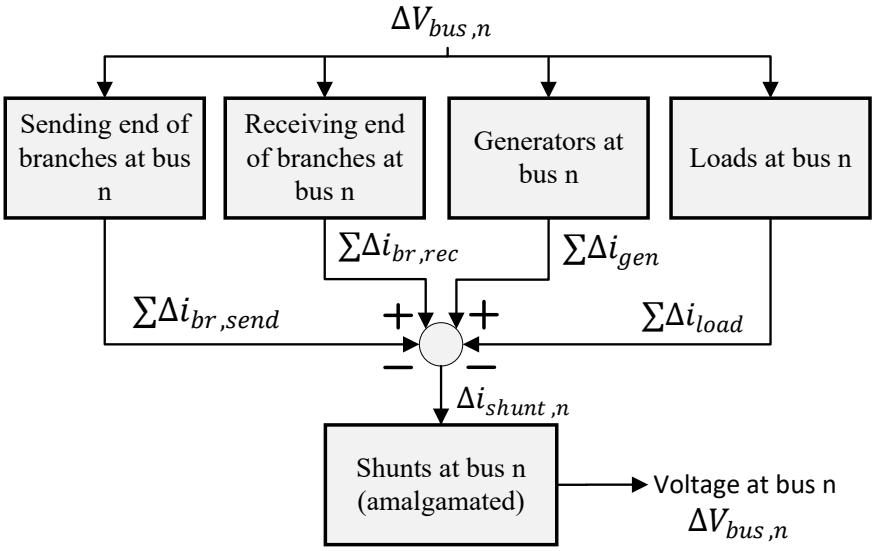

Figure 2.2: Visualisation of the connection approach at each bus.

2.3 Modelling Conventions

This section details the modelling conventions and notation used before the specific system elements are discussed in Sections 2.4 to 2.6.

2.3.1 Reference Frames

For the small-signal modelling, all signals are in a rotating dq0 reference frame in this work [121]. Converting signal vectors from abc coordinates to dq0 coordinates requires a Park transform. The Park transform that is utilised for the converter controllers and for the system reference frame in this work aligns the d-axis with the a-axis and has the q-axis lagging[3] by 90°, and is of the form

[3]The q-axis is lagging if we are considering the b-axis to lead the a-axis by 120° and the c-axis to lag the a-axis by 120°, as per the convention in the Specialized Power Systems library of Simscape Electrical [110, 122] and commonly utilised power system modelling textbooks [10, 11]. Note, the opposite orientation is also often used, whereby we consider the b-axis to lag the a-axis by 120° and the c-axis to lead the a-axis by 120°. Care should be taken with respect to implementation of reference frames, and consistency should be maintained throughout the modelling process.

$$\begin{bmatrix} z_d \\ z_q \\ z_0 \end{bmatrix} = \frac{2}{3} \begin{bmatrix} \cos\theta & \cos\left(\theta - \frac{2\pi}{3}\right) & \cos\left(\theta + \frac{2\pi}{3}\right) \\ \sin\theta & \sin\left(\theta - \frac{2\pi}{3}\right) & \sin\left(\theta + \frac{2\pi}{3}\right) \\ 1/2 & 1/2 & 1/2 \end{bmatrix} \begin{bmatrix} z_a \\ z_b \\ z_c \end{bmatrix}, \tag{2.13}$$

where θ is the angle between the d-axis of the rotating dq0 reference frame and the a-axis of the static abc-frame. At steady-state, the speed of the reference frame is expected to match the frequency of the three-phase current and voltage signals resulting in them being represented by DC quantities (i.e., the d and q components). This results in simpler modelling and analysis. Furthermore, converter controllers are often implemented in the (synchronous) dq0-frame to simplify the control design and enable the use of proportional-integral controllers [123]. The corresponding inverse Park transform is of the form

$$\begin{bmatrix} z_a \\ z_b \\ z_c \end{bmatrix} = \begin{bmatrix} \cos\theta & \sin\theta & 1 \\ \cos\left(\theta - \frac{2\pi}{3}\right) & \sin\left(\theta - \frac{2\pi}{3}\right) & 1 \\ \cos\left(\theta + \frac{2\pi}{3}\right) & \sin\left(\theta + \frac{2\pi}{3}\right) & 1 \end{bmatrix} \begin{bmatrix} z_d \\ z_q \\ z_0 \end{bmatrix}. \tag{2.14}$$

Note, other than the non-linear models implemented in Simulink for validation in Appendix A, no Park or inverse Park transforms are actually required. This is because the modelling (including that of the electrical network) is completed in dq0 coordinates (see Sections 2.4 to 2.6). For more information regarding the concepts of the Park transform and modelling in the rotating dq0-frame, please refer to [10,11,101,103,123]. The remainder of this subsection discusses the particular approach used in this work.

In order to develop a power system model modularly, all elements are implemented in their own rotating reference frame. In this case we consider the dq0-frame with each element considered in its own relevant frame of reference. By adopting this convention, we can simplify the three-phase instantaneous current and voltage signals to a dynamic phasor equivalent[4] with only two representative components (since we are considering a balanced system). That is, a signal, or vector, $\boldsymbol{z}$, can be expanded into its d and q

[4]For more information on the dynamic phasor concept, its computational benefits, and the relationship to the dq0 representation, see [101].

components in the form

$$\boldsymbol{z} = z_d - jz_q. \tag{2.15}$$

Note, the orientation of the d and q axes may be different (e.g., the SG model adopted in this work from [11] and discussed further in Section 2.6 has orientation which aligns the q-axis with the a-axis with the d-axis lagging by 90^o) and therefore consistency should be ensured when converting between the reference frames of different elements of the power system. The choices of orientation for the d and q axes made in this work were based solely on familiarity of the authors. Additionally, we consider a global system reference frame (with rotational speed ω_{sys}) to model the passive network elements and this is taken to rotate at the speed of the chosen reference machine. As such, no reference frame transformation (RFT) is required for the signals at the connection point of the reference machine and the network (provided the d and q axes have the same orientation, as is assumed in this subsection for the sake of describing these concepts). However, the remainder of the components require a simple geometric RFT as in (2.16) and (2.17) and visualised in Fig. 2.3. In particular, this describes the transformation between system and machine reference frames, where the former is distinguished with the sys superscript and the latter by the * superscript. The angle between the two reference frames is denoted by $\delta\theta$ and the speed of the system and machine reference frames are denoted by ω_{sys} and ω_*, respectively.

$$\begin{bmatrix} z_d^* \\ z_q^* \end{bmatrix} = T_{(sys\to *)} \begin{bmatrix} z_d^{sys} \\ z_q^{sys} \end{bmatrix} = \begin{bmatrix} \cos\delta\theta & \sin\delta\theta \\ -\sin\delta\theta & \cos\delta\theta \end{bmatrix} \begin{bmatrix} z_d^{sys} \\ z_q^{sys} \end{bmatrix}, \ or, \ \boldsymbol{z^*} = \boldsymbol{z^{sys}} e^{-j\delta\theta} \tag{2.16}$$

$$\begin{bmatrix} z_d^{sys} \\ z_q^{sys} \end{bmatrix} = T_{(*\to sys)} \begin{bmatrix} z_d^* \\ z_q^* \end{bmatrix} = \begin{bmatrix} \cos\delta\theta & -\sin\delta\theta \\ \sin\delta\theta & \cos\delta\theta \end{bmatrix} \begin{bmatrix} z_d^* \\ z_q^* \end{bmatrix}, \ or, \ \boldsymbol{z^{sys}} = \boldsymbol{z^*} e^{j\delta\theta} \tag{2.17}$$

Note, as already mentioned, care should be taken when converting signals between reference frames with different orientations for the d and q axes. In particular, the RFTs should be held consistent with the orientation in which the modelling was performed.

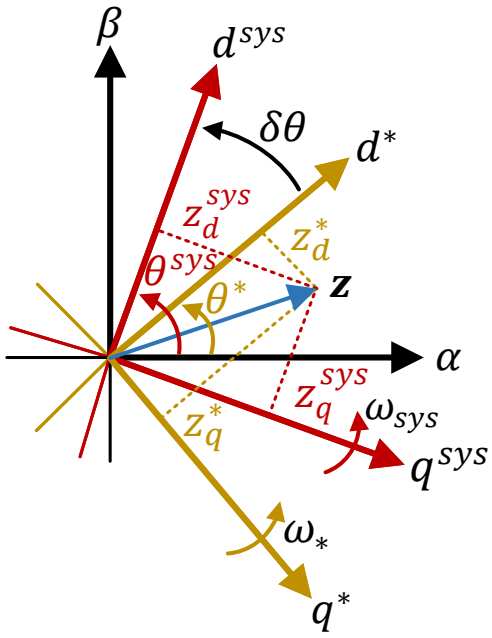

Figure 2.3: Visualisation of the reference frame transformations when both dq0 reference frames have d to a-axis alignment with q-axis lagging by 90°.

2.3.2 Per Unit System

The per unit system is used throughout this thesis [10, 12]. An exception is for the rotational or electrical frequency signals which (unless stated otherwise) are in units of radians per second.

In per unit, the electrical active and reactive power, P_e and Q_e, can be calculated for the voltage, $\boldsymbol{v}$, and current, $\boldsymbol{i}$, at a given measurement point as per [10, 11], with equations

$$P_e = v_d i_d + v_q i_q, \tag{2.18}$$

$$Q_e = v_d i_q - v_q i_d. \tag{2.19}$$

Another key output parameter of interest is the voltage magnitude, $|\boldsymbol{v}|$. This is calculated simply by taking the magnitude of the voltage vector in dq coordinates as

$$|\boldsymbol{v}| = \sqrt{v_d^2 + v_q^2}. \tag{2.20}$$

2.4 Network Elements

In this work, when referring to the *network elements*, it is the passive resistance, inductance, and capacitance components of the transmission lines, transformers, and loads that is meant.

The transmission lines are modelled using the lumped π model (unless stated otherwise). The transformers are represented as series RL impedances, while the constant impedance loads are represented as parallel shunts.

As described in Section 2.2, the shunt capacitances at each bus are amalgamated during the automatic and modular compilation procedure. As such, the RL branches of the transmission lines and the shunt capacitive components are separated.

The RL branches of the transmission lines and the RL impedance modelled transformers are therefore represented, in the system dq0 frame, as

$$\begin{aligned} \frac{X_l}{\omega_b}\dot{i}_d &= v_{send,d} - v_{rec,d} - Ri_d - \omega_{sys,pu}X_l i_q, \\ \frac{X_l}{\omega_b}\dot{i}_q &= v_{send,q} - v_{rec,q} - Ri_q + \omega_{sys,pu}X_l i_d, \end{aligned} \tag{2.21}$$

where ω_b and $\omega_{sys,pu}$ are the base frequency (in rad/s) and the per unit system frequency (as per Section 2.3.1), respectively. Note, the common approximation whereby ω_{sys} is set to ω_b (and hence, $\omega_{sys,pu} = 1$ pu) in the network equations [103] is adopted throughout this thesis. X_l is the inductive reactance and R is the resistance of the series RL component. The voltages at the sending end and receiving end of the RL branch are denoted by $\boldsymbol{v_{send}}$ and $\boldsymbol{v_{rec}}$, respectively. Finally, the current flowing through the RL branch (i.e., into the sending end and out of the receiving end) is denoted by $\boldsymbol{i}$.

The parallel resistance and inductance components of the constant impedance loads

are modelled as

$$\begin{aligned}
\frac{X_{l,load}}{\omega_b}\dot{i_{l,d}} &= v_{load,d} - \omega_{sys,pu}\, X_{l,load}\, i_{l,q}, \\
\frac{X_{l,load}}{\omega_b}\dot{i_{l,q}} &= v_{load,q} + \omega_{sys,pu}\, X_{l,load}\, i_{l,d}, \\
i_{load,d} &= i_{l,d} + \frac{v_{load,d}}{R_{load}}, \\
i_{load,q} &= i_{l,q} + \frac{v_{load,q}}{R_{load}},
\end{aligned} \tag{2.22}$$

where $\boldsymbol{i_l}$ is the current flowing through the inductor branch and $\boldsymbol{i_{load}}$ is the total current flowing into the load. If there is a shunt capacitive element of the load then this is amalgamated with any other shunt capacitive components at the connection bus and, hence, treated separately. The voltage at the connection bus (and hence across the load) is denoted by $\boldsymbol{v_{load}}$. The load resistance, R_{load}, and inductive reactance, $X_{l,load}$, are calculated from the active and reactive power, P_{load} and Q_{load}, and the bus voltage magnitude at the initial operating point, $|\boldsymbol{v_{load,0}}|$, as

$$R_{load} = \frac{|\boldsymbol{v_{load,0}}|^2}{P_{load}}, \tag{2.23}$$

$$X_{l,load} = \frac{|\boldsymbol{v_{load,0}}|^2}{Q_{load}}, \tag{2.24}$$

where the initial operating point is determined as per Section 2.1.1 or similar. If the load is capacitive, the capacitive reactance, $X_{cap,load}$, will be calculated as the negative of (2.24).

The shunt capacitance at each bus is modelled as

$$\begin{aligned}
\frac{1}{\omega_b\, X_{cap}}\dot{v_{cap,d}} &= i_{cap,d} - \omega_{sys,pu}\frac{v_{cap,q}}{X_{cap}}, \\
\frac{1}{\omega_b\, X_{cap}}\dot{v_{cap,q}} &= i_{cap,q} + \omega_{sys,pu}\frac{v_{cap,d}}{X_{cap}},
\end{aligned} \tag{2.25}$$

where $\boldsymbol{v_{cap}}$ is the voltage across the amalgamated capacitance, and, hence, of the connection bus. The current flowing into the capacitor, whose reactance is denoted by X_{cap}, is determined via Kirchhoff's current law as per Section 2.2, and is denoted by $\boldsymbol{i_{cap}}$.

In some instances, some or all of the network elements may be represented using the quasi-static assumption [30] (or, similarly, a static version of the constant impedance load). In this case, the corresponding equations can be determined simply by setting the relevant derivative terms in (2.21)–(2.25) to zero.

2.5 Converter-Interfaced Generation

This section details the general grid-connected converter structure that is considered before discussing the particular control implementations for the GFL and GFM approaches. Note, when discussing "system-level" control, we are referring to the outer controllers that dictate the GFL or GFM behaviour of the device (as per Sections 2.5.3 and 2.5.4). This is not to be confused with "plant-level" or "farm-level" control [124] whereby individual converter controllers are coordinated by a central element. Such a controller is not considered in this work.

2.5.1 Voltage-Sourced Converter

The typical arrangement for a grid-connected voltage-sourced converter (VSC) is displayed in Fig. 2.4. The VSC itself is represented by the averaged model [103] throughout this thesis meaning that the gate switching is neglected. In some instances (which are indicated when relevant in subsequent chapters of the thesis) the pulse width modulation (PWM) and associated switching transients are represented using the common first order approximation with time constant of $0.5/f_{sw}$ [125] where f_{sw} is the switching frequency, or the more conservative approximation taking into account additional delays–such as those associated with control execution and/or PWM–of $1.5/f_{sw}$ [126]. As such, other than any approximated delay, the voltage requested at the output of the converter switches by the control, $\boldsymbol{v}^*_{\boldsymbol{cv}}$, will be generated by the VSC considering only a transformation to *abc* (or physical) coordinates or geometric RFT between dq0 frames, as per Section 2.3.1. The angle of the converter/machine, θ^*, is acquired either from a PLL when using GFL control (Section 2.5.3) or the active power control (APC) when using GFM control (Section 2.5.4).

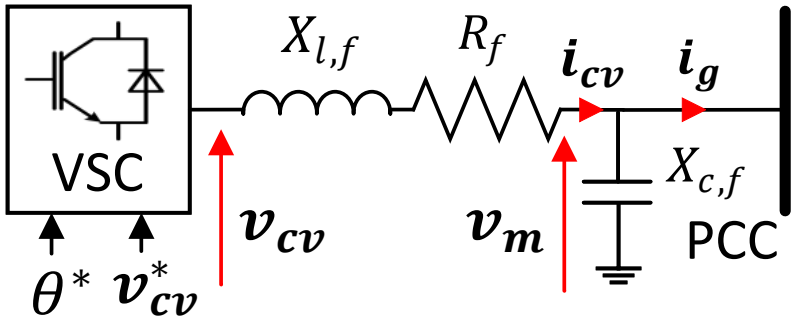

Figure 2.4: Grid-connected voltage-sourced converter. PCC=point of common coupling.

An output (R)LC filter is included (which can be considered an LCL filter if a transformer is connected but this is considered as a separate module in the work in this thesis) with resistance, inductive reactance, and capacitive reactance denoted by R_f, $X_{l,f}$, and $X_{c,f}$, respectively. The RL branch is modelled as per (2.21) and the capacitor is modelled as per (2.25). The current flowing through the RL branch of the output filter and the current injected to the grid at the PCC are denoted by $\boldsymbol{i_{cv}}$ and $\boldsymbol{i_g}$, respectively. The current flowing into the shunt capacitor of the output filter is therefore $\boldsymbol{i_{cv}} - \boldsymbol{i_g}$. The voltage across the filter capacitor is denoted by $\boldsymbol{v_m}$.

The primary energy source–be that a wind turbine/farm, BESS, PV panel, or similar–is considered to supply sufficient power to maintain strict voltage on the DC side capacitor. That is, the dynamics on the DC side of the converter are neglected.

2.5.2 Device-Level Control

The aim of the device-level control is to quickly regulate the local current and voltage signals to the requested values. These requested values are designated by the system-level control which will be discussed in Sections 2.5.3 & 2.5.4. The control which is applied must be sufficiently fast to avoid interfering with the actions of the system-level control.

Note, the analysis in this thesis is limited to balanced systems which is reflected in the fact that we consider only positive sequence control [127]. Furthermore, since

there is a focus on small-signal dynamics, non-linear aspects such as current limitation are only taken into account insofar as they dictate the required controller architecture, such as the inclusion of an ICC, which is discussed further in Section 2.5.5.

Current Vector Control

The current vector through the output RL filter (i.e., $\boldsymbol{i_{cv}}$ in Fig. 2.4) is controlled in the dq0 reference frame of the converter. The structure of the controller, visible in Fig. 2.5, is based around proportional-integral (PI) control of the d and q current signals. It also includes decoupling terms[5] which enables independent control of the d and q axis currents and feed-forward terms which reject disturbances associated with the voltage at the capacitor, $\boldsymbol{v_m}$. The derivation of the decoupling and feed-forward terms is easily apprehended from the dq0 model of the output RL filter [126]. This is based on the concept of internal model control as in [123, 128].

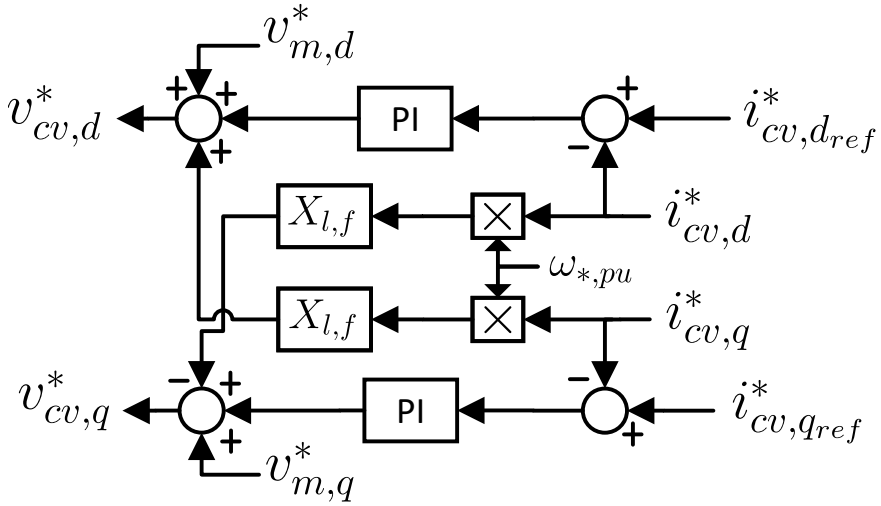

Figure 2.5: Current vector control scheme in dq0 coordinates.

Note, the signal $\omega_{*,pu}$ is considered in this case to be an estimation of the electrical frequency, either from the PLL (Section 2.5.3) or the GFM APC (Section 2.5.4). However, a common assumption–which is adopted for the work in this thesis–is to use a constant value of the base electrical frequency, $\omega_{b,pu}$, within the current vector

[5]Consistency must be ensured with regards to the dq0 frame orientation as per Section 2.3.1. In particular, which decoupling term is summed and which term is subtracted depends on this.

control [120, 129], similar to that in the network equations as seen in Section 2.4.

Voltage Vector Control

Also controlled in the dq0 reference frame is the voltage across the filter capacitor. This uses a similar concept for derivation and resultant structure to the current vector control as can be seen in Fig. 2.6. Note, this is typically only included when using GFM control (if included at all). Furthermore, the assumption of constant electrical frequency whereby the $\omega_{*,pu}$ signal is replaced by $\omega_{b,pu}$ [120, 129] is also adopted within this control structure for the work in this thesis.

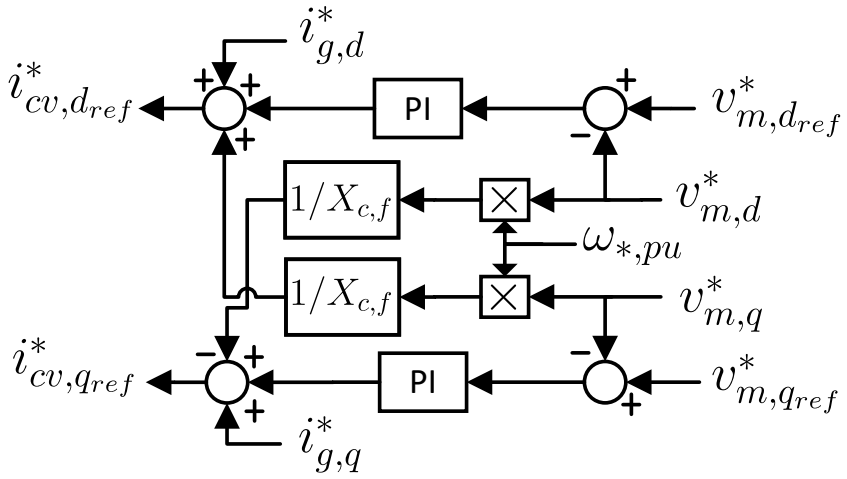

Figure 2.6: Voltage vector control scheme in dq0 coordinates.

2.5.3 System-Level Control: Grid-Following

Having already discussed the high-level philosophy of GFL control in Section 1.2.2, this subsection details the specific implementation utilised in this thesis, along with some common adaptations where relevant.

Active & Reactive Power Control

The APC and reactive power control (RPC) strictly regulate the active and reactive power by manipulating the output RL filter current using PI control, as seen in Fig. 2.7. In a typical GFL converter control scheme, these outer controllers generate the d

and q current references to be fed into an ICC of the form seen in Fig. 2.5. The fact that the ICC decouples the d and q components of the current control means that the active and reactive power is also controlled independently[6].

A low pass filter (LPF)–with cut-off frequency of ω_c–may be applied to the measurement of the active and reactive power (P_e and Q_e, respectively) [132]. It can also be noted that the active and reactive output electrical power that is measured in this case is that being injected into the wider grid (i.e., at the PCC). This can therefore, with consideration of (2.18) and (2.19), be calculated based on the measured voltage and current in the per unit d and q coordinates as

$$P_e = v^*_{m,d} i^*_{g,d} + v^*_{m,q} i^*_{g,q} \tag{2.26}$$

$$Q_e = v^*_{m,d} i^*_{g,q} - v^*_{m,q} i^*_{g,d}. \tag{2.27}$$

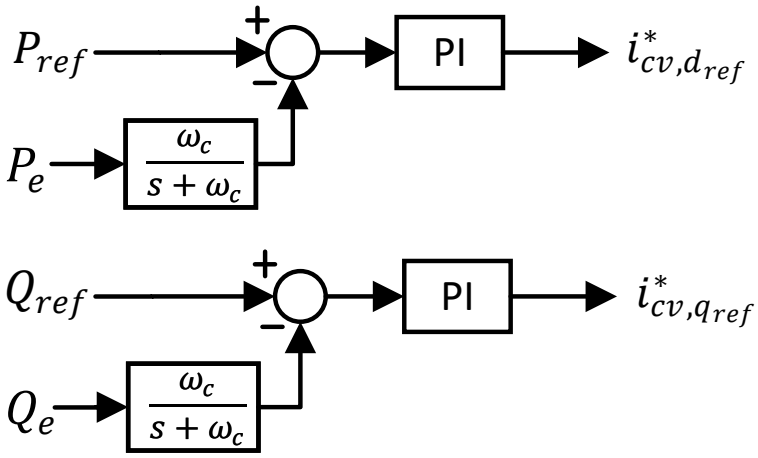

Figure 2.7: Active and reactive power controllers (for GFL control).

A common adaptation is to use a voltage magnitude control (VMC) in place of the RPC whereby the reference and measured reactive power are replaced by the reference and measured voltage magnitude at the PCC[7]. However, this begins to blur

[6]Provided the X/R ratio of the system is high ensuring sufficient natural decoupling of the active and reactive power [31]. Or else some form of decoupling control may be applied such as that suggested in [130], and further discussed in [131], but for GFM control.

[7]Depending on the orientation of the d and q axes, the measured voltage may have to be summed with the reference, rather than subtracted.

the GFL and GFM classifications. In [31], a more encompassing classification approach is suggested whereby the voltage magnitude and frequency aspects are separated with regards to whether they are "followed" or "formed" by the control.

In some instances, the strict PI control is not utilised and in its place is a static calculation [103], derived from (2.26) and (2.27), of the form

$$i^*_{cv,d_{ref}} = \frac{P_{ref} - v^*_{m,q} i^*_{g,q}}{v^*_{m,d}}, \tag{2.28}$$

$$i^*_{cv,q_{ref}} = \frac{Q_{ref} + v^*_{m,q} i^*_{g,d}}{v^*_{m,d}}, \tag{2.29}$$

which is commonly approximated by

$$i^*_{cv,d_{ref}} = \frac{P_{ref}}{v^*_{m,d}}, \tag{2.30}$$

$$i^*_{cv,q_{ref}} = \frac{Q_{ref}}{v^*_{m,d}}, \tag{2.31}$$

because $v^*_{m,q}$ is controlled to zero by the PLL, as will be described in the next subsection. This adaptation is considered in Chapter 4.

Phase-Locked Loop: Synchronisation

In order to synchronise the generated voltage signals at the converter switches with those of the grid, the phase-angle is tracked. A common approach to achieve this is the use of a synchronous reference frame (SRF)-PLL which measures the voltage angle by driving the q component of the measured voltage (in the controller's frame of reference) to zero (see [103, 133] and Chapter 8 of [123] for more information). This is achieved with a PI controller whose output is the measured frequency, and, through a further integrator, the angle. This angle is fed back into the transformation between system and machine reference frames[8]. The implementation used throughout this thesis is displayed in Fig. 2.8.

Note, in actual implementation, the measured signals would be in abc coordinates

[8]Depending on the orientation of the d and q axes, it may be the d-axis component which is controlled to zero and/or the feedback may need to be summed rather than subtracted.

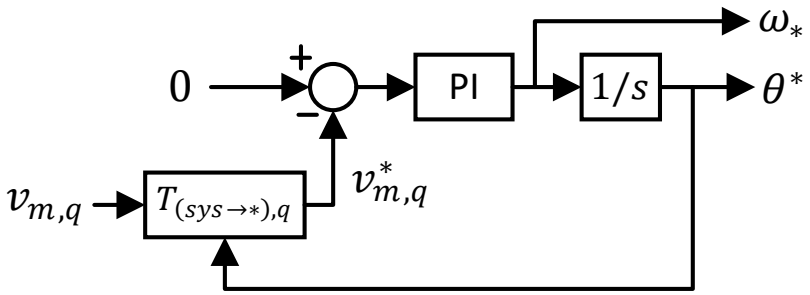

Figure 2.8: Synchronous reference frame phase-locked loop.

and the RFT would therefore be the Park transform. Since we model the network in dq0 coordinates, it is instead the geometric transformation between different dq0 reference frames as described in Section 2.3.1.

2.5.4 System-Level Control: Grid-Forming

Similar to the discussion of the GFL control implementation, we will focus here on the specific implementations of GFM control used in this thesis since the high-level philosophy has already been discussed in Section 1.2.2.

Active Power Control & Synchronisation

For a GFM converter connected to the BPS, the APC is of course tasked with regulating the active power injected to the system, but it is also typically the way in which the converter control synchronises with the frequency of the AC grid. On top of this, a droop characteristic is favourable to enable power sharing with the rest of the system.

Two common implementations for the GFM APC are droop control and the swing equation-based virtual synchronous machine (VSM), as displayed in Fig. 2.9 and Fig. 2.10, respectively. These two basic structures have been shown to be equivalent (at least under small-signal assumptions) [15, 134], where the droop controller parameters can be related to those of the VSM by the calculations:

$$m_p = \frac{1}{K_D}, \tag{2.32}$$

$$\omega_c = \frac{1}{2m_p H} \tag{2.33}$$

where m_p and ω_c are the droop gain and low pass filter cut-off frequency for the droop control, respectively. The inertia and damping constant of the VSM are denoted by H and K_D, respectively. If the low pass filter was not included in Fig. 2.9 then the inertial characteristic would not be observed[9] [15].

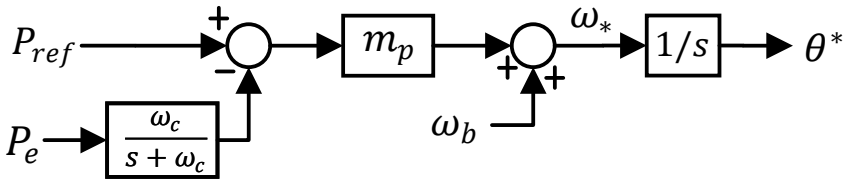

Figure 2.9: Active power droop-based grid-forming active power control.

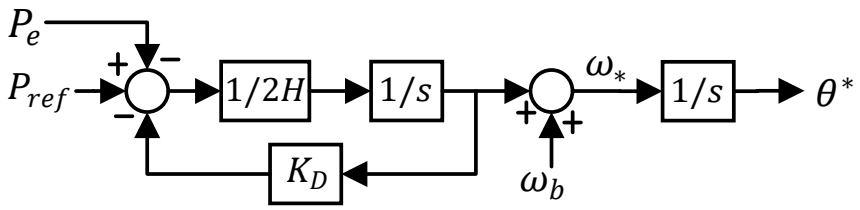

Figure 2.10: Virtual synchronous machine-based grid-forming active power control.

There are several alternate implementations of GFM APC found within the literature, including dispatchable virtual oscillator control [135], matching control [136], hybrid angle control [137], and more [15,63,138,139]. However, the two implementations shown in Fig. 2.9 and Fig. 2.10 are arguably the most commonly adopted within the literature and are certainly simple in terms of their control structure, notwithstanding the intuitive tuning afforded by the use of well-known characteristics such as inertia constant, damping constant, droop, and low-pass filtering. As such, these are the approaches utilised throughout this thesis.

[9] In relation to the inertia of SGs, not simply the instantaneous injection of active power which may be achieved by other means, such as FFR [7].

Voltage Magnitude Control

As the system level control of the GFM directly generates the required voltage phasor, the desired magnitude can be fed directly to the d component of the reference control voltage (see Section 2.5.5 for more information on this signal) with the q component being set to zero [59]. Alternatively, the reference can first be augmented with a reactive power-voltage droop characteristic, as displayed in Fig. 2.11, enabling support for reactive power regulation and sharing on the system [60]. The output of $v^*_{d_{ref}}$ is

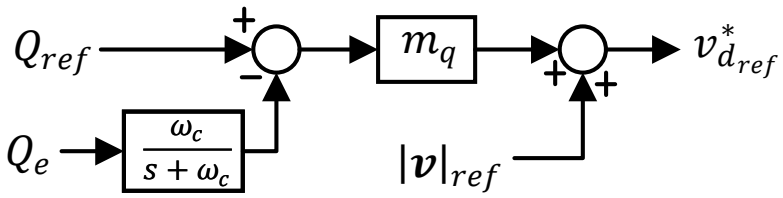

Figure 2.11: Reactive power-voltage droop.

the updated control voltage reference after application of the reactive power droop with gain m_q. As previously described, in a typical implementation of GFM control, this would be equivalent to the magnitude of the control voltage reference, since the q component is set to zero [59].

In GFL control, if VMC is used in place of RPC–as described in Section 2.5.3–then a reactive power droop can also be used to augment the voltage reference. The difference comes in the voltage control whereby the GFL would (typically) use a simple PI controller acting on a similar timescale to that of the RPC [5,140], whereas the GFM would (typically) use a faster IVC of the form seen in Fig. 2.6, if such a controller is used at all: see Section 2.5.5 for more discussion on this.

Virtual Impedance

A common addition to GFM control is the use of a virtual impedance. This can improve the response of the converter through increased X/R ratio–and therefore, the decoupling of active power/frequency and reactive power/voltage–and/or oscillation damping. There are a range of different virtual impedance implementations, often with different target use cases [9]–e.g., oscillation damping [141, 142], active and reactive

power decoupling [143–145], current limitation [146], impedance shaping [142,147,148], etc.–which are out of the scope of this thesis, but a common algebraic approach [59] is of the form seen in Fig. 2.12 with virtual resistance and inductance of R_{VI} and $X_{l,VI}$, respectively. The output of this virtual impedance approach is a deviation of the reference control voltage phasor, denoted in this case as $\boldsymbol{v}_{ref}^{*,dev}$. See Section 2.5.5 for the context in which this control augmentation can be applied.

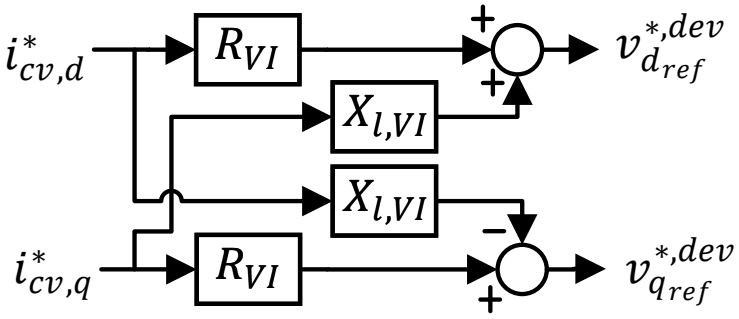

Figure 2.12: Algebraic virtual impedance.

Note, virtual impedance is commonly adopted in GFM control but the concepts are not limited to this control philosophy [9].

2.5.5 Cascaded Control: Putting it All Together

The system-level and device-level controls are typically implemented in a cascaded control structure whereby the ICCs and IVCs quickly regulate the output current and voltage signals as per Section 2.5.2 with system-level controls acting on slower timescales. The concepts of timescale decoupling and singular perturbation theory are key to the cascaded control approach [11, 95, 123, 125, 128, 149, 150].

In this thesis, the term "control architecture" is used to distinguish between the inclusion or neglection of different cascaded controllers, as opposed to different control implementations, such as VSM or droop control for GFMs.

Grid-Following Control Architectures

GFL control approaches tend to always include an ICC such as that of the form in Section 2.5.2. From this, there are two common approaches for determination of the

current references: single loop control (SLC) and double loop control (DLC). The former involves a static calculation based on the system-level active and reactive power references, as described in (2.30) & (2.31), in Section 2.5.3. DLC in this case refers to the approach whereby outer PI controllers are used for strict control of the active and reactive power (or voltage magnitude), as also described in Section 2.5.3. The complete control structure (except RFTs or delay considerations as per Section 2.5.1) with different choices of control architecture is displayed in Fig. 2.13.

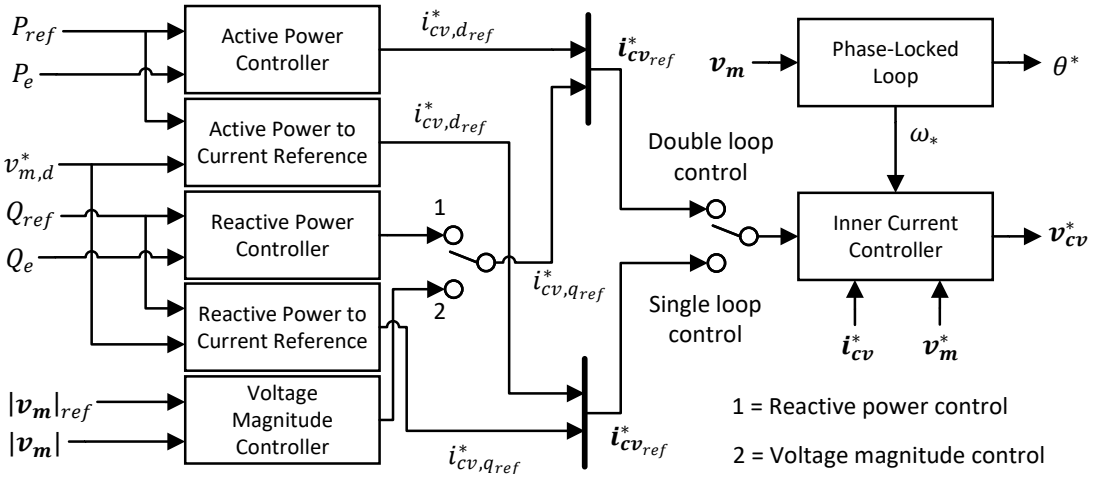

Figure 2.13: Grid-following cascaded control structure.

Grid-Forming Control Architectures

The standardisation of control architectures, in terms of cascaded control structure, is less mature with respect to GFM converters when compared to that of GFL control. This is an active research area within the literature, as will be further discussed in Chapter 3, Chapter 4, and the end of this subsection.

Three key architectures might be considered: direct AC voltage control (DACVC), single inner loop control (SILC), and double inner loop control (DILC). Fig. 2.14 provides an overview of the GFM cascaded control structure, detailing how DACVC, SILC, and DILC differ from each other.

For DACVC, the AC voltage is controlled directly by the APC and VMC, without any ICC or IVC. When using DACVC, the reference control voltage, $\boldsymbol{v}^*_{ref}$, is that of the

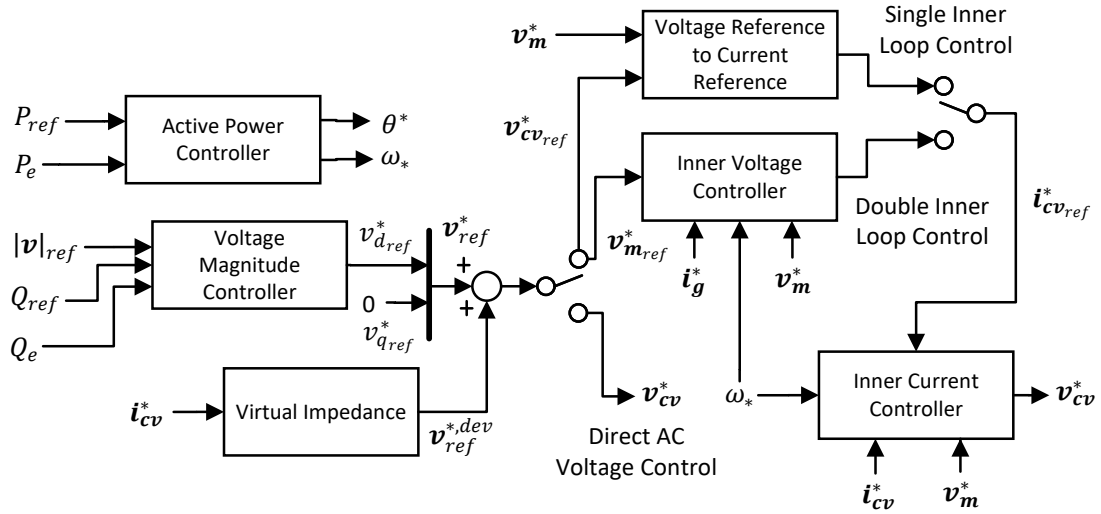

Figure 2.14: Grid-forming cascaded control structure.

converter switches, $\boldsymbol{v}_{\boldsymbol{cv}}^*$, as opposed to the voltage at the coupling filter capacitor, $\boldsymbol{v}_{\boldsymbol{m}}^*$ (i.e., at the PCC as per Fig. 2.4). However, if it is not tuned for a particular purpose such as active stabilisation or power flow control [9], the virtual impedance (Fig. 2.12) can be set to compensate for the voltage drop across the RL coupling filter, so that $\boldsymbol{v}_{ref}^*$ corresponds to $\boldsymbol{v}_{\boldsymbol{m}}^*$, and hence $|\boldsymbol{v}|_{ref}$ is the reference of the voltage magnitude at the PCC. Note, more complex implementations of DACVC can also be found in the literature, such as the use of a linear quadratic regulator [146].

SILC includes an ICC but no IVC. As such, a static reference conversion is used to obtain the ICC input current reference, $\boldsymbol{i}_{\boldsymbol{cv}_{ref}}^*$, from the reference control voltage, $\boldsymbol{v}_{ref}^*$ [151, 152]. With measurement of $\boldsymbol{v}_{\boldsymbol{m}}^*$, this calculation is

$$i_{cv,d_{ref}}^* = \frac{1}{R_f^2 + X_{l,f}^2}\left[R_f\left(v_{d_{ref}}^* - v_{m,d}^*\right) - X_{l,f}\left(v_{q_{ref}}^* - v_{m,q}^*\right)\right], \tag{2.34}$$

$$i_{cv,q_{ref}}^* = \frac{1}{R_f^2 + X_{l,f}^2}\left[R_f\left(v_{q_{ref}}^* - v_{m,q}^*\right) + X_{l,f}\left(v_{d_{ref}}^* - v_{m,d}^*\right)\right], \tag{2.35}$$

where $\boldsymbol{v}_{ref}^*$ is therefore the reference for the voltage at the converter switches, $\boldsymbol{v}_{\boldsymbol{cv}_{ref}}^*$. If it is desired to have $\boldsymbol{v}_{ref}^*$ control the voltage at the output filter capacitor–i.e., $\boldsymbol{v}_{\boldsymbol{m}_{ref}}^*$– instead, then a measurement of the voltage at the converter switches, $\boldsymbol{v}_{\boldsymbol{cv}_{meas}}^*$, should

be made and the calculation rearranged accordingly as

$$i^*_{cv,d_{ref}} = \frac{1}{R_f^2 + X_{l,f}^2}\left[R_f\left(v^*_{cv,d_{meas}} - v^*_{d_{ref}}\right) - X_{l,f}\left(v^*_{cv,q_{meas}} - v^*_{q_{ref}}\right)\right], \tag{2.36}$$

$$i^*_{cv,q_{ref}} = \frac{1}{R_f^2 + X_{l,f}^2}\left[R_f\left(v^*_{cv,q_{meas}} - v^*_{q_{ref}}\right) + X_{l,f}\left(v^*_{cv,d_{meas}} - v^*_{d_{ref}}\right)\right], \tag{2.37}$$

although, when SILC is adopted in this thesis, it is the form described in (2.34) and (2.35) which is used.

Care should also be taken here with respect to the inclusion of the virtual impedance[10]. That is, the static conversion from voltage to current reference requires the correct knowledge of what the actual input voltage reference is, in addition to what the impedance between this voltage and the measured voltage is (i.e., considering the impedance of the output coupling filter and the virtual impedance together), in order to accurately calculate what $\boldsymbol{i}^*_{\boldsymbol{cv}_{ref}}$ should be to achieve $\boldsymbol{v}^*_{ref}$. More complex virtual impedance considerations may mean that such an exact approach is not required, or even desired [9, 147], in which case careful choice of the input voltage magnitude reference, $|\boldsymbol{v}|_{ref}$, should be made. However, such scenarios are not considered in this thesis.

The final architecture considered is DILC which includes a cascaded IVC in addition to the ICC. As such, since this offers strict regulation of the reference control voltage (Section 2.5.2), $\boldsymbol{v}^*_{ref}$, this can be set directly to $\boldsymbol{v}^*_{\boldsymbol{m}_{ref}}$.

Furthermore, the choice of architecture will be important with regards to dynamic response, stability, power quality, potential interactions, amongst other considerations. In Chapter 3 and Chapter 4, the impact of different controller architecture choices on small-signal stability and multi-machine interactions is further investigated. Furthermore, the inclusion of the cascaded ICC and IVC may be motivated by the need for signal limiters. This is primarily from the current limitation perspective, which is

[10]Note, the static reference calculation may also be considered a form of virtual impedance often tuned independently of the output filter reactance [152–154], that is, not being used simply to compensate for the output coupling filter of the VSC [153], but rather to offer an additional degree of freedom with [155] showing how this can be used to improve passivity across the frequency spectrum. This might also be a dynamic virtual impedance as opposed to the static algebraic approximation. However, in this reference to virtual impedance we are referring to the specific implementation of Fig. 2.12.

another very active research area at present, especially for GFM converters [75, 76, 79].

2.6 Synchronous Generator

The discussion of the SG is less detailed than that of the CIG due to the maturity of the former, as well as the targeted interest in the dynamics of the latter in this thesis.

The particular SG model used in this thesis is the linear magnetic circuit model taken from [11]. This is a 9^{th} order model (8^{th} order if considering balanced conditions) with dynamic representation of the field and damper windings of the rotor, in addition to the stator dynamics (unless a quasi-static assumption is applied) and the mechanical rotor. More specifically, the dynamic equations are:

$$\frac{1}{\omega_b}\dot{\psi_d} = R_s I_d + \frac{\omega_*}{\omega_b}\psi_q + V_d \tag{2.38}$$

$$\frac{1}{\omega_b}\dot{\psi_q} = R_s I_q + \frac{\omega_*}{\omega_b}\psi_d + V_q \tag{2.39}$$

$$T_{d0}^{'}\dot{E}_q^{'} = -E_q^{'} - \left(X_d - X_d^{'}\right)\left[I_d - \frac{X_d^{'} - X_d^{''}}{\left(X_d^{'} - X_{\ell s}\right)^2}\left(\psi_{1d} + \left(X_d^{'} - X_{\ell s}\right) I_d - E_q^{'}\right)\right] + E_{fd} \tag{2.40}$$

$$T_{q0}^{'}\dot{E}_d^{'} = -E_d^{'} + \left(X_q - X_q^{'}\right)\left[I_q - \frac{X_q^{'} - X_q^{''}}{\left(X_q^{'} - X_{\ell s}\right)^2}\left(\psi_{2q} + \left(X_q^{'} - X_{\ell s}\right) I_q + E_q^{'}\right)\right] \tag{2.41}$$

$$T_{d0}^{''}\dot{\psi_{1d}} = -\psi_{1d} + E_q^{'} - \left(X_d^{'} - X_{\ell s}\right) I_d \tag{2.42}$$

$$T_{q0}^{''}\dot{\psi_{2q}} = -\psi_{2q} - E_d^{'} - \left(X_q^{'} - X_{\ell s}\right) I_q \tag{2.43}$$

$$\dot{\delta^*} = \omega_* - \omega_b \tag{2.44}$$

$$\frac{2H}{\omega_b}\dot{\omega_*} = T_M - (\psi_d I_q + \psi_q I_d) - T_{FW} \tag{2.45}$$

with accompanying algebraic equations of

$$\psi_d = -X_d^{''} I_d + \frac{\left(X_d^{''} - X_{\ell s}\right)}{\left(X_d^{'} - X_{\ell s}\right)} E_q^{'} + \frac{\left(X_d^{'} - X_d^{''}\right)}{\left(X_d^{'} - X_{\ell s}\right)}\psi_{1d} \tag{2.46}$$

$$\psi_q = -X_q^{''} I_q - \frac{\left(X_q^{''} - X_{\ell s}\right)}{\left(X_q^{'} - X_{\ell s}\right)} E_d^{'} + \frac{\left(X_q^{'} - X_q^{''}\right)}{\left(X_q^{'} - X_{\ell s}\right)}\psi_{2q} \tag{2.47}$$

where ψ_d and ψ_q are the stator flux linkage states. The flux linkage states of the rotor circuit are denoted by ψ_{1d} and ψ_{2q}. The transient voltages are denoted by $E_d^{'}$ and $E_q^{'}$ and are primarily associated with one of the q-axis damper windings and with the field winding, respectively[11]. The stator current variables are denoted by I_d and I_q, while the terminal voltage variables are denoted by V_d and V_q. The field winding voltage is E_{fd}. As mentioned previously, ω_b is the base frequency and ω_* is the machine frequency, the latter of which is the rotor speed in this case. Furthermore, as stated in Section 2.3.2, angular frequency states/variables are in units of radians per second, despite the remaining variables being in per unit. The stator resistance is R_s and the stator leakage reactance is $X_{\ell s}$. The X_d and X_q parameters represent the d and q components of the synchronous reactance, respectively. The d and q component transient reactances are $X_d^{'}$ and $X_q^{'}$ respectively, and the subtransient reactances are $X_d^{''}$ and $X_q^{''}$. The time constants $T_{d0}^{'}$, $T_{q0}^{'}$, $T_{d0}^{''}$, and $T_{q0}^{''}$ are the d and q transient, and then subtransient, open circuit time constants, respectively. Finally, (2.44) and (2.45) are the swing equation of the rotor, with δ^* (in radians) and ω_* being the rotor angle and speed states, respectively. The input mechanical torque is denoted by T_M and the friction windage torque is denoted by T_{FW}. The inertia constant is denoted by H. Note, the terminology in terms of state, variable, and parameter names may be used in similar models in slightly different ways. For further discussion on this and to learn more about the specific implementation used, see [11].

Common controls adopted for SGs are an automatic voltage regulator (AVR)/exciter, PSS, and speed governor/turbine. Common versions of these control elements for power system dynamic studies are the DC1A AVR [157], PSS1A PSS [157], and IEEEG1 speed governor/turbine [158]. The specific controls utilised (if any) for each case study are described where relevant in this thesis. If no speed governor/turbine or AVR is connected, then it is a fixed mechanical power input that is used (as opposed to a fixed mechanical torque) and a DC constant excitation, respectively.

[11] This can be better understood by considering the definitions of these variables in [11]: $E_d^{'} \triangleq -(X_{mq}/X_{1q})\,\psi_{1q}$ and $E_q^{'} \triangleq (X_{md}/X_{fd})\,\psi_{fd}$ where ψ_{1q} and ψ_{fd} are flux linkages of one of the q-axis damper windings and the field winding, respectively. Furthermore, X_{md} and X_{mq} are the magnetising reactances [156], and X_{1q} and X_{fd} are the reactance of one of the q-axis damper windings and of the field winding, respectively.

Chapter 3

Interaction Analysis of Grid-Forming Converters in a Transmission Scale Power System with Associated Bandwidth Restrictions

3.1 Introduction

3.1.1 Motivation

As detailed in Section 1.2, transitioning to a carbon-free power system will result in new dynamic phenomena and interactions involving GFM converters as their proliferation occurs to support this transition. The DILC architecture, incorporating cascaded IVCs and ICCs, often utilised within GFMs are generally expected to cause interactions in higher frequency ranges than the (well-studied) dynamics of interest associated with a purely SG-based system. However, the restricted control bandwidth associated with low switching frequency of large power rated 2- or 3-level VSCs results in the need for much slower control time constants, causing potentially destabilising interactions,

even in lower frequency ranges. This chapter offers an extensive insight into the small-signal, multi-machine interactions involving large power-rated GFMs in a transmission network: the IEEE 39-bus New-England test system. Furthering the contribution of this chapter, DILC is employed within the GFMs, offering an insight into their interactions with other power system elements to help aid the ongoing discussions on model appropriateness and DACVC versus the use of cascaded inner controllers. Finally, parametric sweep sensitivity analyses are performed for the GFMs which are implemented as VSMs.

GFMs are one of the promising solutions for enabling ever increasing penetrations of CIGs, primarily in the form of wind and solar energy resources. In the transitional period before SGs are fully phased out, a combination of SGs, GFMs and GFLs are expected to be present in power systems (for investigations including GFLs, refer to Chapter 4). The interactions among such devices with each other and existing power system elements are of significant interest [33], especially in terms of small-signal behaviour. As of yet, the GFM concept, despite being utilised for microgrid applications [159, 160], has not been fully explored from a small-signal perspective, especially in the context of large, interconnected power systems.

3.1.2 Literature Review

The literature pertaining to GFMs in larger power systems in previous years has been restricted to defining general penetration level limits [161]. More recently, the impact of GFMs on power system stability has been an increasing topic of interest. [59] produced an extensive small-signal analysis of CIGs from a small, two-machine with infinite bus system, up to a large-scale system in the form of the 59-bus South-East Australian network. This work offers invaluable insights into the nature of the most influential interactions between SGs, GFMs and GFLs, albeit with limited discussion into the nature of the specific modes when in the large system due to a focus on CIG penetration limits. For example, it is seen from PF analysis that there are destabilising interactions between the fast voltage control of the converters and the relatively slow voltage control of the PSS and AVR of the SG. It is also found that as GFL penetration increases

there reaches a point where there is not enough contribution from the SG (or GFM) to slow the frequency variations and therefore the PLL of the GFL loses synchronism. Provided in [162] is a study focused on inter-area oscillations, whereby they exhibit the potential improvement of damping by replacing a SG with a VSM-based GFM in both the Kundur two-area system as well as the IEEE 68-bus system. Despite these studies, there remains scope to describe extensively the small-signal interactions seen in a large-scale power system with GFMs, especially since the most influential interactions can easily change depending on a multitude of factors including operating points as [59] highlights.

In terms of GFMs in one machine-infinite bus (OMIB) systems, [163, 164] and [165] investigate the small-signal behaviour of different GFM control schemes with the last of which focusing on tuning through eigenvalue analysis before validation with a modified IEEE 39-bus New-England test system. Similar OMIB small-signal analysis examples include [166] which investigates the interaction between inner and outer control loops and its effect on small-signal stability, and [143] which proposes active and reactive power decoupling approaches for GFMs incorporating the power synchronisation control scheme. In particular, this is aimed at resistive networks and they make use of both "virtual power" and virtual impedance to enhance the small-signal stability. Furthermore, they validate their results (i.e., stability improvement) using the IEEE 39-bus network. A similar active and reactive power decoupling approach is adopted in [144] but for a droop-based GFM control scheme connecting a wind farm with a BESS to the AC grid. Another study in this vein is found in [145] which makes use of the IEEE 9-bus system. An eigenvalue based study (along with a bifurcation approach) is performed in [167] with both GFL and GFM control approaches. They offer detailed insights into potential stability ranges with respect to SCR network conditions in addition to varying primary control parameters. Despite this, they do not investigate the PF-based characteristics of the eigenvalues.

Furthermore, small-signal analysis of GFMs in parallel, connected to an infinite bus, has been investigated in [119]. Additional small-signal analyses looking at robust stability margins using the μ factor has been performed by the same authors in [168].

These papers look at synchronverters, a type of swing equation based VSM, operating in parallel as well as synchronverters in parallel with GFLs. Another multi-machine investigation in a small system is performed in [169] whereby they adopt very detailed models of a wind turbines to investigate the potential impact on (or interaction with), the electromechanical dynamics of a SG.

Although not the focus of this chapter, it can be noted that extensive literature exists pertaining to small-signal analyses with GFL control. In addition to several of the papers already discussed, some examples which focus solely on GFLs include [5, 170–175].

This brief review of the general literature pertaining to the small-signal analysis of GFMs (in addition to that discussed in the context of the changing dynamic landscape in Section 1.2) highlights the wide range of potential small-signal interactions and stability issues, in addition to the plethora of different base control approaches and adaptations, further motivating the need for continuing detailed investigations to illuminate the expected behaviour, interactions, and stability of GFMs, especially in BPSs.

Significant research into GFMs has been focused on the important issue of current limitation [146, 176]. Two promising approaches are DACVC with threshold-induced virtual impedance [9,146] and the use of DILC [125]. The latter constitutes a cascaded IVC and ICC, allowing for a limitation to be applied to the current reference generated by the former and applied to the latter[1]. The idea of DACVC refers to the creation of a voltage phasor from the GFM control section and bypassing inner controllers by applying the reference directly to the AC voltage modulation of the converter terminals. This approach can also incorporate virtual impedance [59] or alternative control such as linear-quadratic regulators [146].

Traditionally, IVCs and ICCs are much faster than that of the outer active and reactive power (or voltage magnitude) control. This allows sufficient timescale separation from the inner loops to the outer loop and electromechanical dynamics that

[1]Note, the use of an ICC is not solely to enable current limitation but, amongst other considerations, is used for fast regulation of the output filter current, using fast PI-controller action and feed-forward terms for disturbance rejection. For more information, see Section 2.5.2.

dominate power systems [59]. In GFMs, the tuning of the inner cascaded controllers has been discussed in [125] and [149], both of which find conventional tuning methods insufficient due to low switching frequencies of VSCs at large power ratings. This is due to limited bandwidth of the inner controllers resulting in increased potential for instability. Therefore, through different tuning procedures, [125] and [149] find new parameters which suffice. They are of much higher time constants, and from [149] are the values adopted for the small-signal analysis described earlier [59]. Although [125] and [149] displayed the nature of the small-signal interactions at conventional tuning, they did not show how this changes after re-tuning.

In this chapter, the interaction of the inner controllers of multiple, distant GFMs with controller bandwidth restrictions, as well as with the electromechanical and PSS dynamics of SGs is observed. In particular, we provide a comprehensive break down of the small-signal interactions which have participation from the VSM-based GFMs [134] found at transmission-scale. Specifically, for the modified IEEE 39-bus network being studied. This is completed for the GFMs utilising DACVC but also when using DILC. Finally, parametric sweep sensitivity analyses of relevant GFM parameters are performed. Note, a preliminary study, with simplified models, focusing on electromechanical interactions between SGs and GFMs (or between two GFMs) can be found in Appendix B.

The work in this chapter was published in the proceedings of the Innovative Smart Grid Technologies (ISGT) Europe 2022 conference [177].

3.2 Modelling and Analysis Methodology

3.2.1 Small-Signal Analysis

The key elements and use cases of small-signal eigenvalue analysis have been discussed in detail in Section 1.2.4 and Section 2.1.2.

To identify the GFM dominant eigenvalues, of which we are interested in this work, a minimum participation from the sum of PFs of all GFM states of 10% is required for further analysis. Additionally, any eigenvalue that was fully damped with real value

less than -10 (i.e., damping time constant less than 0.01 s) was considered irrelevant for the analyses in this chapter. It was found that those eigenvalues with participation from only GFM output filter states and network states were extremely stable and had no sensitivity to any GFM control parameters. Therefore, the output filter states were not considered GFM states when determining the modes of interest. Note, this might not be true with higher bandwidth inner controllers. The determination of relevant eigenvalues was performed for the DACVC scenario before the IVCs and ICCs are added to the GFMs.

Knowing the eigenvalues that exist is not sufficient as we require an idea of how the important system parameters impact the stability of these eigenvalues to gain a complete picture. Therefore, parametric sweep-based sensitivity analyses are performed to determine how the dynamics are impacted. This involves eigenvalue plots for a parameter value being considered across an appropriate range with all other parameters held constant. In this work, the sensitivity analysis is performed only for the DILC scenario.

In this work, a mode is considered to be an interaction if multiple machines and/or elements are present in terms of the dominant dynamics states with respect to the mode's PFs. Interactions are generally expected to be undesirable, however, we also ensure to discuss the eigenvalue-based characteristics of such modes as well to determine if they exhibit low stability margin, in which case we would explicitly consider such interactions to be adverse or undesirable.

3.2.2 Power System Modelling

The small-signal models are developed in accordance with the procedure outlined in Chapter 2.

SG model: is of the balanced, 8^{th} order machine as in [11]. The SG is also fitted with an AVR/exciter combination of type EXCST1. Additionally, there is a PSS of type PSS1A and finally, there is a governor/turbine combination of type IEEEG1. Implementation of all controllers are found in [178].

GFM model: is based on the VSM approach, with a VMC incorporating a reactive

power-voltage droop, as per Section 2.5.4. An RLC filter is adopted as per Fig. 2.4. In this case, the current and voltage measurements are passed through a LPF (as opposed to the active and reactive power) and transformed into the machine's local rotating reference frame in dq coordinates [103] (Section 2.3.1). The IVCs and ICCs are of the form described in Section 2.5.2, with only the former including feed-forward terms. Additionally, in this case the PWM/control delay is approximated by a first-order time delay[2] [125, 126]. No virtual impedance is included in this GFM implementation.

Network model: incorporates dynamic π circuit representations of the transmission lines and dynamic RL circuits for both the transformers and (constant impedance) loads.

3.2.3 Modified IEEE 39-Bus System with Added Grid-Forming Converters

The parameters of the IEEE 39-bus network and the SGs within are adopted from [178]. From the base case presented there, 600 MVA rated GFMs were added at bus locations 5, 16 and 26 as in Fig. 3.1: each set to output 300 MVA at a power factor of 0.95. The IEEE 39-bus network is common in small-signal analysis studies and was chosen due to its relatively complex and meshed nature with the potential for multi-machine interactions on transmission-scale. Parameters related to GFMs are presented in Table 3.1. The initial tuning for the inner controllers were determined using the modulus optimum technique for the ICC (with closed-loop time constant set to $10 \times (1/f_s)$ where f_s is the switching frequency) and the symmetrical optimum approach for the IVC [125]. The latter requires a damping factor to be chosen which is obtained in this case from a parametric sweep (Fig. 3.2a which is discussed further in Section 3.5). Note, such an approach has been shown to exhibit poor performance in OMIB systems [149, 179, 180] and the work in this chapter extends the analysis of such limitations to multi-machine systems and the potential for multi-machine interactions.

[2] In this case the PWM/control delay time constant is taken as $1/(2f_s)$ where f_s is the VSC switching frequency. Different sources suggest different values for this as discussed in Section 2.5.1.

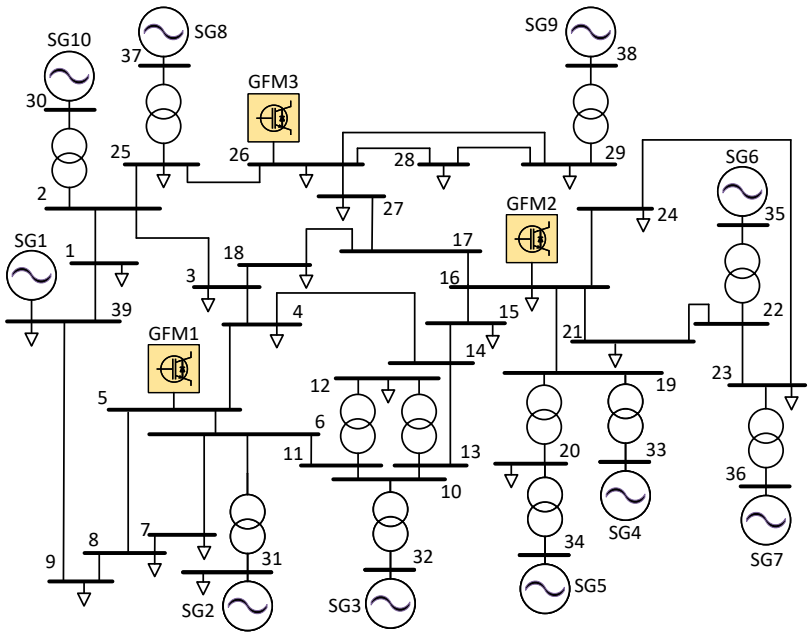

Figure 3.1: Modified IEEE 39-bus network for use in the bandwidth-restricted GFM small-signal analysis case studies.

Table 3.1: Parameters of the GFM for the base case in the bandwidth-restricted small-signal analysis case studies.

Parameter	Symbol	Value
RLC resistance	R_f	0.03 pu
RLC inductive reactance	$X_{l,f}$	0.08 pu
RLC capacitive reactance	$X_{c,f}$	1/0.074 pu
Measurement filter cut-off frequency	f_c	100 Hz
Switching frequency	f_s	2 kHz
PWM/control time delay	τ_{pwm}	$1/(2f_s)$ s
ICC proportional gain, integral gain	$K_{p,icc}, K_{i,icc}$	$\{0.0424, 6\}$ $\mathrm{V_{pu}/A_{pu}}$
IVC proportional gain, integral gain	$K_{p,ivc}, K_{i,ivc}$	$\{0.1406, 0.0108\}$ $\mathrm{A_{pu}/V_{pu}}$
IVC damping factor	ζ	25
VMC reactive power droop	m_q	0.1%
APC virtual inertia, virtual damping	H, K_D	4 s, 10 pu

3.3 Eigenvalue Analysis with GFMs adopting Direct AC Voltage Control

This section regards the analysis performed on the test system described previously with all GFMs implemented without the inner controllers. That is, they employ DACVC. All eigenvalues of interest are shown in Table 3.2 along with their frequency, damping ratio and most dominant states, characterised by a minimum of 5% PF unless stated otherwise. Those with participation above 10% are presented in bold.

There are six modes in the range of 21.63 Hz to 21.66 Hz. These modes have participation purely from the input measurement filters of the GFMs. They are very well damped with damping ratio of approximately 0.869 and do not move throughout the parametric sweeps and so have not been included in Table 3.2. Similar modes were found in the DILC scenario and again have not been included (in Table 3.3 or the display of the parametric sweeps in Fig. 3.2).

Table 3.2: Eigenvalues of interest for the direct AC voltage control scenario.

Eigenvalue	Coordinates	Frequency (Hz)	Damping Ratio	Dominant States	Category
$\lambda_{1\&2}$	$-0.5879 \pm j12.2031$	1.9422	0.0481	$\boldsymbol{\omega_{GFM,2}}$, $\boldsymbol{\delta_{GFM,2}}$, $\omega_{r,4}$	Electro-mechanical
$\lambda_{3\&4}$	$-1.5704 \pm j11.4504$	1.8224	0.1359	$\boldsymbol{\omega_{r,8}}$, $\boldsymbol{\delta_{GFM,3}}$, $\boldsymbol{\delta_{r,8}}$, $\omega_{GFM,3}$, $E^{'}_{q,8}$	Electro-mechanical
$\lambda_{5\&6}$	$-0.7167 \pm j11.2226$	1.7861	0.0637	$\boldsymbol{\delta_{GFM,1}}$, $\boldsymbol{\omega_{GFM,1}}$, $\omega_{GFM,3}$	Electro-mechanical
$\lambda_{7\&8}$	$-1.6783 \pm j10.6958$	1.7023	0.1550	$\boldsymbol{\omega_{r,8}}$, $\boldsymbol{\delta_{r,8}}$, $E^{'}_{q,8}$, $\omega_{r,4}$, $\delta_{GFM,3}$, $\omega_{GFM,3}$, $\omega_{r,9}$	Electro-mechanical
$\lambda_{9\&10}$	$-1.0650 \pm j7.4529$	1.1862	0.1415	$\boldsymbol{\delta_{r,9}}$, $\boldsymbol{\omega_{r,9}}$, $\delta_{GFM,3}$, $\omega_{r,10}$, $E^{'}_{q,9}$	Electro-mechanical

Dominant state subscript numbers refer to the machine number and should be cross-referenced with Fig. 3.1.

All of the eigenvalues highlighted in Table 3.2 are seen to be in the electromechanical range with frequencies between 1.1862 Hz and 1.9422 Hz. The electromechanical nature of these modes is also confirmed with the PFs showing dominant modes associated with the rotor speed and angle of SGs with ω_r and δ_r, as well as the GFMs with ω_{GFM} and δ_{GFM}. There is also some small participation from states associated with the rotor field windings, $E^{'}_{q}$. All modes involve multiple generators (GFMs and/or

SGs). Additionally, for this timescale, all modes are well damped, with the minimum being 4.81%. Typically, a damping ratio of above 3% is considered sufficient for electromechanical modes.

3.4 Eigenvalue Analysis with GFMs adopting Double Inner Loop Control

The eigenvalues and their characteristics for this test case are displayed in Table 3.3. We find the same electromechanical modes as observed in Table 3.2 with small changes to the frequency and damping. However, there are additional modes now found to be of interest. All of the additional modes are in close proximity to the stability boundary and are related to the inner controllers of the GFMs. The ICC states are denoted by $\gamma_{CC_{1\&2}}$ and the IVC states are denoted by $\gamma_{VC_{1\&2}}$. The eigenvalues can be split into three main categories: electromechanical, ICC-related, and IVC-related. The ICC-related modes, λ_{23to30}, are seen to be low frequency or non-oscillatory and may have participation from the PSSs of SGs, whose states are denoted by $\gamma_{PSS_{1\&2\&3}}$, or even the rotor speed dynamics as in $\lambda_{23\&24}$ and $\lambda_{25\&26}$. The IVC-related modes, λ_{31to36} are seen to be very close to the origin with very low frequency and close to the unstable region. It is important to note that all of the inner controller related modes except $\lambda_{23\&24}$ involve the inner controllers of multiple (or all) GFMs throughout the system, proving the need to perform system-level small-signal studies.

An additional note of interest is the lack of any important modes consisting of interactions between the GFM control states and the network dynamics. Likely due to the restricted control bandwidth of the GFMs, this might suggest the possibility of model order reduction in relation to time separation for an algebraic representation of the network in this case.

3.5 Parametric Sensitivity Analysis

Parametric sweeps are performed for the DILC case and are displayed in Fig. 3.2 to further the understanding of how the identified mode categories can be influenced.

Table 3.3: Eigenvalues of interest for the double inner loop control scenario.

Eigenvalue	Coordinates	Frequency (Hz)	Damping Ratio	Dominant States	Category
$\lambda_{11\&12}$	$-0.5577 \pm j12.4033$	1.9740	0.0449	$\boldsymbol{\omega_{GFM,2}}$, $\boldsymbol{\delta_{GFM,2}}$, $\omega_{r,4}$, $\delta_{GFM,3}$, $\delta_{GFM,1}$	Electro-mechanical
$\lambda_{13\&14}$	$-1.5240 \pm j11.8298$	1.8828	0.1278	$\boldsymbol{\omega_{r,8}}$, $\boldsymbol{\delta_{GFM,3}}$, $\omega_{GFM,3}$, $\delta_{r,8}$, $E^{'}_{q,8}$	Electro-mechanical
$\lambda_{15\&16}$	$-0.7015 \pm j11.4685$	1.8253	0.0610	$\boldsymbol{\delta_{GFM,1}}$, $\boldsymbol{\omega_{GFM,1}}$, $\omega_{GFM,3}$	Electro-mechanical
$\lambda_{17\&18}$	$-1.7469 \pm j10.6211$	1.6904	0.1623	$\boldsymbol{\omega_{r,8}}$, $\boldsymbol{\delta_{r,8}}$, $E^{'}_{q,8}$, $\omega_{r,4}$, $\omega_{r,9}$, $\delta_{GFM,3}$	Electro-mechanical
$\lambda_{19\&20}$	$-0.9950 \pm j7.4804$	1.1905	0.1319	$\boldsymbol{\delta_{r,9}}$, $\boldsymbol{\omega_{r,9}}$, $\omega_{r,10}$, $\delta_{GFM,3}$, $E^{'}_{q,9}$	Electro-mechanical
$\lambda_{21\&22}$	$-0.6295 \pm j7.0821$	1.1272	0.0885	$\boldsymbol{\delta_{r,10}}$, $\boldsymbol{\omega_{r,10}}$, $\omega_{r,2}$, $\delta_{GFM,3}$	Electro-mechanical
$\lambda_{23\&24}$	$-0.2350 \pm j0.0770$	0.0123	0.9503	$\boldsymbol{\gamma_{CC2,2}}$, $\boldsymbol{\gamma_{CC1,2}}$, $\boldsymbol{\omega_{r,1}}$	ICC-related
$\lambda_{25\&26}$	$-0.0526 \pm j0.0541$	0.0086	0.6970	$\boldsymbol{\gamma_{CC1,2}}$, $\gamma_{PSS3,7}$, $\gamma_{CC2,2}$, $\gamma_{PSS3,6}$, $\gamma_{CC1,1}$, $\gamma_{CC1,3}$, $\omega_{r,1}$	ICC-related
λ_{27}	-0.2373	0	1	$\boldsymbol{\gamma_{CC2,1}}$, $\boldsymbol{\gamma_{CC1,1}}$, $\gamma_{CC2,2}$	ICC-related
λ_{28}	-0.2131	0	1	$\boldsymbol{\gamma_{CC2,3}}$, $\boldsymbol{\gamma_{CC2,2}}$, $\gamma_{CC1,3}$, $\gamma_{CC2,1}$	ICC-related
λ_{29}	-0.0670	0	1	$\boldsymbol{\gamma_{CC1,1}}$, $\boldsymbol{\gamma_{CC1,2}}$, $\boldsymbol{\gamma_{CC2,1}}$, $\gamma_{CC2,2}$	ICC-related
λ_{30}	-0.0847	0	1	$\boldsymbol{\gamma_{CC1,3}}$, $\boldsymbol{\gamma_{CC1,1}}$, $\gamma_{PSS3,9}$, $\gamma_{CC1,2}$, $\gamma_{CC2,3}$, $\gamma_{PSS3,7}$	ICC-related
$\lambda_{31\&32}$	$-3.52 \times 10^{-6} \pm j7.97 \times 10^{-4}$	1.269×10^{-5}	0.0044	$\boldsymbol{\gamma_{VC2,1}}$, $\boldsymbol{\gamma_{VC1,1}}$, $\boldsymbol{\gamma_{VC2,2}}$, $\boldsymbol{\gamma_{VC1,2}}$, $\boldsymbol{\gamma_{VC2,3}}$, $\boldsymbol{\gamma_{VC1,3}}$	IVC-related
$\lambda_{33\&34}$	$-7.73 \times 10^{-6} \pm j8.01 \times 10^{-4}$	1.275×10^{-5}	0.0097	$\boldsymbol{\gamma_{VC1,3}}$, $\boldsymbol{\gamma_{VC2,3}}$, $\boldsymbol{\gamma_{VC1,1}}$, $\boldsymbol{\gamma_{VC2,1}}$	IVC-related
$\lambda_{35\&36}$	$-9.30 \times 10^{-6} \pm j8.03 \times 10^{-4}$	1.278×10^{-5}	0.0116	$\boldsymbol{\gamma_{VC1,2}}$, $\boldsymbol{\gamma_{VC2,2}}$, $\boldsymbol{\gamma_{VC1,1}}$, $\boldsymbol{\gamma_{VC2,1}}$	IVC-related

Dominant state subscript numbers refer to the machine number and should be cross-referenced with Fig. 3.1.

Note, the sweeps of any given parameter are performed on all the GFMs at once. From Fig. 3.2a we can observe that the damping factor, ζ, associated with the tuning of the IVC has a small impact on the ICC-related modes and significant influence over the stability of the IVC-related interactions. For the latter, the real-parts curve from instability into the stable region and then back towards the instability boundary but without reaching it. The chosen parameter value for the base case investigated previously was 25, at approximately the maximum negative real part for these modes within the range investigated. Fig. 3.2b displays the influence that the ICC time constant, τ_{CC}, (and hence IVC time constant) has over the inner controller related modes. When considering the IVC-related modes specifically, the increase of τ_{CC} brings the eigenvalues closer to the origin.

Moving our attention to the slower outer controllers, Fig. 3.2c confirms that the inertia constant of the VSM-based GFM, H, has a significant impact on the electromechanical modes with the potential for instability to occur if the parameter is set too high. H can also be seen to have an impact on the ICC-related modes but to a lesser extent and causing no instability in this case. In terms of the IVC-related interactions, H has no impact. The damping constant, K_D, is also seen to have significant impact on the electromechanical modes in Fig. 3.2d. However, for the range of parameter values evaluated no instability is observed. Similar to H, K_D has a small impact on the ICC-related modes, without causing any issues in this case, and has no impact at all on the IVC-related modes. The final parametric sweep in Fig. 3.2e finds that the reactive power droop gain, m_q, has negligible impact on the electromechanical modes as well as the ICC-related modes. However, it does impact the IVC-related interactions with increasing values bringing increased damping.

It should be noted that the conclusions drawn from these results are specific to the test system utilised at the operating point of interest. Also, the elements connected to the system and their specific parameter tuning values will have significant impact on the small-signal behaviour. This work aims to shed light on potential interactions that can occur in transmission systems containing a mix of SGs and bandwidth-restricted GFMs.

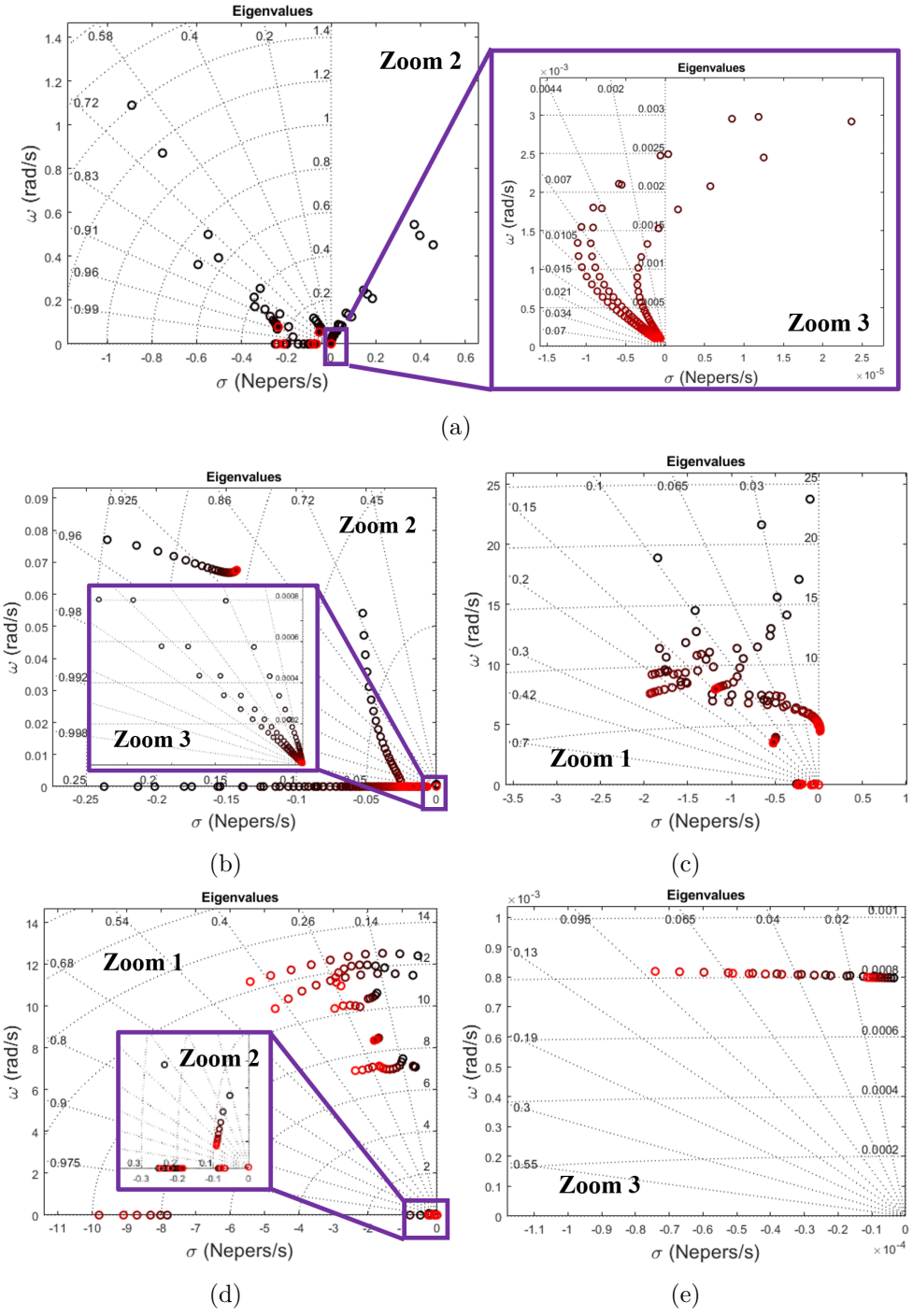

Figure 3.2: Parametric sweeps of eigenvalues with lowest values in black and highest values in red: (a) ζ : 1 to 50 in steps of 1 (b) τ_{CC} : $10 \times 1/f_s$ to $100 \times 1/f_s$ in steps of $1.8 \times 1/f_s$, (c) H : 2 s to 50 s in steps of 2 s, (d) K_D : 10 pu to 100 pu in steps of 10 pu and (e) m_q : 0.1% to 1% in steps of 0.1%.
Zoom key: 1=electromechanical modes, 2=ICC-related modes, 3=IVC-related modes.

3.6 Chapter Summary and Conclusions

This chapter provides a small-signal analysis focusing on multi-machine interactions in a GFM-penetrated transmission network. More specifically, this work utilises a modified IEEE 39-bus system with the addition of bandwidth-restricted CIGs utilising the VSM GFM control scheme (with and without inner loops). The interactions observed are split into three main categories of electromechanical, IVC-related, and ICC-related modes. The latter of which might also involve the PSSs, or even the rotor speed dynamics, of SGs. It was found that all types of mode typically involve participation from multiple machines (GFMs and/or SGs) within the system.

The sensitivity of these interactions to different GFM parameters is also investigated for this specific system. The IVC tuning damping factor is important for stabilising the IVC-related multi-unit interactions (although they still remain close to the stability boundary with resultant large damping time constant). The ICC time constant has influence over the ICC-related modes. There is a destabilising impact on electromechanical modes from the virtual inertia constant of the VSM. The virtual damping constant and reactive power droop gain have less impact on the overall stability of the system. Although, they do have some influence over the electromechanical and IVC-related modes, respectively. For this test system, it can be determined that removing the IVCs would be beneficial. Maintaining the ICCs would be sufficient for the current reference limitation approach and although ICC-related modes are close to the stability boundary, they cause no stability issues (in this case). This might suggest that SILC could be a beneficial approach and, as such, this architecture is included in the investigations of Chapter 4.

Note, modal analysis tends to provide results that are specific to the system, operating point, model-fidelity, and a range of other contributing factors. Nevertheless, the results of this chapter highlight important interactions that can exist when adopting bandwidth-restricted multi-loop control of GFMs in transmission-scale power systems. Understanding that such interactions exist, as well the dynamic states that participate, is vital for avoidance, mitigation, and control design in CIG-permeated power systems.

Chapter 4

Interaction Analysis of Multi-Machine Systems with Grid-Forming and Grid-Following Converters Under Different Control Architectures

4.1 Introduction

4.1.1 Motivation

This chapter continues in the same vein as Chapter 3 with the overarching goal of interaction identification, characterisation, and analysis in CIG-permeated power systems. Extending on the previous studies, we now also consider systems which include GFLs. Furthermore, there is a focus on the impact of different CIG controller architectures (see Fig. 2.13 and Fig. 2.14). In doing so, the work in this chapter contributes towards the ongoing conversation around the benefits and drawbacks of different cascaded controllers (especially with regards to GFMs), revealing the care that must be taken with respect to the possibilities for novel small-signal interactions,

as well as system conditions under which different architectures can cause smalls-signal instability.

Note, the investigation in Chapter 3 also considered different controller architectures for the GFM in terms of DACVC and DILC (but not SILC). However, this was focused on the situation in which the switching frequency, and subsequently the controller bandwidth, is restricted whereas this is not the case in this chapter, allowing for a situation in which conventional tuning approaches are appropriate. Although this might be unrealistic for transmission-scale BPS-connected CIGs adopting a two- or three-level VSC hardware implementation, it is more likely in such systems that a modular multilevel converter (MMC) architecture is utilised due to the capability for reduced switching losses in high-voltage systems [181–183]. For example, offshore wind farms are typically connected to the AC power system through HVDC links that make use of MMCs [184]. In such a case, a higher effective switching frequency can be achieved for the same submodule switching frequency [185]. This results in a less restricted control bandwidth, even in transmission-scale BPSs.

As detailed in Section 1.2, the uptake of CIGs, and subsequent reduction of SGs, is causing major changes to the dynamic characteristics of the power system [33, 38]. This includes the potential for new dynamic interactions between the wide bandwidth control of the CIGs with existing power system elements, each other, and even the electromagnetic dynamics of the network [59, 186]. Consequently, extensive research into potential small-signal multi-machine (or multi-element) interactions is required to capture those with notable influence over the dynamic response or the stability of the power system.

The flexibility of the digital implementation of CIG control results in a huge potential for differing control architectures and parameter tuning. In particular, there are ongoing questions regarding the optimal controller architectures to adopt for GFM control approaches due to the difficulty with standard tuning practices in high power applications and multi-machine networks [153,187], while various topologies can be also found in the literature regarding GFL control schemes.

The common approach for realising a GFM scheme relies on a multi-loop control

structure, with an ICC and IVC regulating filter current and voltage, and an outer loop responsible for the primary control objectives [120], i.e., voltage and frequency regulation and power sharing. Further adaptations based on the concept of virtual impedance are common but are not considered in this work [9,59,147,188]. Alterations of the multi-loop approach are also met in the literature, with the most common being not including inner loop control schemes, or including only an ICC [189]. In a similar manner, derivatives of the common GFL schemes consisting of a single current controller, may focus on including a further control loop directly regulating the output active and reactive power [190]. However, the impact of adopting each different GFM or GFL control architecture to the stability of the converter-dominated multi-machine power system has not been investigated to the required depth.

4.1.2 Literature Review

The impact of GFM controller architecture choice on the small-signal stability of OMIB systems has been investigated in [152]. Additionally, small-signal analyses of the interactions between multiple CIGs have been performed in the literature, including [191] and [192]. However, these do not consider how the choice of controller architecture affects the specific small-signal stability and interactions. In [59], which was also discussed in Section 3.1, an extensive small-signal analysis is performed to determine the major causes of instability with increasing penetrations of CIGs, considering a generation mixture of SGs, GFMs, and GFLs. They utilise a two-machine system for detailed analysis of interactions between SGs & GFLs, SGs & GFMs, and GFMs & GFLs. They also investigate the IEEE 9-bus[1] and South-East Australian systems but only in terms of stability margins. The work in this chapter adds to the analysis in [59] with a comparison of controller architecture combinations. Additionally, comprehensive PF analysis of the interactions involving CIGs is performed, rather than focusing only on the modes which cause instability.

A small-signal study with two to three CIGs connected to an infinite bus while including or neglecting a GFM, and then including or neglecting an ICC for the GFM,

[1] Alternatively named the Western System Coordinating Council (WSCC) 9-bus system.

was performed in [193]. They find that reducing the grid-strength causes instability when there is only GFLs (excepting the infinite-bus) or when the GFM includes an ICC. In addition, they highlight that an increasing penetration of GFM compared to GFL ensures stability in their system. Compared to this, the following work considers more controller architecture combinations as well as further parametric variation studies. Additionally, there is no infinite-bus in this work.

In this chapter is a comparison of potential multi-machine small-signal interactions and the impact of network parametric variations under different combinations of GFM and GFL architectures, supporting discussions regarding the benefits and drawbacks of each controller choice and the potential appearance of instabilities.

Following this introduction, Section 4.2 describes the small-signal modelling. Section 4.3 details the case studies that are performed, with Section 4.4 displaying the corresponding results. The conclusions are detailed in Section 4.5.

The work in this chapter was published in a special issue of Electric Power Systems Research for the proceedings of Power System Computation Conference (PSCC) 2024 [151].

4.2 Modelling

This section details the models adopted for the network elements, SG, and VSC. It also describes the controller architecture choices that are utilised for the GFL and GFM control.

4.2.1 Network

The passive components of the network are modelled dynamically to account for potential high frequency interactions with converter control [38, 186]. Transmission lines are represented by the π equivalent model and the transformers and loads by series RL impedances.

4.2.2 Synchronous Generator

The SG model adopted is the 8^{th} order linear magnetic model [11] as detailed in Section 2.6. The per unit parameters used are those of the Kundur two-area system in Example 12.6 in [10] but with inertia constant of 6.5 s used for all machines. In this work the SG has constant excitation and there is initially no AVR, governor-turbine, or PSS connected to allow us to focus on the fundamental interactions with the dynamics of the SG itself, rather than with controllers whose parameters and designs can be more varied. Following this, SG controllers are added (in Section 4.4.3) to provide an understanding of how this might affect the small-signal stability and interactions for the different combinations of CIG controllers.

4.2.3 Voltage-Sourced Converter

All connected CIGs include an LCL filter (if the external transformer is considered), as illustrated in Fig. 2.4. As a reminder, the superscript * corresponds to signals in the converter control reference frame and the bold italic lowercase letters represent a dynamic phasor in the dq0 notation [186] as $\boldsymbol{x} = x_d - jx_q$. The converter itself is represented by the averaged model, taking the modulation voltage signal, $\boldsymbol{v}_{\boldsymbol{cv}}^*$, from the control and applying it to $\boldsymbol{v}_{\boldsymbol{cv}}$ via a RFT (i.e., there is no PWM or control delay approximation). This transform is between the control reference frame, aligned with the internal machine angle, and the system reference frame which is aligned with a chosen reference machine. The resistance, R_f, inductive reactance, $X_{l,f}$, and capacitive reactance, $X_{c,f}$, have values of 0.03 pu, 0.08 pu, and 13.51 pu, respectively.

4.2.4 Grid-Following Converter

For the GFL control realisation, two approaches are often found in the literature, 1) SLC and 2) DLC. In the first case, only an ICC is required with the current references being calculated through a static calculation based on the power references and the measured voltage [194]. In the second case, an extra control loop is included, generating the current reference values based on PI controllers regulating the output power to their reference value [190]. The described implementation is further explained in Section

2.5.3 and Fig. 2.13, with the reactive power control variant being used in these studies. In this work, the proportional and integral gains of the PI controllers are 0.25 pu and 25 pu for both outer controllers, 60 pu and 1400 pu for the PLL, and 1 pu and 10 pu for the ICC. For these controllers, this tuning achieves closed-loop bandwidths of 3.3 Hz, 13 Hz, and 747.6 Hz, respectively. This tuning was based on [132] and aims to ensure bandwidth separation to avoid controller coupling. The power measurement filter time constant is 0.0318 s.

4.2.5 Grid-Forming Converter

Various alternative implementations of GFM control schemes are presented in the literature. Apart from the variety of different droop control schemes, virtual impedances, or the inclusion or not of feed-forward terms [59,160,195], the architecture with regards to inner control loops may also vary [189], a fact raising rather important concerns for the stability of CIG-dominated power systems, due to the different timescales of the inner and outer loop control schemes. Hence, three different approaches are considered in this chapter for the GFM control realisation, 1) DACVC, 2) SILC and 3) DILC, with their realisation being further described in Section 2.5.5 and graphically depicted in Fig. 2.14. For the structure of the inner and outer control loops the reader is referred to Section 2.5.2 and Section 2.5.4. In this case, the outer loop consists of droop-based active power and reactive power/voltage magnitude control, and there is no virtual impedance. Furthermore, as described in Section 2.5.4, low-pass filtering of the measured power is used to provide virtual inertia characteristics [134]. Note, the static calculation required for SILC can be regarded as a form of virtual admittance with parameters chosen to compensate for the RL impedance of the VSC output filter [152] (see Section 2.5.5). However, this should not be confused with virtual impedance additions used for supplementary control or impedance shaping such as in [9, 147, 188].

Control elements common with the GFL have the same tuning. The droop gain is 0.02 pu and 0.0289 pu for the active and reactive power controllers respectively, based on [59]. The proportional and integral gains for the IVC are 1 pu and 100 pu

respectively. This tuning was chosen for sufficient timescale separation from both the ICC and outer controllers, with a resultant closed-loop bandwidth of 471.4 Hz [125].

4.3 Case Studies

A two-machine system and the IEEE 9-bus are described in this section along with the case studies applied to them and the approach for generation of system operating points. These two example networks were chosen for their relative simplicity, allowing for detailed investigation of the small-signal dynamics and interactions with respect to the different combinations of generation mixture and controller architectures.

4.3.1 Two-machine System, Generation Mixtures, Controller Combinations, and Parameters to be Varied

The two-machine system is displayed in Fig. 4.1 with dotted section included. It is based on the Kundur two-area system with G1 and G2 being rated at 1800 MVA and 20 kV. The transformers are also rated at 1800 MVA with a voltage base of 20 kV : 230 kV. Also, the loads in area 1 and area 2 are absorbing active and reactive powers of 967 MW and 100 MVAr, and 1767 MW and 100 MVAr, respectively.

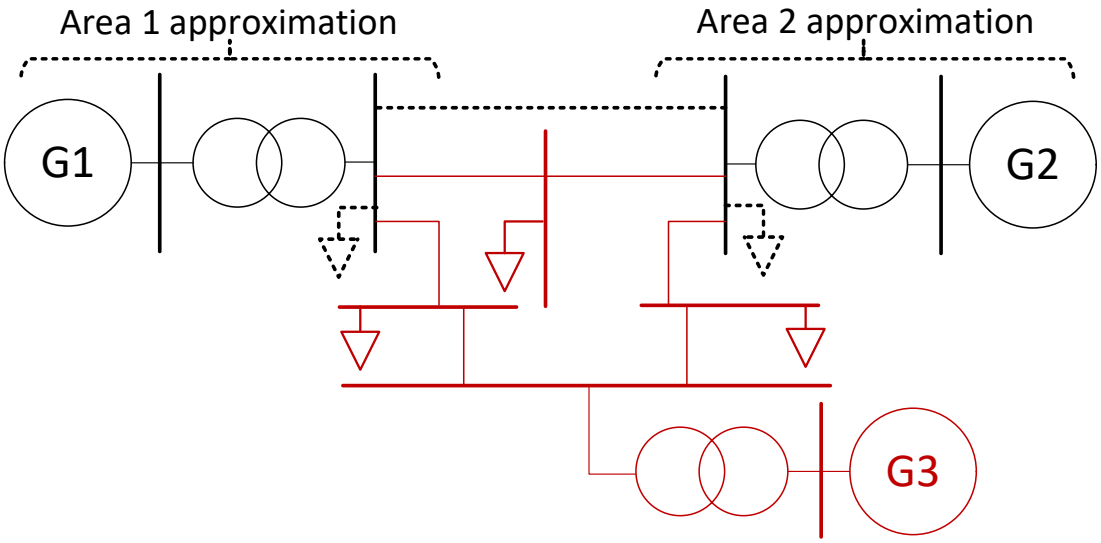

Figure 4.1: Study networks: two-machine system when including dotted section or IEEE 9-bus when including red section.

The following generation mixtures (G1/G2) are considered:

- SG/GFL (2 combinations of GFL control)
- SG/GFM (3 combinations of GFM control)
- GFM/GFL (6 combinations of GFM/GFL control)
- GFM/GFM (3 combinations of GFM control)

Note, the GFL/GFL scenario is not considered as this was found to be unstable due to the lack of a unit forming the voltage phasor.

For each of the generation combinations outlined above, the following investigations are performed:

- Interaction analysis (eigenvalues and corresponding PFs) at the base operating point described in Section 4.3.3.
- Varying length of the transmission line interconnection.
- Varying system loading.
- Varying the installed capacity between G1 and G2.

4.3.2 IEEE 9-Bus System

Also considered is the IEEE 9-bus system which is displayed in Fig. 4.1 with the red section included. The generators G1, G2, and G3 are set to be a GFM, GFL, and SG, respectively. The test case parameters can be found in [196].

With this system, the penetration of each type of machine is varied by considering firstly the penetration of SG installed capacity, $SG/Total$, as well as the penetration of GFM installed capacity with respect to the remaining converter installed capacity, $GFM/(GFM + GFL)$.

4.3.3 Generation of System Operating Points

The total installed capacity of the system is shared between the machines depending on the specified ratios. This total value is taken as the total installed capacity of the

base system, i.e., 1800 MVA + 1800 MVA for the two-machine system and 247.5 MVA + 192 MVA + 128 MVA for the 9-bus system. The change is reflected in the dynamic modelling with a reduction or increase of the machine's rated power. The ratings for the transformers of each generator are updated correspondingly. To vary the loading, a multiplication factor is applied to each load. Finally, the active and reactive power injections of the generators are updated in the power flow case file by extracting the total values for the base case and splitting between the generators, based again on the specified ratios.

The power flow is then run and the results are leveraged to calculate the initial states of the generator dynamic models. This is achieved by setting the derivative terms in the differential equations to zero (i.e., steady state) and solving the resultant system of non-linear equations (Section 2.1.1).

For both systems, the base case is considered with the installed capacity split evenly between the generators, and a load multiplier of 1. Additionally, the transmission line in the two-machine system is set to 50 km.

4.4 Results: Eigenvalue-Based Interaction Analysis and Impact of Varying Key System Parameters

4.4.1 Two-Machine System Results

This section details the results obtained from performing the case studies outlined in Section 4.3.1.

For the base operating point (Section 4.3.3), the eigenvalues are displayed in Fig. 4.2. This includes a plot for each generation mix with the different control architecture combinations distinguished as described by the legend in the Fig. 4.2 caption.

Also shown, in Fig. 4.3 to Fig. 4.5, are the results of the parametric variations of the transmission line interconnection, system loading, and the ratio of installed capacity (and resultant generation dispatch) between G1 and G2. This includes results for each generation mix with the different control architecture combinations distinguished as described by the legend in the Fig. 4.3 to Fig. 4.5 captions. Note, only the results

considered relevant for each case are included, i.e., not all eigenvalues are displayed. The $G1/(G1+G2)$ ratio parametric sweeps are performed for ratios 0.01 up to 0.99 in steps of 0.01, however, from 0.82 onward the power flow does not converge.

The PF vectors used to characterise modes are representative values taken at the base case which is a limitation of this analysis considering the capability for PFs, similar to the eigenvalues, to vary significantly depending on the system operating point. When describing a mode's PFs, those with value above 2.5% are specified.

The modes of interest in this work involve the CIG control. As such, any modes with relative contribution less than 5% from CIG control states are neglected. For this purpose a mode will only be neglected if it is found to have less than 5% participation from CIG states across all parametric variations. Additionally, modes with damping time constant less than 0.01 s are deemed to have negligible impact on system dynamics and are not considered.

Interactions and impact of parameter variations in the system with a SG and a GFL

From analysis of the eigenvalue plot in Fig. 4.2a, the differences between using SLC and DLC for the GFL are clear with the former containing a single oscillatory mode at $-13.8 \pm j20.1$ and the latter containing three at $-6.0 \pm j23.5$, $-23.1 \pm j30.3$, and $-28.5 \pm j2.4$. The SLC oscillation has participation from the GFL's PLL and, to a lesser extent, the SG damper windings. For the DLC, the first two modes that were mentioned have participation from the PLL and outer controllers of the GFL, and the remaining oscillation involves the same controllers and the damper windings of the SG.

From the parametric sweep in Fig. 4.3a, it is found that increasing the transmission line length brings a mode towards the unstable region but without reaching it. This is more emphasised with the DLC but a similar mode trajectory is seen in the SLC case. These modes are the $-13.8 \pm j20.1$ and $-6.0 \pm j23.5$ modes in the SLC and DLC cases, respectively.

It can be observed from Fig. 4.4a that at low loading the system is unstable due to a mode with participation from the rotor and damper windings of the SG. Similar non-

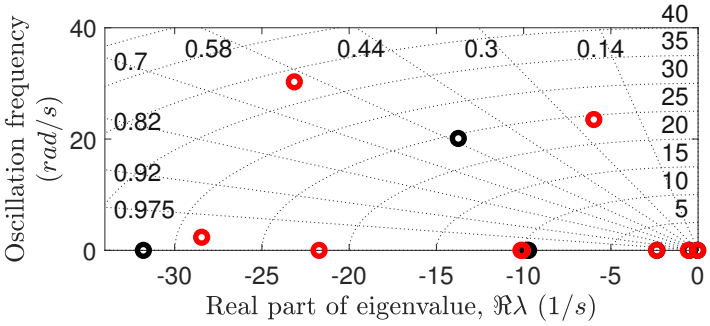

(a) SG/GFL scenario.

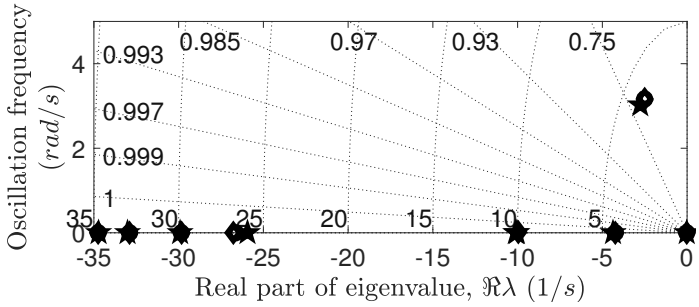

(b) SG/GFM scenario.

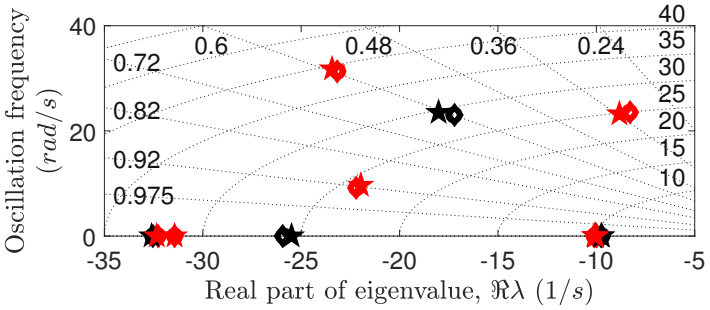

(c) GFM/GFL scenario.

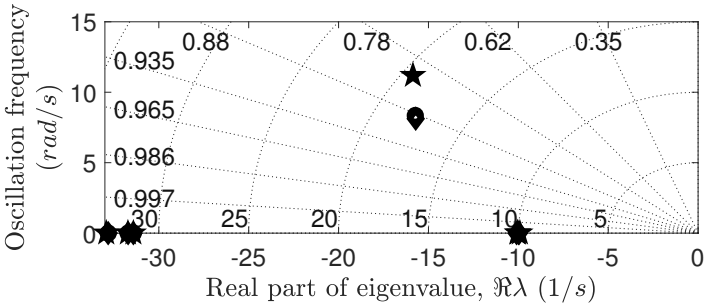

(d) GFM/GFM scenario (with homogeneous GFM control).

Figure 4.2: Eigenvalues with minimum 5% contribution from CIG control states and damping time constant above 0.01 s at the base operating point. Legend: black=single loop control (when GFL is present), and red=double loop control; circle=direct AC voltage control (when GFM is present), diamond=single inner loop control, and star=double inner loop control. Note, lines of constant damping ratio and natural frequency are included.

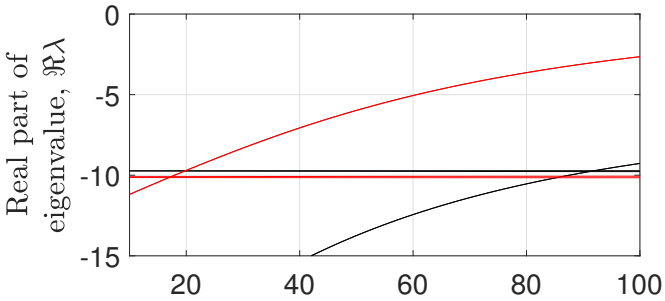

(a) SG/GFL scenario.

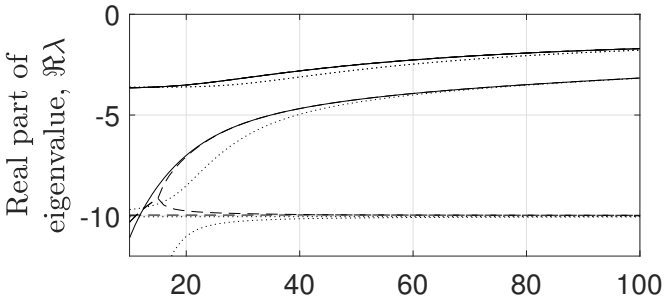

(b) SG/GFM scenario.

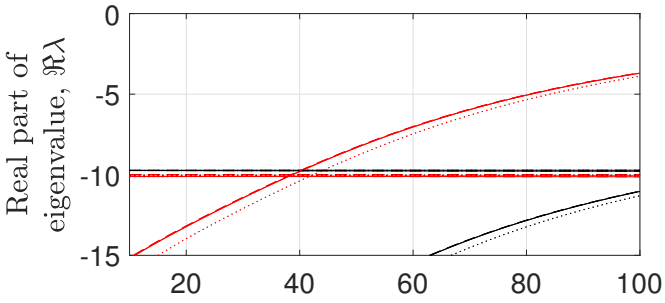

(c) GFM/GFL scenario.

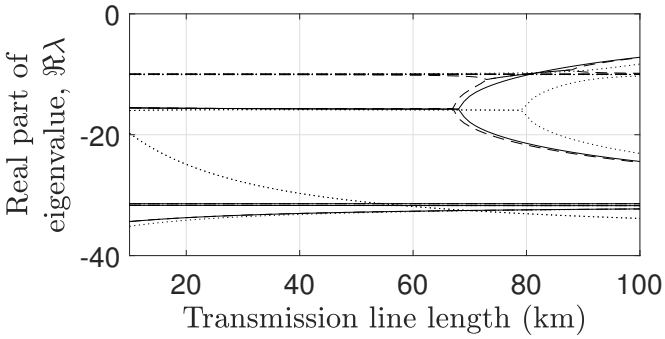

(d) GFM/GFM scenario.

Figure 4.3: Real part of eigenvalues with minimum 5% contribution from CIG control states for transmission line length parametric variation. Legend: black=single loop control (when GFL is present), and red=double loop control; solid line=direct AC voltage control (when GFM is present), dashed line=single inner loop control, and dotted line=double inner loop control.

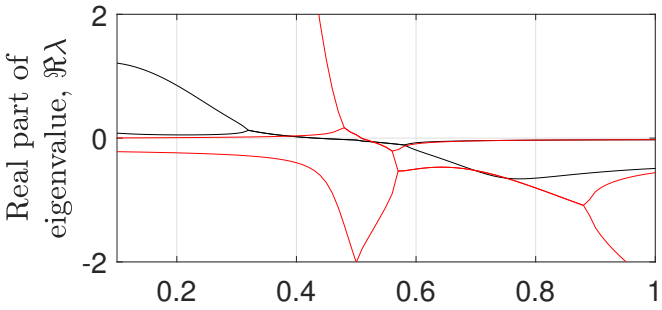

(a) SG/GFL scenario.

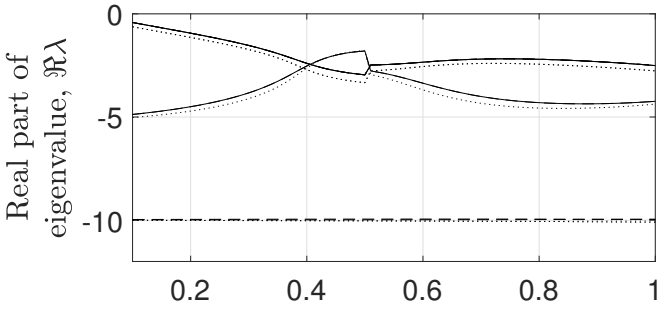

(b) SG/GFM scenario.

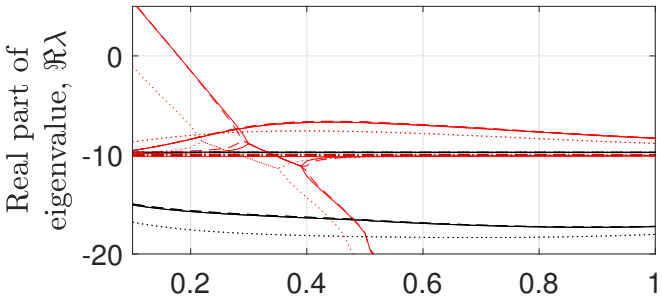

(c) GFM/GFL scenario.

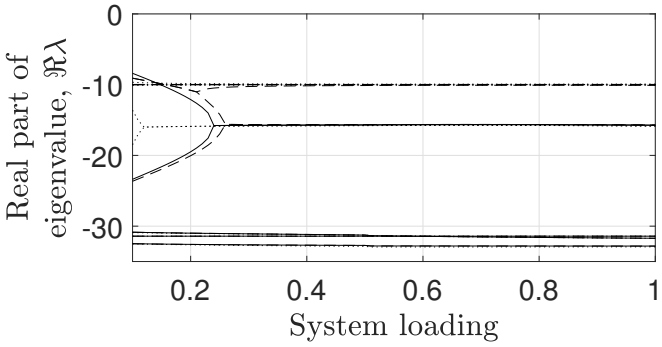

(d) GFM/GFM scenario.

Figure 4.4: Real part of eigenvalues with minimum 5% contribution from CIG control states for system loading parametric variation. Legend: black=single loop control (when GFL is present), and red=double loop control; solid line=direct AC voltage control (when GFM is present), dashed line=single inner loop control, and dotted line=double inner loop control.

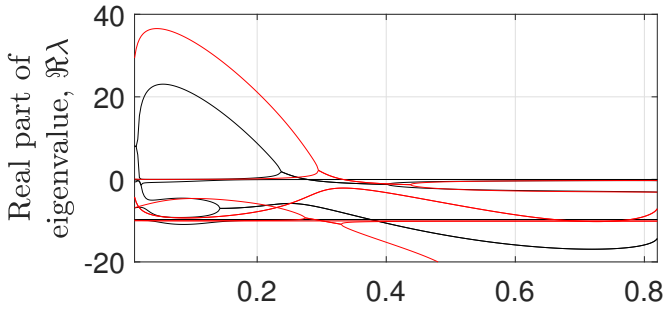

(a) SG/GFL scenario.

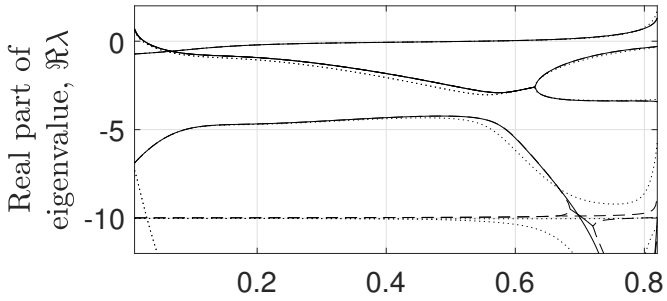

(b) SG/GFM scenario.

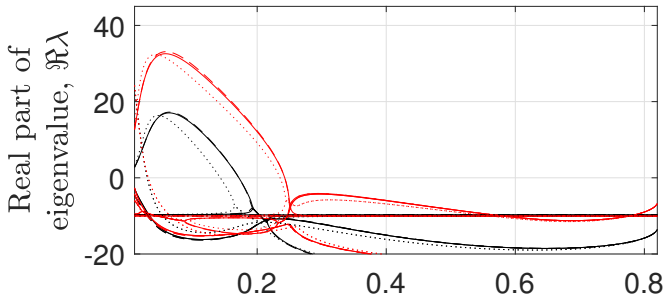

(c) GFM/GFL scenario.

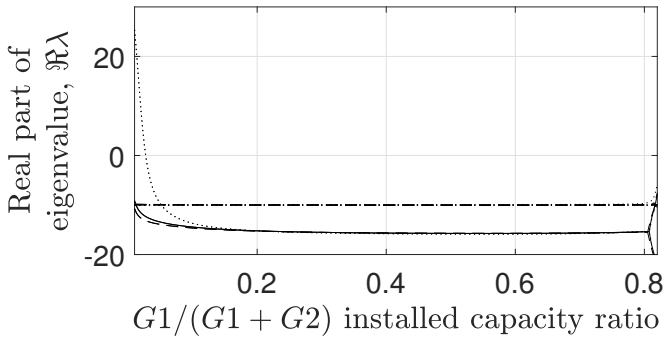

(d) GFM/GFM scenario.

Figure 4.5: Real part of eigenvalues with minimum 5% contribution from CIG control states for installed capacity ratio parametric variation. Legend: black=single loop control (when GFL is present), and red=double loop control; solid line=direct AC voltage control (when GFM is present), dashed line=single inner loop control, and dotted line=double inner loop control.

oscillatory modes with high damping time constant and participation from SG rotor and damper windings are known to exist in Kundur's two area system [10]. It becomes stable at a lower value of loading in the SLC case compared to the DLC case. Note, the PFs of this mode are found to involve the GFL outer controller and PLL at lower loading values, hence the significant impact of the choice of GFL architecture despite the base case PFs suggesting no GFL contribution. This is an example of the difficulty in drawing conclusions for specific interactions due to the variability of PFs (a concept which is returned to, and addressed through the use of modal clustering, in Chapter 5).

For the installed capacity variation, displayed in Fig. 4.5a, both controller architectures cause instability with low SG and high GFL penetration. The mode causing instability in both cases is related to the PLL of the GFL and the rotor and damper windings of the SG. It is seen that when using DLC, the system requires at least 34% SG penetration to maintain stability while using SLC requires only 28% SG penetration.

Generally, the SLC case has better stability margins and boundaries for the same modes (i.e., with similar participating states and mode trajectories) than the DLC case. However, using the SLC brings the obvious drawback of an inability to control exactly the active and reactive power.

N.B. for the parametric sweeps there are instances in which a single mode appears to split (or branch) or where two separate modes seem to combine. This is the result of a single complex-conjugate paired oscillatory mode becoming non-oscillatory resulting in two separate real eigenvalues when splitting and the reverse is true when combining.

Interactions and impact of parameter variations in the system with a SG and a GFM

From analysis of the eigenvalue plot in Fig. 4.2b it can be determined that the choice of GFM controller architecture has very limited impact on the dominant modes of the system. There is one oscillatory mode, for all control architectures, at $-2.5 \pm j3.2$, which is found to be an electromechanical interaction between the SG and the GFM. i.e., with

participation from the rotor of the SG and the "virtual rotor" of the GFM. Additionally, not shown is an oscillation at $-25.9 \pm j355.3$ present only for the DILC case. This oscillation has participation from the electromagnetic dynamics of the network currents.

The parametric sweeps in Fig. 4.3b, Fig. 4.4b, and Fig. 4.5b again confirm the lack of impact of controller architecture choice on the dominant modes in this scenario. Similar to the SG/GFL scenario, Fig. 4.3a shows that there is no instability resulting from the transmission line length variation. However, the instability seen at low loading in the SG/GFL scenario is not present in this scenario (Fig. 4.4b). From Fig. 4.5b, it is observed that very low SG penetration and high GFM penetration causes instability, but also when there is very high SG penetration and low GFM penetration. The cause of instability for both of these cases is different with the former being the electromechanical interaction between the SG and GFM, and the latter being a non-oscillatory mode involving the SG damper windings and rotor.

Interactions and impact of parameter variations in the system with a GFM and a GFL

The eigenvalue plot in Fig. 4.2c can be compared to the plot for the SG/GFL scenario with one oscillation for the SLC at approximately $-17.2 \pm j23.0$ and the DLC containing three oscillations at $-8.3 \pm j23.5$, $-22.2 \pm j9.2$ and $-23.2 \pm j31.4$. However, the least damped oscillation is this time seen to have a greater stability margin with respect to the eigenvalue real part. The dominant states of these modes resemble their SG/GFL counterparts but where in the SG/GFL case these modes had contribution from the SG rotor and damper windings, in this case it is instead contribution from the GFM virtual rotor. Additionally, several non-oscillatory modes with low damping time constant, that correspond primarily to the SG damper windings, are no longer present.

The impact of GFL controller architecture choice is clearly greater on these dominant modes compared to the choice for the GFM. However, there is a slight improvement in terms of damping for the least damped mode when using DILC as opposed to DACVC or SILC.

The parametric sweeps in Fig. 4.3c, Fig. 4.4c, and Fig. 4.5c again highlight the

similarities to the SG/GFL case and the limited impact of GFM controller architecture choice. However, the loading variation, as observed from Fig. 4.4c, reveals no instability for the SLC at low loading values and a greatly increased stability region for the DLC. This is due to the lack of the SG damper windings/rotor mode that caused the issues in the SG/GFL case. Additionally, the relative lack of impact of the choice of GFM architecture is again observed. There is a slight impact of using DILC, especially at low loading (where this prevents instability) and low GFM penetration scenarios (Fig. 4.5c).

Interactions and impact of parameter variations in the system with two GFMs

The eigenvalue plot in Fig. 4.2d can be compared to the corresponding plot for the SG/GFM scenario. There is again a single oscillatory mode which in this case is much more damped and at a higher frequency, at approximately $-15.8 \pm j11.2$. In this scenario, this electromechanical mode is an interaction between the virtual rotors of the GFMs. Also in this scenario there is another high frequency oscillation (not shown), at $-31.0 \pm j328.7$, with participation from the current dynamics of the network. Again, the lack of a SG means the removal of several non-oscillatory modes with low damping time constant.

From Fig. 4.4d, this scenario poses no threat to stability under the range of parametric variations, other than at very low penetrations of G1. In this exceptional circumstance, only the use of DILC causes the instability and it is the oscillatory mode described earlier that is the culprit.

Two-machine system results discussion

A high level conclusion is that, for the specific system set up, the small-signal stability is affected much more by the choice of GFL architecture than the choice of GFM architecture (although there is small impact when adopting DILC). This is likely due to the fact that the interactions that cause stability issues in this system are generally related to slower dynamic phenomena, of which the different GFL control architecture

choices are focused. Contrastingly, the differing controller architecture choices for the GFM involve the inclusion of the inner controllers which ideally are sufficiently decoupled from the slower dynamics of the primary control.

Additionally, although not observed from Fig. 4.3 to Fig. 4.5 (due to them displaying the change of the eigenvalue real part), the frequency of the modes can vary in response to the parametric variations. As an example, in the GFM/GFL case, when the GFL uses SLC and the GFM uses DILC, there is a mode which is unstable at low penetrations of $G1/(G1+G2)$. This mode varies in frequency from 6.74 Hz to 2.30 Hz, and when using DACVC or SILC, a similar mode is seen which varies from 10.41 Hz to 1.82 Hz (although this mode is never unstable). However, such a variation is not guaranteed. For example, in the transmission line length sweep in Fig. 4.4a the highlighted modes, which are at $-13.8 \pm j20.1$ and $-6.0 \pm j23.5$ in the base case, are found to have relatively constant oscillation frequency as the parameter varies. This highlights the care required when performing interaction analyses as well as the wide range of frequencies that may require monitoring in converter-permeated systems.

4.4.2 IEEE 9-bus System Results

The resulting stability margins from varying the installed capacity of each generator, as described in Section 4.3.2, are displayed in Fig. 4.6. The immediately obvious conclusion is that, in this system, the stability is affected much more by the choice of GFM controller architecture than that of the GFL.

The choice of GFL architecture has a small impact on stability boundaries, with the use of DLC causing an additional region of instability when the SG and GFM penetrations are low (i.e., the GFL penetration is high). The modes found to be causing instability in this region are non-oscillatory and attributed to the PLL and outer controllers of the GFL. When the GFM utilises DACVC or SILC, the use of DLC reduces the instability region at high SG and GFM penetration (region which doesn't exist when using DILC for the GFM). The cause of instability in this region is a non-oscillatory mode with participation from the SG rotor and damper windings.

The significant unstable region existing when using SILC, generally towards low

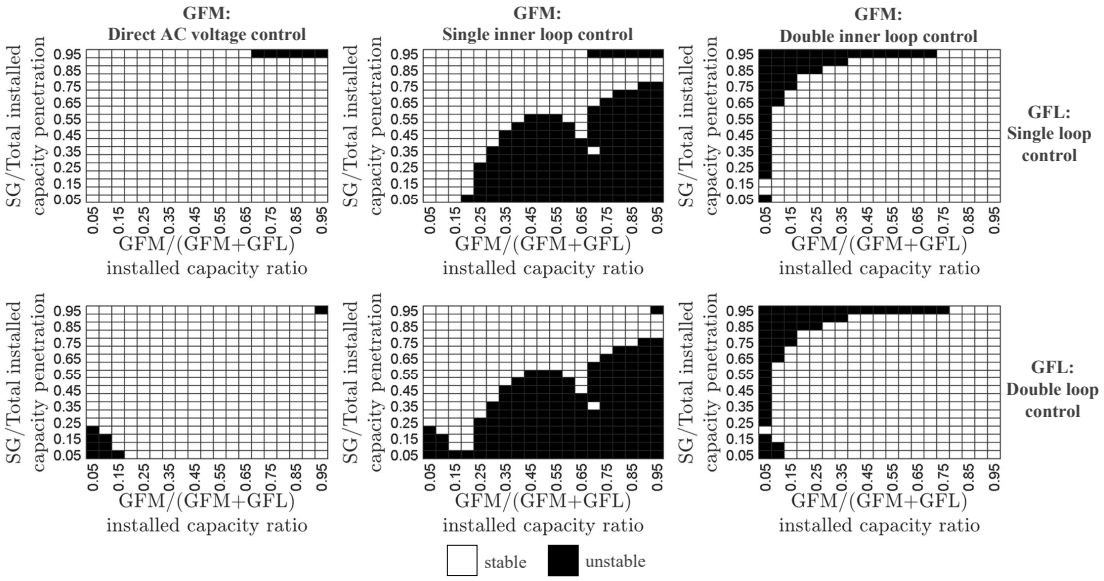

Figure 4.6: Stability maps for 9-bus system considering variation of generator penetrations. Y-axis gives proportion of total installed capacity coming from the SG. X-axis gives proportion of converter installed capacity coming from the GFM converter. Therefore, the remainder of the installed capacity comes from the GFL converter.

penetration of SG and high penetration of GFM, is attributed to a very high frequency mode (above 2 kHz) with participation from the output LC filter of the GFM.

The unstable region when using DILC is opposing that when using the SILC, with high SG penetration and low GFM penetration causing instability. For this case, the instability is caused by an oscillation ranging from 9.46 Hz to 12.53 Hz with participation from the GFM APC, VMC, and IVC.

It can be noted that, for this system setup, none of the instability inducing modes are multi-machine interactions.

4.4.3 Impact of Including Synchronous Generator Controllers

As has been revealed already, the results of these types of small-signal interaction analyses are very sensitive to the system under test. However, SGs are generally always equipped with some form of AVR and associated exciter. Additionally, they will often utilise a PSS. Therefore, these controllers have been added to the SG to determine how this might impact the previously discussed results. The DC1A AVR and exciter

combination is adopted as well as the PSS1A PSS. The per unit parameters used for these controllers are taken from Examples 12.6.b.i and 12.6.b.iv of [10], respectively.

The eigenvalues displayed in Figs. 4.2a and 4.2b were largely unaltered other than the addition of an oscillatory mode of approximately $-0.3 \pm j1.4$ and $-0.61 \pm j0.5$, respectively. The GFL controller architecture choice has a small influence on this mode. It was seen to have participation primarily from the SG damper windings, rotor, AVR, and PSS. For the SG/GFL base case the participation from CIG states is only 1.11% and 0.52% when using SLC and DLC, respectively. For the SG/GFM case there is 2.36% contribution from CIG states.

As an example of the influence of these controllers on the results of the parametric variations, Fig. 4.7 displays the loading sweep for the SG/GFM case. It is observed

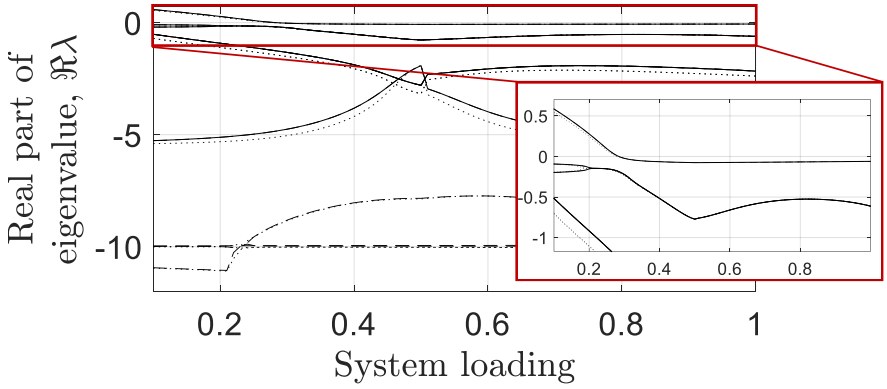

Figure 4.7: Real part of eigenvalues with minimum 5% contribution from CIG control states for variation of loading in SG/GFM case with inclusion of AVR, exciter and PSS.

that the trajectories seen in Fig. 4.4b are impacted little but there are two additional modes with low stability margin. In particular, one mode is unstable for low loading values. This is a non-oscillatory mode related to the SG damper windings, AVR, and GFM rotor when unstable, and related mostly to the PSS at high values of loading. Checking all system modes (i.e., not just those with contribution from CIG) reveals that this instability does not occur in the system without SG controls. The other mode with low stability margin is the aforementioned oscillation.

These results highlight the importance of including all relevant controllers in small-signal interaction analyses.

4.5 Chapter Summary and Conclusions

This chapter investigates the small-signal interactions that might occur in two multi-machine systems, namely a two-machine system and the IEEE 9-bus system. It also explores the impact on mode stability and trajectories as a result of varying system parameters. There is a focus on the impact of controller architecture variations with respect to the inclusion or neglection of cascaded controllers.

For the two-machine system, the choice of GFL controller architecture is of significant importance, with regards to the number of oscillations and influence over stability margins. In particular, the use of DLC tends to reduce the region of stability when considering low loading and low SG (or GFM) penetration. The inclusion of a GFM tends to increase stability regions compared to scenarios with either GFL or SG in its place. Additionally, the choice of controller architecture for the GFM has limited influence in this system.

For the 9-bus system, the GFL control architecture choice has less of an impact but does result in a small region of instability at low SG and GFM penetrations when using DLC. Contrastingly, the GFM controller architecture choice in this case has a significant impact, with SILC resulting in a large region of instability with low SG and high GFM penetrations, related to a high frequency mode with contribution from the CIG output filter. When using DILC there is a region of instability towards high SG and low GFM penetration caused by a (9.46 Hz to 12.53 Hz) mode involving the primary control and inner voltage control of the GFM.

The variability of modes (and their PFs) with regards to system parameters and operating points, controller tunings and architecture choice, amongst others, makes generalising conclusions for these types of analyses very challenging. This is strengthened through a study in which the AVR and PSS were added to the SG, revealing the addition of an instability at low loading for the SG/GFM case which is not present without these controllers. Therefore, it is recognised that there is a crucial need for performing extensive multi-machine interaction investigations for more complex systems with different layouts, controllers, tuning, operating points, and more.

This is true not just for small-signal interaction studies but also the expansion to non-linear analysis such as investigation of fault ride-through capabilities.

Despite these difficulties, this chapter illuminates potential small-signal interactions and mode trajectories from parametric variations, furthering discussions regarding the benefits and drawbacks of GFL and GFM controller architecture choices. As a general note, the fact that very different behaviours are observed raises an important point about potential effects coming from specific control structure choices and the need to describe the implementation of GFM and GFL control in sufficient detail for system stability studies. In addition, converter-connected units through various vendors with different implementations might exist in different networks, making a unique recommendation challenging.

Chapter 5

Enabling Characterisation of Dynamic Interactions with Probabilistic Small-Signal Analysis in Converter-Permeated Power Systems

5.1 Introduction

5.1.1 Motivation

Although continuing with an interest in novel small-signal interactions, we now begin to focus on developing analysis methodologies appropriate for CIG-permeated BPSs. In particular, in this chapter, a framework for PSSA is developed which enables the characterisation of new interactions in power systems incorporating CIGs, across the full operating range (with increasing variability due to the increase in variable RES-based generation), as well as understanding their probabilistic behaviour. This includes a systematic characterisation procedure as well as modal clustering and the introduction of a stability weighted participation index (SWPI).

The need for probabilistic analysis methods more generally is increasingly recognised in both academia and industry. For example, in the UK, NESO (along with industry partners such as TNEI) have been developing tools that take advantage of probabilistic dataset generation for determination of operational boundaries [197].

5.1.2 Literature Review

To reiterate the discussion at the beginning of Chapter 3, previous works have investigated the small-signal dynamics associated with the energy transition, but they have mostly focused on OMIB systems [5, 125, 149, 152], small systems with multiple machines in close proximity [198, 199], or larger systems but only in terms of stability with limited information on the dynamic characteristics or interactions themselves [200, 201]. A comprehensive small-signal analysis of power systems with a SG, GFL, and GFM converter generation mix is provided in [59]. Potential interactions occurring between SGs, GFLs and GFMs from a small-signal perspective are investigated, focusing also on identifying maximum permissible CIG penetration levels. Additionally, [172] performs similar analysis of small-signal interactions in systems with SGs and GFLs. Impedance modelling is a highly effective and scalable alternative approach for small-signal stability analysis [28]. However, this does not provide the detailed characterisation of interactions that can be achieved with methods like PFs [11]. Furthermore, while the impact of different operating points is briefly investigated in [59] and their importance highlighted, a probabilistic approach is employed in our work to offer a comprehensive analysis of the behaviour of interactions across an extensive range of operating conditions.

The use of PSSA approaches is increasingly necessary as the range of operating conditions increases with the inclusion of variable RESs. In particular, the impact on emerging interactions in CIG-permeated power systems, including their PF-based characteristics and probabilistic behaviour, has not been adequately addressed. PSSA methods have been used in the literature either for conventional power systems or for targeted studies in CIG-permeated systems such as determining the impact of wind variation, however, to the best of our knowledge only GFL control approaches have been

studied [19, 21, 24, 202, 203], except [204] which includes consideration of GFM control in a OMIB system, displaying how their proposed control can decrease the likelihood of instability in their particular case. As highlighted by a recent review paper [57], such studies often focus on stability boundaries or likelihood [18, 20, 22]–using worst-case stability metrics such as damping ratio of least damped mode–without delving into the interaction characteristics, including which system elements are participating, something that we address in this chapter. Those that do somewhat delve into characterisation of interactions have used mean values of PFs [202, 205, 206] (or similar properties such as controllability and observability [207]), which may fail to fully detail the breadth of information available from probabilistic studies, or have not specified the operating point at which the PFs are calculated [208]. Detailed reporting of the controllability across the whole operating range was applied in [209], however, this was for only a selected few (easily distinguishable) modes. Distributions of PFs for the least damped mode were analysed in [210]. This is very useful but highlights the difficulty in analysing such properties due to the variability of the PFs across the operating range. In fact, the most dominant states are seen to have the potential to have significant contribution of around 0.2 for some operating points, but almost 0 for others. Furthermore, such visual distribution analysis can be useful for a single mode of interest, but does not scale well when we have to investigate a broader range of modes/dynamics. In this chapter, the SWPI is instead introduced, as part of a systematic characterisation procedure, to ensure the characteristics of a given interaction are prioritised for the eigenvalues with lowest stability margin.

To enable the application of our proposed systematic characterisation procedure, and to analyse the probabilistic behaviour of specific interactions, we group similar modes based on their PF-based characteristics. As the operating point varies, eigenvalues (and their eigenvectors and PFs) can vary significantly. Some works have attempted to circumvent this issue with a rudimentary mode tracking approach based on the Euclidean distance between right eigenvectors [206], seemingly based on the work in [211] which appears to be used for small sequential variations of operating point. However, in PSSA studies, the right eigenvectors can vary significantly due to

the potentially large changes of operating point resulting from the random sampling. If modes are easily distinguishable in the complex plane (such as for the analysis in [209]) then this is not a challenge. However, in power systems permeated with complex and detailed models, including those of CIGs, modes are not so easily distinguished, as highlighted in the results of this chapter. Therefore, this chapter adopts clustering to group modes with similar PF-based characteristics.

To summarise, this chapter introduces a framework for detailed probabilistic analysis and characterisation of the behaviour of new types of interactions in CIG-permeated power systems. The main proposals in this chapter include:

- A systematic characterisation method for detailed dynamic interaction analysis across the operating range. This involves: PF-based categories to characterise modes; and a stability weighted participation index for characterising interactions (clusters of modes with similar PFs) with a (real part of eigenvalue) weighted average of PFs.

- The application of clustering to decompose the full range of modes across the operating range into key distinct interactions based on their PFs.

- An in-depth PSSA study of dynamic interactions in a transmission scale power system (IEEE 68-bus) using detailed high-order models of SGs, GFLs, GFMs, and network dynamics. That is, including a thorough investigation of novel small-signal interactions in CIG-permeated systems. This has included highlighting of potential SSOs related primarily to the inner voltage controllers of GFMs.

The remainder of this chapter is structured as follows: Section 5.2 presents the proposed probabilistic small-signal interaction analysis procedure; Section 5.3 outlines the power system modelling performed; Section 5.4 describes the adopted modified IEEE 68-bus system and Section 5.5 displays the corresponding results; finally, avenues of future work are outlined in Section 5.6 with Section 5.7 concluding the chapter.

The work in this chapter has been submitted to IEEE Transactions on Power Systems.

5.2 Methodology: Probabilistic Small-Signal Interaction Analysis Framework

The proposed procedure consists of three parts: ***probabilistic data generation; mode screening and PF-based clustering; and systematic characterisation & probabilistic analysis***.

The probabilistic data generation includes any approach by which we can obtain the eigenvalues and eigenvectors of the linearised power system model, for a range of operating points as determined from probabilistic inputs. The mode screening involves removing modes that are of limited influence on the system dynamics (e.g., "passive modes", as defined in Section 5.2.2), for simplification of the analysis as well as computational benefits, and the clustering (Section 5.2.3) enables detailed analysis of the dynamic behaviour of any given interaction across the operating range. Within the third stage, system states are combined into user-defined categories (such as individual generators or dynamic phenomena) from which interactions can be characterised using the SWPI, the definition of which is explained further in Section 5.2.4.

The above descriptions constitute the general concepts of the proposed framework. The remainder of this section details the specific implementation of the framework as used in our work, outlined in Fig. 5.1, with potential improvements on this specific approach discussed in Section 5.5.4 and Section 5.6.

5.2.1 Probabilistic Modelling

Uncertain Parameters Considered, and Sampling

Variable input parameters are sampled from probability density functions as in [22,212]. Considered in this work is the variation of wind generation and loading conditions. Specifically, data for a chosen day in the UK (24^{th} July 2024, the day with highest normalised range of wind generation) obtained from the Monthly Operational Metered Wind Output 2024-2025 and Historic Demand Data 2024 datasets, available through the NGESO (now NESO) data portal [213]. Although this illustrative data is taken from historical records, we could just as easily replace such a daily profile with that of

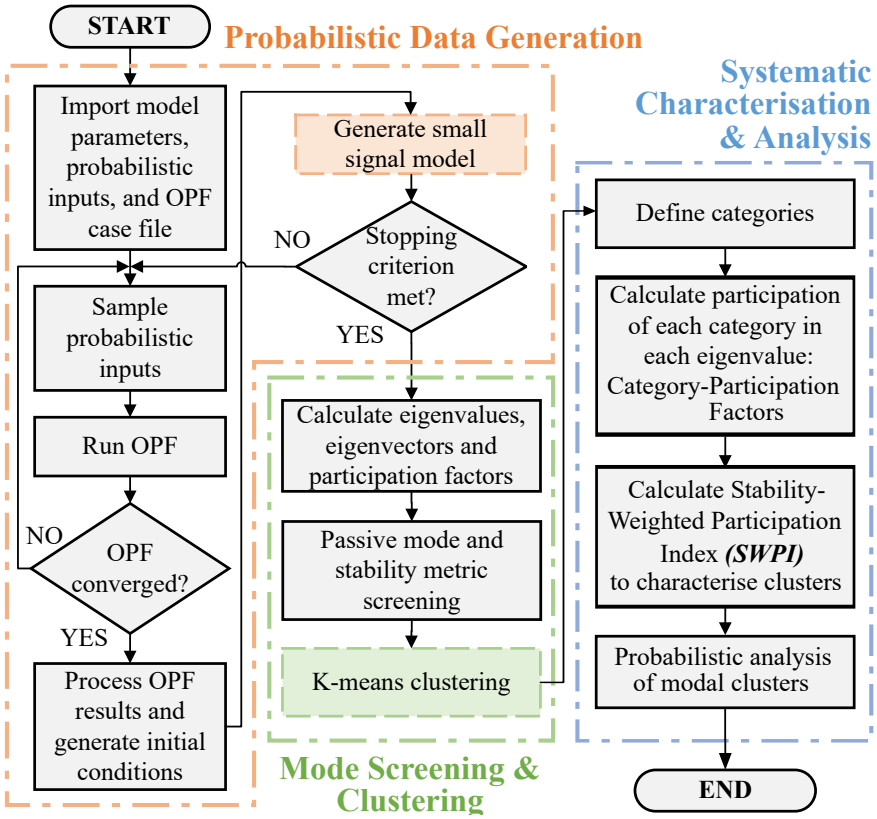

Figure 5.1: Flowchart of procedural steps for the proposed small-signal interaction analysis framework.

a day-ahead forecast.

The sampling procedure based on [212] starts with a uniform distribution of integers between 1 and 48 representing half-hourly periods of the day, which is then randomly sampled. The wind and load profiles are used to determine the mean value, $\bar{X}$. On top of this mean value, uncertainty is added following a Gaussian distribution with $3\sigma = 0.1 \times \bar{X}$ giving a 99.7% chance of the distribution being within ±10% of $\bar{X}$. For our specific data, this gives the 3σ range as displayed in Fig. 5.2. This distribution

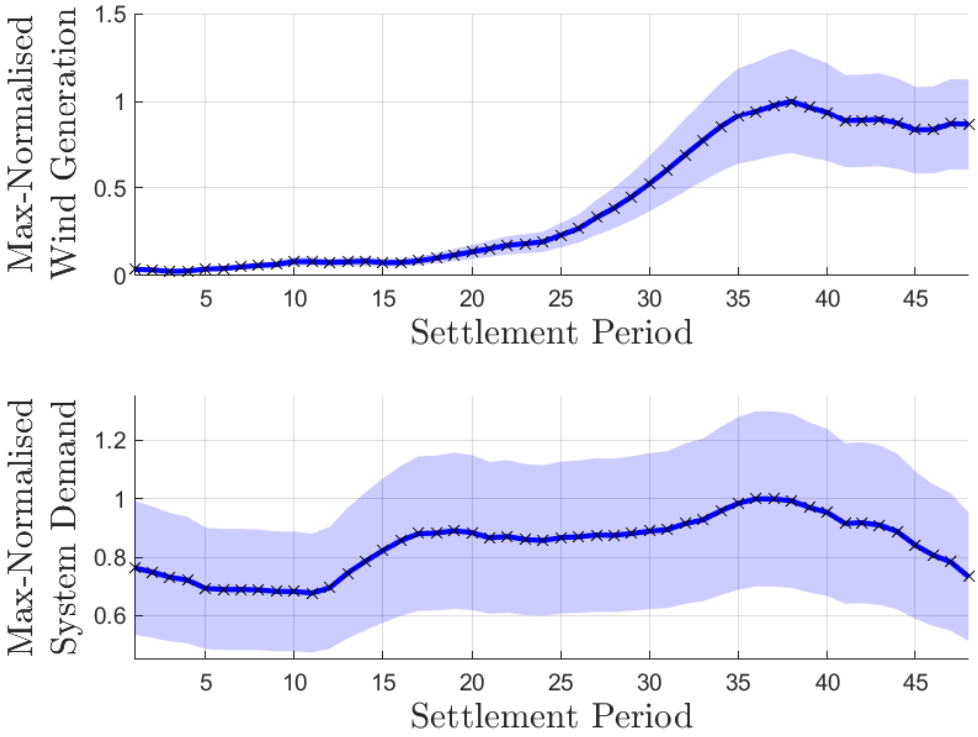

Figure 5.2: Max-normalised wind generation and system demand data. Filled area represents the 3σ range of the Gaussian probability density function.

is then randomly sampled independently to find the final values of output generation for each CIG as well as the loading value for each load on the system. Note that, use of the proposed framework is not restricted to the uncertain parameters and sampling approach outlined here. The idea of the framework is to enable the characterisation and study of key small-signal dynamics present on the system with considerations of uncertainty, whether that be related to forecast uncertainty (similar to the approach used for illustration in this chapter), modelling uncertainty, or other. Furthermore,

other than those associated with computational burden (see Section 5.5.4), there are no restrictions on the timescale that this framework can be applied, whether that be day-ahead or on longer planning timescales. However, the specific approach outlined here could be used with day-ahead forecasts to provide a comprehensive understanding of the PF-based characteristics and probabilistic behaviour of the small-signal dynamics present on the system for the following day.

A Monte Carlo approach is used whereby the process is repeated until a stopping criterion is met, similar to [19, 206, 214]. The error of the sample mean, based on a Gaussian distribution assumption, with a predetermined confidence level of 95% for a chosen output index (real part of the modes within each cluster) is used as the criterion. The threshold is set to 2%. As will be seen in Section 5.2.3, similar modes are clustered to enable characterisation of the prevalent interactions in the system under test. As such, we want to ensure that each cluster (after screening, see Section 5.2.2) meets the stopping criterion–signifying convergence of the characteristics of each modal cluster. Therefore, as the Monte Carlo process progresses, the clustering algorithm is applied periodically (every 1920 iterations) with data in intermediate steps assigned to a cluster based on which centroid it is closest to in terms of Euclidean distance. This is to improve the computational efficiency through avoiding the need to perform the full clustering algorithm for every iteration. Furthermore, we check the stopping criterion after every 48 iterations (i.e., a single iteration per settlement period), which enabled us to parallelise the data generation within those 48 samples.

Generation of System Operating Point

Following sampling of uncertainties, an OPF is performed to obtain the operating point of the network. To set the sampled output generation values of the CIGs, the costs of these generators are set to zero, so that their output is prioritised. Their maximum output is then set as the sampled values from the probability distributions as explained above. This means that the OPF will set the CIGs to output the sampled value of generation, provided all constraints are met. The OPF is performed using the MATLAB extension MATPOWER [113] and the cost for the SG used in this work is

taken from the benchmark values in [215]. Note, the proposed framework does not impose this specific approach outlined in this subsection.

Small-Signal Modelling and Eigenvalue Analysis

Key to the PSSA is of course the creation of the power system small-signal model. This is completed as per the approach outlined in Chapter 2. As a reminder, the fundamentals of small-signal modelling were described in Section 2.1 with the calculation of eigenvalues and PFs, in particular, being outlined in Section 2.1.2. Note, the small-signal analysis is performed for every operating point, derived by the process outlined in prior subsections. As such, the output metrics, such as the stability margins of modal clusters (see Section 5.2.3) will be probabilistic in nature.

5.2.2 Initial Screening

Prior to any further analysis, purely passive modes (i.e., with negligible participation from generator or converter states) are removed from further consideration. These are, typically, high frequency resonances associated with the inductances and capacitances of the network with no risk of instability [11]. Therefore, a heuristic rule is applied whereby any mode with a combined PF from states associated with passive elements above 97% is removed from the analysis. Results have shown that this threshold value is appropriate for the studies undertaken in this research. Formally, this threshold is

$$\sum_{j=1}^{N_{ps}} (p_{\alpha_j,n}) > 0.97, \tag{5.1}$$

where $\boldsymbol{\alpha}_{N_{ps}\times 1}$ is the vector of indices corresponding to the passive network states of the system. We use n to denote the mode here instead of the previously used k to avoid confusion with the number of clusters which is denoted by k as used in Section 5.2.3.

An additional screening focuses on eigenvalue impact on stability. For this, the real part $\Re(\lambda)$ of the eigenvalue is considered. Another common stability metric is the damping ratio, ζ. However, it has been seen (both in literature [59] and the results found in Section 5.5 but, to the best of my knowledge, not yet seen in practice) that

in converter-permeated systems, non-oscillatory modes may give rise to stability issues which would not be identified by use of ζ alone (until the moment of instability). The threshold for removal for our analyses is

$$\Re(\lambda_n) < -10. \tag{5.2}$$

This threshold can be reduced at the consequence of an increased number of eigenvalues which require clustering and analysis. For our case studies, -10 was found to be sufficient for simplifying the complexity of analysis, while still enabling analysis of the most dominant small-signal dynamics.

5.2.3 Clustering

Clustering is used in this work to obtain groups of modes with similar PF-based characteristics which can therefore be considered to represent similar types of dynamic interactions. The inputs to the clustering algorithm are the max-normalised PFs of each mode. That is, $\hat{\boldsymbol{p}}_n = \{\hat{p}_{i,n} : i \in \{1, 2, \ldots, N\}\}$ where $\hat{p}_{i,n} = p_{i,n}/\max_i(p_{i,n})$, denotes the max-normalisation. Consequently, the similarity of clustered modes is on the basis of having similar PFs. The well-established *k-means* clustering algorithm was chosen for this purpose [216], along with the elbow method to determine the optimal number of clusters, since it suits the purpose of grouping similar modes. Furthermore, implementation requires only the input data matrix and number of clusters, avoiding the need for heuristic tuning of input parameters such as Euclidean distance metrics (such as for partitioning clusters in hierarchical dendrograms [216]) which can be difficult considering the high dimensionality of the data points (i.e., the modes' PF vectors).

Despite this, there is a well-known limitation to *k-means* in that it is sensitive to the initialisation of the cluster centroids. To mitigate this, the *k-means++* seeding approach [217] is adopted as well as the use of multiple initialisations. The latter of which involves performing the clustering several times (5 in this case) and choosing the run which provides the minimum within-clusters sum of squares (WCSS) [218].

Furthermore, the number of clusters, k, chosen with the elbow method is determined once the *variance explained* [219] is above 95% for all initialisation instances, with the final cluster solution taken as the run with k clusters which provides the highest *variance explained* or, equivalently, the lowest WCSS.

5.2.4 Systematic Characterisation

The systematic characterisation procedure outlined in this section can be summarised as:

- Define categories (e.g., generator types, individual generators/elements, dynamic phenomena of interest).
- Calculate category-PFs as the sum of the PFs of each state of the category.
- Calculate the SWPI for characterisation of modal clusters.

The remainder of this section will further explain the process above. It will also clarify the particular uses of the category-PFs and SWPI.

Defining Categories Based on Participation Factors

The PFs for any given mode are combined into groups which represent categories of interest. In this work, these include individual generators, and custom categories as defined in Table 5.1. This approach can provide useful information by decomposing the participating dynamic phenomena and thereby simplifying the analysis, especially for high state-order systems. This is the basis for characterising the interactions within this work. Each state associated with the category of interest is combined and the PFs of all states, $\boldsymbol{x}$, in a given category, c, are summed to give the category-PF in the given mode, $p^*_{c,n}$, described in (5.3) for the n^{th} eigenvalue.

$$p^*_{c,n} = \sum_{j=1}^{N_{cs}} (p_{\beta_j,n}) \tag{5.3}$$

In (5.3), $\boldsymbol{\beta}_{N_{cs}\times 1}$ is the vector of indices corresponding to the states for category c. Note, the number of states, N_{cs}, may be different for each category. Furthermore, we

can note that this approach enables consistency of characterisation, even if a component was to be disconnected. For example, if a GFM is disconnected for a given operating point, then the corresponding states will simply have zero participation (factor).

The categories defined in Table 5.1 are chosen to reflect the main dynamic phenomena and interactions from known control or physical power system components. For example, the categories can reflect different timescales such as inner voltage controller-related (IVCr), inner current controller-related (ICCr), measurement filter- & delay-related (MF&Dr), and network dynamics, or known distinct interaction mechanisms such as between active power-frequency (P-F) and reactive power-voltage (Q-V) dynamics[1]. Note, that without loss of generality, the categories can also be defined differently based on the focus of particular studies, e.g., to target specific controllers that are known to cause specific dynamic interactions of interest like SSOs.

Table 5.1: Custom dynamic phenomena categories.

Categories	Elements
Active power-frequency (P-F)	Active power control (APC), PLL, SG rotor, SG gov, SG rotor windings
Reactive power-voltage (Q-V)	Voltage magnitude control (VMC)/reactive power control (RPC), SG AVR/exciter, SG PSS
IVC-related (IVCr)	Inner voltage controller
ICC-related (ICCr)	Inner current controller
Measurement filter- & delay-related (MF&Dr)	PWM/control delay, input measurement filters (power filters are included in APC/VMC/RPC)
Network	Branch currents, capacitor voltages, VSC output RLC filters, SG stator

Stability Weighted Participation Index

While category-PFs can be useful in the characterisation of *individual modes*, in a small-signal study with detailed models across a large range of operating points, the complexity can introduce challenges in extracting such useful information. As

[1]Clearly, there is a degree of freedom in defining categories. As such, any analyses should be interpreted accordingly, following the specific definition of categories. A possible alternative is to use the modal PFs of algebraic variables from [220] in place of the category-PFs which would enable analysis based on output variables such as voltages or power injections.

previously discussed, the use of clustering can help characterise the dynamic behaviour of the system. However, the PFs (and hence category-PFs) of modal clusters will vary across the operating range. Essentially, every modal cluster can be described by a number of category-PF distributions, an example of which (in terms of state-PFs) can be found in [210]. To avoid the complexity of interpretability that this brings, a weighted average can be considered whereby the category-PFs of a mode within a cluster is prioritised (weighted) if it is closer to the stability boundary (defined by the real part of the eigenvalue).

Consequently, a new index is proposed in this chapter, namely the SWPI. This is calculated as in (5.4) for category c, with the eigenvalue real part, $\Re(\lambda)$, as the chosen stability metric for weighting. Note, min-max normalisation is applied to the real parts of each modal cluster, denoted by the superscript $\square'$.

$$SWPI_c = \frac{\sum_{n=1}^{N_{mwc}} \left[p^*_{c,n} \cdot \Re(\lambda_n)' \right]}{\sum_{c=1}^{N_C} \left(\sum_{n=1}^{N_{mwc}} \left[p^*_{c,n} \cdot \Re(\lambda_n)' \right] \right)} \tag{5.4}$$

The numerator represents the sum of the category-PFs of category c for the N_{mwc} modes within the cluster. Before summing, each mode, n, is weighted by $\Re(\lambda_n)'$ so that instances with poorer stability margin will have a higher impact on the overall value, ensuring that information on important modes is not lost. The denominator performs an ℓ_1 normalisation. A high value of SWPI (i.e., towards 1) for a given category indicates that state variables participating in that category participate in modes of the cluster that tend to have worse stability margin and are consequently of interest.

Overview of the Systematic Characterisation Indices

Category-PFs: combine the PFs of states associated with a pre-defined category such as generating units or particular control mechanisms (Table 5.1). These are similar to normal state-PFs but instead quantify how each *category* participates in each mode (and vice versa), rather than each *state*.

SWPI: provides a weighted average of category-PFs for modal clusters. To reduce the complexity of the analysis, a weighted average is taken which places more emphasis

on the category-PF-defined characteristics of the modes within the cluster which are closer to the stability boundary.

5.3 Power System Modelling

As has been the case throughout the investigations in this thesis, the modelling approach adopted is described in detail in Chapter 2.

An 8^{th} order model of the SG is adopted [11]. Additionally, both the DC1A and ST1A_v2 type AVRs (and exciters) from [157, 221] have been implemented, in addition to the PSS1A PSS model [157, 221]. The transmission lines are modelled as lumped π circuits and the transformers and loads are RL equivalents (series and parallel respectively). Other than the static impedance loads[2], all elements (including network components) are modelled using differential equations to account for their dynamic behaviour. The components common to models incorporating a VSC, i.e., GFLs and GFMs, are displayed in Fig. 2.4. For converter modelling, averaged models are used and the PWM/control delay is approximated by a first order transfer function [149]. A power measurement LPF and geometric transformations between the converter control reference frame and the system reference frame are also included. Signals in the former are differentiated by the $\square^*$ superscript, not to be confused with that in (5.3).

5.3.1 Grid-Following Converter

Current vector control [5] (Section 2.5.2) is implemented for the GFL converter in this work. In particular, an outer PI-based APC and RPC are utilised (Fig. 2.7). The ICC scheme adopted is that seen in Section 2.5.2 and Fig. 2.5. The SRF-PLL [38] (Section 2.5.3) is used for synchronisation. The full control structure is displayed in Fig. 5.3.

[2]Prior literature [222] has shown that different types of static load model have limited impact on small-signal dynamics, even with the inclusion of CIGs. In particular, [222] has shown that the real part of the most dominant mode only moves by 0.08 s^{-1} when changing from constant impedance to constant power loads in the IEEE 39-bus system. However, the generalisability of this study is not clear, and detailed investigations into load modelling requirements are an important avenue of future work. In fact, the framework proposed in this chapter could be a useful tool in performing such studies.

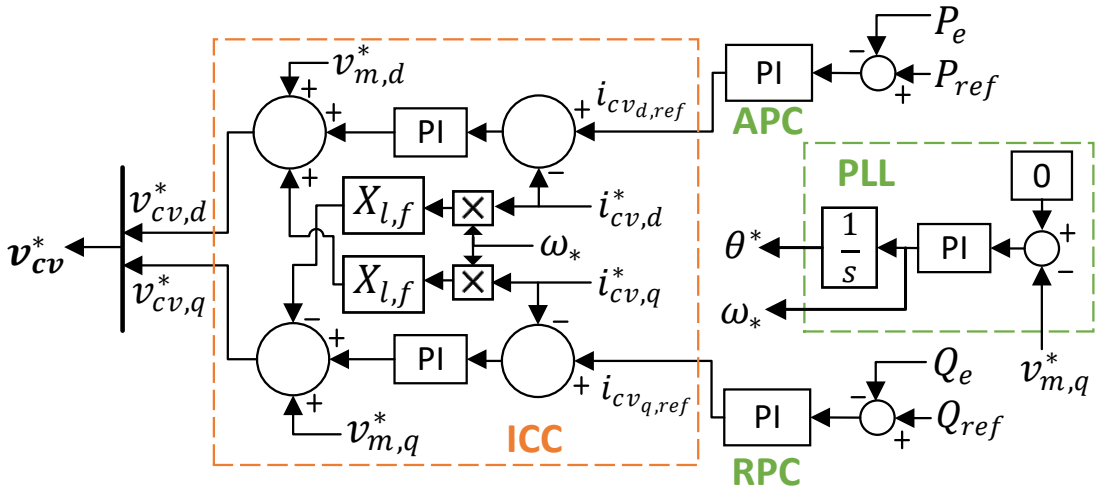

Figure 5.3: Block diagram for GFL control as used in the probabilistic analysis case studies.

5.3.2 Grid-Forming Converter

The VSM GFM approach is commonly utilised in the literature and has been chosen for this work (Section 2.5.4). The full control structure is displayed in Fig. 5.4. The APC being a VSM means no additional LPF is required. The VMC is a reactive power-voltage droop. There is also a virtual impedance[3] which improves damping as well as the X/R ratio and hence decoupling between active and reactive power [59, 225]. In this work, the GFM controller employs a DILC architecture incorporating an ICC and an IVC (as per Section 2.5.2 but without feed-forward terms) [59, 125, 149, 152].

5.4 Modified IEEE 68-Bus Test System

The IEEE 68-bus system, a common benchmark model, is employed. We intend to maintain a relatively realistic representation of the benchmark system but with the addition of CIGs distributed across the network. As such, we modify the benchmark by introducing CIGs at buses 26, 29, 33, 45, 59, and 65. These locations were chosen based on the location feasibility as described in [226]. This is illustrated in Fig. 5.5. We consider three case studies in this work, as outlined in Table 5.2. Each CIG is set

[3]The virtual impedance is of the form in Section 2.5.4 but negated. This is in line with the virtual impedance implementation in [59], [223], and [224].

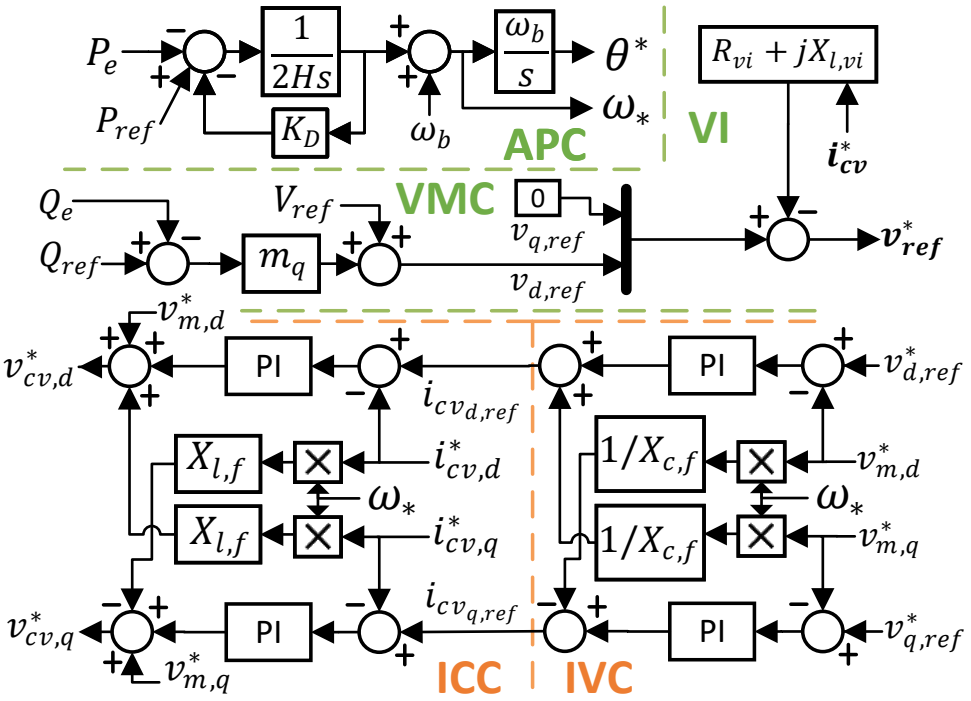

Figure 5.4: Block diagram for GFM control as used in the probabilistic analysis case studies.

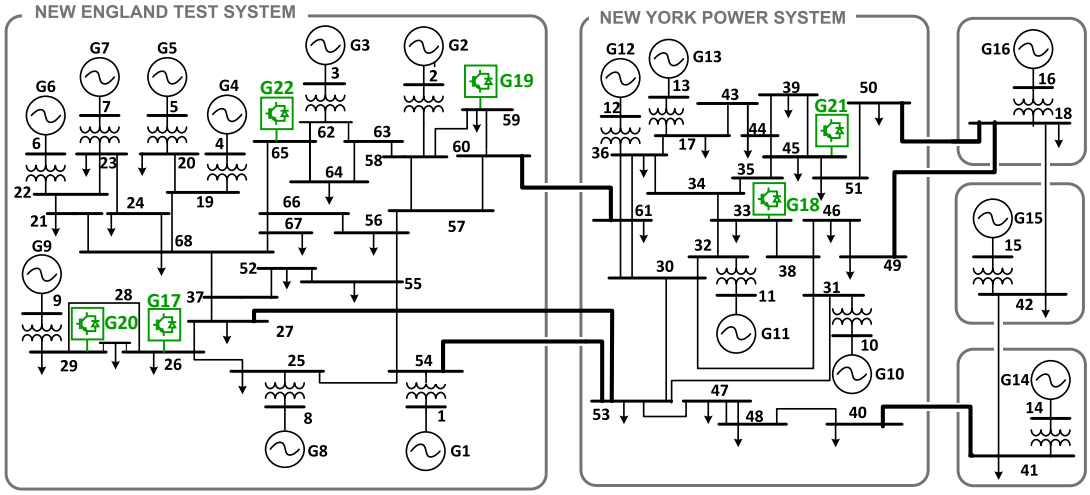

Figure 5.5: Modified IEEE 68-bus test system.

to be of equivalent rating, with the total CIG installed capacity being 11 817 MVA, or 25%. Also, the sampling of the loads is normalised to a maximum of 1.3× the load capacity of the benchmark 68-bus network to account for the additional generation capacity introduced by the CIGs.

Table 5.2: Probabilistic analysis case studies.

Case Study	GFM Locations	GFL Locations
1	26, 33, 59	29, 45, 65
2	26, 33, 59, 29, 45, 65	N/A
3	N/A	26, 33, 59, 29, 45, 65

For each iteration in the Monte Carlo simulation, the normalised output apparent power, S_{samp}, of the CIGs is determined through sampling as described in Section 5.2.1. The requested per unit active power generation, P_G, of each CIG is 95% of S_{samp} to allow for CIG contribution to the reactive power generation requirements of the system [227].

The parameters for the SGs and the network elements in the benchmark 68-bus system can be found in [221]. Note, as per [221], G1-G8 are equipped with DC1A AVR/exciter while G9 is equipped with the ST1A_v2 approach. The remainder of the SGs are manually excited. G9 is also equipped with the PSS. Parameters of CIGs and associated controls are found in the Table 5.3. The ICCs are tuned to achieve a closed-loop 5% settling time (hereafter referred to as the time constant for simplicity) and damping ratio of 3 ms and 1, respectively. The IVCs are set to a closed loop time constant and damping ratio of 7.5 ms and 0.7071 [123]. The PLLs are tuned according to suggestions from [5].

5.5 Results

The method outlined in Section 5.2 is applied to the system described in Section 5.4. For case studies 1, 2 and 3, the stopping criterion described in Section 5.2.1 was reached after a total of 18 432, 23 088, and 15 408 iterations respectively, 17 701, 22 149, and 14 785 of which resulted in OPF convergence, respectively. Further discussion on the

Table 5.3: Parameters for CIGs in probabilistic analysis case studies.

Parameter	**Symbol**	**Value**
RLC resistance	R_f	0.03 pu
RLC inductive reactance	$X_{l,f}$	0.08 pu
RLC capacitive reactance	$X_{c,f}$	1/0.074 pu
Transformer resistance	R_t	0 pu
Transformer inductive reactance	$X_{l,t}$	0.2 pu
Power filter time constant	τ_p	0.0318 s
Switching frequency	f_s	10 kHz
PWM/control time delay	τ_{pwm}	$1.5/f_s$ s
ICC proportional gain, integral gain	$K_{p,icc}, K_{i,icc}$	$\{0.3944, 212.2066\}$ $\mathrm{V_{pu}/A_{pu}}$
IVC proportional gain, integral gain	$K_{p,ivc}, K_{i,ivc}$	$\{0.1570, 62.8144\}$ $\mathrm{A_{pu}/V_{pu}}$
GFL APC proportional gain, integral gain	$K_{p,apc}, K_{i,apc}$	$\{0.25, 25\}$ $\mathrm{A_{pu}/MW_{pu}}$
GFL RPC proportional gain, integral gain	$K_{p,rpc}, K_{i,rpc}$	$\{0.25, 25\}$ $\mathrm{A_{pu}/MVAr_{pu}}$
PLL proportional gain, integral gain	$K_{p,pll}, K_{i,pll}$	$\{60, 1400\}$ $(\mathrm{rad^{-s}})$ / $\mathrm{V_{pu}}$
GFM APC virtual inertia, virtual damping	H, K_D	4 s, 10 pu
GFM VMC reactive power droop	m_q	1%
Virtual resistance, virtual inductive reactance	$R_{vi}, X_{l,vi}$	0 pu, 0.2 pu

computational burden of obtaining such large datasets can be found in Section 5.5.4.

5.5.1 Modal Clusters

The application of clustering using the PF vectors not only allows us to group modes across the operating range based on their participating states, it also allows us to distinguish between modes with such underlying dynamics where this would be impossible with clustering based on the complex coordinates of the eigenvalues. For example, Fig. 5.6 displays the modal clusters obtained from Case Study 1 (see Table 5.2 for more information). It is clear that several clusters overlap in the complex plane. In fact, we see two overlapping modal clusters which exhibit instability in Fig. 5.6c (whose characteristics will be further explored in Section 5.5.2, for example using the SWPI heatmaps of Fig. 5.12).

5.5.2 Targeted Analysis of Chosen Modal Clusters

The complexity reduction achieved through clustering (e.g., 938 990 modes after screening are reduced to 73 clusters in Case Study 1) makes the identification and analysis of key small-signal interactions much more manageable. For example, we choose here to further investigate the SSOs, the clusters with unstable modes, and the clusters which contain the rightmost oscillatory mode and the rightmost non-oscillatory mode (across the whole operating range). For Case Study 1, this corresponds to clusters C1 to C6 as indicated by the annotations in Fig. 5.6. For Case Study 2 and Case Study 3, the selected clusters of interest (only) are displayed in Figs. 5.7 and 5.8, respectively. Note, the overlapping nature of the electromechanical oscillations in Case Study 3: the empirical cumulative distribution functions (ECDFs) in the following subsection allows us to better visualise the distributions of these clusters.

Probabilistic Analysis of Chosen Modal Clusters

ECDFs are used here to analyse the probabilistic behaviour of modal clusters. In particular, we investigate the real part of the rightmost eigenvalue (i.e., the stability margin) per operating point for each cluster of interest. Note, we will look at the

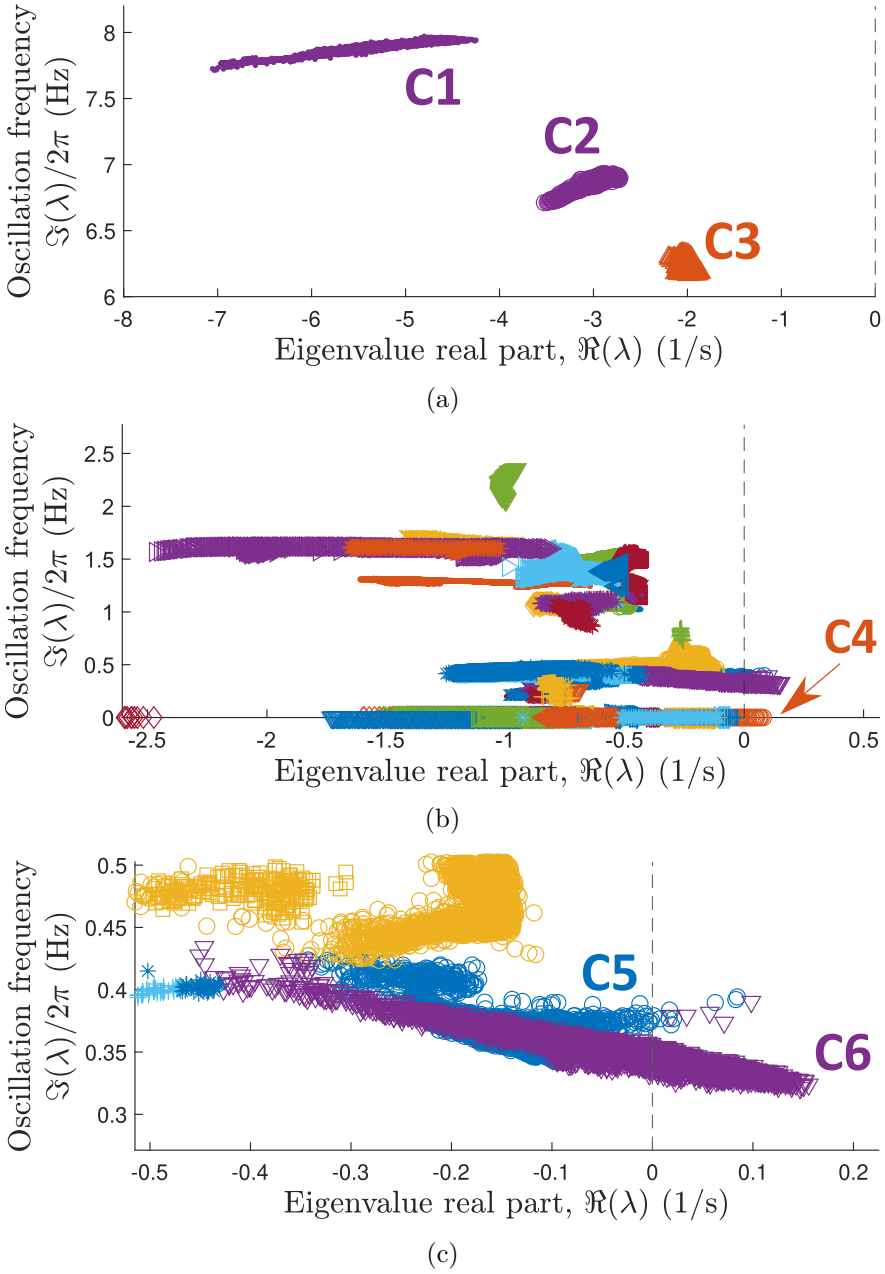

Figure 5.6: Dominant modal clusters in the (a) sub-synchronous and (b) low frequency and non-oscillatory range for Case Study 1. Also displayed in (c) is a zoomed image of overlapping, destabilising modal clusters. Each cluster is represented by a different colour and marker style combination.

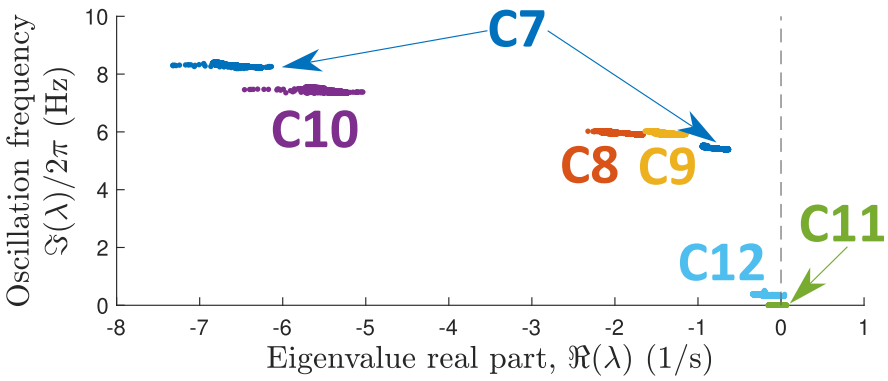

Figure 5.7: Modal clusters of interest for Case Study 2.

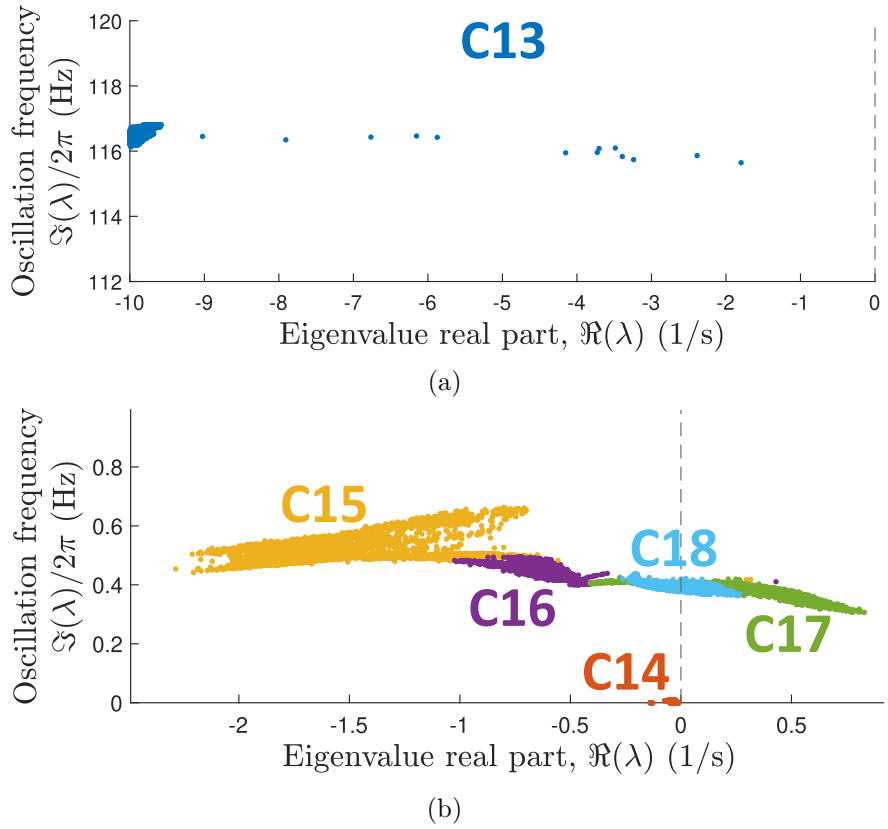

Figure 5.8: Modal clusters of interest for Case Study 3 in the (a) high frequency and (b) low frequency ranges.

SWPI-based characteristics of each cluster of interest in the following subsection (in particular, Fig. 5.12).

For Case Study 1, the corresponding ECDFs are displayed in Fig. 5.9. From this, we clearly see three clusters which exhibit instability (i.e., with real eigenvalue parts going above zero), corresponding to the two overlapping clusters of approximately 0.3 Hz to 0.45 Hz in Fig. 5.6c (C5 and C6), as well as the non-oscillatory modal cluster seen in Fig. 5.6b (C4). In particular, C4 induces instability for 47.0% of the converged operating points studied, while C5 and C6 induce instability 0.47% and 24.5% of the time, respectively. It can also be observed that C5 and C6 do not exist for all operating points, and their maximum cumulative probability is therefore adjusted to account for this. For example, C5 is seen to exist for only 75.9% of converged operating points, and the corresponding ECDF therefore has a maximum value of 0.759. This analysis is useful for understanding how often a given cluster or interaction is expected to induce instability–or even to exist. However, it is also important to understand the total likelihood of instability for the system. Therefore, we can observe the ECDF for the stability margin of the system as a whole: the real part of the rightmost eigenvalue, considering all eigenvalues and not just those within a given cluster. This overall stability margin is also plotted in Fig. 5.9, showing that the system will be unstable 64.8% of the time.

As was also seen in Fig. 5.6a, the SSO clusters do not induce instability (see Section 5.5.3 for a case in which this is not true) in Case Study 1. Also, the two SSO clusters which are closer to the stability boundary (C2 and C3) exhibit limited variation of stability margin across the operating range, as highlighted by ECDFs having a more vertical characteristic in Fig. 5.9.

The ECDFs for the clusters of interest in Case Study 2 are displayed in Fig. 5.10. There are only two modal clusters which cause instability: a non-oscillatory modal cluster (C11), and an oscillatory modal cluster between 0.31 Hz and 0.51 Hz (C12). Additionally, there are four SSO clusters in this case, with stability margins reduced as a whole compared to those in Case Study 1. The probability of instability caused by C11 and C12 are 32.8% and 4.22%, while the former is seen to exist only 80.7% of the

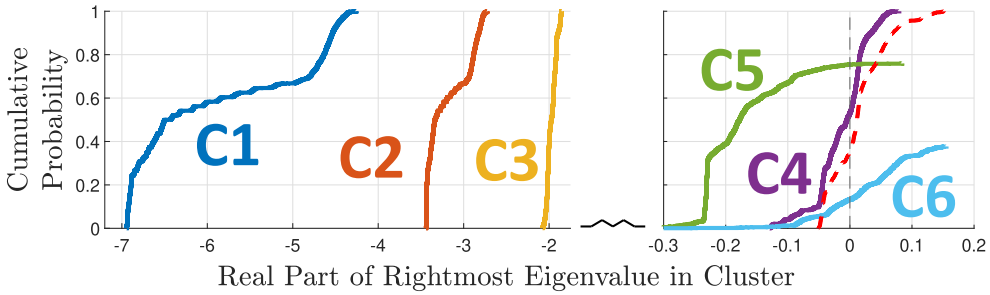

Figure 5.9: Empirical cumulative distribution functions for the real part of the rightmost eigenvalue (i.e., the stability margin) per operating point for each identified cluster of interest in Case Study 1. Dashed red line = system stability margin.

time. Furthermore, the total probability of instability of the system is 37.0%, a 27.8 percentage point reduction when compared to that of Case Study 1.

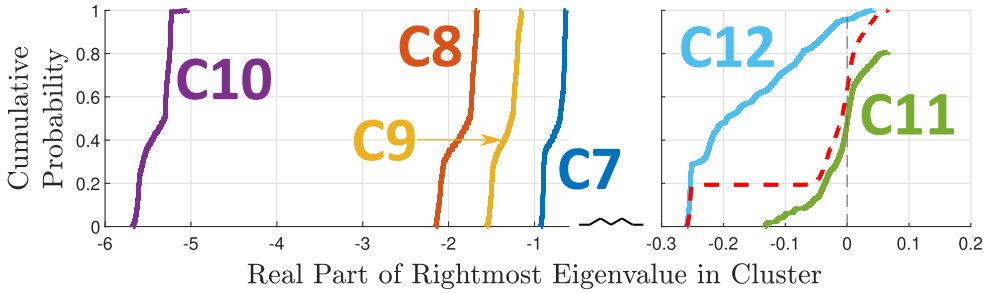

Figure 5.10: Empirical cumulative distribution functions for the real part of the rightmost eigenvalue (i.e., the stability margin) per operating point for each identified cluster of interest in Case Study 2. Dashed red line = system stability margin.

Finally, the ECDFs for the clusters of interest in Case Study 3 are displayed in Fig. 5.11. For this case study, we observe four clusters which induce instability, those being the overlapping clusters between 0.4 Hz and 0.7 Hz in Fig. 5.7 (C15 to C18). In this case, the rightmost non-oscillatory mode (C14) does not induce any instability, unlike the prior case studies. The overall probability of instability for this case study is 47.1%.

Furthermore, there is a high frequency modal cluster at around 116 Hz as observed in Fig. 5.8b, which has a limited number of outliers exhibiting much reduced stability margin (hence the near horizontal line on the corresponding ECDF). In fact, this cluster is seen to exist for only 39.74% of the converged operating points (in the region of the complex plane studied), while it has 38.65% probability to have real part of the

rightmost eigenvalue between −10 and −9.59, with only 1.09% probability to be within a much wider range of −9.59 and −1.80. This suggests very low probability for high-risk scenarios (i.e., low stability margin) related to this modal cluster. The limited number of operating points at which this cluster exhibits lower stability margins (indicated by the sparsity in Fig. 5.8b) could clearly be missed if not performing such comprehensive probabilistic studies[4].

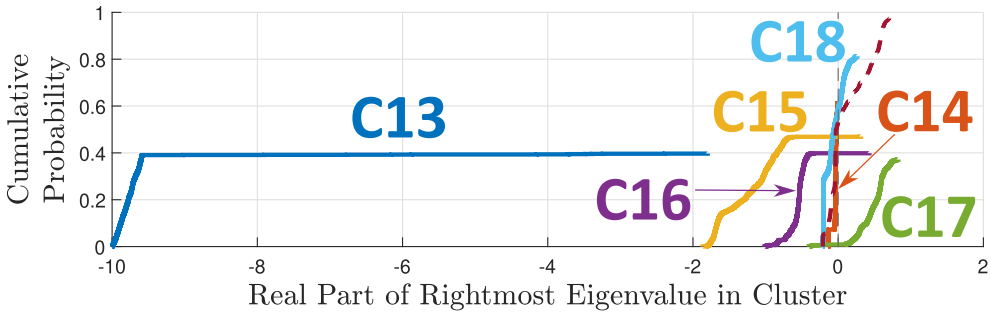

Figure 5.11: Cumulative distribution functions for the real part of the rightmost eigenvalue (i.e., the stability margin) per operating point for each identified cluster of interest in Case Study 3. Dashed red line = system stability margin.

Characterisation of Chosen Modal Clusters

In addition to the capability to identify and probabilistically analyse modal clusters, a key contribution of the proposed framework is to enable their characterisation. Using the SWPI (Section 5.2.4), we can characterise the contributing elements in each cluster. This is displayed for all clusters of interest in Fig. 5.12.

The SSOs in Case Study 1 (C1 to C3) are revealed to be related mostly to the dynamics of the IVCs of the GFMs, also with limited contribution from the network, P-F, and Q-V dynamics (Fig. 5.12a). Also, from Fig. 5.12c, these are seen to constitute multi-machine interactions between two GFMs, namely G17 and G19 (for C1 and C2), or involving only one GFM in the form of G18 (C3). The destabilising non-oscillatory modal cluster (C4) in Case Study 1 is found to be related primarily to P-F type dynamics with limited contribution from Q-V dynamics. Furthermore, it is

[4]In fact, it could even be argued that the stopping criterion converged too soon for this case study. See further discussion of future work regarding the stopping criterion in Section 5.5.4.

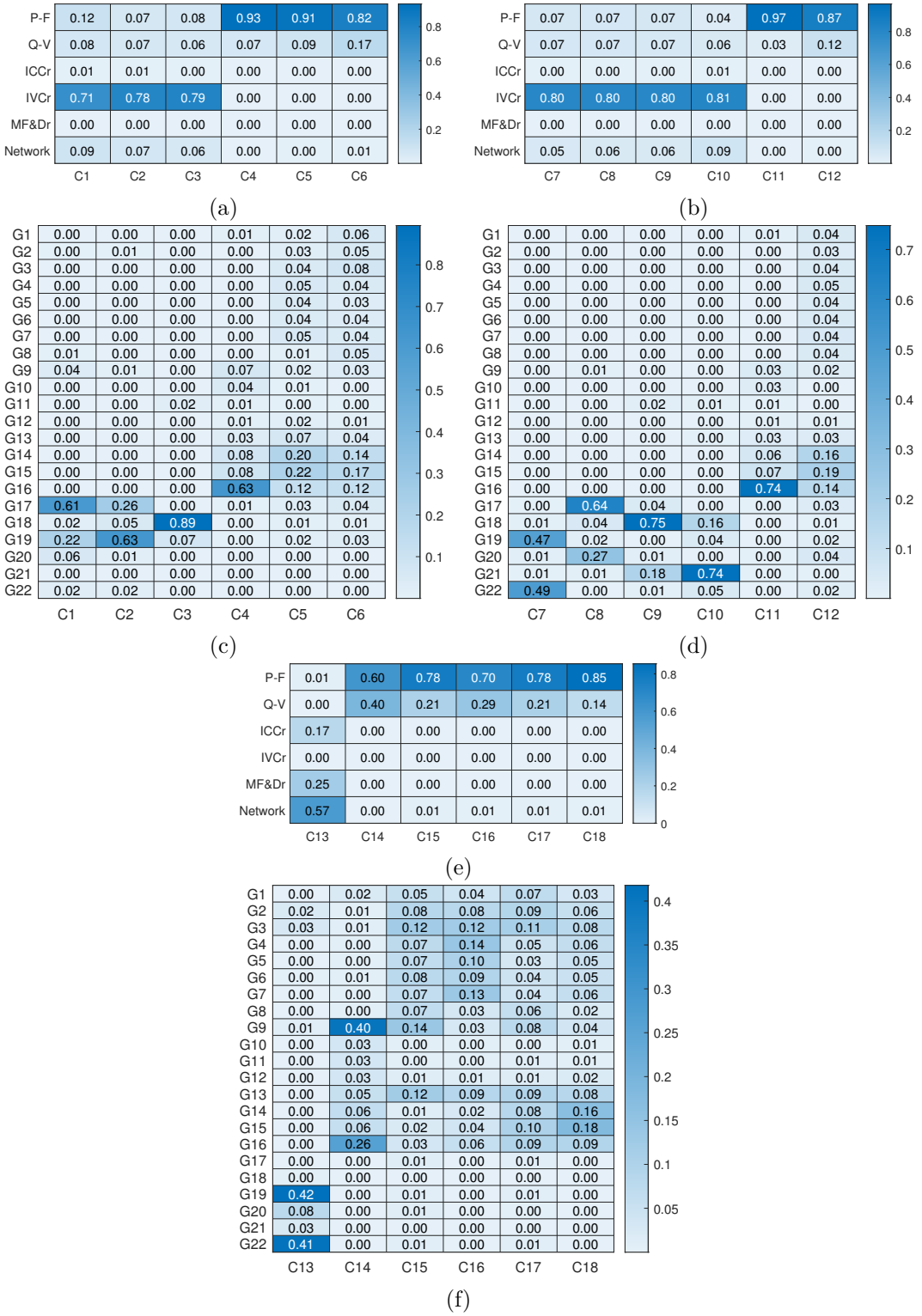

Figure 5.12: SWPI for clusters of interest based on dynamic phenomena-type categories (Table 5.1) in (a) Case Study 1, (b) Case Study 2, and (e) Case Study 3, as well as individual generator categories in (c) Case Study 1, (d) Case Study 2, and (f) Case Study 3.

related to G16 (a SG) with limited contribution from G9, G14, and G15 (all of which are SGs). The destabilising oscillatory modes in Case Study 1 (C5 & C6) involve a range of generators, with the most contributing being G14, G15, and G16 (which are aggregated representations of three separate areas, as per Fig. 5.5). They differ slightly with respect to the dynamic phenomena categories which dictate their characteristics, with both being related mostly to P-F dynamics, but C6 being influenced more by Q-V dynamics than C5.

All SSO modal clusters seen in Case Study 2 are found from Figs. 5.12b and 5.12d, to be multi-machine interactions, each between two GFMs. In particular, C7 is related to G19 and G22, C8 is related to G17 and G20, while C9 and C10 are both related to G18 and G21. Interestingly, the interacting machines are all in close proximity to each other in this Case Study (Fig. 5.5). Similar to Case Study 1, these SSOs are seen to be related mostly to the IVCs of the GFMs, as well as (to a much lesser extent) the P-F, Q-V, and network dynamics on the system. The destabilising non-oscillatory mode in this case study (C11) is found to be similar to its counterpart in Case Study 1 wherein it is related primarily to the P-F dynamics and G16 (a SG). The destabilising oscillatory modal cluster (C12) is found to be similar to C6 of Case Study 1, constituting a multi-machine interaction with most contributing generators being G14, G15, and G16, and being related mostly to P-F dynamics with lesser contribution from Q-V dynamics.

For Case Study 3 (Figs. 5.12e and 5.12f), the high frequency modal cluster (C13) is seen to be related mostly to network dynamics, as well as MF&Dr and ICCr dynamics (which makes logical sense due to the faster dynamic action of these components). Note, no IVCs exist in this case study, hence the IVCr related dynamics being assigned a value of 0 for the SWPI. Furthermore, it is an interaction between G19, G22, and to a lesser extent G20 (all of which are GFLs in this case study). The rightmost non-oscillatory modal cluster (C14), which does not cause instability in this case study, is found to be an interaction between primarily G9 and G16, both of which are SGs. Furthermore it is also related to P-F dynamics, but has much more contribution from the Q-V dynamics compared to its counterparts in Case Study 1 and Case Study 2. The destabilising oscillatory modal clusters in this case study (C15 to C18) are

related mostly to P-F dynamics with some contribution from Q-V dynamics. They all have dominant contributions from a large number of SGs (i.e., seemingly global interactions across the whole system), although the specific generators involved, and the contributions thereof (as quantified by the SWPI) vary from cluster to cluster.

This subsection has detailed the depth of characterisation that can be obtained through modal clustering and the SWPI. However, it can be noted that even further granularity can be achieved from different choices of categories (Section 5.2.4). For example, we could decompose P-F or Q-V dynamics into specific controllers (similar to how we have separated the ICC and IVC dynamics in our analysis). The level of granularity adopted is therefore a trade-off between interpretability of results vs. complexity of analysis.

5.5.3 Probabilistic Analysis of Destabilising Sub-Synchronous Oscillations

It was shown in Figs. 5.12a and 5.12c that the SSOs of Case Study 1 (Fig. 5.6a) are primarily related to the dynamics of the IVCs of the GFMs. Therefore, we incite an interesting case study whereby such an SSO can induce instability due to poor (but standard) tuning. Starting from the base case of the system for Case Study 1 (i.e., with nominal system demand, and each CIG set to output 1 pu active power), a parametric sweep is performed whereby the closed-loop time constants of the IVCs of the GFMs are increased from 7.5 ms ($2.5 \times \tau_{ICC}$) to 10.44 ms ($3.48 \times \tau_{ICC}$), as displayed in Fig. 5.13. This degrades the stability margin of the SSOs, ultimately bringing one of the modes to instability. Note that the change of time constant in this parametric sweep is within expected values for tuning such a controller. In fact, a general rule of thumb for timescale separation would suggest that the time constant of the IVC should be increased to at least 10× that of the ICC, which actually brings a further two modes to instability in this case.

The slower value of IVC time constant of 10.44 ms is used to perform probabilistic analysis on the destabilising SSO. Focusing on only the destabilising cluster, we can observe the stability margin ECDF in Figure 5.14. This reveals that instability will

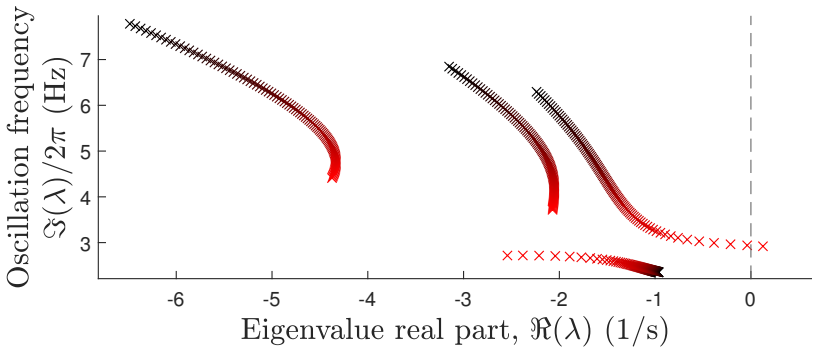

Figure 5.13: Trajectories of SSOs in the base case as the closed-loop 5% settling time of the GFMs' inner voltage controllers, τ_{IVC}, are increased from 7.55 ms to 10.44 ms (black to red).

occur 69.0% of the time when adopting this tuning.

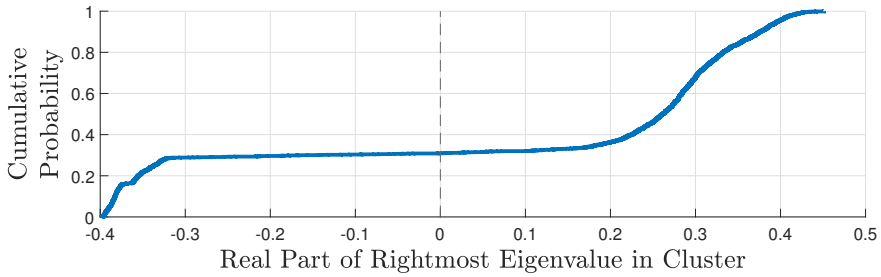

Figure 5.14: Cumulative distribution function for the real part of the rightmost eigenvalue (i.e., the stability margin) per operating point for the unstable SSO cluster after slowing the IVCs of the GFMs.

Furthermore, the dominant categories contributing to the cluster, based on analysis of the SWPI, are found to be related to the IVCr (0.518) and P-F (0.425) dynamics, with the main contributing generators being G18 (0.761) and G11 (0.217), which are a GFM and SG respectively. We can compare this to the characterisation of C3 from Figs. 5.12a and 5.12c, which showed that the dynamic characteristics of the SSO, before slowing of the IVCs of the GFMs, was related primarily to the IVCr (0.79) and G18 (0.89). That is, this destabilising sub-synchronous modal cluster now resembles an interaction between a GFM and a SG, associated strongly with both the P-F and IVCr dynamics, whereas before the slowing of the IVCs, the SSO resembled a local interaction related to a single GFM with much more emphasis on the IVCr dynamics.

This analysis reveals the potential for unstable oscillations related to (relatively) slow tuning of the IVCs of GFMs, along with its probabilistic characteristics. However, further analysis is required to better understand the root cause of these oscillations, and the conditions under which they might appear and/or become unstable.

5.5.4 Comment on Computational Burden and Scalability

The particular computation times for the case studies discussed throughout this section are summarised in Table 5.4, with the number of operating points evaluated reported at the start of Section 5.5. Note, with respect to clustering, we have utilised parallelisation to perform the full five initialisations. All tests were performed on a HP Elitebook 840 G10 with 32GB RAM, SSD storage, and 13th Gen Intel Core i7-1355U, 1.70 GHz (10 cores, 12 threads) processor.

Table 5.4: Computational requirements for application of the proposed framework to the case studies.

Case Study	**Activity**	**Time**
1	Probabilistic data generation	6.11 hours
	Clustering (five initialisations with final value of $k = 73$)	612.2 seconds
2	Probabilistic data generation	8.92 hours
	Clustering (five initialisations with final value of $k = 71$)	1966.6 seconds
3	Probabilistic data generation	4.80 hours
	Clustering (five initialisations with final value of $k = 77$)	482.5 seconds

Scalability is primarily dependent on the data generation process and clustering for the proposed framework, considering the computational cost for the calculation of indices in the systematic characterisation procedure is negligible in comparison. As long as the eigenvalues and eigenvectors can be determined, and the clustering algorithm can converge with the amount of generated data, then the proposed framework is applicable. Potential computational improvements (and therefore increase of scalability) might include: the use of importance/efficient sampling [19]; parallelisation of the data generation process (as discussed in Section 5.2.1); loosening the stopping criterion (or

applying an alternative stopping criterion) if deemed acceptable[5]; the use of order reduction methods such as principal component analysis [228] prior to clustering; reducing the number of initialisations required to be tested with *k-means* clustering; targeting the clustering on a subset of modes, or using eigenvalue algorithms which allow for calculation of only eigenvalues within a subset of the complex plane [220]; the adoption of more efficient clustering techniques for high dimensional data [228, 229]; amongst others.

The scalability of the state-space small-signal modelling procedure is evidenced by the automatic and modular approach [108], which can be compared to the CCM whose benefits for scalability are detailed in [39].

5.6 Potential Future Investigations using the Proposed Framework

Probabilistic modelling: is not restricted to the specific approach that we have adopted for our case studies. Amongst others, some potential alternative approaches might include: the use of copula-based correlated probability distributions; the inclusion of solar-dependent uncertain generation; different power flow formulations, including security-constrained OPF; and consideration of other categories of uncertainty such as modelling uncertainty, something that might be important in CIG-permeated power systems whereby many specific vendor models are not available, necessitating system identification techniques [230] for analytical studies (the models from which are estimates and therefore by definition will include uncertainty).

Research case studies: for which the proposed framework would be applicable are plentiful. We have already included an example of an SSO. Some additional examples could include: comprehensive investigation into GFM location and sizing; identification of novel interactions caused by the inclusion of different and/or more complex models such as converter-interfaced loads; identification of novel multi-machine interactions

[5] An area of improvement identified for future work is the definition of a more appropriate, and computationally efficient, stopping criterion that can also target low-probability (but potentially high-risk) modes.

with different converter control implementations; investigating the impact of different uncertain parameters on small-signal interactions; probabilistic investigation of known dynamics of interest (such as SSOs caused by poor PLL tuning [50]); amongst many others.

5.7 Chapter Summary and Conclusions

This chapter has presented a framework for probabilistic small signal analysis and characterisation of dynamic interactions in power systems with high penetration of CIGs. In particular, for systems with detailed dynamic models and different CIG control philosophies such as GFL and GFM. A systematic characterisation method is proposed, including the definition of PF-based categories (e.g., individual units or types of dynamic phenomena) to characterise modes as well as the introduction of the SWPI for identifying the prevalent dynamic behaviour of key modal clusters present on the system. Supported by a modal clustering approach based on PFs, the probabilistic behaviour of the identified types of interactions present on the system can also be studied.

The framework is applied to a modified version of the IEEE 68-bus network with inclusion of GFM and/or GFL controlled CIGs. Modal clusters of interest are identified and it is illustrated how the proposed framework can enable analysis of their probabilistic behaviour and SWPI-based characteristics. For example, amongst others, there are modal clusters indicating SSOs (between approximately 5 Hz and 8 Hz) related primarily to interactions involving the IVCs of the GFMs. There are also electromechanical interactions and non-oscillatory modal clusters inducing instability, related mostly to the active power and frequency dynamics of SGs. Empirical cumulative distribution functions were also used to reveal the likelihood of an interaction/cluster to exist for any given operating point, induce instability, or have stability margin below a given threshold.

The complex detail that the proposed framework is able to convey was further exemplified through case studies whereby only GFMs or only GFLs were connected to the system. In the former case, we observed an increased number of SSOs (again

related primarily to IVCs of GFMs), but reduced probability of instability from the electromechanical and non-oscillatory modal clusters. In the Case Study with only SGs and GFLs, we observed a high frequency modal cluster with low probability to have low stability margin (i.e., low probability, high-risk) related to interactions involving the ICCs and MF&Dr dynamics of the GFLs, in addition to the network dynamics.

Overall the proposed framework offers a way to characterise and understand complex dynamic interactions, the individual units and mechanisms involved in them as well as their probabilistic behaviour across a range of operating conditions.

The application of the proposed methodology of course requires the white-box state-space model (either a full-order or reduced-order model depending on computational requirements/feasibility). As such, for system operators/planners to make use of the benefits outlined in this chapter, improved model sharing is required from original equipment manufacturers. This could take the form of the impedance-circuit model [231] concept which maintains a certain level of intellectual property protection for the original equipment manufacturers. Despite this, it can be noted that the proposed methodology can also be adopted for research purposes with generic models, akin to the studies performed in this chapter, and discussed further in Section 5.6.

Chapter 6

A Modal Contribution Metric for Quantifying Small-Signal Variability in Power Systems with Converter-Interfaced Generation

6.1 Introduction

6.1.1 Motivation

Maintaining an interest in small-signal dynamic interactions, we now shift the focus to the fact that the changing power system dynamic behaviour (as discussed in Section 1.2 and throughout this thesis) is not necessarily captured by traditional static grid strength metrics. This chapter uses the modal superposition concept to derive metrics and information with respect to locational (small-signal) variability, defined in terms of the maximum deviation of system variables in different network locations. Going beyond typical grid strength metrics, the analysis considers voltage magnitude and frequency variability separately, reflecting the complexities arising from the transition to converter

control-permeated power system dynamics. A further benefit of the approach is the derivation of a clear relationship between the variability of output variables and specific modal interactions via their contribution to the response. That is, the interactions which significantly influence the time-domain maximum deviation of the output signal of interest. Finally, it is exhibited that the proposed method can be used to focus on the characteristics and causes of variability at different timescales.

With the integration of CIGs and the subsequent surge of complexity in power system dynamics, new approaches and appropriate metrics for power system analysis are required. The limitations of SCR based grid strength indicators are being discussed [27,232,233], necessitating new approaches for the determination of locational information with respect to the magnitude of changes expected in power systems variables.

The increasing complexity of the analysis of power systems associated with including CIGs is highlighted in [30,38]. In addition, complex control strategies are not reflected in proxy steady state indices such as SCR [232]. The implementation and analysis of small-signal models [14], as well as the inclusion of relevant dynamic information, suggests the possibility to extract useful locational trends and offer insights into complex dynamic behaviours. This is related to the *small-signal system strength* concept as discussed in [29].

A further motivating factor is the decoupling of voltage magnitude and frequency variability, something that is not necessarily described by traditional system strength based metrics. In traditional SG-dominated systems, frequency and voltage regulation were closely linked to the generation capacity and inertia since both services were typically offered by SGs. This cohesion cannot be assumed with CIGs and the wide range of control possibilities. The separation of the voltage magnitude and frequency forming aspects are discussed in more detail in [15, 30, 31, 77]. In this context, the locational variability of both voltage magnitude and frequency are investigated separately in this chapter. A further consequence of the integration of CIGs is the concept of increasing variability in regional frequency [234]. To address this, the local frequency is estimated at each bus using the frequency divider formula introduced

in [234].

6.1.2 Literature Review

Improvements to system strength metrics have been attempted, with those including small-signal considerations focusing on impedance modelling and singular metrics based on stability margins or impedance coupling [27–29, 233]. In particular, the impedance margin ratio, generalised SCR, and the grid strength impedance metric are examples of the state-of-the-art in this regard. The impedance margin ratio [29] and generalised SCR [28] are based on stability margins with the former considering the allowed variation of the impedance and the latter using a metric derived based on decoupling of the system into a series of OMIB systems. The grid strength impedance metric offers an alternative to SCR whereby the perspective of electrical distance from an ideal voltage source is maintained but the impedance of CIGs and their control are incorporated into the calculation of the metric [233], offering better reflection of their impact on voltage strength. In addition, their work expands the consideration of system strength across the frequency spectrum, going beyond simply the fundamental frequency. These metrics are proving more adequate in reflecting CIG impact on stability/oscillation damping [235]. However, they do not consider the decoupling of voltage magnitude and frequency, nor do they provide specific information regarding the variability of any given output signal (which in this work is found to not necessarily relate to traditional stability metrics) and the contributing dynamic interactions.

Notably, some of the recently introduced grid strength metrics are developed in such a manner that they relate to system stability margins. There is of course a relation between grid strength and stability, whereby a stronger grid *implies* a higher stability margin. However, in this work we propose a quantification approach based on variability (i.e., how much a signal deviates) which can be directly linked to the concept of strength. Note, in traditional grid strength metrics such as SCR–and some more modern approaches such as the grid strength impedance metric–the grid strength is considered from an (in)variability perspective whereby the electrical distance from an ideal voltage source represents strictness of control of the voltage phasor (magnitude

and frequency) and therefore less variability of said phasor. That is, these metrics were aiming at offering a quantification of how much or not the voltage and frequency will vary. Our approach provides a more direct measure of how the voltage and/or frequency (or any output variable of interest) will vary in the time domain-response for any given disturbance. Furthermore, existing electrical distance-based grid strength metrics suggest either variability or invariability regardless of disturbance type or location, as well as the lack of decoupling between "strength" of voltage and frequency (as previously discussed). We will see in this chapter that this can in fact have a significant impact on the variability from one location (or output variable) to another.

The method proposed in this chapter comes from a modal decoupling perspective with relation to the concepts of small-signal observability and controllability. Similarly, within the framework of dynamic grid flexibility [236], the inertial distribution index is proposed. This index uses the mode shape of the "most global" mode to extract information regarding the inertial distribution of the system. However, although undoubtedly useful, this index is focused on a single mode (and output). Consequently, it has the potential to miss variability information related to other modes. This is especially true considering the changing dynamic timescales and control approaches associated with CIGs. [220] has relation to the inertial distribution concept whereby it can consider the locational relation between a single mode and specified outputs but through their derived PFs of algebraic variables. Additionally, the output of interest is not focused on the locational frequency but is applied to any algebraic variable or output.

Compared to prior works described above, the metric and method proposed in this chapter focuses on capturing locational information that drive the variability of system output variables (i.e., frequency and voltage). This can be extracted using the modal superposition concept, without neglecting the effect of multiple modes that can affect specific power system variables. This involves defining a metric based on the analytical solution of the individual modal responses and their contribution to the system output variable of interest, the details of which are dependent on the corresponding eigenvalues and eigenvectors as well as the excitation–i.e., utilising concepts from observability

and controllability analysis [10, 13] but extending these concepts to enable tracing the dynamic interactions that affect the variation of output variables which in turn allows for the definition of a variability metric. That is, going beyond an approach similar to PFs for output variables by quantifying and understanding directly the impact of a disturbance to the output magnitude.

Consequently, the main aim of the proposed method is to determine a metric to analytically quantify the impact of disturbances across different locations of the system on the time-domain response of relevant power system output variables (i.e., voltage and frequency), referred to as the outputs' *variability*. This provides a quantification of small-signal grid strength linked to the physical meaning of the amplitude of deviations observed in time domain simulations, while accounting for the detailed dynamic responses of systems, including the response of CIGs. To summarise, the proposed method and illustrative analyses include:

- An alternative viewpoint for system strength from the perspective of small-signal variability. A method is proposed for the analysis of locational small-signal voltage and frequency variability considering different disturbance types and locations. This includes a metric to quantify small-signal variability based on modal superposition. It allows to take into account detailed aspects related to system dynamics and interactions, contrary to conventional system strength metrics.

- A clear indication of the contribution of a specific mode/interaction to the variability of the time domain response of any given output through the analytical calculation of the maximum deviation of the decoupled modal response.

- The capability to extract distinct variability trends across different timescales and the respective fast or slow dynamic modes that contribute.

- An analysis of the impact of the introduction of CIGs with both GFL [140, 237] and GFM [15] control on the locational small-signal variability of the system is carried out.

The remainder of the chapter is structured as follows: Section 6.2 details the relation between modal responses and power system output variables as well as deriving the analytical solution of the response and the corresponding variability metric; Section 6.3 describes the dynamic modelling of the power system and relevant components; Section 6.4 outlines the specific test cases; Section 6.5 displays the corresponding results; and Section 6.6 concludes the chapter.

The work in this chapter has been published in IEEE Transactions on Power Systems [238].

6.2 Methodology: Introducing a Power System Variability Measure

This section begins by defining the concept of small-signal variability as utilised in this work. On this foundation, a metric for the quantification of said variability is proposed. This is achieved through the decoupling of modal responses, followed by the derivation of the analytical solution of the maximum deviation of said decoupled responses.

6.2.1 Defining Variability

In this work, we define variability based on the maximum deviation of power system output variables in their time domain responses. Since small-signal (impulse) disturbances are considered, the maximum deviation is taken from the initial operating value of the output variable of interest. The motivation behind this is to derive metrics and perform relevant analysis that identifies situations where power system variables (e.g., voltage and frequency) throughout different parts of a system tend to exhibit high deviations from their initial values. Such situations could indicate possible limit violations, system stress and generally the tendency of high amplitude oscillations. This definition of variability therefore relates to a way of quantifying system strength while taking into account detailed dynamic responses, becoming especially relevant in power systems with high converter penetration.

Also, to reiterate one of the key points from the introduction of this chapter, the

variability is related to the idea of strength whereby an increase in the latter means a decrease of the former. However, strength is also sometimes linked to the idea of stability and therefore stability margin metrics are used in some more modern grid strength quantifications. Therefore, it should be highlighted that although there is a relationship between variability and stability through the idea of strength, they are not directly linked and a decrease in variability does not necessarily mean an increase in stability (margin). For example, a damped oscillation with a high amplitude would have high variability but not necessarily low stability margin. Such a disconnect between variability and stability margin is further highlighted in Section 6.5.5.

6.2.2 Decoupled Modal Responses on System Output Variables

The fundamentals of small-signal modelling have been described in detail in Section 2.1, including the calculation of eigenvalues, eigenvectors, and PFs. As a reminder, $\boldsymbol{x}_{N\times 1}$, $\boldsymbol{u}_{N_i\times 1}$, and $\boldsymbol{y}_{N_o\times 1}$ are the vectors of states, inputs, and outputs, respectively. The state, input, output, and feed-forward matrices are denoted by $\boldsymbol{A}_{N\times N}$, $\boldsymbol{B}_{N\times N_i}$, $\boldsymbol{C}_{N_o\times N}$, and $\boldsymbol{D}_{N_o\times N_i}$, respectively. The diagonal elements of the matrix $\boldsymbol{\Lambda}_{N\times N}$ are the system eigenvalues (or modes), $\{\lambda_1, \lambda_2, ..., \lambda_k, ...\lambda_N\}$. The matrices denoted by $\boldsymbol{\phi}$, $\boldsymbol{\psi}$ and $\boldsymbol{p}$ have columns corresponding to the right eigenvectors, left eigenvectors, and PF vectors, respectively.

The free response of a linear dynamic system [10] is represented by a superposition of individual modal responses:

$$\Delta x_i(t) = \phi_{i,1}c_1e^{\lambda_1 t} + \phi_{i,2}c_2e^{\lambda_2 t} + \cdots + \phi_{i,n}c_ne^{\lambda_n t} + \cdots + \phi_{i,N}c_Ne^{\lambda_N t}, \tag{6.1}$$

$$c_n = \boldsymbol{\psi_n}\Delta\boldsymbol{x}\,\boldsymbol{(0)}, \tag{6.2}$$

$$\Delta y_j = \left[\frac{\delta y_j}{\delta x_1}, \cdots, \frac{\delta y_j}{\delta x_n}, \cdots \frac{\delta y_j}{\delta x_N}\right]\Delta\boldsymbol{x} = \boldsymbol{C_j}\Delta\boldsymbol{x}, \tag{6.3}$$

where $\Delta x_i(t)$ is the time-domain response of the i^{th} state whose relation to the output is specified in (6.3). In this work, the output Δy_j is either the voltage magnitude or frequency at any bus of interest, with the latter calculated using the frequency divider formula [234] (see Section 6.3 for more information). The initial deviations $\Delta\boldsymbol{x}\,\boldsymbol{(0)}$ will

depend on the chosen disturbance type (active power load disturbance in this work) and location. The combined mode shape, $\phi_{i,n}$, and excitation terms–i.e., c_n, which relates the disturbance to the excitation of the mode in (6.2) through the controllability [239]–constitute the amplitude and phase of the individual modal responses (before damping), as seen in (6.1). If we focus on a single state, i, then the unitary excitation of only this state, $\Delta x_i(0)$, will cause the coefficient terms of each modal response to be the corresponding PF [240].

Knowing the relationship between states and outputs as in (6.3), we can then determine the output as a superposition of modal responses with

$$\begin{aligned}\Delta y_j(t) &= \sum_{i=1}^{N} C_{j,i}\Delta x_i(t) = \sum_{i=1}^{N}\sum_{n=1}^{N} C_{j,i}\phi_{i,n}c_n e^{\lambda_n t} \\ &= \sum_{n=1}^{N}\left[\sum_{i=1}^{N} C_{j,i}\phi_{i,n}\right] c_n e^{\lambda_n t} = \sum_{n=1}^{N} \Phi_{j,n}c_n e^{\lambda_n t},\end{aligned} \tag{6.4}$$

where $\mathbf{\Phi}_{N_o\times N}$ can be considered the *output mode shape* (or the modal observability [239]) which is compared to the right eigenvectors from (2.10) but for any given mode's observability on the chosen outputs instead of the system states. Note that, if we focus on a single output, j, and consider the unitary excitation of each state, i, prior to performing the sum in the square brackets of (6.4), the resultant modal coefficient term for each mode is found to be the *participation factors of algebraic variables* derived in [220]. This can be expressed for each mode, n, as

$$\pi_{j,n} = \sum_{i=1}^{N} C_{j,i}\phi_{i,n}\psi_{i,n}. \tag{6.5}$$

6.2.3 Calculating the Maximum Deviation (or Contribution) of Decoupled Modal Responses on Output Variables

Having decoupled the modal responses with respect to system output variable (voltage or frequency), the maximum deviation of each modal response can be determined as a measure of their contribution to the output small-signal variability. Hence, we calculate the maximum deviation of each modal response whose characteristics are described fully

by their eigenvalue and eigenvectors as well as the excitation.

As can be seen from (6.1), the time-domain response for each (stable) mode can be described either by an exponential reduction, in which case the time at which the maximum deviation occurs will be zero seconds (the occurrence of the disturbance), or an oscillation whose amplitude is exponentially decaying. Whether it is the former or latter depends on whether the eigenvalue is real or complex, respectively. The oscillatory response can be described in familiar mathematical terminology as

$$\chi(t) = Ae^{\sigma t}cos(\omega t + \theta), \tag{6.6}$$

with A, θ, σ, and ω being the amplitude, initial phase, damping constant, and oscillation frequency, respectively.

In order to get from a decoupled modal response in (6.1) to the form in (6.6) we can consider that an oscillation comprises of two eigenvalues, one with positive and one with negative frequency. Similarly, the polarity of the complex values in the corresponding eigenvectors will be reversed with the result being that the initial phase will also be opposite [10]. Consequently, for output j and mode n,

$$A = 2|\Phi_{j,n}c_n|, \tag{6.7}$$

$$\theta = \angle\Phi_{j,n}c_n, \tag{6.8}$$

$$\lambda_n = \sigma \pm j\omega. \tag{6.9}$$

Unlike an exponential decay, the maximum deviation of (6.6) will not necessarily occur at zero seconds. However, the simple second order response allows us to solve analytically the time at which the maximum deviation/value will occur. Note, this solution is dependent on the assumption that we have constant, real values for A, σ, and θ, with the additional requirement that σ is positive. We want to determine the first instance at which the derivative of (6.6) is zero, i.e., the first maxima or minima of the solution, because the absolute value of any succeeding maxima or minima will

be smaller due to the damping of the mode. The resultant equation is,

$$\frac{d\chi(t)}{dt} = Ae^{\sigma t}(\sigma cos(\omega t + \theta) - \omega sin(\omega t + \theta)) = 0, \tag{6.10}$$

which can be simplified to

$$cos(\omega t + \theta) - \frac{\omega}{\sigma} sin(\omega t + \theta) = 0. \tag{6.11}$$

Solving (6.11) for t gives

$$t = \frac{n\pi - \left(\theta + jln\left(\pm\frac{\sqrt{-\sigma^2-\omega^2}}{\sigma+j\omega}\right)\right)}{\omega}. \tag{6.12}$$

The choice of value for n is dependent on the fact that we are considering a causal system (i.e., $t \geq 0$) and hence,

$$n\pi - \theta - jln\left(\pm\frac{\sqrt{-\sigma^2-\omega^2}}{\sigma+j\omega}\right) \geq 0, \tag{6.13}$$

and considering the positive damping of the oscillation, we require the first integer value of n for which this criterion is met, resulting in

$$n = \left\lceil \left(\theta + jln\left(\pm\frac{\sqrt{-\sigma^2-\omega^2}}{\sigma+j\omega}\right)\right)/\pi \right\rceil, \tag{6.14}$$

where the ceiling operator is $\lceil \square \rceil$. Note, considering the dual solution to (6.12), there will be two solutions to (6.14) but as long as the value of n is matched to the corresponding equation then the result of (6.12) will be the same. That is, the $\pm$ operator can be replaced with either a $+$ or a $-$, provided consistency is ensured throughout. Therefore, we can determine that the maximum deviation of the solution to (6.6) will occur at either the positive solution of (6.12), i.e., the first maxima/minima, or at the instance of the disturbance.

The next step is to relate the known parameters, i.e., the eigenvalues and eigenvectors, in (6.4) to the parameters required to solve (6.12) and substitute the resultant equation back into (6.6). This is achieved with reference to (6.7) to (6.9) and

by substituting everything back into (6.6) we get the final maximum deviation value associated with any given mode, which is

$$\Delta y_{j,n}^{max} = 2\left|\Phi_{i,n}c_n\right| e^{\sigma t_{max}} cos\left(\omega t_{max} + \angle \Phi_{i,n}c_n\right), \tag{6.15}$$

where t_{max} is either calculated with (6.7) to (6.9), (6.12), and (6.14), or $t_{max} = 0$ s, depending on which choice of t_{max} gives the larger value of $\left|\Delta y_{j,n}^{max}\right|$. Note, for a real-valued mode, the maximum deviation occurs at 0 s and is equivalent to $A/2$ with respect to (6.7).

A question that arises from this proposed approach is why not to use the well-known residues [239] for quantifying the contribution of each mode to the small-signal variability of the time-domain response of the chosen output (voltage and/or frequency at each bus)? In fact, the residues were tested alongside our proposed approach and found to have lesser ability to predict the small-signal variability trends. This is likely due to their lack of consideration of the damping of the modes, which plays a key role in the maximum value that their decoupled modal response can reach in the time-domain.

6.2.4 Deriving a Variability Metric

The maximum deviations of the decoupled modal responses, used to reflect the modal contributions to a single output, can be condensed to a single metric to enable comparison between several outputs. Particularly, this gives a proxy for the variability (maximum deviation) of voltage magnitude or frequency at each bus location. The adopted approach takes the maximum absolute value of maximum deviation, or the maximum absolute modal contribution (MAMC), as the indicator. This is described for the j^{th} output as

$$\text{MAMC}_j = max\left(\left|\Delta \boldsymbol{y}_{\boldsymbol{j}}^{\boldsymbol{max}}\right|\right), \tag{6.16}$$

where $\Delta \boldsymbol{y}_{\boldsymbol{j},N\times 1}^{\boldsymbol{max}}$ is the vector for output j whose entries are the modal response maximum deviations calculated as described in Subsection 6.2.3.

Prior to the extraction of the MAMC through (6.16), there is the possibility to

focus on modes with specific characteristics. E.g., if specific damping timescales are of interest, a weighting of zero can be applied to any mode whose damping time constant is outwith that of interest. This provides an indication of the variability differences depending on timescales as well as an understanding of the different modes that dominate at these different timescales (as later presented in Section 6.5.6). It should be noted that the main assumption of (6.16) is that the output response will closely resemble the response of the mode which provided the MAMC: neglecting potential constructive or destructive interference caused by the remaining modes.

6.2.5 Application of Disturbance

For the input disturbances in this chapter, a negative injection of current corresponding to 0.1 pu active power is applied at each bus. The relation between the disturbance of interest and the excitation terms are through the initial state deviations, $\Delta \boldsymbol{x}\,\boldsymbol{(0)}$. As a proxy for the initial state deviations, the input matrix is used in (6.17) to determine the rate of change of any given state resulting from the input disturbance which in turn is assigned to the initial deviations as $\Delta x_n(0) := \Delta \dot{x}_n$.

$$\Delta \dot{x}_n = \left[\frac{\delta \dot{x}_n}{\delta u_1}, \cdots, \frac{\delta \dot{x}_n}{\delta u_{N_i}} \right] \Delta \boldsymbol{u} = \boldsymbol{B_n} \Delta \boldsymbol{u} \tag{6.17}$$

If an impulse disturbance is considered, the forced response collapses to the same representation as the free response with such proxy initial states (see Chapter 4.1 of [241]).

It may be more appropriate to consider a step disturbance to extract a variability indicator as this represents better an actual disturbance that might occur on the system. However, in doing this, the eigendecomposition of the output becomes significantly more complex, concealing the useful link between variability and system interactions (as the impact of natural system changes also influences the time-domain response). Extension of this method to step disturbances is reserved for future work. Furthermore, the choice of disturbance variable will also influence the outputs' variability. While we choose a specific variable to introduce disturbances (current injection) when presenting our

results in this chapter, the proposed method can accommodate different disturbances such as voltage magnitude perturbations. Future work could systematically investigate the impact of such different disturbances.

6.3 Modelling

As in previous chapters, the small-signal modelling has been explained in detail in Chapter 2. The SGs are balanced 8^{th} order models [11], equipped with the DC1A exciter and AVR as in Example 12.6 of [10].

Common to GFLs and GFMs are power measurement filters and output RLC filter [140]. The converter is averaged with switching transients and PWM/control delay neglected [237].

Additionally, the passive network, stator, and converter output filter elements have been modelled with the quasi-static assumption [11], [10]. Before making this simplification, the impact on the eigenvalues of the systems were checked and it was confirmed that the dynamics included in the quasi-static model (i.e., all except electromagnetic network transients) matched closely their counterparts in the full-detail [30] model. Consequently, the focus of our study is mostly on converter and generator dynamics and how these can affect the variability of outputs. Although, theoretically network dynamics could be included as part of the proposed methodology, this might lead to challenges related to modal combination at very fast timescales. Most notably, impulse disturbances, as applied in this work, can excite modes that are related purely to dummy network variables as utilised for modular component connections (for more information see Section 2.2 and [242]). Some further discussion on related aspects is provided in Section 6.5.1 but mostly falls out of the scope of this chapter and is reserved for future work. Furthermore, provided the focus of an investigation is on converter and generator dynamics (as is the case in this chapter), the ability to separate the timescales on which the variability is analysed, as in Section 6.5.6, would also be expected to alleviate potential issues.

As discussed previously, the frequency divider formula [234] was adopted to obtain an estimation of the frequency at each bus. In particular, this includes consideration

of the SG internal impedance and the GFM coupling filter. For the frequency at a bus with GFL converter, the PLL measurement is used as input to the formula (note, this is an estimation and this should be taken into consideration when analysing results). Note, an alternative approach is to take the derivative of the voltage angle directly at each bus, or to adopt the complex frequency representation [243].

6.3.1 Grid-Following Converters

The GFL used in this work, displayed in Fig. 6.1, is a standard current vector control consisting of PI-based APC and RPC (Section 2.5.3 and Fig. 2.7), ICC (Section 2.5.2 and Fig. 2.5), and a PLL (Section 2.5.3 and Fig. 2.8). The tuning of the ICC is based on the modulus optimum technique [244], whereas the APC, RPC, and PLL are tuned to maintain stability in a weak grid with the approach in [140].

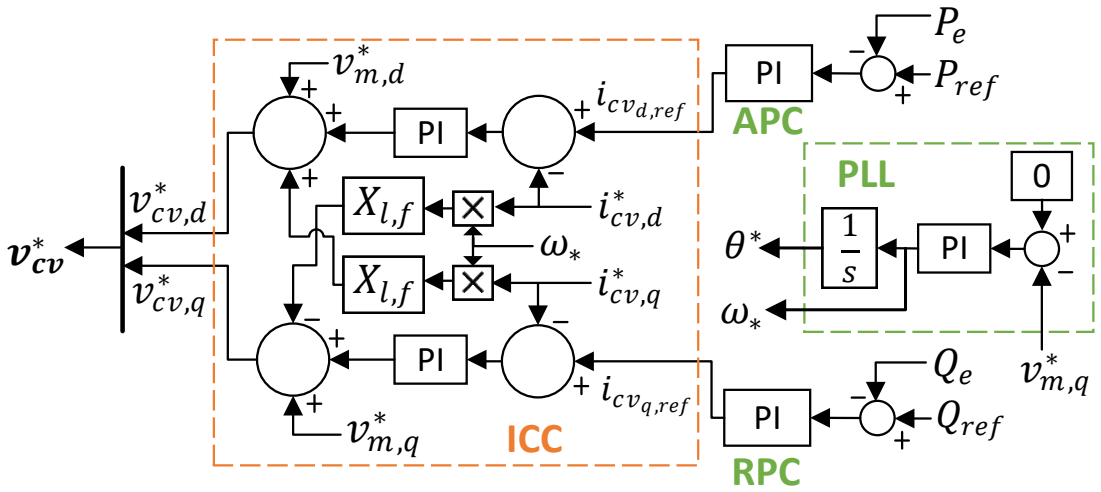

Figure 6.1: GFL control system block diagram for small-signal variability analysis case studies.

6.3.2 Grid-Forming Converters

The GFM used in this work, displayed in Fig. 6.2, consists of an outer loop which synthesises the voltage phasor through an APC, in the form of a VSM [15], a VMC, in the form of a reactive power-voltage droop [59], and a virtual impedance[1]. The choice

[1]The virtual impedance is of the form in Section 2.5.4 but negated. This is in line with the virtual impedance implementation in [59], [223], and [224].

of virtual inertia constant, H, of 6.5 s ensures proper comparison with the SGs. Note, the active power measurement is not filtered since the VSM swing equation effectively achieves this [15].

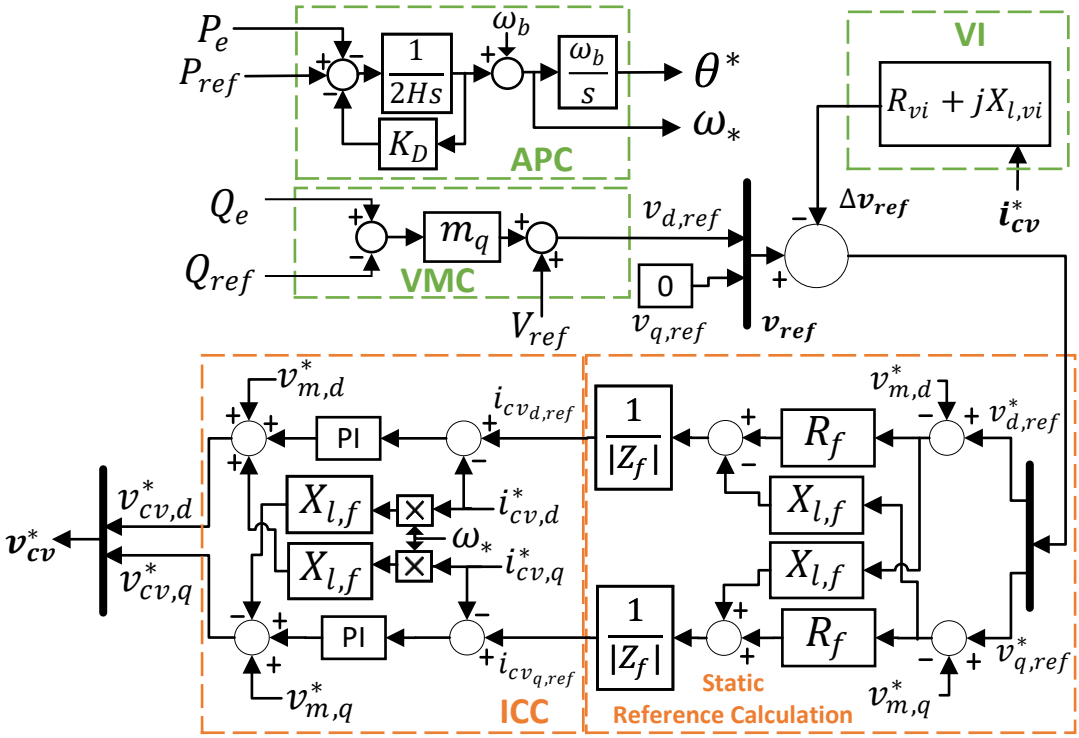

Figure 6.2: GFM control system block diagram for small-signal variability analysis case studies.

The GFM adopts an SILC architecture with an ICC and a static reference calculation based on the coupling filter impedance $Z_f = R_f + jX_{l,f}$ [152] as further described in Section 2.5.5.

6.4 Test Cases

Since the focus of this work is identifying the small-signal variability at different locations, we choose the Kundur two-area test system [10] for its clearly distinct electrical regions. This incorporates two similar areas with a weak tie line between them as displayed in Fig. 6.3. All SG and system information is available in [10]. This SG-only test system was taken as the base case with the only change from [10] being

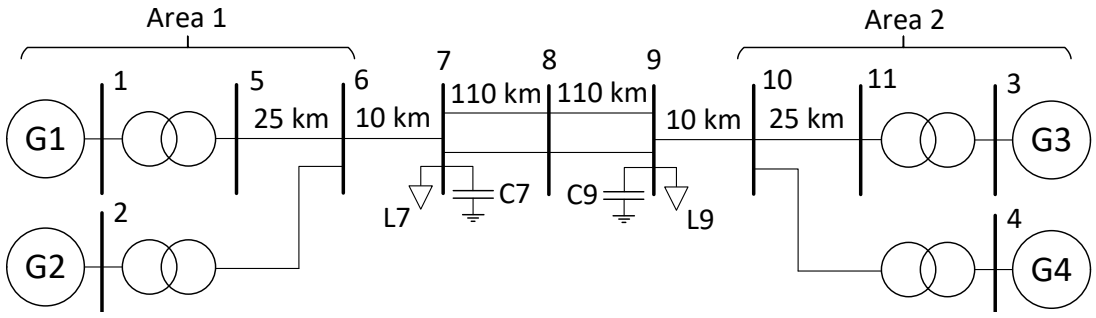

Figure 6.3: Kundur's two-area four-generator system. Figure adapted from [10].

the setting of all SGs' inertia constants to an equivalent 6.5 s.

Of interest in this work is the impact of CIG on the locational small-signal variability of voltage magnitude and frequency. As such, the SGs in area 2 are first replaced by GFLs and then by GFMs. Finally, the GFMs are instead placed in area 1 which results in a case which clarifies the capability of the method to focus on particular timescales of interest. The parameters associated with GFLs and GFMs are summarised in Table 6.1. Note, per unit values are on the generator bases of 900 MVA and 20 kV, as is the case with the SGs.

6.5 Results

The visualisation approach for the MAMC is a 3-dimensional bar graph. For these plots, the "disturbed bus"-axis displays the disturbance location, allowing visualisation of areas in which the the output variability is excited. The "observed bus"-axis refers to the location at which the variability is being "measured", or observed. That is, we can observe the buses which display the most variability after a disturbance at any given bus. The buses have been reordered on these axes to better represent the layout of the system (Fig. 6.3).

The data generated by the case studies, from which the following analysis is performed, can be found in [245].

Table 6.1: Parameters for CIGs in small-signal variability analysis case studies.

Parameter	**Symbol**	**Value**
RLC resistance	R_f	0.03 pu
RLC inductive reactance	$X_{l,f}$	0.08 pu
RLC capacitive reactance	$X_{c,f}$	13.51 pu
Power filter time constant	τ_p	0.0318 s
Switching frequency	f_s	10 kHz
ICC proportional gain, integral gain	$K_{p,icc}, K_{i,icc}$	$\{0.2122, 30\}$ $\mathrm{V_{pu}/A_{pu}}$
GFL APC proportional gain, integral gain	$K_{p,apc}, K_{i,apc}$	$\{0.02122, 3\}$ $\mathrm{A_{pu}/MW_{pu}}$
GFL RPC proportional gain, integral gain	$K_{p,rpc}, K_{i,rpc}$	$\{0.0118, 1.6667\}$ $\mathrm{A_{pu}/MVA_{pu}}$
PLL proportional gain, integral gain	$K_{p,pll}, K_{i,pll}$	$\{20, 25\}$ rad/s/$\mathrm{V_{pu}}$
GFM APC virtual inertia, virtual damping	H, K_D	6.5 s, 10 pu
GFM VMC reactive power droop	m_q	0.1%
Virtual resistance, virtual inductive reactance	$R_{vi}, X_{l,vi}$	0 pu, 0.2 pu

6.5.1 Validation of Maximum Absolute Modal Contribution (MAMC) as a Variability Metric

One Machine-Infinite Bus (OMIB)

By reducing the system to a OMIB with a single mode, we ensure that the output response is equal to the modal response. As such, the MAMC should be equal to the maximum deviation of the output following the specified disturbance. To test this, a OMIB system is considered with the SG classical model. The synchronous reactance of the machine was set to 0.3 pu and the inertia and damping constants were 3.5 s and 10 pu. The Thévenin equivalent reactance of the grid was set to 0.65 pu. The initial conditions included the 60 Hz grid frequency, the active and reactive power outputs of 0.9 pu and 0.3 pu, respectively, as well as the infinite bus and SG terminal voltages of 0.995 pu and $1\angle 36°$ pu, respectively.

The responses to the SG rotor speed, ω_r, and the output electrical torque, T_e, were simulated using the MATLAB `impulse()` [107] function for a disturbance to both the infinite bus frequency, ω_{ib} (of 1 rad/s) and voltage magnitude $V_{m,ib}$ (of 1 pu). The corresponding values calculated for the MAMC are summarised in Table 6.2 alongside the maximum deviation values obtained from the time-domain response and the error between the two metrics. It can be seen that the MAMC matches exactly the maximum deviation value obtained from the time-domain impulse response up to at least 4 decimal places, confirming the theoretical derivation of (6.16). Note, the sizes of disturbances applied are not realistic and only used for proof of concept.

Table 6.2: OMIB validation results.

Input / Output	MAMC	Time-Domain Maximum	Error
ω_{ib} / ω_r	5.5493 rad/s	5.5493 rad/s	0
ω_{ib} / T_e	292.3498 pu	292.3498 pu	0
$V_{m,ib}$ / ω_r	0.9044 rad/s	0.9044 rad/s	0
$V_{m,ib}$ / T_e	34.3085 pu	34.3085 pu	0

Two-area system validation of locational trends

For a system with multiple modes, e.g., the base SG-only two-area system, the MAMC is not expected to match exactly the maximum deviation of the output. This is due to the output being a superposition of modal responses and the MAMC being an approximation based only on the most contributing mode at any given disturbance and observation location. However, we are interested in the comparative relationships between the voltage magnitude and frequency, at different locations. Therefore, in this section we investigate the correlation between the MAMC and the corresponding maximum deviation in the time-domain response, across buses. That is, the locational distribution of the *variability*.

The 3D bar graphs displaying the MAMC and time-domain response maximum deviation (TDRMD) for the bus frequencies in response to an active power disturbance are displayed in Fig. 6.4a and Fig. 6.4b, respectively. Note, qualitative assessment of how the MAMC variability metric relates to the time-domain response is further explored in Section 6.5.6.

The similarities in trends are immediately obvious, although, the disturbance applied to area 1 and observed in area 2 is slightly raised compared to the rest of the locations in the TDRMD compared to the MAMC results. To further highlight the matching in variability trends, the linear correlation coefficient (LCC) can be calculated between the arrays representing each disturbed bus. For example, there is an array for each disturbance location, whose elements are either the MAMC or TDRMD at each observed location. These arrays are referred to as the observational distributions. Note, that the opposite can also be done whereby there is an array for each observation bus location whose elements are the MAMC or TDRMD for each disturbance location. These arrays are referred to as the excitation distributions. The LCC was calculated using the MATLAB function `corr()` [107] which makes use of Pearson's metric. The LCC between the observational distributions of the MAMC and corresponding TDRMD for each disturbed bus is displayed in Fig. 6.5a. Similarly, the LCC between the excitation distributions follows in Fig. 6.5b. There is generally a good match with high LCC values observed. The result of the increase in variability for the TDRMD

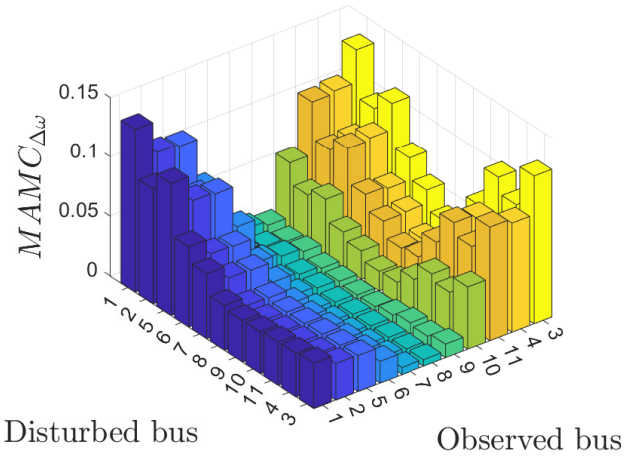

(a)

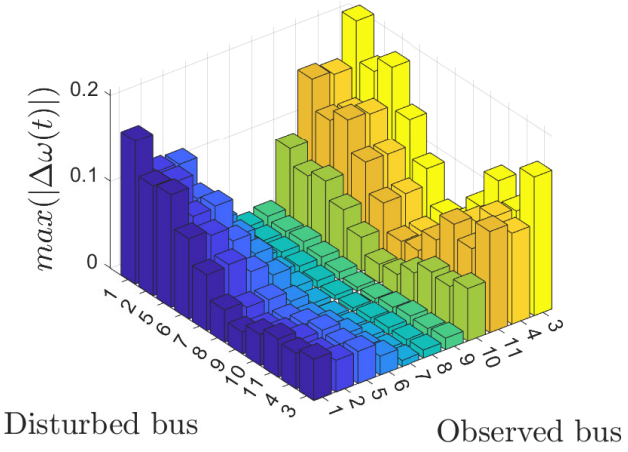

(b)

Figure 6.4: (a) MAMC and (b) maximum deviation in time-domain of each bus frequency for an active power disturbance in the base SG-only system.

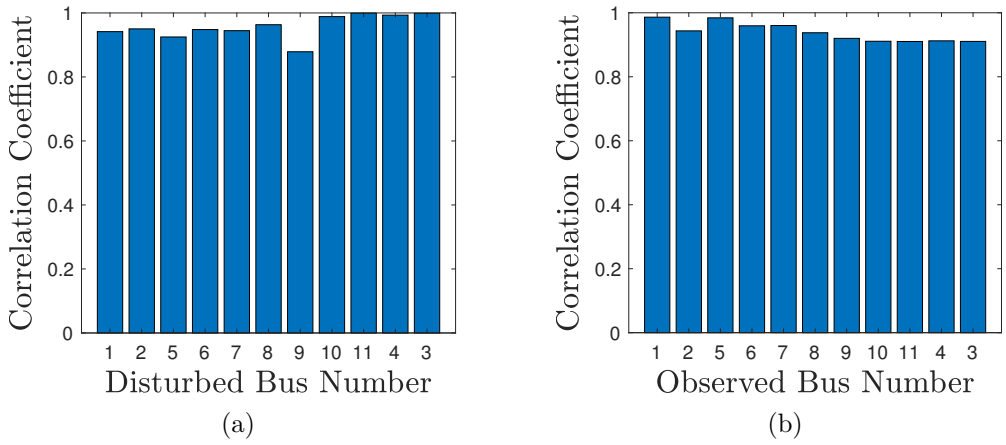

Figure 6.5: Linear correlation coefficient between the MAMC and TDRMD of the (a) observational distributions and (b) excitation distributions for the frequency variability analysis in the base SG-only system.

compared to the MAMC (visible in Fig. 6.4b), for a disturbance in area 1 observed in area 2, is that there is a dip in correlation for area 1 and area 2 in Fig. 6.5a and Fig. 6.5b, respectively.

By creating a single array which is the concatenation of all observational, or equivalently excitation, distribution arrays, we can determine the LCC between the two metrics for the variability trends as a whole. That is, comparing the full graphs in Fig. 6.4a and Fig. 6.4b. In this case, the resultant correlation coefficient is 0.9588. This will be termed the full LCC and is the accuracy measure used in the remainder of this work.

The same approach is applied when considering the voltage magnitude at each bus as the output variable of interest. The resultant bar graphs for MAMC and TDRMD are shown in Fig. 6.6a and Fig. 6.6b, respectively.

The errors in this case are more significant. In particular, there are peaks in the TDRMD that are not represented accurately by the MAMC which are observed in area 1 when area 1 is disturbed, and observed in area 2 when area 2 is disturbed (i.e., more local in nature). Similarly, there is slightly increased variability excited by a disturbance on bus 8 for all observed locations. Whereas the MAMC suggests there should be higher variability observed in area 2 when area 1 is disturbed. These deviations in the voltage results are reflected in the full LCC of 0.7644.

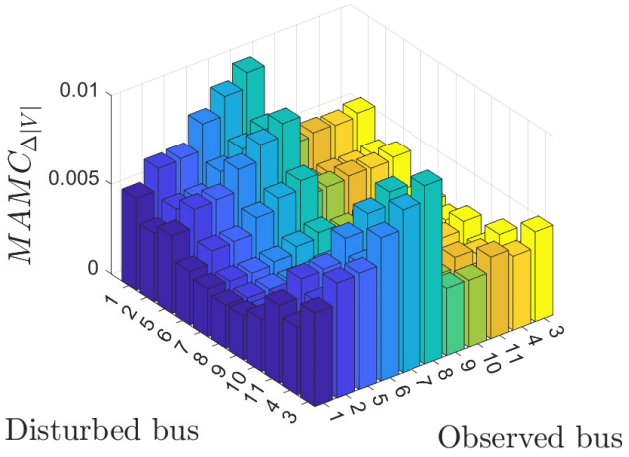

(a)

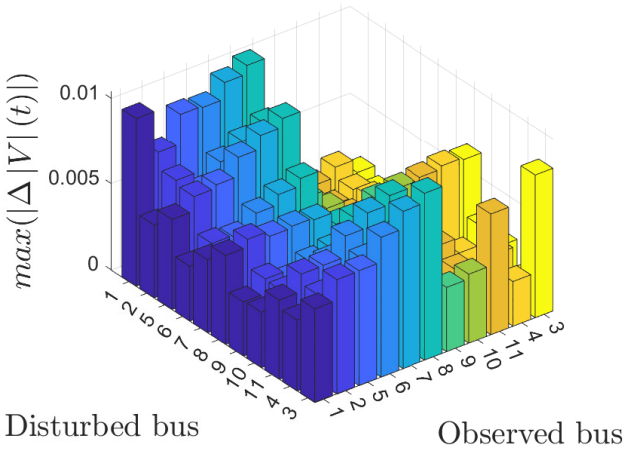

(b)

Figure 6.6: (a) MAMC and (b) maximum deviation in time-domain of each bus voltage magnitude for an active power disturbance in the base SG-only system.

To observe the reasoning behind the lower performance in the case of voltages, the modal contributions (maximum deviation of decoupled modal responses whose calculation is derived in Subsection 6.2.3) in the areas with weakest matches can be investigated. When disturbing bus 1 and observing the same bus, several modes with similarly high values of contribution are identified. The main mode is oscillatory with a value of $-0.0703 \pm j3.2531$, which is in fact the expected inter-area mode of the system [10], whose TDRMD occurs at approximately 0.51 s. However, there are also several non-oscillatory modes with sufficient contribution to influence the time-domain response, one in particular which has a value of $-30.4339 + j0$. On its own, this eigenvalue has just less modal contribution than the inter-area mode but when combined with the other non-oscillatory modes, whose peaks all occur at the instance of the disturbance, the contribution becomes higher but is not accounted for in the MAMC (future work will look to improve the accuracy of the method through modal combination techniques, which may also be required for cases in which repeated eigenvalues occur [220]). This is illustrated in Fig. 6.7 whereby the voltage magnitude deviation is initially brought to -0.01 pu at the instance of the (active power impulse) disturbance due to the non-oscillatory modes which then damp out quickly leaving the inter-area mode to dominate the response. However, noting the fast damping time constant of the non-oscillatory mode mentioned, it can be found that delaying the start of the measurement for TDRMD by 0.05 s gives a result which the MAMC matches much better with a full LCC of 0.9258. As such, the lack of modal combination approach means that some information is lost but the MAMC is still seen to identify some of the main underlying trends. More importantly, the method can be used to identify underlying reasons between the discrepancies and help in understanding their importance (or lack thereof).

Having highlighted the capability of the MAMC to reflect interesting variability trends, in addition to particular limitations, variability analysis is performed using the developed approach on the case studies from Section 6.4.

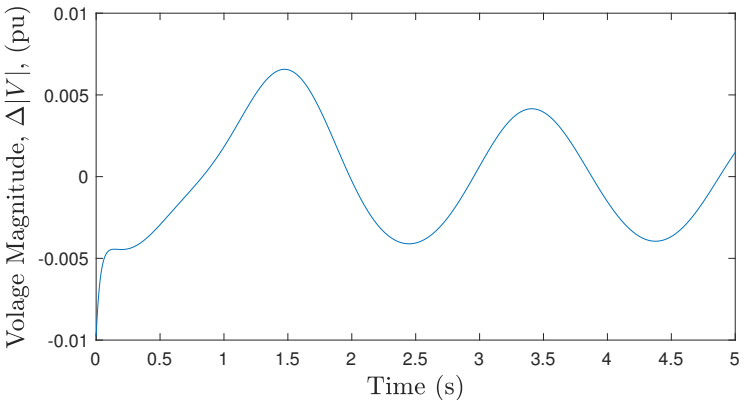

Figure 6.7: Response of voltage magnitude at bus 1 to 0.1 pu active power disturbance at bus 1 in SG-only system.

6.5.2 Variability Analysis of the Base Kundur Two Area System (SG-Only)

Fig. 6.4a reveals that for the base system, increased frequency variability is exhibited primarily when a disturbance is applied close to the SG locations (except for the observed variability in area 1 when area 2 is excited). When said disturbance occurs in area 1, the variability is observed mostly near the SGs in area 1 and in area 2; however, when the disturbance is applied in area 2, the variability is excited near the generators in area 2 but does not propagate to area 1. The highest contributing mode in the former case for both areas is a 0.145 Hz oscillation with the PFs revealing that it is related to the damper windings and rotor speed of the SG in area 1 and, to a lesser but still significant extent, area 2. An important note here is that this mode has a damping ratio of 0.86 and so would often be ignored in traditional small-signal analyses and stability metric-focused grid strength indicators such as the impedance margin ratio [29]. Nevertheless, this is the mode that causes high amplitude deviations in the time domain responses of frequency throughout the system which can be revealed by observing the maximum deviations of the decoupled modal responses. For a disturbance in area 2, the variability observed in area 1 has most contribution from the 0.145 Hz oscillation but to a lesser extent than the disturbance in area 1. Also, the observed variability in area 2 is caused mostly by the system's inter-area mode. Focusing on the mode shape of this inter-area

oscillation, its observability is focused on the rotor speed states of the SGs in area 2 with limited observability in area 1, hence the fact that the 0.145 Hz oscillation is the most impactful in this area.

This ability to highlight different modes contributing most to the observed variability in different locations for the same disturbances is one of the key benefits of the proposed method. i.e., the MAMC is a measure of locational variability that is not restricted to focusing on a single mode. Using a PF-based analysis approach such as in [220] is very useful for understanding the relationship between a single mode and the outputs of interest; however, it will not reveal the general locational trends of output variability that is the interest of this work.

As discussed previously, the voltage variability excited and observed in area 1 of Fig. 6.6a is mostly caused by the inter-area mode. It is also the same mode contributing most to the observed voltage variability in area 1 when a disturbance is applied in area 2. The observed variability in area 2 is found to be a result of the 0.145 Hz mode mentioned earlier for disturbances in area 1 and a non-oscillatory mode of value $-30.43 + j0$ for disturbances in area 2. For any given disturbance location, the inter-area mode is observed most in area 1 and has less impact in area 2, contrary to what was seen for the frequency variability analysis. Since the mode will be excited the same amount for the same disturbance, the difference lies in the observability of the mode on the frequency vs. the voltage magnitude of each bus, highlighting the distinctive variability characteristics between them.

6.5.3 Variability Analysis After Replacing Synchronous Generators in Area 2 with Grid-Following Converters

For this case, the full LCC for the MAMC of frequency and voltage are 0.8745 and 0.8142, respectively, highlighting generally good match.

In Fig. 6.8a it can be seen that frequency variability is observed most in area 2, where the SGs have been replaced with GFL converters. It is also in this area where disturbances are seen to excite variability the most. The mode contributing most to the variability in this region is non-oscillatory with value of $-18.33 + j0$ and PFs suggesting

it is related mostly to the PLL angles of both GFLs and the outer active power controller of GFL3. For contrast, the mode contributing most to the variability for disturbances in area 1 with observation in area 1 (i.e., area with SGs) is also non-oscillatory with value of $-0.0042 + j0$ but is related to the rotor speed states of the SGs.

From Fig. 6.8b it is clear that the most significant voltage variability is observed in area 2 in response to disturbances in area 2 (i.e., where GFL converters are placed). The most contributing mode in this region is non-oscillatory with value $-7.77 + j0$ and the PFs reveal that it is an interaction mainly between the APCs of the two GFLs.

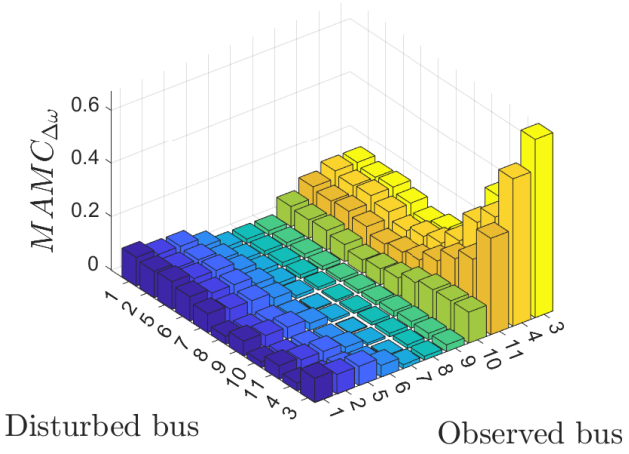

(a)

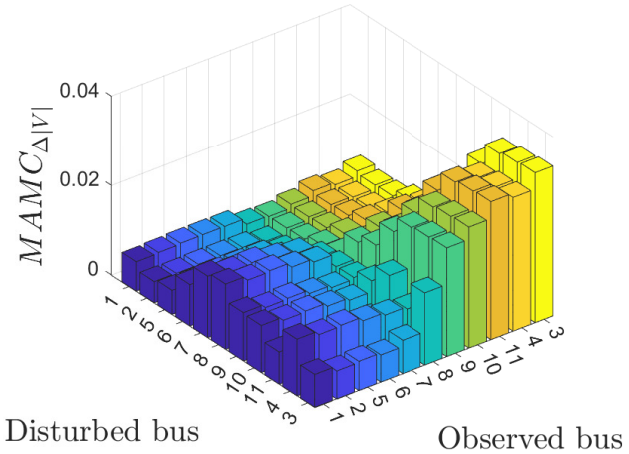

(b)

Figure 6.8: MAMC for bus (a) frequencies and (b) voltage magnitude for an active power disturbance in the system with GFLs in area 2.

An important observation is that the most contributing modes for the majority (but not all) of disturbance and observational locations were non-oscillatory in this system. Therefore, care should be taken in systems with GFLs with respect to the potential for exacerbation of the MAMC limitations highlighted in Section 6.5.1. However, as mentioned previously, the full LCC highlighted the general validity of the MAMC in this specific scenario. It was also observed in [59] that non-oscillatory instability may become a more pertinent phenomenon in converter-permeated systems.

6.5.4 Variability Analysis After Replacing Synchronous Generators in Area 2 with Grid-Forming Converters

The full LCC for the MAMC of frequency and voltage for this case are 0.9010 and 0.8735, respectively, showing again a good match.

In Fig. 6.9a, the frequency variability trends are shown to be similar to the corresponding case of the SG-only system with the exception of less observed variability in area 2 in response to disturbances in area 2, where the GFMs have replaced the SGs. The cause of the variability for disturbances in area 1 and observation in area 1 is a non-oscillatory mode of $-0.86 + j0$ and is related primarily to the AVRs and damper windings of the SGs and small contribution from the virtual rotors of the GFMs. When observing area 2 after disturbances in area 1, it is primarily a mode of $-1.38 \pm j0.63$ which contributes most to the variability. The main PFs are of the damper windings and the AVRs of the SGs as well as the rotor speed of SG1 and small contributions from the virtual rotors of the GFMs. This mode also contributes heavily for disturbances in area 2. For such disturbances, when observing the variability in area 2, there is also a mode of $-0.38 \pm j3.04$ which contributes heavily, related to the GFMs' virtual rotors and, to a lesser extent, the SGs' rotors (i.e., the inter-area mode). Although non-oscillatory modes do contribute to the variability in this case, the majority are oscillatory in nature, contrary to the case with the GFLs.

From Fig. 6.9b, a disturbance applied to area 1 is found to cause voltage variability much more in area 1 than in area 2. However, a disturbance in area 2 is seen to excite variability in both area 1 and area 2 and especially towards the centre of the system

at bus 8. There is also seen to be significant values of MAMC observed in area 1 in response to a disturbance of the buses between the area 1 SG locations and the central bus 8. Analysis of the most contributing modes for disturbance to observation location, respectively, reveals that: area 1 to area 1 is caused mostly by the $-0.86+j0$ mentioned previously; area 2 to area 2 is caused by an oscillatory mode with very fast damping and value of $140.25 \pm j0.60$, which is related to the ICCs of the GFMs; area 2 to area 1 is a result of the inter-area mode ($-0.38 \pm j3.04$); and finally, the area 1 central region to area 1 more generally is caused by a non-oscillatory mode of value $-14.94 + j0$, related to the AVRs of the SGs.

6.5.5 Influence of Introducing GFLs and GFMs on the Base Case Modes That Contribute Most to Variability

As shown in Sections 6.5.3 and 6.5.4, the introduction of GFLs and GFMs can significantly affect the variability observed in the system in both frequency and voltage. In addition, the dynamic phenomena driving the observed variability can also be different, notably also affected significantly by non-oscillatory modes.

From the frequency variability analysis in Section 6.5.2, two main modes which contributed strongly to variability were identified: the inter-area mode (≈ 0.517 Hz) and the ≈ 0.145 Hz oscillation. Therefore, this subsection looks to establish how the introduction of GFLs and then GFMs to area 2 has impacted these modes. A summary is displayed in Table 6.3. A key observation from this analysis is the potential for very different modal contributions, even when a mode has very similar eigenvalue characteristic (i.e., frequency and damping).

Table 6.3: Influence of introducing GFL and GFM on the key modes of the base case.

	Eigenvalue | Average $AMC_{\Delta\omega}$ ($\times 10^{-3}$)*	
System	**≈0.517 Hz mode**	**≈0.145 Hz mode**
SGs-only	$-0.07 \pm j3.25$ | 0.417	$-1.52 \pm j0.91$ | 12.6
GFLs in area 2	$-1.56 \pm j2.83$ | 8.7	$-1.43 \pm j0.92$ | 6.2
GFMs in area 2	$-0.38 \pm j3.04$ | 0.424	$-1.38 \pm j0.63$ | 24.4

*$AMC_{\Delta\omega}$ = absolute modal contribution to frequency output. Average of which is across all disturbance and observational locations.

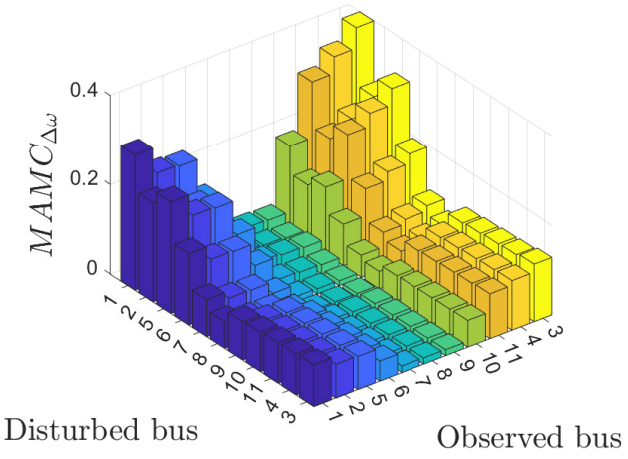

(a)

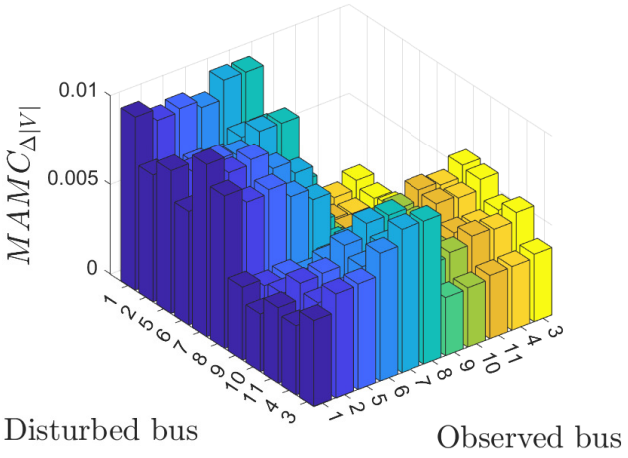

(b)

Figure 6.9: MAMC for bus (a) frequencies and (b) voltage magnitude for an active power disturbance in the system with GFMs in area 2.

GFLs in area 2

The mode that has most similar characteristics to the ≈ 0.517 Hz mode in this case can be seen in Table 6.3 and has PFs showing an interaction between the SGs' rotors and the GFLs' PLLs, APCs, and RPCs. It is noted that this mode has slightly reduced frequency and much better stability margin (real part of mode). Additionally, the corresponding overall contribution, measured as an average of the absolute modal contribution (maximum deviation) across all disturbance and observational locations, is increased in this case compared to the base case (8.7 vs. 0.417). The fact that this mode was not highlighted in Section 6.5.3 highlights the extent to which the non-oscillatory modes were contributing. On the other hand, the ≈ 0.145 Hz mode is still present with PF-derived characteristics similar to those of the base case. However, this mode is found to have less average contribution across all disturbance and observational locations with 6.2 compared to its base case counterpart which has 12.6.

GFMs in area 2

In this case the inter-area mode exists as an interaction between the GFMs' virtual rotors and, to a lesser extent, the SGs' rotors. It is found to have improved stability margin compared to the equivalent in the base case. This also has (slightly) increased average contribution, of 0.424. The mode most similar to the ≈ 0.145 Hz oscillation of the base case, in terms of value and dominant PFs, is the $-1.38 \pm j0.63$ mode mentioned previously. This in fact has increased average contribution as might be expected from its significant influence described in Section 6.5.4.

6.5.6 Variability Over Different Timescales

Swapping the GFMs to area 1 in addition to replacing the static reference calculation in Fig. 6.2 with an IVC[2] revealed a scenario in which the variability across timescales can vary significantly and hence is useful for illustrative purposes. The response of

[2]The proportional and integral gains of the IVC are tuned using the symmetrical optimum technique [244] and have values of 0.0813 pu and 13.9637 pu, respectively. The IVC also has decoupling and feed-forward terms (the latter of which is not present on the ICC in this case to enhance the stability of the system [149]).

the voltage magnitude at each bus in said system is displayed in Fig. 6.10 for a 0.1 pu active power disturbance at bus 1. For around the first second, the responses of the buses in area 1 are dominated by a relatively high frequency oscillation which subsequently damps out leaving a slower oscillation as the dominant mode, as the simulation continues. For the responses in area 2, the higher frequency mode has less of an impact and it is the slower mode that dominates the responses.

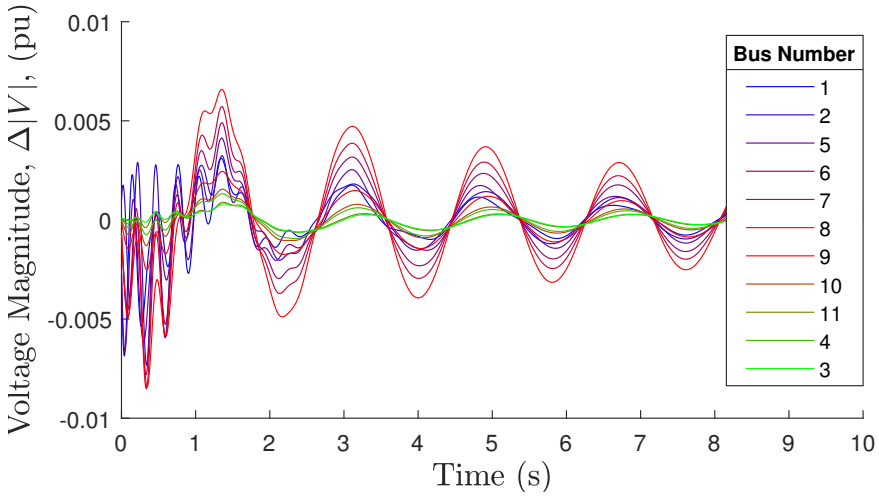

Figure 6.10: Response of voltage magnitude to 0.1 pu active power disturbance at bus 1 in the system with GFMs in area 1.

To highlight the effect of these two distinct timescales, the MAMC is calculated twice: once considering only modes whose damping time constant was 1 s or less and again with consideration only of modes whose damping time constant was above 1 s, i.e., decoupling the fast and slow phenomena shown in Fig. 6.10. The resultant voltage magnitude MAMC for each observed bus is displayed in Fig. 6.11a and Fig. 6.11b for the two scenarios, respectively. For the former case, the variability is observed most in area 1 and the mode most contributing is a relatively high frequency oscillation of value $-1.78 \pm j20.89$ with participation from the GFMs' ICCs and IVCs. The variability observed in area 2 is lesser with the most contributing mode this time found to be the slow inter-area mode. This agrees with the qualitative analysis of the first second of the response in Fig. 6.10. When evaluating Fig. 6.11b it is seen that the maximum variability occurs at the central bus 8 with lesser variability occurring at the generator

locations. The most contributing mode for the observed variability for all buses except bus 3 and 4 have contribution most from the inter-area mode. For bus 3 and bus 4 it is a very low frequency mode of value $-0.48 \pm j0.31$ that impacts the variability the most. Again, this agrees with the qualitative assessment of Fig. 6.10.

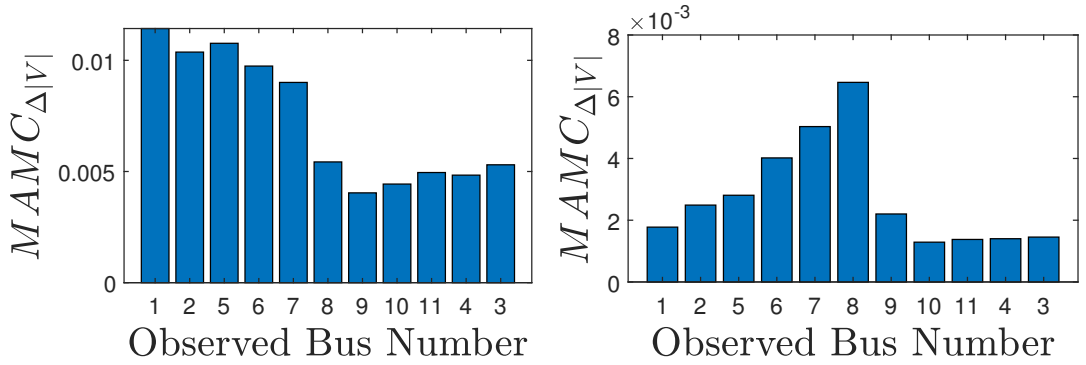

Figure 6.11: MAMC for the voltage magnitude variability at each observed bus in response to a disturbance on bus 1–in the system with GFMs in area 1–for the timescale of (a) less than, and (b) more than 1 s.

Analysis of the MAMC for differing timescales is seen to reflect the changing nature of variability through time as well as allowing us to identify the specific modal interactions that are contributing to the variability at these different timescales. This can offer useful insights, especially for systems with high penetration of converters where higher frequency modes (in particular, SSOs) can appear and become more prominent as seen in real world examples [43].

6.6 Chapter Summary and Conclusions

This chapter has outlined an approach for studying small-signal variability of voltage magnitude or frequency at any given bus, for chosen disturbance locations. A metric is derived called the maximum absolute modal contribution (MAMC), which uses the analytical solution of the individual modal responses. This approach goes beyond typical system static strength metrics, capturing the effect on voltage and frequency variation of complex power system dynamics, in systems with high CIG penetration and different types of control (e.g., GFL and GFM). In particular, it was shown that

the approach will capture, and hence highlight, dynamics which may be neglected using stability metrics such as the damping ratio which can have significant impact on the variability of the output. Additionally, the benefits of the proposed metric not focusing on a single mode are highlighted through the fact that a range of modes can contribute most to the variability at different disturbance and observation locations. The link between the MAMC and the mode contributing most to the variability was used throughout to gain an in-depth understanding of the causes of output variability. Furthermore, the need to investigate voltage magnitude and frequency variability separately, as the proposed method enables, is reinforced by showing distinct differences in frequency/voltage variability trends, driven by different phenomena.

The proposed method and metric is first validated on a simple OMIB system and then applied to the Kundur two-area system. GFLs were then introduced and it was found that the modes contributing most to the variability of voltage magnitude and frequency were often non-oscillatory, strengthening the hypothesis seen in prior literature that these types of eigenvalues may become more influential in CIG-permeated systems. When GFMs were introduced, there was again increased contribution from non-oscillatory modes but to a lesser extent. An interesting finding was that the frequency variability as observed across observation and disturbance locations was similar for the SG-only case and the case when GFMs are introduced. However, when the GFLs are introduced, the frequency variability was much more concentrated for disturbances and observation in the area in which the GFLs were placed. For both scenarios the modes that contributed most to the variability of the output variables were discussed based on their PF characteristics. Further to this, it was shown how the introduction of GFLs or GFMs to the system can influence the contribution that certain modes provide to the output variability, without necessarily altering their frequency and damping characteristics.

Finally, the capability and importance of focusing on different timescales has been studied. Separating the modes included in the variability metric calculation and analysis by damping time constant reveals the different locational variability trends as time evolves. Also, it allows the most influential mode at different time periods to

be identified.

Similar to the PSSA framework presented in Chapter 5, the application of the proposed methodology in this chapter is predicated on the obtainment of the white-box state-space model. As such, it is either applicable for research studies with generic models, or for use by system operators/planners if original equipment manufacturers will share their models (even if in a semi-transparent form such as with impedance circuit models [231]). However, the concepts of small-signal variability more generally can be applied in a wider range of contexts. For example, relevant disturbances can be applied at each bus location, and the corresponding voltage and frequency variability can be measured at each bus, even if the model includes black-box elements. Although less computationally efficient than using the analytical approximation proposed in this chapter, and losing the ability to quantify the contribution of specific modes to the variability, such an approach can still provide vital information with respect to the regulation (or strength) of voltage and frequency across the network.

Furthermore, the system operator/planner could provide the original equipment manufacturer with a range of operating conditions with respect to voltage and frequency variability at the connection point. This would allow the original equipment manufacturer to model the external grid with a more realistic representation of its voltage and frequency dynamics, as opposed to assuming an infinite bus which perfectly regulates both voltage magnitude and frequency.

Ultimately, it is recommended that decoupled voltage and frequency variability, and not just the more abstract concept of grid strength, is taken into account going forward. Furthermore, the impact of modes on the time-domain response is not sufficiently discussed in small-signal analyses, especially considering the evidence in this chapter that modes with high damping may still have a large impact on key power system variables such as voltage and frequency. Adoption of the method and metric proposed in this chapter can help bridge the gap between the dynamic modal characteristics, the grid strength, and the variability of power system variables in the time-domain.

Chapter 7

Conclusions and Future Work

There have been two primary, intertwining paths of study which have been motivated, investigated, and discussed throughout this thesis: the investigation of small-signal interactions in CIG-permeated BPSs; and the development of novel small-signal analysis methodologies accounting for the integration of CIGs in BPSs. The latter has included PSSA to account for operating point stochasticity, and small-signal variability analysis which offers an alternative viewpoint on small-signal grid strength quantification. To facilitate the small-signal modelling, a modular and automatic power system small-signal modelling tool was developed in MATLAB. This chapter summarises the key conclusions observed throughout these investigations in addition to proposing options for continuation or improvement in terms of future work. Additionally, a summary of the CIG-related interactions that were identified throughout this thesis is made available at the end of this chapter in Table 7.1.

7.1 Thesis Summary and Conclusions

Small-Signal Analysis in Converter-Permeated Multi-Machine Systems

The potential for novel multi-machine interactions and the need for targeted eigenvalue-based investigative studies were discussed in Chapter 1.2 and further contextualised with respect to the state-of-the-art in the literature reviews of Chapter 3 and Chapter 4.

Two investigations have been performed which focus directly on multi-machine small-signal interactions involving CIGs. The first of these, found in Chapter 3, performed eigenvalue analyses and parametric sweep sensitivity analyses on a modified version of the IEEE 39-bus system with the addition of bandwidth-restricted GFMs (i.e., GFMs adopting two- or three-level VSCs connected to a transmission-scale BPS). Three key categories of GFM-related interaction were discovered: electromechanical, ICC-related, and IVC-related. The influence on these interactions of varying GFM controller tuning was also investigated. In particular, the IVC-related interactions were highly likely to cause instability, with careful tuning of the IVC PI gains required (note, the reactive power-voltage droop gain also had some capability to improve the damping of these modes). They were close to the origin, and reached a maximum oscillatory frequency of only (approximately) 0.003 rad/s across the sweep of the IVC damping factor. It would be suggested from these results that, for GFMs with restricted control bandwidths, avoidance of the use of an IVC would be preferable (be that through use of DACVC or possibly SILC). More information on the identified interactions from this investigation are found in Table 7.1.

The second multi-machine interaction-based investigation is found in Chapter 4. In this case, a more thorough study of the different control architectures is performed for both GFLs and GFMs (this time adopting conventional tuning approaches with no bandwidth restriction). Two different multi-machine systems are considered, namely a two-machine system (with varying combinations of SG, GFL, and GFM) in addition to the IEEE 9-bus (three-machine) system with a SG, GFL, and GFM generation mixture. Specific interactions present for different controller architectures were detailed (more information can be found in Table 7.1), and the impact of varying transmission line length, system loading, and installed capacities of the connected generators were studied. The first two of which were for the two-machine system only, while the installed capacity variation was performed for both the two-machine and IEEE 9-bus system scenarios. A key overarching conclusion was the fact that very different results can be obtained for different systems, making it difficult to suggest an optimal controller architecture, unless using the very specific systems and scenarios that were studied. For

example, the GFL controller architecture choice was seen to have significant impact on the eigenvalues (including parametric sweep trajectories) for the two-machine system whereas the choice of GFM controller architecture had minimal impact. Contrastingly, the choice of GFM controller architecture was much more influential than that of the GFL on the small-signal stability of the IEEE 9-bus system.

Ultimately, the multi-machine small-signal analysis studies reveal the sensitivity of multi-machine interactions (and their PF-based characteristics) to a multitude of factors, including system parameters and operating points, controller tuning and architectures, network layouts, and so on.

Note, when performing exemplary case studies for the small-signal analysis methodologies developed in this thesis, whose conclusions are discussed in subsequent subsections, several interesting interactions were identified. These are also included in Table 7.1

Probabilistic Small-Signal Analysis with Dynamic Interaction Characterisation

Addressing one of the primary issues identified in Chapter 3 and Chapter 4, a framework is developed in Chapter 5 which enables the identification, characterisation, and probabilistic analysis of key distinct dynamic interactions *which exist across the full range of expected operating conditions* in a CIG-permeated BPS.

Identification of key distinct interactions is achieved using clustering based on eigenvalue PFs, meaning that modes are grouped based on their dynamic characteristics in terms of participating states. In addition to this, a systematic characterisation procedure is developed which includes the introduction of the SWPI to characterise clusters of eigenvalues (i.e., distinct interactions) whereby more importance is given to the modes of the clusters with worse stability margin (based on the real-part of the eigenvalues). Furthermore, having identified and characterised the prevalent dynamic interactions on the system of interest, the probabilistic behaviour can be evaluated: e.g., likelihood of an interaction to be unstable, or even the likelihood of an interaction to exist at all.

The capabilities of the proposed framework are confirmed through case studies utilising the IEEE 68-bus system with the addition of 6 CIGs constituting three scenarios: all GFLs, all GFMs, and a 50/50 split of GFLs and GFMs. Particular CIG-related interactions that are identified and investigated are summarised in Table 7.1. Modal clusters of interest are identified and it is illustrated how the proposed framework can enable analysis of their probabilistic behaviour and SWPI-based characteristics. For example, amongst others, there are modal clusters indicating SSOs (between approximately 5 Hz and 8 Hz) related primarily to interactions involving the IVCs of the GFMs. There are also electromechanical interactions and non-oscillatory modal clusters inducing instability, related mostly to the active power and frequency dynamics of SGs. Empirical cumulative distribution functions were also used to reveal the likelihood of an interaction/cluster to exist for any given operating point, induce instability, or have stability margin below a given threshold.

The complex detail that the proposed framework is able to convey was further exemplified through the case studies whereby only GFMs or only GFLs were connected to the system. In the former case, we observed an increased number of SSOs (again related primarily to IVCs of GFMs), but reduced probability of instability from the electromechanical and non-oscillatory modal clusters. In the case study with only SGs and GFLs, we observed a high frequency modal cluster with low probability to have low stability margin (i.e., low probability, high-risk) related to interactions involving the ICCs and MF&Dr dynamics of the GFLs, in addition to the network dynamics.

Small-Signal Variability Analysis

In response to the reducing validity of conventional static grid strength metrics, discussed in the motivation and literature review of Chapter 6, a method and associated metric are developed in Chapter 6 to quantify the small-signal *variability* (in terms of the maximum deviation) of chosen system output signals, considering an impulse disturbance at each bus. In particular, this is applied to voltage magnitude and frequency (using the frequency divider formula) signals at different bus locations on the system under test. The method is based on the concept of modal superposition for the

free response of a linear system, and hence the decoupling of individual modal responses, thereby incorporating detailed information with regards to the small-signal dynamics of the system, including those of the CIG controllers. The small-signal variability metric is derived based on the analytical calculations of the maximum absolute deviations of the individual modal responses, and is consequently named the maximum absolute modal contribution (MAMC). As a result of these analytical calculations, the contribution of each mode to the small-signal variability of any given output can be determined. This means that, in addition to an overall quantification of small-signal variability, the influence of individual modes (which might represent a multi-machine or multi-element interaction) on the small-signal variability can be determined. Finally, as demonstrated with a case study, the small-signal variability can be quantified along with the extraction of the most influential modes, at different timescales. This is achieved through modal screening based on the damping time constant of the modes/eigenvalues.

The validity of the proposed method and metric are evaluated and confirmed in a OMIB system in addition to Kundur's two-area system. Following this, small-signal variability analysis (of both locational voltage magnitude and frequency) is performed after the introduction of GFLs, and then GFMs. Finally, as previously mentioned, the capability of the approach to extract small-signal variability information, including the most contributing modes/interactions, across different timescales is evaluated. Several CIG-related interactions are highlighted throughout these case studies, as summarised in Table 7.1.

7.2 Future Work

Small-Signal Analysis in Converter-Permeated Multi-Machine Systems

It has been discussed that multi-machine interactions (and their PF-based characteristics) in CIG-permeated power systems are sensitive to a multitude of factors, including system parameters and operating points, controller tuning and architectures, network layouts, and so on. This motivates the direction for future work in which extensive small-signal interaction analyses should be performed across a range of

different systems and operating conditions (e.g., using the proposed framework in Chapter 5), with different CIG controllers, and the inclusion of expected dynamic elements on the power system (e.g., dynamic and converter-interfaced loads, FACTS devices, HVDC interconnectors, etc.).

Expanding on the eigenvalue-based small-signal analysis studies as performed in this thesis, great benefit could be achieved by investigating new interactions from a non-linear perspective. For example, non-linear modal analysis and PFs can enable similar studies while reducing the approximations accompanying small-signal analyses. Meanwhile, analytical studies of non-linear dynamics associated with CIGs should enable better understanding of underlying interaction and instability mechanisms, including from a bifurcation perspective. Furthermore, modern machine-learning models can help in identifying energy functions (e.g., Lyapunov analysis), potentially offering useful insights into the underlying dynamics of CIG-permeated BPSs through examination of energy-exchanges.

Probabilistic Small-Signal Analysis with Dynamic Interaction Characterisation

A potential avenue for future work with respect to the proposed probabilistic small-signal interaction analysis framework in Chapter 5 would be to improve the clustering approach. As it stands, the framework suggests the use of *k-means* clustering along with the *k-means++* seeding approach and the use of multiple initialisations to mitigate issues associated with the sensitivity to the initialisation of cluster centroids. However, although these mitigation approaches are adopted, the repeatability of the results are still not guaranteed using this approach. Furthermore, adoption of the modal PFs of algebraic variables suggested in [220] would likely enable a more intuitive classification approach compared to the manual selection process that is currently adopted for the development of the category-PFs. Additionally, improvements could be made in terms of computational burden through the adoption of efficient sampling techniques and/or development of a more appropriate (i.e., application specific) stopping criterion that can still capture any low-probability, high-risk scenarios.

Small-Signal Variability Analysis

There are several options for the continuation and improvement of the proposed small-signal variability analysis methodology and quantification metric. Firstly, an impulse is considered for the input disturbance but it might be more realistic to consider a step disturbance which would better reflect the actual behaviour of an expected small-signal disturbance on a power system. However, this will require a more complex analytical solution and might obscure the useful link between specific individual modes/interactions and the output variability. Furthermore, the input disturbance applied for the case studies was an active power current injection at each bus. Future work should explore more varied types of input disturbance to observe their influence on the results, potentially leading to the development of a more comprehensive, systematic analysis procedure. Additionally, a potential alternative quantification for variability could be established based on the energy of the signal and decoupled modal responses (e.g., a simple implementation might be the integral squared error of the decoupled modal response from the steady-state value). Such an alternative quantification should be compared to the maximum-deviation implementation adopted in this thesis in terms of accuracy and interpretability.

An important assumption, highlighted several times in Chapter 6, is that the mode whose individual modal response has maximum deviation will resemble the overall output small-signal variability (since the approach uses the former as a proxy measure for the latter). To avoid any potential issues that might arise from this due to constructive and destructive interference of the individual modal responses, the use of modal combination techniques such as those adopted for seismic analysis should be investigated.

7.3 Summary of CIG-Related Interactions

Table 7.1: CIG-related dynamic interactions highlighted throughout the thesis.

Chapter: System Under Test	Observed frequencies	Participating states/variables/elements
3: IEEE 39-bus with GFMs	1.186 Hz to 1.975 Hz	Virtual rotor of VSM-based GFMs and (potentially) rotor of SGs.
3: IEEE 39-bus with GFMs	0 Hz to 0.012 Hz	ICCs of GFMs and (potentially) PSSs and rotor speed of SGs
3: IEEE 39-bus with GFMs	$\approx 1.3 \times 10^{-5}$ Hz	IVCs of GFMs.
4: SG-GFL system	3.199 Hz	PLL and SG damper windings.
4: SG-GFL system	3.74 Hz & 4.822 Hz	PLL and GFL outer active and reactive power controllers.
4: SG-GFL system	0.382 Hz	PLL and GFL outer active and reactive power controllers and SG damper windings.
4: SG-GFL system	0 Hz	Rotor and damper windings of SG with (at low loading) GFL outer controllers and PLL.
4: SG-GFM system	≈ 0.509 Hz	Virtual rotor of GFM and rotor of SG.
4: SG (with AVR and PSS)-GFM system	0 Hz	At low loading: Damper windings and AVR of the SG and the virtual rotor of the GFM.
4: GFM-GFL system	3.661 Hz	GFM virtual rotor and PLL of the GFL.
4: GFM-GFL system	3.740 Hz & 4.997 Hz	PLL and GFL outer active and reactive power controllers.
4: GFM-GFL system	1.464 Hz	PLL and GFL outer active and reactive power controllers and GFM virtual rotor.
4: GFM-GFM system	1.783 Hz	Virtual rotors of two GFMs.
4: IEEE 9-bus with SG, GFL, & GFM	0 Hz	PLL and outer controllers of the GFL.
4: IEEE 9-bus with SG, GFL, & GFM	$>$ 2 kHz	Output LC filter of the GFM.
4: IEEE 9-bus with SG, GFL, & GFM	9.46 Hz to 12.53 Hz	APC, VMC, and IVC of the GFM.
5: IEEE 68-bus with GFMs, SGs, & (with or without) GFLs	≈ 5 Hz $-$ 8.5 Hz	IVCr dynamics of GFMs and (to a lesser extent) P-F, Q-V, and network dynamics.
5: IEEE 68-bus with GFMs (with slowed IVCs), & SGs	≈ 3 Hz	IVCr and P-F dynamics involving both GFMs and SGs.
5: IEEE 68-bus with GFLs, & SGs	≈ 116 Hz	Network, MF&Dr, and ICCr dynamics with involvement of GFLs.
6: Kundur's 2-area system with GFLs in area 2	0 Hz	PLLs and APCs of GFLs.
6: Kundur's 2-area system with GFLs in area 2	0 Hz	APCs of the GFLs.
6: Kundur's 2-area system with GFLs in area 2	0.450 Hz	Rotors of the SGs, and the PLLs, APCs, and RPCs of the GFLs.
6: Kundur's 2-area system with GFMs in area 2	0 Hz	AVRs and damper windings of the SGs, and the virtual rotors of the GFMs.
6: Kundur's 2-area system with GFMs in area 2	0.100 Hz	AVRs and damper windings, and rotors of the SGs, and the virtual rotors of the GFMs.
6: Kundur's 2-area system with GFMs in area 2	0.484 Hz	Virtual rotors of the GFMs and rotors of the SGs.
6: Kundur's 2-area system with GFMs in area 2	0.095 Hz	ICCs of the GFMs.
6: Kundur's 2-area system with GFMs in area 1	3.325 Hz	ICCs and IVCs of the GFMs.

Acronyms are used due to limited space. Cross-reference with the List of Abbreviations in the front matter.

Bibliography

[1] Intergovernmental Panel on Climate Change (IPCC), *Climate Change 2022: Impacts, Adaptation and Vulnerability*, H.-O. Pörtner, D. Roberts, M. Tignor, E. Poloczanska, K. Mintenbeck, A. Alegría, M. Craig, S. Langsdorf, S. Löschke, V. Möller, A. Okem, and B. Rama, et al., Eds. UK and New York, NY, USA: Cambridge University Press, 2022. [Online]. Available: https://www.ipcc.ch/report/ar6/wg2/

[2] Climate Change Committee (CCC), "Independent assessment of the third national adaptation programme (NAP3)," UK, 2023. [Online]. Available: https://www.theccc.org.uk/publication/independent-assessment-of-the-third-national-adaptation-programme/

[3] United Nations Environment Programme (UNEP), "Emissions Gap Report 2023: Broken Record - Temperatures hit new highs, yet world fails to cut emissions (again)," Nairobi, 2023, doi:10.59117/20.500.11822/43922.

[4] International Energy Agency (IEA), "Renewables 2024," Paris, October 2024, License: CC BY 4.0. [Online]. Available: https://www.iea.org/reports/renewables-2024

[5] J. Z. Zhou, H. Ding, S. Fan, Y. Zhang, and A. M. Gole, "Impact of short-circuit ratio and phase-locked-loop parameters on the small-signal behavior of a VSC-HVDC converter," *IEEE Transactions on Power Delivery*, vol. 29, no. 5, pp. 2287–2296, 2014, doi:10.1109/TPWRD.2014.2330518.

[6] Y. Li, Y. Gu, and T. C. Green, "Revisiting grid-forming and grid-following inverters: A duality theory," *IEEE Transactions on Power Systems*, vol. 37, no. 6, pp. 4541–4554, 2022, doi:10.1109/TPWRS.2022.3151851.

[7] D. A. Kez, A. M. Foley, and D. J. Morrow, "Analysis of fast frequency response allocations in power systems with high system non-synchronous penetrations," *IEEE Transactions on Industry Applications*, vol. 58, no. 3, pp. 3087–3101, 2022, doi:10.1109/TIA.2022.3160997.

[8] M. Céspedes and J. Sun, "Impedance shaping of three-phase grid-parallel voltage-source converters," in *2012 Twenty-Seventh Annual IEEE Applied Power Electronics Conference and Exposition (APEC)*, 2012, pp. 754–760, doi:10.1109/APEC.2012.6165904.

[9] X. Wang, Y. W. Li, S. Member, and F. Blaabjerg, "Virtual-impedance-based control for voltage-source and current-source converters," *IEEE Transactions on Power Electronics*, vol. 30, no. 12, pp. 7019–7037, 2015, doi:10.1109/TPEL.2014.2382565.

[10] P. S. Kundur, *Power System Stability and Control*. New York: McGraw-Hill, 1994.

[11] P. W. Sauer and M. A. Pai, *Power System Dynamics and Stability*. The University of Illinois, 1997. [Online]. Available: https://courses.engr.illinois.edu/ece576/sp2018/SauerandPaibook-Jan2007.pdf

[12] F. Milano, *Power System Modelling and Scripting*. Berlin, Heidelberg: Springer Berlin Heidelberg, 2010, doi:10.1007/978-3-642-13669-6_4.

[13] K. Ogata, *Modern Control Engineering*, 5th ed. Upper Saddle River, New Jersey: Prentice Hall, 2010.

[14] M. Cheah-Mane, A. Egea-Àlvarez, E. Prieto-Araujo, H. Mehrjerdi, O. Gomis-Bellmunt, and L. Xu, "Modeling and analysis approaches for small-signal

stability assessment of power-electronic-dominated systems," *WIREs Energy and Environment*, vol. 12, no. 1, p. e453, 2023, doi:10.1002/wene.453.

[15] E. Rokrok, T. Qoria, A. Bruyere, B. Francois, and X. Guillaud, "Classification and dynamic assessment of droop-based grid-forming control schemes: Application in HVDC systems," *Electric Power Systems Research*, vol. 189, p. 106765, 2020.

[16] J. V. Milanović, "Probabilistic stability analysis: The way forward for stability analysis of sustainable power systems," *Philosophical Transactions of the Royal Society A*, vol. 375, no. 2100, 2017, doi:10.1098/rsta.2016.0296.

[17] A. M. Hakami, K. N. Hasan, M. Alzubaidi, and M. Datta, "A review of uncertainty modelling techniques for probabilistic stability analysis of renewable-rich power systems," *Energies*, vol. 16, no. 1, 2023, doi:10.3390/en16010112.

[18] S. Q. Bu, W. Du, and H. F. Wang, "Investigation on probabilistic small-signal stability of power systems as affected by offshore wind generation," *IEEE Transactions on Power Systems*, vol. 30, no. 5, pp. 2479–2486, 2015.

[19] R. Preece and J. V. Milanović, "Efficient estimation of the probability of small-disturbance instability of large uncertain power systems," *IEEE Transactions on Power Systems*, vol. 31, no. 2, pp. 1063–1072, 2016.

[20] M. Maharjan, A. Ekic, and D. Wu, "Probabilistic grid strength assessment of power systems with uncertain renewable generation based on probabilistic collocation method," in *2022 17th International Conference on Probabilistic Methods Applied to Power Systems (PMAPS)*, Manchester, UK, 2022.

[21] H. Gholami-Khesht, P. Davari, M. Novak, and F. Blaabjerg, "A probabilistic framework for the robust stability and performance analysis of grid-tied voltage source converters," *Applied Sciences*, vol. 12, no. 15, 2022.

[22] R. F. Mochamad, R. Preece, and K. N. Hasan, "Probabilistic multi-stability operational boundaries in power systems with high penetration of power

electronics," *International Journal of Electrical Power & Energy Systems*, vol. 135, p. 107382, 2022.

[23] R. Cao, J. Xing, Z. Li, and H. Ma, "Probabilistic small signal stability analysis with wind power based on maximum entropy theory," *Electric Power Components and Systems*, pp. 1–12, 2024, doi:10.1080/15325008.2024.2310775.

[24] G. Wang, H. Xin, D. Wu, and P. Ju, "Data-driven probabilistic small signal stability analysis for grid-connected PV systems," *International Journal of Electrical Power & Energy Systems*, vol. 113, pp. 824–831, 2019.

[25] P. Pareek and H. D. Nguyen, "Probabilistic robust small-signal stability framework using gaussian process learning," *Electric Power Systems Research*, vol. 188, p. 106545, 2020, doi:10.1016/j.epsr.2020.106545.

[26] C. Henderson, A. Egea-Àlvarez, T. Kneuppel, G. Yang, and L. Xu, "Grid strength impedance metric: An alternative to SCR for evaluating system strength in converter dominated systems," *IEEE Transactions on Power Delivery*, vol. 39, no. 1, pp. 386–396, 2024, doi:10.1109/TPWRD.2022.3233455.

[27] W. Dong, H. Xin, D. Wu, and L. Huang, "Small signal stability analysis of multi-infeed power electronic systems based on grid strength assessment," *IEEE Transactions on Power Systems*, vol. 34, no. 2, pp. 1393–1403, 2019.

[28] C. Liu, H. Xin, D. Wu, H. Gao, H. Yuan, and Y. Zhou, "Generalized operational short-circuit ratio for grid strength assessment in power systems with high renewable penetration," *IEEE Transactions on Power Systems*, vol. 39, no. 4, pp. 5479–5494, 2024, doi:10.1109/TPWRS.2023.3340158.

[29] Y. Zhu, T. C. Green, X. Zhou, Y. Li, D. Kong, and Y. Gu, "Impedance margin ratio: A new metric for small-signal system strength," *IEEE Transactions on Power Systems*, vol. 39, no. 6, pp. 7291–7303, 2024, doi:10.1109/TPWRS.2024.3371231.

[30] M. Paolone, T. Gaunt, X. Guillaud, M. Liserre, S. Meliopoulos, A. Monti, T. Van Cutsem, V. Vittal, and C. Vournas, "Fundamentals of power systems modelling in the presence of converter-interfaced generation," *Electric Power Systems Research*, vol. 189, p. 106811, 2020, doi:10.1016/j.epsr.2020.106811.

[31] U. Markovic, O. Stanojev, P. Aristidou, and G. Hug, "Partial grid forming concept for 100% inverter-based transmission systems," in *2018 IEEE Power & Energy Society General Meeting (PESGM)*, Portland, OR, USA, 2018, pp. 1–5, doi:10.1109/PESGM.2018.8586114.

[32] N. Hatziargyriou, J. V. Milanović, C. Rahmann, V. Ajjarapu, C. Cañizares, I. Erlich, D. J. Hill, I. Hiskens, I. Kamwa, B. Pal, P. Pourbeik, J. J. Sanchez-Gasca, A. M. Stankovic, T. V. Cutsem, V. Vittal, and C. Vournas, "Stability definitions and characterization of dynamic behavior in systems with high penetration of power electronic interfaced technologies," IEEE PES, Tech. Rep., 2020, PES-TR77. [Online]. Available: https://resourcecenter.ieee-pes.org/publications/technical-reports/pes_tp_tr77_psdp_stability_051320

[33] N. Hatziargyriou, J. V. Milanović, C. Rahmann, V. Ajjarapu, C. Cañizares, I. Erlich, D. Hill, I. Hiskens, I. Kamwa, B. Pal, P. Pourbeik, J. J. Sanchez-Gasca, A. Stanković, T. V. Cutsem, V. Vittal, and C. Vournas, "Definition and classification of power system stability – revisited & extended," *IEEE Transactions on Power Systems*, vol. 6, no. 4, pp. 3271 – 3281, 2021, doi:10.1109/TPWRS.2020.3041774.

[34] V. Sewdien, X. Wang, J. R. Torres, and M. V. D. Meijden, "Critical review of mitigation solutions for SSO in modern transmission grids," *Energies*, vol. 13, no. 13, 2020, doi:10.3390/en13133449.

[35] J. Shair, H. Li, J. Hu, and X. Xie, "Power system stability issues, classifications and research prospects in the context of high-penetration of renewables and power electronics," *Renewable and Sustainable Energy Reviews*, vol. 145, p. 111111, 2021, doi:10.1016/j.rser.2021.111111.

[36] P. Kundur, J. Paserba, V. Ajjarapu, G. Andersson, A. Bose, C. Canizares, N. Hatziargyriou, D. Hill, A. Stankovic, C. Taylor, T. Van Cutsem, and V. Vittal, "Definition and classification of power system stability IEEE/CIGRE joint task force on stability terms and definitions," *IEEE Transactions on Power Systems*, vol. 19, no. 3, pp. 1387–1401, 2004, doi:10.1109/TPWRS.2004.825981.

[37] X. Xie, X. Zhang, H. Liu, H. Liu, Y. Li, and C. Zhang, "Characteristic analysis of subsynchronous resonance in practical wind farms connected to series-compensated transmissions," *IEEE Transactions on Energy Conversion*, vol. 32, no. 3, pp. 1117–1126, 2017, doi:10.1109/TEC.2017.2676024.

[38] Y. Gu and T. C. Green, "Power system stability with a high penetration of inverter-based resources," *Proceedings of the IEEE*, vol. 111, no. 7, pp. 832–853, 2023, doi:10.1109/JPROC.2022.3179826.

[39] C. Eckel, D. Babazadeh, and C. Becker, "Classification of converter-driven stability and suitable modelling and analysis methods," *IEEE Access*, vol. 12, pp. 53 056–53 073, 2024, doi:10.1109/ACCESS.2024.3388098.

[40] Energy Systems Integration Group, "Diagnosis and mitigation of observed oscillations in IBR-dominant power systems: A practical guide," Reston, VA, Tech. Rep., 2024. [Online]. Available: https://www.esig.energy/oscillations-guide/

[41] M. Hurtado, M. Jafarian, T. Kërçi, S. Tweed, M. V. Escudero, E. Kennedy, and F. Milano, "Stability assessment of low-inertia power systems: A system operator perspective," in *2024 IEEE Power & Energy Society General Meeting (PESGM)*, Seattle, WA, USA, 2024, pp. 1–5, doi:10.1109/PESGM51994.2024.10688904.

[42] CIGRE JWG C4/B4.52, "Guidelines for Subsynchronous Oscillation Studies in Power Electronics Dominated Power Systems," Tech. Rep., June 2023, Technical Brochure Reference 909.

[43] Y. Cheng, L. Fan, J. Rose, S.-H. Huang, J. Schmall, X. Wang, X. Xie, J. Shair, J. R. Ramamurthy, N. Modi, C. Li, C. Wang, S. Shah, B. Pal, Z. Miao,

A. Isaacs, J. Mahseredjian, and J. Zhou, "Real-world subsynchronous oscillation events in power grids with high penetrations of inverter-based resources," *IEEE Transactions on Power Systems*, vol. 38, no. 1, pp. 316–330, 2023, doi:10.1109/TPWRS.2022.3161418.

[44] National Grid Electricity System Operator, "ESO Operational Transparency Forum 08 November 2023," November 2023, Delivery Format: Webinar. Slides accessed on: March 18, 2024. [Online]. Available: https://www.nationalgrideso.com/what-we-do/electricity-national-control-centre/operational-transparency-forum

[45] ——, "Operability Strategy Report 2023," Tech. Rep., December 2023, Accessed on: March 18, 2024. [Online]. Available: https://www.nationalgrideso.com/news/operability-strategy-report-2023

[46] National Grid Electricity System Operator (NGESO), "System oscillation assessment of inverter based resources (IBRs)," NGESO, Tech. Rep., January 2024, accessed: October 4, 2024. [Online]. Available: https://www.neso.energy/document/301686/download

[47] Australian Energy Market Operator (AEMO) System Operations, "Power system stability guidelines," AEMO, Tech. Rep., December 2022, accessed: October 4, 2024. [Online]. Available: https://aemo.com.au/-/media/files/electricity/nem/security_and_reliability/congestion-information/power-system-stability-guidelines.pdf?la=en

[48] J. Shair, X. Xie, L. Wang, W. Liu, J. He, and H. Liu, "Overview of emerging subsynchronous oscillations in practical wind power systems," *Renewable and Sustainable Energy Reviews*, vol. 99, pp. 159–168, 2019, doi:10.1016/j.rser.2018.09.047. [Online]. Available: https://www.sciencedirect.com/science/article/pii/S1364032118306956

[49] Y. Cheng, L. Fan, J. Rose, J. Schmall, F. Huang, J. R. Ramamurthy, A. Mulawarman, P. G. Mysore, Z. Miao, Y. Li, Y. Xu, M. Zhang, S. Shah,

P. Koralewicz, R. Wallen, V. Gevorgian, F. Salehi, M. Tabrizi, W.-J. Lee, X. Xie, A. Issac, A. Dissanayaka, P. Zadkhast, D. Howard, L. Xu, M. Lwin, A. Goharrizi, B. Pal, H. R. Ali, L. Kunjumuhammed, J. Sun, Y. Gong, U. Karaagac, J. Mahseredjian, I. Kocar, A. Trevisan, H. Gras, and R. Gagnon, "Wind energy systems sub-synchronous oscillations: Events and modeling," 2020, Technical Report PES-TR80. [Online]. Available: https://resourcecenter.ieee-pes.org/publications/technical-reports/pes_tp_tr80_amps_wsso_070920#

[50] L. Fan, Z. Miao, S. Shah, Y. Cheng, J. Rose, S.-H. Huang, B. Pal, X. Xie, N. Modi, S. Wang, and S. Zhu, "Real-world 20-Hz IBR subsynchronous oscillations: Signatures and mechanism analysis," *IEEE Transactions on Energy Conversion*, vol. 37, no. 4, pp. 2863–2873, 2022, doi:10.1109/TEC.2022.3206795.

[51] N. Verma, N. Kumar, S. Gupta, H. Malik, and F. P. García-Márquez, "Review of sub-synchronous interaction in wind integrated power systems: classification, challenges, and mitigation techniques," *Protection and Control of Modern Power Systems*, vol. 8, no. 1, 2023, doi:10.1186/s41601-023-00291-0.

[52] X. Xie and J. Shair, *Oscillatory Stability of Converter-Dominated Power Systems*. Gewerbestrasse 11, 6330 Cham, Switzerland: Springer, 2024, doi:10.1007/978-3-031-53357-0.

[53] C. Duggan, X. Liu, P. Brogan, R. Best, and D. J. Morrow, "Very low-frequency oscillation source localization on ireland's power system," *IEEE Open Journal of Industry Applications*, vol. 3, pp. 192–201, 2022, doi:10.1109/OJIA.2022.3194140.

[54] C. Li, "Unstable operation of photovoltaic inverter from field experiences," *IEEE Transactions on Power Delivery*, vol. 33, no. 2, pp. 1013–1015, 2018, doi:10.1109/TPWRD.2017.2656020.

[55] Australian Energy Market Operator (AEMO), "West murray zone sub-synchronous oscillations: National electricity market summary of real-time observations from august 2020 to december 2021," October 2022.

[56] C. Mishra, C. Wang, L. Vanfretti, and K. Jones, "IBR oscillations in the dominion energy system," March 2022, presentation slides. [Online]. Available: https://www.naspi.org/sites/default/files/2022-04/03_20220411_naspi_workshop_chetan.pdf

[57] A. Pepiciello and J. L. Domínguez-García, "Small-signal stability analysis of uncertain power systems: A comprehensive survey," *Renewable and Sustainable Energy Reviews*, vol. 200, p. 114576, 2024.

[58] National Grid ESO, "National Grid ESO Data Portal," https://data.nationalgrideso.com/, accessed Jul. 17, 2024.

[59] U. Markovic, O. Stanojev, P. Aristidou, E. Vrettos, D. Callaway, and G. Hug, "Understanding small-signal stability of low-inertia systems," *IEEE Transactions on Power Systems*, vol. 36, no. 5, pp. 3997–4017, 2021, doi:10.1109/TPWRS.2021.3061434.

[60] J. Rocabert, A. Luna, F. Blaabjerg, and P. Rodríguez, "Control of power converters in AC microgrids," *IEEE Transactions on Power Electronics*, vol. 27, no. 11, pp. 4734–4749, 2012, doi:10.1109/TPEL.2012.2199334.

[61] B. Bahrani, M. H. Ravanji, B. Kroposki, D. Ramasubramanian, X. Guillaud, T. Prevost, and N.-A. Cutululis, "Grid-forming inverter-based resource research landscape: Understanding the key assets for renewable-rich power systems," *IEEE Power and Energy Magazine*, vol. 22, no. 2, pp. 18–29, 2024, doi:10.1109/MPE.2023.3343338.

[62] A. Hoke, J. C. Boemer, B. Badrzadeh, J. MacDowell, D. Kurthakoti, B. Marszalkowski, and M. Meuser, "Foundations for the future power system: Inverter-based resource interconnection standards," *IEEE Power and Energy Magazine*, vol. 22, no. 2, pp. 42–54, 2024, doi:10.1109/MPE.2023.3341795.

[63] M. Tozak, S. Taskin, I. Sengor, and B. P. Hayes, "Modeling and control of grid forming converters: A systematic review," *IEEE Access*, vol. 12, pp. 107 818–107 843, 2024, doi:10.1109/ACCESS.2024.3437236.

[64] J. Matevosyan, J. MacDowell, N. Miller, B. Badrzadeh, D. Ramasubramanian, A. Isaacs, R. Quint, E. Quitmann, R. Pfeiffer, H. Urdal, T. Prevost, V. Vittal, D. Woodford, S. H. Huang, and J. O'Sullivan, "A future with inverter-based resources: Finding strength from traditional weakness," *IEEE Power and Energy Magazine*, vol. 19, no. 6, pp. 18–28, 2021, doi:10.1109/MPE.2021.3104075.

[65] J. Matevosyan, B. Badrzadeh, T. Prevost, E. Quitmann, D. Ramasubramanian, H. Urdal, S. Achilles, J. MacDowell, S. Hsien Huang, V. Vital, J. O'Sullivan, and R. Quint, "Grid-forming inverters: Are they the key for high renewable penetration?" *IEEE Power and Energy Magazine*, vol. 21, no. 2, pp. 77–86, 2023, doi:10.1109/MPAE.2023.10083082.

[66] B. Badrzadeh, C. Cardozo, M. Hishida, S. Shah, I. Huq, N. Modi, and A. Morton, "Grid-forming inverters: Project demonstrations and pilots," *IEEE Power and Energy Magazine*, vol. 22, no. 2, pp. 66–77, 2024, doi:10.1109/MPE.2023.3342766.

[67] R. Musca, A. Vasile, and G. Zizzo, "Grid-forming converters. a critical review of pilot projects and demonstrators," *Renewable and Sustainable Energy Reviews*, vol. 165, p. 112551, 2022, doi:10.1016/j.rser.2022.112551.

[68] North American Electric Reliability Corporation (NERC), "White paper: Grid forming functional specifications for BPS-connected battery energy storage systems," NERC, White Paper, September 2023. [Online]. Available: https://www.nerc.com/comm/RSTC_Reliability_Guidelines/White_Paper_GFM_Functional_Specification.pdf

[69] ——, "Grid forming technology: Bulk power system reliability considerations," NERC, Tech. Rep., December 2021, accessed: September 17, 2024. [Online]. Available: https://www.nerc.com/comm/RSTC_Reliability_Guidelines/White_Paper_Grid_Forming_Technology.pdf

[70] H. Luo, Y. Xiao, Y. Zhu, Y. Yang, N. P. Papanikolaou, and M. Molinas, "A review of recent requirements for inverter-based resources and grid-forming technologies," in *2023 25th European Conference on*

Power Electronics and Applications (EPE'23 ECCE Europe), 2023, doi:10.23919/EPE23ECCEEurope58414.2023.10264649.

[71] C. R. Shah, M. Molinas, R. Nilsen, and M. Amin, "Limitations in impedance reshaping of grid forming converters for instability prevention," in *2023 IEEE International Future Energy Electronics Conference (IFEEC)*, 2023, pp. 526–531, doi:10.1109/IFEEC58486.2023.10458509.

[72] National Grid ESO, "GC0137: Minimum Specification Required for Provision of GB Grid Forming (GBGF) Capability (formerly Virtual Synchronous Machine/VSM Capability)," November 2021, accessed: September 17, 2024. [Online]. Available: https://www.nationalgrideso.com/industry-information/codes/gc/modifications/gc0137-minimum-specification-required-provision-gb-grid-forming-gbgf-capability-formerly-virtual-synchronous-machinevsm-capability

[73] V. Häberle, L. Huang, X. He, E. Prieto-Araujo, and F. Dörfler, "Dynamic ancillary services: From grid codes to transfer function-based converter control," *Electric Power Systems Research*, vol. 234, p. 110760, 2024, doi:10.1016/j.epsr.2024.110760.

[74] X. Wang, M. G. Taul, H. Wu, Y. Liao, F. Blaabjerg, and L. Harnefors, "Grid-synchronization stability of converter-based resources—an overview," *IEEE Open Journal of Industry Applications*, vol. 1, pp. 115–134, 2020, doi:10.1109/ojia.2020.3020392.

[75] M. A. Desai, X. He, L. Huang, and F. Dörfler, "Saturation-informed current-limiting control for grid-forming converters," *Electric Power Systems Research*, vol. 234, p. 110746, 2024, doi:10.1016/j.epsr.2024.110746.

[76] X. He, M. A. Desai, L. Huang, and F. Dörfler, "Cross-forming control and fault current limiting for grid-forming inverters," *IEEE Transactions on Power Electronics*, vol. 40, no. 3, pp. 3980–4007, 2025, doi:10.1109/TPEL.2024.3500885.

[77] C. Ai, Y. Li, Z. Zhao, Y. Gu, and J. Liu, "An extension of grid-forming: A frequency-following voltage-forming inverter," *IEEE Transactions*

on Power Electronics, vol. 39, no. 10, pp. 12 118–12 123, 2024, doi:10.1109/TPEL.2024.3387705.

[78] T. Qoria, H. Wu, X. Wang, and I. Colak, "Variable virtual impedance-based overcurrent protection for grid-forming inverters: Small-signal, large-signal analysis and improvement," *IEEE Transactions on Smart Grid*, vol. 14, no. 5, pp. 3324–3336, 2023, doi:10.1109/TSG.2022.3232987.

[79] A. D. Paquette and D. M. Divan, "Virtual impedance current limiting for inverters in microgrids with synchronous generators," *IEEE Transactions on Industry Applications*, vol. 51, no. 2, pp. 1630–1638, 2015, doi:10.1109/TIA.2014.2345877.

[80] A. Thant, H. Ma, A. Isaacs, L. Unruh, R. Quint, D. Ramasubramanian, J. Matevosyan, and A. Hoke, "Grid forming functional specifications and verification tests for north american bulk power system connected battery energy storage systems," in *CIGRE Paris Session 2024*. Paris, France: CIGRE, August 2024.

[81] J. D. Lara, R. Henriquez-Auba, D. Ramasubramanian, S. Dhople, D. S. Callaway, and S. Sanders, "Revisiting power systems time-domain simulation methods and models," *IEEE Transactions on Power Systems*, vol. 39, no. 2, pp. 2421–2437, 2024, doi:10.1109/TPWRS.2023.3303291.

[82] D. Groß, M. Colombino, J.-S. Brouillon, and F. Dorfler, "The effect of transmission-line dynamics on grid-forming dispatchable virtual oscillator control," *IEEE Transactions on Control of Network Systems*, vol. 6, no. 3, pp. 1148–1160, 2019, doi:10.1109/TCNS.2019.2921347.

[83] D. Ramasubramanian, L. Yu, Y. Cheng, R. Majumder, A. Isaacs, A. Shattuck, and S. Pant, "Techniques and methods for validation of inverter-based resource unit and plant simulation models across multiple simulation domains: An engineering judgment-based approach," *IEEE Power and Energy Magazine*, vol. 22, no. 2, pp. 55–65, 2024, doi:10.1109/MPE.2023.3343679.

[84] S. Li, J. Bélanger, M. Cervantes Martinez, M. Kazemtabrizi, J.-N. Paquin, V. Lapointe, W. Li, and J. Paez-Alvarez, "Accelerated and online electromagnetic transient simulations: Key for swift and accurate stability analysis in large-scale low-inertia power systems," *IEEE Power and Energy Magazine*, vol. 22, no. 2, pp. 110–118, 2024, doi:10.1109/MPE.2023.3346365.

[85] L. Karunaratne, N. R. Chaudhuri, A. Yogarathnam, and M. Yue, "On modeling adequacy and stability analysis of IBR-related subsynchronous oscillations in multimachine systems," *arXiv*, 2024, doi:10.48550/arXiv.2403.07835.

[86] V. A. Lacerda, E. P. Araujo, M. Cheah-Mañe, and O. Gomis-Bellmunt, "Phasor modeling approaches and simulation guidelines of voltage-source converters in grid-integration studies," *IEEE Access*, vol. 10, pp. 51 826–51 838, 2022, doi:10.1109/ACCESS.2022.3174958.

[87] G. De Carne, M. Langwasser, M. Ndreko, R. Bachmann, R. W. De Doncker, R. Dimitrovski, B. J. Mortimer, A. Neufeld, F. Rojas, and M. Liserre, "Which deepness class is suited for modeling power electronics?: A guide for choosing the right model for grid-integration studies," *IEEE Industrial Electronics Magazine*, vol. 13, no. 2, pp. 41–55, 2019, doi:10.1109/MIE.2019.2909799.

[88] K. Sano, S. Horiuchi, and T. Noda, "Comparison and selection of grid-tied inverter models for accurate and efficient EMT simulations," *IEEE Transactions on Power Electronics*, vol. 37, no. 3, pp. 3462–3472, 2022, doi:10.1109/TPEL.2021.3117633.

[89] G. Misyris, S. Chatzivasileiadis, and T. Weckesser, "Zero-inertia systems: Sufficient conditions for phasor modeling," *arXiv*, 2020, doi:10.48550/arXiv.2002.11209.

[90] G. S. Misyris, S. Chatzivasileiadis, and T. Weckesser, "Grid-forming converters: Sufficient conditions for rms modeling," *Electric Power Systems Research*, vol. 197, p. 107324, 2021, doi:10.1016/j.epsr.2021.107324.

[91] P. Vorobev, P.-H. Huang, M. Al Hosani, J. L. Kirtley, and K. Turitsyn, "High-fidelity model order reduction for microgrids stability assessment," *IEEE Transactions on Power Systems*, vol. 33, no. 1, pp. 874–887, 2018, doi:10.1109/TPWRS.2017.2707400.

[92] Q. Huang, D. Ramasubramanian, V. Vittal, B. Keel, and J. Silva, "Effect of accurate modelling of converter interfaced generation on a practical bulk power system," *IET Generation, Transmission and Distribution*, vol. 14, no. 15, p. 3108 – 3116, 2020.

[93] D. Ramasubramanian, Z. Yu, R. Ayyanar, V. Vittal, and J. Undrill, "Converter model for representing converter interfaced generation in large scale grid simulations," *IEEE Transactions on Power Systems*, vol. 32, no. 1, pp. 765–773, 2017, doi:10.1109/TPWRS.2016.2551223.

[94] D. Ramasubramanian, P. Pourbeik, E. Farantatos, and A. Gaikwad, "Simulation of 100% inverter-based resource grids with positive sequence modeling," *IEEE Electrification Magazine*, vol. 9, no. 2, pp. 62–71, 2021, doi:10.1109/MELE.2021.3070938.

[95] J. Chow, J. Winkelman, M. Pai, and P. Sauer, "Singular perturbation analysis of large-scale power systems," *International Journal of Electrical Power & Energy Systems*, vol. 12, no. 2, pp. 117–126, 1990, doi:10.1016/0142-0615(90)90007-X.

[96] J. Belikov and Y. Levron, "Uses and misuses of quasi-static time-varying phasor models in power systems," *IEEE Transactions on Power Delivery*, vol. 33, no. 6, pp. 3263–3266, 2018, doi:10.1109/TPWRD.2018.2852950.

[97] X. Guo, Z. Lu, B. Wang, X. Sun, L. Wang, and J. M. Guerrero, "Dynamic phasors-based modeling and stability analysis of droop-controlled inverters for microgrid applications," *IEEE Transactions on Smart Grid*, vol. 5, no. 6, pp. 2980–2987, 2014, doi:10.1109/TSG.2014.2331280.

[98] J. Belikov and Y. Levron, "Comparison of time-varying phasor and dq0 dynamic models for large transmission networks," *International Journal*

of Electrical Power & Energy Systems, vol. 93, pp. 65–74, 2017, doi:10.1016/j.ijepes.2017.05.017.

[99] G. Grdenić, M. Delimar, and J. Beerten, "Chapter 9 - AC grid modeling in power electronics-based power systems for eigenvalue stability studies," in *Power Systems Operation with 100% Renewable Energy Sources*, S. Chenniappan, S. Padmanaban, and S. Palanisamy, Eds. Elsevier, 2024, pp. 131–147, doi:10.1016/B978-0-443-15578-9.00006-6.

[100] Y. Chen, L. Benedetti, R. Preece, P. N. Papadopoulos, M. Barnes, and A. Egea-Àlvarez, "Investigating small-disturbance stability in power systems with grid-following and grid-forming VSCs using hybrid modelling approaches," *Electric Power Systems Research*, vol. 211, p. 108448, 2022, doi:10.1016/j.epsr.2022.108448.

[101] T. Demiray, "Simulation of power system dynamics using dynamic phasor models," Ph.D. dissertation, Swiss Federal Institute of Technology (ETH) Zurich, Zurich, Switzerland, 2008.

[102] G. Grdenić, F. J. C. García, N. d. M. D. Campos, F. Villella, and J. Beerten, "Model order reduction of voltage source converters based on the AC side admittance assessment: From EMT to RMS," *IEEE Transactions on Power Delivery*, vol. 38, no. 1, pp. 56–67, 2023, doi:10.1109/TPWRD.2022.3179836.

[103] A. Egea-Àlvarez, A. Junyent-Ferré, and O. Gomis-Bellmunt, "Active and reactive power control of grid connected distributed generation systems," in *Modeling and Control of Sustainable Power Systems*, 2012, pp. 47–81.

[104] S. H. Strogatz, *Nonlinear Dynamics and Chaos: With Applications to Physics, Biology, Chemistry and Engineering.* Westview Press, 2000.

[105] Q. Chen, S. Bu, and C. Y. Chung, "Small-signal stability criteria in power electronics-dominated power systems: A comparative review," *Journal of Modern Power Systems and Clean Energy*, vol. 12, no. 4, pp. 1003–1018, 2024, doi:10.35833/MPCE.2023.000526.

[106] M. Amin and M. Molinas, "Small-signal stability assessment of power electronics based power systems: A discussion of impedance- and eigenvalue-based methods," *IEEE Transactions on Industry Applications*, vol. 53, no. 5, pp. 5014–5030, 2017, doi:10.1109/TIA.2017.2712692.

[107] "MATLAB version: 9.11 (r2021b)," The MathWorks Inc., Natick, MA, 2021. [Online]. Available: https://www.mathworks.com

[108] L. I. Benedetti, A. Egea-Àlvarez, and P. N. Papadopoulos, "Power system small-signal modelling tool in MATLAB," 2025, University of Manchester. Software. https://doi.org/10.48420/26502361.v2.

[109] "Simulink version: 10.4 (r2021b)," The MathWorks Inc., Natick, MA, 2021. [Online]. Available: https://www.mathworks.com

[110] "Simscape electrical version: 7.6 (r2021b)," The MathWorks Inc., Natick, MA, 2021. [Online]. Available: https://www.mathworks.com/products/simscape-electrical.html

[111] J. Bezanson, A. Edelman, S. Karpinski, and V. B. Shah, "Julia: A fresh approach to numerical computing," *SIAM review*, vol. 59, no. 1, pp. 65–98, 2017. [Online]. Available: https://doi.org/10.1137/141000671

[112] J. D. Lara, R. Henriquez-Auba, M. Bossart, D. S. Callaway, and C. Barrows, "Powersimulationsdynamics.jl – an open source modeling package for modern power systems with inverter-based resources," *arXiv*, 2024. [Online]. Available: doi:10.48550/arXiv.2308.02921

[113] R. D. Zimmerman and C. E. Murillo-Sanchez, "Matpower." [Online]. Available: https://matpower.org

[114] "Symbolic math toolbox version: 9.0 (r2021b)," The MathWorks Inc., Natick, MA, 2021. [Online]. Available: https://www.mathworks.com

[115] Y.-Y. Hsu and C.-L. Chen, "Identification of optimum location for stabiliser applications using participation factors," *IEE Proceedings C (Generation,*

Transmission and Distribution), vol. 134, no. 3, pp. 238–244, May 1987. [Online]. Available: doi:10.1049/ip-c.1987.0037

[116] G. Tzounas, "Small-signal stability techniques for power system modal analysis, control, and numerical integration," Ph.D. dissertation, School of Electrical & Electronic Engineering, University College Dublin, Dublin, Ireland, 2020.

[117] "Control system toolbox version: 10.11 (r2021b)," The MathWorks Inc., Natick, MA, 2021. [Online]. Available: https://www.mathworks.com

[118] O. Wasynczuk and R. Decarlo, "The component connection model and structure preserving model order reduction," *Automatica*, vol. 17, no. 4, pp. 619–626, 1981, doi:10.1016/0005-1098(81)90033-9.

[119] R. Rosso, S. Engelken, and M. Liserre, "Analysis of the behavior of synchronverters operating in parallel by means of component connection method (CCM)," in *2018 IEEE Energy Conversion Congress and Exposition (ECCE)*, 2018, pp. 2228–2235, doi:10.1109/ECCE.2018.8558426.

[120] N. Pogaku, M. Prodanovic, and T. C. Green, "Modeling, analysis and testing of autonomous operation of an inverter-based microgrid," *IEEE Transactions on Power Electronics*, vol. 22, no. 2, pp. 613–625, 2007, doi:10.1109/TPEL.2006.890003.

[121] R. H. Park, "Two-reaction theory of synchronous machines generalized method of analysis-part I," *AIEE Transactions*, vol. 48, pp. 716–730, 1929.

[122] The MathWorks, Inc. (2025) Park Transform (Simscape Electrical). Accessed: 2025-04-23. [Online]. Available: https://www.mathworks.com/help/physmod/sps/ref/parktransform.html

[123] A. Yazdani and R. Iravani, *Voltage-Sourced Converters in Power Systems: Modeling, Control, and Applications*. Hoboken, NJ, USA: Wiley-IEEE Press, 2010, online ISBN: 9780470551578. [Online]. Available: https://ieeexplore.ieee.org/servlet/opac?bknumber=6739364

[124] M. Altin, R. Teodorescu, B. Bak-Jensen, P. Rodriguez, F. Iov, and P. C. Kjaer, "Wind power plant control - an overview," in *Proceedings of the 9th International Workshop on Large-Scale Integration of Wind Power into Power Systems*. Québec, Canada: Energynautics GmbH, 2010, pp. 1–8.

[125] S. D'Arco, J. A. Suul, and O. B. Fosso, "Automatic tuning of cascaded controllers for power converters using eigenvalue parametric sensitivities," *IEEE Transactions on Industry Applications*, vol. 51, no. 2, pp. 1743–1753, 2015.

[126] V. Blasko and V. Kaura, "A new mathematical model and control of a three-phase AC-DC voltage source converter," *IEEE Transactions on Power Electronics*, vol. 12, no. 1, pp. 116–123, 1997, doi:10.1109/63.554176.

[127] G. Amico, A. Egea-Àlvarez, P. Brogan, and S. Zhang, "Small-signal converter admittance in the *pn*-frame: Systematic derivation and analysis of the cross-coupling terms," *IEEE Transactions on Energy Conversion*, vol. 34, no. 4, pp. 1829–1838, 2019, doi:10.1109/TEC.2019.2924922.

[128] L. Harnefors and H. P. Nee, "Model-based current control of AC machines using the internal model control method," *IEEE Transactions on Industry Applications*, vol. 34, no. 1, pp. 133–141, 1998, doi:10.1109/28.658735.

[129] H. Zhang, W. Xiang, W. Lin, and J. Wen, "Grid forming converters in renewable energy sources dominated power grid: Control strategy, stability, application, and challenges," *Journal of Modern Power Systems and Clean Energy*, vol. 9, no. 6, pp. 1239–1256, 2021, doi:10.35833/MPCE.2021.000257.

[130] F. Zhao, X. Wang, and T. Zhu, "Power dynamic decoupling control of grid-forming converter in stiff grid," *IEEE Transactions on Power Electronics*, vol. 37, no. 8, pp. 9073–9088, 2022, doi:10.1109/TPEL.2022.3156991.

[131] F. Zhao, T. Zhu, Z. Li, and X. Wang, "Low-frequency resonances in grid-forming converters: Causes and damping control," *IEEE Transactions on Power Electronics*, vol. 39, no. 11, pp. 14 430–14 447, 2024, doi:10.1109/TPEL.2024.3424296.

[132] L. Fan, Z. Miao, D. Ramasubramanian, and H. Ding, "Operational challenges of solar PV plus storage power plants and modeling recommendations," *IEEE Open Access Journal of Power and Energy*, vol. 10, pp. 477–489, 2023.

[133] V. Purba, S. V. Dhople, S. Jafarpour, F. Bullo, and B. B. Johnson, "Reduced-order structure-preserving model for parallel-connected three-phase grid-tied inverters," in *2017 IEEE 18th Workshop on Control and Modeling for Power Electronics (COMPEL)*, Stanford, CA, USA, 2017, pp. 1–7, doi:10.1109/COMPEL.2017.8013389.

[134] S. D'Arco and J. A. Suul, "Equivalence of virtual synchronous machines and frequency-droops for converter-based microgrids," *IEEE Transactions on Smart Grid*, vol. 5, no. 1, pp. 394–395, 2014, doi:10.1109/TSG.2013.2288000.

[135] G.-S. Seo, M. Colombino, I. Subotic, B. Johnson, D. Groß, and F. Dörfler, "Dispatchable virtual oscillator control for decentralized inverter-dominated power systems: Analysis and experiments," in *2019 IEEE Applied Power Electronics Conference and Exposition (APEC)*, Anaheim, CA, USA, 2019, pp. 561–566, doi:10.1109/APEC.2019.8722028.

[136] C. Arghir, T. Jouini, and F. Dörfler, "Grid-forming control for power converters based on matching of synchronous machines," *Automatica*, vol. 95, pp. 273–282, 2018, doi:10.1016/j.automatica.2018.05.037.

[137] A. Tayyebi, "Grid-forming hybrid angle control for power converters in low-inertia power systems," Ph.D. dissertation, Swiss Federal Institute of Technology (ETH) Zurich, Zurich, Switzerland, 2023.

[138] D. B. Rathnayake, M. Akrami, C. Phurailatpam, S. P. Me, S. Hadavi, G. Jayasinghe, S. Zabihi, and B. Bahrani, "Grid forming inverter modeling, control, and applications," *IEEE Access*, vol. 9, pp. 114 781–114 807, 2021, doi:10.1109/ACCESS.2021.3104617.

[139] R. Rosso, X. Wang, M. Liserre, X. Lu, and S. Engelken, "Grid-forming converters: Control approaches, grid-synchronization, and future trends—a

review," *IEEE Open Journal of Industry Applications*, vol. 2, pp. 93–109, 2021, doi:10.1109/OJIA.2021.3074028.

[140] C. Li, S. Wang, and J. Liang, "Tuning method of a grid-following converter for the extremely-weak-grid connection," *IEEE Transactions on Power Systems*, vol. 37, no. 4, pp. 3169–3172, 2022.

[141] W. Ning, X. Wu, Y. J. Guan, and F. Chen, "Method to suppress sub-synchronous oscillation of DFIG-based wind farms based on virtual impedance," *The Journal of Engineering*, vol. 2017, no. 13, pp. 2173–2177, 2017, doi:10.1049/joe.2017.0715.

[142] L. Harnefors, M. Bongiorno, and S. Lundberg, "Input-admittance calculation and shaping for controlled voltage-source converters," *IEEE Transactions on Industrial Electronics*, vol. 54, no. 6, pp. 3323–3334, 2007, doi:10.1109/TIE.2007.904022.

[143] C. Liyanage, I. Nutkani, L. Meegahapola, and M. Jalili, "Stability enhancement of power synchronisation control based grid-forming inverter under varying network characteristics," *IEEE Transactions on Sustainable Energy*, vol. 15, no. 3, pp. 1799–1813, 2024, doi:10.1109/TSTE.2024.3379548.

[144] R. Liu, Z. Wang, Y. Wang, Y. Shan, W. Wang, and J. Wu, "Power decoupling control for grid-forming battery energy storage system in wind farm," *TechRxiv*, Sep. 2024, doi:10.36227/techrxiv.172720313.35299016/v1.

[145] A. A. Maruf, A. Dubey, and S. Roy, "Small-signal dynamics of lossy inverter-based microgrids for generalized droop controls," in *2024 IEEE 63rd Conference on Decision and Control (CDC)*, Milan, Italy, 2024, pp. 5359–5366, doi:10.1109/CDC56724.2024.10886313.

[146] T. Qoria, C. Li, K. Oue, F. Gruson, F. Colas, and X. Guillaud, "Direct AC voltage control for grid-forming inverters," *Journal of Power Electronics*, vol. 20, no. 1, pp. 198–211, 2020, doi:10.1007/s43236-019-00015-4.

[147] D. Yang, X. Ruan, and H. Wu, "Impedance shaping of the grid-connected inverter with LCL filter to improve its adaptability to the weak grid condition," *IEEE Transactions on Power Electronics*, vol. 29, no. 11, pp. 5795–5805, 2014.

[148] X. Zhang, X. Ruan, and Q.-C. Zhong, "Improving the stability of cascaded DC/DC converter systems via shaping the input impedance of the load converter with a parallel or series virtual impedance," *IEEE Transactions on Industrial Electronics*, vol. 62, no. 12, pp. 7499–7512, 2015, doi:10.1109/TIE.2015.2459040.

[149] T. Qoria, F. Gruson, F. Colas, X. Guillaud, M.-S. Debry, and T. Prevost, "Tuning of cascaded controllers for robust grid-forming voltage source converter," in *2018 Power Systems Computation Conference (PSCC)*, Dublin, Ireland, 2018, pp. 1–7, doi:10.23919/PSCC.2018.8443018.

[150] T. Qoria, S. E. Ben Haoua, R. S. Munoz Aguilar, H. Fakham, and X. Guillaud, "Optimization of cascaded control gains of grid-forming based energy conversion system," *Electric Power Systems Research*, vol. 235, p. 110703, 2024, doi:10.1016/j.epsr.2024.110703.

[151] L. Benedetti, A. Paspatis, P. N. Papadopoulos, A. Egea-Àlvarez, and N. Hatziargyriou, "Investigation of grid-forming and grid-following converter multi-machine interactions under different control architectures," *Electric Power Systems Research*, vol. 234, p. 110813, 2024, doi:10.1016/j.epsr.2024.110813.

[152] M. Beza and M. Bongiorno, "Impact of converter control strategy on low- and high-frequency resonance interactions in power-electronic dominated systems," *International Journal of Electrical Power and Energy Systems*, vol. 120, p. 105978, 2020, doi:10.1016/j.ijepes.2020.105978.

[153] A. Narula, M. Bongiorno, and M. Beza, "Comparison of grid-forming converter control strategies," in *2021 IEEE Energy Conversion Congress and Exposition (ECCE)*, Vancouver, BC, Canada, 2021, pp. 361–368.

[154] P. Rodriguez, I. Candela, C. Citro, J. Rocabert, and A. Luna, "Control of grid-connected power converters based on a virtual admittance control loop," in *2013*

15th European Conference on Power Electronics and Applications (EPE), Lille, France, 2013, pp. 1–10, doi:10.1109/EPE.2013.6634621.

[155] M. Beza, M. Bongiorno, and A. Narula, "Impact of control loops on the passivity properties of grid-forming converters with fault-ride through capability," *Energies*, vol. 14, no. 19, 2021, doi:10.3390/en14196036.

[156] P. C. Krause, O. Wasynczuk, and S. D. Sudhoff, *Analysis of Electric Machinery and Drive Systems*. Hoboken, NJ, USA: Wiley-IEEE Press, 2002. [Online]. Available: https://ieeexplore.ieee.org/servlet/opac?bknumber=5265638

[157] Identification, Testing, and Evaluation of the Dynamic Performance of Excitation Control Systems Working Group, "IEEE Recommended Practice for Excitation System Models for Power System Stability Studies," *IEEE Std 421.5-2016 (Revision of IEEE Std 421.5-2005)*, 2016, doi:10.1109/IEEESTD.2016.7553421.

[158] Task Force on Turbine-Governor Modeling, "Dynamic models for turbine-governors in power system studies," IEEE, Technical Report PES-TR1, 2013. [Online]. Available: https://resourcecenter.ieee.org/publications/technical-reports/pestr1

[159] N. Pogaku, M. Prodanovic, and T. C. Green, "Modeling, analysis and testing of autonomous operation of an inverter-based microgrid," *IEEE Transactions on Power Electronics*, vol. 22, no. 2, pp. 613–625, 2007, doi:10.1109/TPEL.2006.890003.

[160] W. Du, Z. Chen, K. P. Schneider, R. H. Lasseter, S. P. Nandanoori, F. K. Tuffner, and S. Kundu, "A comparative study of two widely used grid-forming droop controls on microgrid small-signal stability," *IEEE Journal of Emerging and Selected Topics in Power Electronics*, vol. 8, no. 2, pp. 963–975, 2020.

[161] M. Ndreko, S. Rüberg, and W. Winter, "Grid forming control scheme for power systems with up to 100% power electronic interfaced generation: A case study on Great Britain test system," *IET Renewable Power Generation*, vol. 14, no. 8, pp. 1268–1281, 2020, doi:10.1049/iet-rpg.2019.0700.

[162] T. Xue, J. Zhang, and S. Bu, "Inter-area oscillation analysis of power system integrated with virtual synchronous generators," *IEEE Transactions on Power Delivery*, vol. 39, no. 3, pp. 1761–1773, 2024, doi:10.1109/TPWRD.2024.3376523.

[163] Y. Liao, X. Wang, F. Liu, K. Xin, and Y. Liu, "Sub-synchronous control interaction in grid-forming VSCs with droop control," in *2019 4th IEEE Workshop on the Electronic Grid (eGRID)*, Xiamen, China, 2019, pp. 1–6, doi:10.1109/eGRID48402.2019.9092640.

[164] S. Leitner, M. Yazdanian, A. Mehrizi-Sani, and A. Muetze, "Small-signal stability analysis of an inverter-based microgrid with internal model-based controllers," *IEEE Transactions on Smart Grid*, vol. 9, no. 5, pp. 5393–5402, 2018, doi:10.1109/TSG.2017.2688481.

[165] S. Dong and Y. C. Chen, "Analysis of feasible synchronverter pole-placement region to facilitate parameter tuning," *IEEE Transactions on Energy Conversion*, vol. 36, no. 4, pp. 2782–2793, 2021, doi:10.1109/TEC.2021.3068758.

[166] J. Liu, Y. Xia, W. Wei, Q. Feng, and P. Yang, "Effect of control damping on small-signal stability of grid-forming VSCs considering interaction between inner and outer loops," *IEEE Transactions on Power Electronics*, vol. 39, no. 6, pp. 7685–7695, 2024, doi:10.1109/TPEL.2024.3381148.

[167] U. Markovic, J. Vorwerk, P. Aristidou, and G. Hug, "Stability analysis of converter control modes in low-inertia power systems," in *2018 IEEE PES Innovative Smart Grid Technologies Conference Europe (ISGT-Europe)*, Sarajevo, Bosnia and Herzegovina, 2018, pp. 1–6, doi:10.1109/ISGTEurope.2018.8571583.

[168] R. Rosso, S. Engelken, and M. Liserre, "Robust stability analysis of synchronverters operating in parallel," *IEEE Transactions on Power Electronics*, vol. 34, no. 11, pp. 11 309–11 319, 2019, doi:10.1109/TPEL.2019.2896707.

[169] L. Rouco, "Dynamic patterns in the small-signal behavior of power systems with wind power generation," *Energies*, vol. 17, no. 7, 2024, doi:10.3390/en17071784.

[170] J. Vorwerk, M. G. Dozein, P. Mancarella, and G. Hug, "Analytical discussion on dynamics of inverter-based resources under small-signal conditions," in *2023 IEEE PowerTech*, Belgrade, Serbia, 2023, pp. 1–6, doi:10.1109/PowerTech55446.2023.10202679.

[171] L. Fan, "Inter-IBR oscillation modes," *IEEE Transactions on Power Systems*, vol. 37, no. 1, pp. 824–827, 2022, doi:10.1109/TPWRS.2021.3124667.

[172] P. Zoghby, B. Marinescu, A. Rossé, and G. Prime, "Exhaustive classification and quantification of coupling modes in power systems with power electronics," *arXiv*, 2024, doi:10.48550/arXiv.2402.04701.

[173] ——, "Study of new types of dynamic interactions in power systems with mixed conventional and renewable generation," in *CIGRE Paris Session 2024*. Paris, France: CIGRE, August 2024, pp. 1–13, HAL Id: hal-04683104 , version 1.

[174] G. S. Pereira, V. Costan, A. Bruyère, and X. Guillaud, "Impact of synchronous machine dynamics on the stability of a power grid with high penetration of variable renewable energies," in *15th IET International Conference on AC and DC Power Transmission (ACDC 2019)*, Coventry, UK, 2019, pp. 1–6, doi:10.1049/cp.2019.0087.

[175] ——, "Synchronous machine representations for stability studies of power systems with inverters," in *2019 IEEE PowerTech*, Milan, Italy, 2019, pp. 1–6, doi:10.1109/PTC.2019.8810485.

[176] R. Rosso, S. Engelken, and M. Liserre, "Current limitation strategy for grid-forming converters under symmetrical and asymmetrical grid faults," in *2020 IEEE Energy Conversion Congress and Exposition (ECCE)*, Detroit, MI, USA, 2020, pp. 3746–3753, doi:10.1109/ECCE44975.2020.9236314.

[177] L. Benedetti, P. N. Papadopoulos, and A. Egea-Àlvarez, "Small signal study of grid-forming converters and impact of different control structures and parameters," in *2022 IEEE PES Innovative Smart Grid Technologies Conference*

Europe (ISGT-Europe), Novi Sad, Serbia, 2022, pp. 1–5, doi:10.1109/ISGT-Europe54678.2022.9960644.

[178] L. Gérin-Lajoie, O. Saad, and J. Mahseredjian, "Report on the EMTP-RV 39-bus system (New England reduced model) version 1.5," IEEE PES Task Force on Benchmark Systems for Stability Controls, Tech. Rep., 2005. [Online]. Available: http://www1.sel.eesc.usp.br/ieee/

[179] M. Chen, D. Zhou, A. Tayyebi, E. Prieto-Araujo, F. Dorfler, and F. Blaabjerg, "Augmentation of generalized multivariable grid-forming control for power converters with cascaded controllers," in *2022 International Power Electronics Conference (IPEC-Himeji 2022- ECCE Asia)*, 2022, pp. 998–1004, doi:10.23919/IPEC-Himeji2022-ECCE53331.2022.9807103.

[180] M. Javaid, B. Chaudhuri, F. Tang, and Z. Akhtar, "A novel tuning method of grid-forming inverter voltage control," in *2025 IEEE Kiel PowerTech*, Kiel, Germany, 2025, pp. 1–6.

[181] R. H. Chandio, F. A. Chachar, J. B. Soomro, J. A. Ansari, H. M. Munir, H. M. Zawbaa, and S. Kamel, "Control and protection of MMC-based HVDC systems: A review," *Energy Reports*, vol. 9, pp. 1571–1588, 2023, doi:10.1016/j.egyr.2022.12.056.

[182] M. N. Raju, J. Sreedevi, R. P Mandi, and K. Meera, "Modular multilevel converters technology: a comprehensive study on its topologies, modelling, control and applications," *IET Power Electronics*, vol. 12, no. 2, pp. 149–169, 2019, doi:10.1049/iet-pel.2018.5734.

[183] N. S. Hasan, N. Rosmin, D. A. A. Osman, and A. H. Musta'amal, "Reviews on multilevel converter and modulation techniques," *Renewable and Sustainable Energy Reviews*, vol. 80, pp. 163–174, 2017, doi:10.1016/j.rser.2017.05.163.

[184] S. Coffey, V. Timmers, R. Li, G. Wu, and A. Egea-Àlvarez, "Review of MVDC applications, technologies, and future prospects," *Energies*, vol. 14, no. 24, 2021, doi:10.3390/en14248294.

[185] A. Antonopoulos, "Control, modulation and implementation of modular multilevel converters," Ph.D. dissertation, KTH Royal Institute of Technology, Stockholm, 2011.

[186] R. Henriquez-Auba, J. D. Lara, C. Roberts, and D. S. Callaway, "Grid forming inverter small signal stability: Examining role of line and voltage dynamics," in *IECON Proceedings (Industrial Electronics Conference)*, vol. 2020-October, Singapore, 2020, pp. 4063–4068.

[187] T. Qoria and X. Guillaud, "Grid-forming control suitable for large power transmission system applications," *TechRxiv*, 2021, doi:10.36227/techrxiv.17089199.v1.

[188] L. Huang, H. Xin, H. Yuan, G. Wang, and P. Ju, "Damping effect of virtual synchronous machines provided by a dynamical virtual impedance," *IEEE Transactions on Energy Conversion*, vol. 36, no. 1, pp. 570–573, 2021, doi:10.1109/TEC.2020.3040605.

[189] K. Vatta Kkuni, S. Mohan, G. Yang, and W. Xu, "Comparative assessment of typical control realizations of grid forming converters based on their voltage source behaviour," *Energy Reports*, vol. 9, pp. 6042–6062, 2023, doi:10.1016/j.egyr.2023.05.073.

[190] L. Huang, C. Wu, D. Zhou, and F. Blaabjerg, "Comparison of three small-signal stability analysis methods for grid-following inverter," in *2021 International Aegean Conference on Electrical Machines and Power Electronics & 2021 International Conference on Optimization of Electrical and Electronic Equipment*, Moeciu, Fundata, Brasov, Romania, 2021, pp. 34–41, doi:10.1109/OPTIM-ACEMP50812.2021.9590036.

[191] R. Rosso, S. Engelken, and M. Liserre, "Robust stability investigation of the interactions among grid-forming and grid-following converters," *IEEE Journal of Emerging and Selected Topics in Power Electronics*, vol. 8, no. 2, pp. 991–1003, 2020.

[192] A. Sajadi, R. W. Kenyon, M. Bossart, and B.-M. Hodge, "Dynamic interaction of grid-forming and grid-following inverters with synchronous generators in hybrid power plants," in *2021 IEEE Kansas Power and Energy Conference, KPEC 2021*, Manhattan, KS, USA, 2021, pp. 1–6, doi:10.1109/KPEC51835.2021.9446204.

[193] Y. Lamrani, F. Colas, T. V. Cutsem, C. Cardozo, T. Prevost, and X. Guillaud, "On the stabilizing contribution of different grid-forming controls to power systems," *IET Gener. Transm. Distrib.*, vol. 18, p. 3863–3877, 2024, doi:10.1049/gtd2.13269.

[194] A. G. Paspatis and G. C. Konstantopoulos, "Voltage support under grid faults with inherent current limitation for three-phase droop-controlled inverters," *Energies*, vol. 12, no. 6, 2019, doi:10.3390/en12060997.

[195] G. Denis, T. Prevost, P. Panciatici, X. Kestelyn, F. Colas, and X. Guillaud, "Improving robustness against grid stiffness, with internal control of an AC voltage-controlled VSC," in *IEEE Power & Energy Society General Meeting (PESGM)*. Boston, MA, USA: IEEE, 2016.

[196] P. M. Anderson and A. A. Fouad, *Power System Control and Stability*, 2nd ed. Wiley-IEEE Press, 2003, doi:10.1109/9780470545577. [Online]. Available: https://ieeexplore.ieee.org/servlet/opac?bknumber=5264012

[197] D. Chakravorty, G. McFadzean, G. Edwards, M. McFarlane, D. Gutschow, S. Abdelrahman, and R. AziziPanah-Abarghooee, "A probabilistic approach to stability analysis for boundary transfer capability assessment," in *CIGRE Paris Session 2022*, no. C1-10197, Paris, France, 2022, pp. 1–12.

[198] S. Wang, Z. Liu, J. Liu, D. Boroyevich, and R. Burgos, "Small-signal modeling and stability prediction of parallel droop-controlled inverters based on terminal characteristics of individual inverters," *IEEE Transactions on Power Electronics*, vol. 35, no. 1, pp. 1045–1063, 2020.

[199] V. Häberle, A. Tayyebi, X. He, E. Prieto-Araujo, and F. Dörfler, "Grid-forming and spatially distributed control design of dynamic virtual power

plants," *IEEE Transactions on Smart Grid*, vol. 15, no. 2, pp. 1761–1777, 2024, doi:10.1109/TSG.2023.3311481.

[200] C. Collados-Rodriguez, M. Cheah-Mane, E. Prieto-Araujo, and O. Gomis-Bellmunt, "Stability and operation limits of power systems with high penetration of power electronics," *International Journal of Electrical Power and Energy Systems*, vol. 138, 2022, doi:10.1016/j.ijepes.2021.107728.

[201] M. Yu, A. J. Roscoe, A. Dyśko, C. D. Booth, R. Ierna, J. Zhu, and H. Urdal, "Instantaneous penetration level limits of non-synchronous devices in the British power system," *IET Renewable Power Generation*, vol. 11, no. 8, pp. 1211–1217, 2017, doi:10.1049/iet-rpg.2016.0352.

[202] Z. Xu, Z. Dong, and P. Zhang, "Probabilistic small signal analysis using Monte Carlo simulation," in *IEEE Power Engineering Society General Meeting*, vol. 2, San Francisco, CA, USA, 2005, pp. 1658–1664, 10.1109/PES.2005.1489425.

[203] Z. W. Wang, C. Shen, and F. Liu, "Probabilistic analysis of small signal stability for power systems with high penetration of wind generation," *IEEE Trans. Sustain. Energy*, vol. 7, no. 3, pp. 1182–1193, 2016.

[204] W. Weiyu, L. Fang, T. Yi, H. Jinhua, T. Shengwei, L. Yong, and C. Yijia, "Virtual synchronous generator strategy for VSC-MTDC and the probabilistic small signal stability analysis," *IFAC-PapersOnLine*, vol. 50, no. 1, pp. 5424–5429, 2017, 20th IFAC World Congress, Toulouse, France, doi:10.1016/j.ifacol.2017.08.1077.

[205] Z. Xu, M. Ali, Z. Dong, and X. Li, "A novel grid computing approach for probabilistic small signal analysis," in *2006 IEEE Power Engineering Society General Meeting*, Montreal, QC, Canada, 2006, pp. 1–8, doi:10.1109/PES.2006.1709449.

[206] J. L. Rueda, D. G. Colome, and I. Erlich, "Assessment and enhancement of small signal stability considering uncertainties," *IEEE Transactions on Power Systems*, vol. 24, no. 1, pp. 198–207, 2009.

[207] J. L. Rueda and I. Erlich, "Probabilistic framework for risk analysis of power system small-signal stability," *Proc. Inst. Mech. Eng., Part O: J. Risk Reliab.*, vol. 226, no. 1, pp. 118–133, 2012, doi:10.1177/1748006X11424534.

[208] S. Q. Bu, W. Du, and H. F. Wang, "Probabilistic analysis of small-signal rotor angle/voltage stability of large-scale AC/DC power systems as affected by grid-connected offshore wind generation," *IEEE Transactions on Power Systems*, vol. 28, no. 4, pp. 3712–3719, 2013.

[209] J. W. Shim, G. Verbič, and K. Hur, "Stochastic eigen-analysis of electric power system with high renewable penetration: Impact of changing inertia on oscillatory modes," *IEEE Transactions on Power Systems*, vol. 35, no. 6, pp. 4655–4665, 2020, doi:10.1109/TPWRS.2020.3000577.

[210] Z. Wang and S. Bu, "Probabilistic analysis of small-signal stability of power systems affected by wind power generation uncertainties considering wake effects," *IEEE Transactions on Power Systems*, vol. 40, no. 2, pp. 1955–1968, 2025, doi:10.1109/TPWRS.2024.3450909.

[211] L. Wang, F. Howell, P. Kundur, C. Chung, and W. Xu, "A tool for small-signal security assessment of power systems," in *PICA 2001, Innovative Comput. for Power - Electr. Energy Meets the Market. 22nd IEEE Power Eng. Soc. Int. Conf. Power Ind. Comput. Appl. (Cat. No. 01CH37195)*, Sydney, NSW, Australia, 2001, pp. 246–252, doi:10.1109/PICA.2001.932356.

[212] P. N. Papadopoulos and J. V. Milanović, "Probabilistic framework for transient stability assessment of power systems with high penetration of renewable generation," *IEEE Transactions on Power Systems*, vol. 32, no. 4, pp. 3078–3088, 2017, doi:10.1109/TPWRS.2016.2630799.

[213] NESO, "National Energy System Operator (NESO) Data Portal," https://www.neso.energy/data-portal, accessed Feb. 04, 2025.

[214] J. Rueda and D. Colomé, "Probabilistic performance indexes for small signal stability enhancement in weak wind-hydro-thermal power systems," *IET Generation, Transmission & Distribution*, vol. 3, no. 8, pp. 733–747(14), 2009.

[215] C. Machado Ferreira, F. P. Maciel Barbosa, and C. I. Faustino Agreira, "Transient stability preventive control of an electric power system using a hybrid method," in *2008 12th International Middle-East Power System Conference*, Aswan, Egypt, 2008, pp. 141–145, doi:10.1109/MEPCON.2008.4562306.

[216] S. L. Brunton and J. N. Kutz, *Data-Driven Science and Engineering: Machine Learning, Dynamical Systems, and Control*, 2nd ed. Cambridge University Press, 2022.

[217] D. Arthur and S. Vassilvitskii, "k-means++: the advantages of careful seeding," in *Proceedings of the Eighteenth Annual ACM-SIAM Symposium on Discrete Algorithms*, New Orleans, LA, USA, 2007, p. 1027–1035, doi:10.5555/1283383.1283494.

[218] M. E. Celebi, H. A. Kingravi, and P. A. Vela, "A comparative study of efficient initialization methods for the k-means clustering algorithm," *Expert Systems with Applications*, vol. 40, no. 1, pp. 200–210, 2013, doi:10.1016/j.eswa.2012.07.021.

[219] P. Jones and P. Harris, "Developing an empirically based typology of delinquent youths," *J. Quant. Criminol.*, vol. 15, 1999, doi:10.1023/A:1007524414432.

[220] G. Tzounas, I. Dassios, and F. Milano, "Modal participation factors of algebraic variables," *IEEE Transactions on Power Systems*, vol. 35, no. 1, pp. 742–750, 2020, doi:10.1109/TPWRS.2019.2931965.

[221] R. Preece, "A probabilistic approach to improving the stability of meshed power networks with embedded HVDC lines preece," PhD thesis, University of Manchester, Aug. 2013.

[222] I. Pasiopoulou, E. Kontis, T. Papadopoulos, and G. Papagiannis, "Effect of load modeling on power system stability studies," *Electr. Power Syst. Res.*, vol. 207, p. 107846, 2022, doi:10.1016/j.epsr.2022.107846.

[223] S. D'Arco, J. A. Suul, and O. B. Fosso, "A virtual synchronous machine implementation for distributed control of power converters in smartgrids," *Electric Power Systems Research*, vol. 122, pp. 180–197, 2015, doi:10.1016/j.epsr.2015.01.001.

[224] J. Guerrero, L. G. de Vicuna, J. Matas, M. Castilla, and J. Miret, "Output impedance design of parallel-connected ups inverters with wireless load-sharing control," *IEEE Transactions on Industrial Electronics*, vol. 52, no. 4, pp. 1126–1135, 2005, doi:10.1109/TIE.2005.851634.

[225] M. Miranbeigi, P. M. Gajare, J. Benzaquen, P. Kandula, and D. Divan, "On the passivity of grid-forming converters — role of virtual impedance," in *2022 IEEE Applied Power Electronics Conference and Exposition (APEC)*, Houston, TX, USA, 2022, pp. 650–656, doi:10.1109/APEC43599.2022.9773656.

[226] A. M. Khalil and R. Iravani, "Impact of high-depth penetration of wind power on low-frequency oscillatory modes of interconnected power systems," *Int. J. Electr. Power Energy Syst.*, vol. 104, pp. 827–839, 2019, doi:10.1016/j.ijepes.2018.07.062.

[227] "The Grid Code," National Grid Electricity System Operator Limited, Tech. Rep. Issue 6, Revision 20, 2023.

[228] S. Manakkadu and S. Dutta, "Efficient feature clustering for high-dimensional datasets: A non-parametric approach," *Procedia Computer Science*, vol. 237, pp. 576–585, 2024, doi:10.1016/j.procs.2024.05.142.

[229] A. McCallum, K. Nigam, and L. H. Ungar, "Efficient clustering of high-dimensional data sets with application to reference matching," in *Proceedings of the sixth ACM SIGKDD international conference on Knowledge discovery and data mining*, New York, NY, USA, 2000, pp. 169–178, doi:10.1145/347090.347123.

[230] S. Helman, H. Jung, N. Baeckeland, D. Ramasubramanian, and S. Dhople, "Grey-box system identification of grid-forming inverters," in *9th IEEE Workshop on the Electronic Grid (eGRID)*, Santa Fe, NM, USA, 2024, pp. 1–6, doi:10.1109/eGRID62045.2024.10842804.

[231] Y. Li, Y. Gu, Y. Zhu, A. Junyent-Ferré, X. Xiang, and T. C. Green, "Impedance circuit model of grid-forming inverter: Visualizing control algorithms as circuit elements," *IEEE Transactions on Power Electronics*, vol. 36, no. 3, pp. 3377–3395, 2021, doi:10.1109/TPEL.2020.3015158.

[232] O. Damanik, O. C. Sakinci, G. Grdenic, and J. Beerten, "Evaluation of the use of short-circuit ratio as a system strength indicator in converter-dominated power systems," in *2022 IEEE PES Innovative Smart Grid Technologies Conference Europe (ISGT-Europe)*, Novi Sad, Serbia, 2022, doi:10.1109/ISGT-Europe54678.2022.9960381.

[233] C. Henderson, A. Egea-Àlvarez, P. Papadopoulos, R. Li, L. Xu, R. D. Silva, A. Kinsella, I. Gutierrez, and R. Pabat-Stroe, "Exploring an impedance-based SCR for accurate representation of grid-forming converters," in *IEEE Power & Energy Society General Meeting*, Denver, CO, USA, 2022, doi:10.1109/PESGM48719.2022.9916733.

[234] F. Milano and Álvaro Ortega, "Frequency divider," *IEEE Transactions on Power Systems*, vol. 32, no. 2, pp. 1493–1501, 2017.

[235] C. Yang, L. Huang, H. Xin, and P. Ju, "Placing grid-forming converters to enhance small signal stability of PLL-integrated power systems," *IEEE Transactions on Power Systems*, vol. 36, no. 4, pp. 3563–3573, 2021.

[236] D. Brahma and N. Senroy, "Sensitivity-based approach for assessment of dynamic locational grid flexibility," *IEEE Transactions on Power Systems*, vol. 35, no. 5, pp. 3470–3480, 2020.

[237] A. Egea-Àlvarez, S. Fekriasl, F. Hassan, and O. Gomis-Bellmunt, "Advanced vector control for voltage source converters connected to weak grids," *IEEE Transactions on Power Systems*, vol. 30, no. 6, pp. 3072–3081, 2015.

[238] L. Benedetti, P. N. Papadopoulos, and A. Egea-Àlvarez, "A modal contribution metric for quantifying small-signal variability in power systems with converter-interfaced generation," *IEEE Transactions on Power Systems*, vol. 40, no. 3, pp. 2636–2647, 2025, doi:10.1109/TPWRS.2024.3500786.

[239] B. Pal and B. Chaudhuri, *Robust Control in Power Systems*. New York, NY, USA: Springer, 2005.

[240] I. J. Perez-Arriaga, G. C. Verghese, and F. C. Schweppe, "Selective modal analysis with applications to electric power systems, part I: Heuristic introduction," *IEEE Transactions on Power Apparatus and Systems*, vol. PAS-101, no. 9, pp. 3117–3125, 1982.

[241] A. K. Chopra, *Dynamics of Structures: Theory and Applications to Earthquake Engineering*, 4th ed. Upper Saddle River N.J: Prentice Hall, 2012.

[242] A. Tomás-Martín, J. Suárez-Porras, B. Kazemtabrizi, J. García-Aguilar, L. Sigrist, and A. García-Cerrada, "A vector-based flexible-complexity tool for simulation and small-signal analysis of hybrid AC/DC power systems," in *12th Bulk Power System Dynamics and Control Symposium - IREP 2025*, Sorrento, Italy, June 2025, pp. 1–15.

[243] F. Milano, "Complex frequency," *arXiv*, 2021, doi:10.48550/arXiv.2105.07769.

[244] C. Bajracharya, M. Molinas, J. A. Suul, and T. M. Undeland, "Understanding of tuning techniques of converter controllers for VSC-HVDC," in *Proceedings of the Nordic Workshop on Power and Industrial Electronics (NORPIE/2008)*, Helsinki, Finland, 2008, pp. 1–8.

[245] L. Benedetti, A. Egea-Àlvarez, and P. Papadopoulos, "Results data: A modal contribution metric for quantifying small-signal variability in power systems

with converter-interfaced generation," Jul 2024, doi:10.48420/26412331. [Online]. Available: https://figshare.manchester.ac.uk/articles/dataset/_/26412331/0

[246] G. S. Pereira, V. Costan, A. Bruyére, and X. Guillaud, "Simplified approach for frequency dynamics assessment of 100% power electronics-based systems," *Electric Power Systems Research*, vol. 188, p. 106551, 2020, doi:10.1016/j.epsr.2020.106551.

[247] J.-S. Brouillon, M. Colombino, D. Groß, and F. Dörfler, "The effect of transmission-line dynamics on a globally synchronizing controller for power inverters," in *2018 European Control Conference (ECC)*, Limassol, Cyprus, 2018, pp. 2242–2247, doi:10.23919/ECC.2018.8550600.

[248] L. Benedetti, P. N. Papadopoulos, and A. Egea-Àlvarez, "Small signal interactions involving a synchronous machine and a grid forming converter," in *2021 IEEE PowerTech*, Madrid, Spain, 2021, pp. 1–6, doi:10.1109/PowerTech46648.2021.9494923.

[249] M. Reta-Hernández, "Transmission line parameters," in *Electric Power Generation, Transmission, and Distribution*, 3rd ed., L. Grigsby, Ed. CRC Press, 2012, ch. 13. [Online]. Available: https://doi.org/10.1201/9781315222424

Appendix A

Small-Signal Model Validation

The mathematical models and linearisation process adopted in this work are well established and do not require validation in and of themselves. Rather, this appendix validates the correctness of the model implementation through comparison with corresponding non-linear Simulink models (for validation of OMIB systems) and the Julia [111] open-source Sienna modelling framework by National Renewable Energy Laboratory (NREL) [112] (for multi-machine model validation). The Simulink models that have been constructed make use of the Specialized Power Systems library of Simscape Electrical [110]. This doubles as a validation for the linearity of the models for small-disturbances, especially for relatively novel control schemes or tuning. The step sizes used are 10% of the base power or voltage and, therefore, the models can be considered accurate for disturbances of this size. Note, when using Simulink models for validation, the simulation is run until steady-state is reached before comparing against the corresponding small-signal models.

In this subsection, responses of active and reactive power output, P_e and Q_e, voltage magnitude at the PCC, $|\boldsymbol{v_m}|$, and the speed/rotational frequency of the machine are considered. Depending on the type of generator, the machine speed will either correspond to the rotor (SG), ω_r, virtual rotor (GFM), ω_{GFM}, or PLL (GFL), ω_{PLL}. Step disturbances are applied to the active power and reactive power (or voltage magnitude) references of the devices. For the sake of brevity, only the response of active power output and machine speed to a step of active power reference are considered, in

addition to the response of reactive power (or voltage magnitude) to a step in reactive power (or voltage magnitude) reference.

A.1 Simulink Model Elements Common to Both Grid-Following– and Grid-Forming–Infinite Bus Systems

There are some common Simulink blocks which are not explicitly labelled in the figures in this appendix. For the sake of clarity, these will be described when first displayed.

As discussed in Section 2.3.1, CIG controllers are typically implemented in dq coordinates. As such, a Park transform is required to translate the signal phasors in abc coordinates to d and q coordinates (and an inverse Park transform for the reverse). The work in this thesis uses (2.13) and (2.14) for the Park and Inverse Park transforms, respectively. These are implemented in the Simulink models as displayed in Fig. A.1 and Fig. A.2, respectively. Subsystems are seen as blocks with grey background colouring, such as the Park transform implementation seen in Fig. A.1a with input of theta (i.e., angle) and output of Park (transform matrix). This subsystem is what is displayed in Fig. A.1b. The numbered oval blocks represent inputs and outputs to the subsystem being displayed.

The averaged model of the converter is adopted whereby the switching transients are neglected. This takes the form of controllable voltage sources, where the controlling signals are generated by the CIG control scheme (Section 2.5.1). This is implemented as displayed in Fig. A.3a. The hexagonal blocks are output *ports* which are similar to the signal output blocks but are for Simscape Electrical Specialized Power Systems electrical connections. Furthermore, a first-order LPF approximation of the PWM/control delay (also described in Section 2.5.1) may be considered, as illustrated in Fig. A.3b. Note, the filtering is performed with "`Transfer Fcn`" blocks set to act as LPFs whereby "s" represents the Laplace operator.

The calculation of voltage magnitude is implemented in the Simulink models using the standard "`Clarke Transform`" block. The α and β transformed voltage signals are then translated to a complex phasor using the "`Real-Imag to Complex`" block, whose

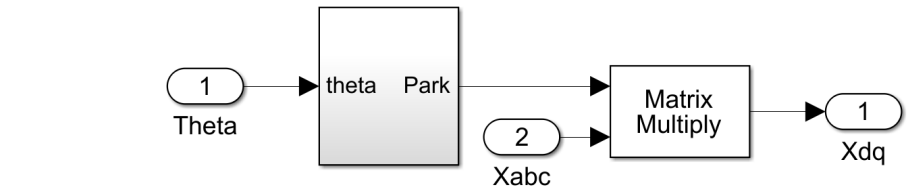

(a)

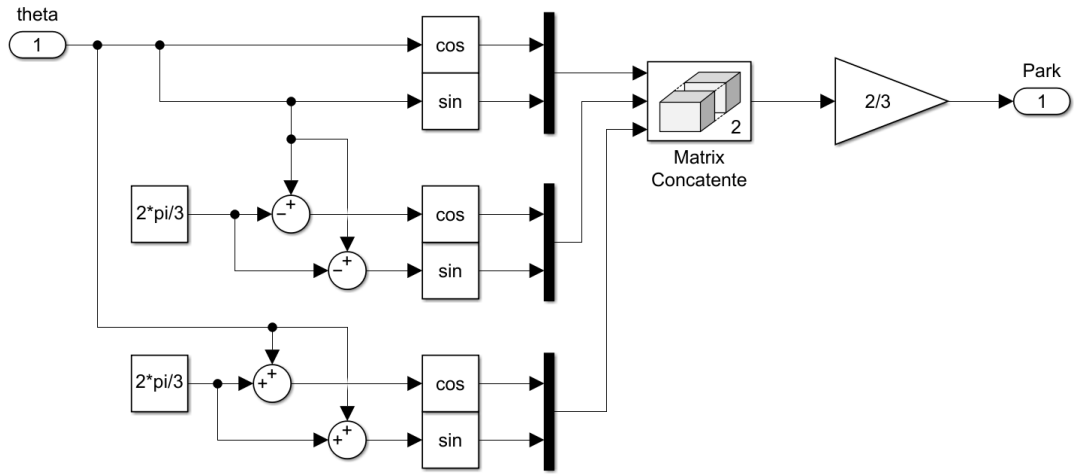

(b)

Figure A.1: Simulink implementation of the Park transform.

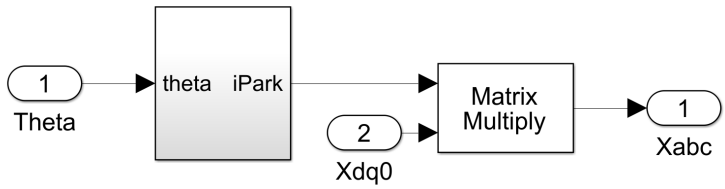

(a)

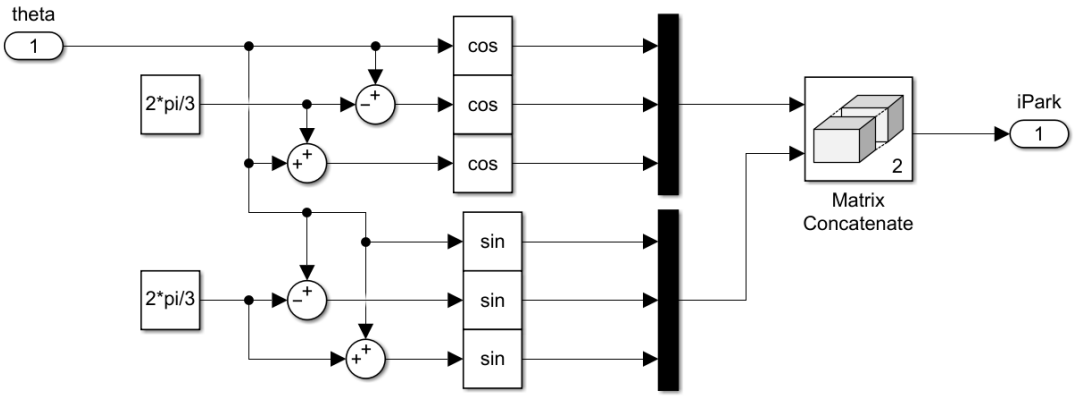

(b)

Figure A.2: Simulink implementation of the inverse Park transform.

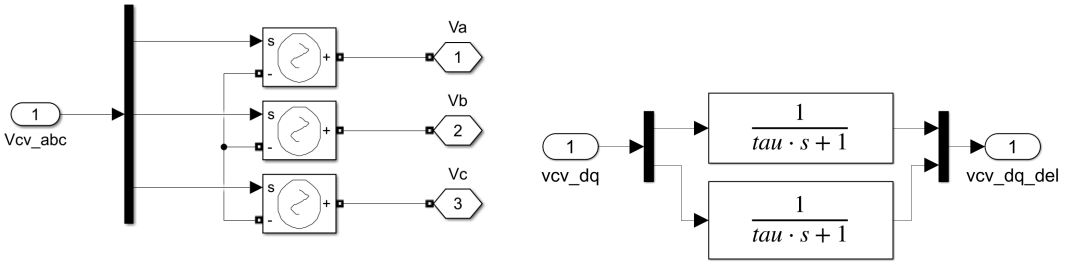

(a) (b)

Figure A.3: Simulink implementation of (a) converter averaged-model and (b) PWM/control delay first-order approximation where *tau* is the time constant of the LPF.

magnitude is then determined as the output of the subsystem. This is seen in Fig. A.4.

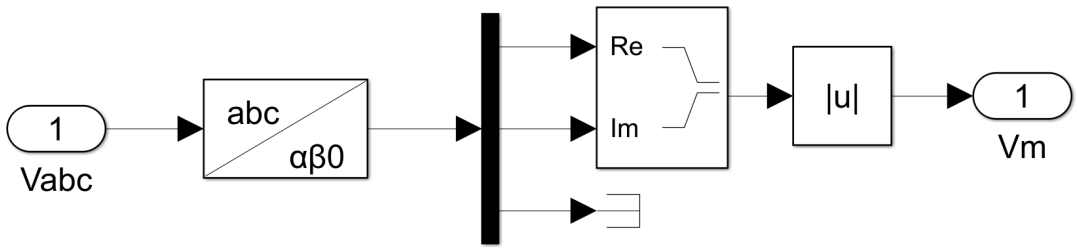

Figure A.4: Simulink implementation of voltage magnitude calculation.

Also common to both the GFL and GFM (when adopting either SILC or DILC) is an ICC. The Simulink implementation, in accordance with that of Fig. 2.5, is displayed in Fig. A.5. The "PI(s)" block is of course that of the proportional-integral controller. The parameters "Lcv" and "wsys" are the converter output filter inductance (in SI units) and the base frequency (in rad/s), respectively. Note, the triangular "`gain`" blocks whose parameter value is not seen but is instead replaced with the general term "-K-" represents a conversion to per unit parameters (i.e., in this case "-K-" is the inverse of the base impedance). This will be seen several times throughout the remainder of the Simulink model figures in this appendix. It either represents conversion to per unit as in this situation, or similarly, a conversion from per unit values back to SI units. Note, to maintain consistency of the control parameters with that of the small-signal model, the voltage and current signals in the control algorithms are converted from peak-per-phase (which is the output of the Park transform) in SI units to RMS-line-to-line in per unit.

A.2 Grid-Following Converter–Infinite Bus

Simulink Model

The upper-level of the GFL–infinite bus Simulink model, displaying the Simscape Electrical Specialized Power Systems electrical system, the current and voltage measurement locations, the active and reactive power measurement LPFs, and the

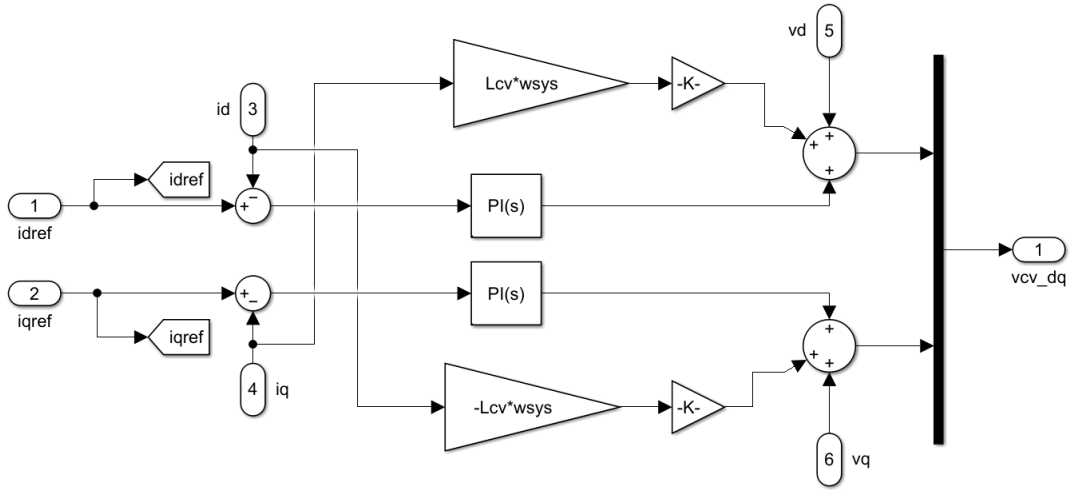

Figure A.5: Simulink implementation of ICC.

signal interconnections is displayed in Fig. A.6. The block which contains the text "Discrete 1e-05 s." is the "`powergui`" block which is used to set up the Simscape Electrical Specialized Power Systems simulation environment.

The flags (e.g., Pe, Pe_nf, and Qe_nf. The latter two of which are the active and reactive power measurements prior to low-pass filtering) are "`Goto`" blocks, which enable signals to be accessed in the "Recorded signals" subsystem. In this subsystem, output signals are recorded to the MATLAB workspace using the "`To Workspace`" block.

The SLC and DLC realisations are displayed in Fig. A.8a and Fig. A.8b, respectively. To switch between these control modes, there is a "`switch`" block as observed in the purple area in Fig. A.7.

The GFL used for validation is based on active and reactive power control, as per Section 2.5.3, with both SLC and DLC. The structure, within the "GFL controller" subsystem seen in Fig. A.6, is displayed in Fig. A.7.

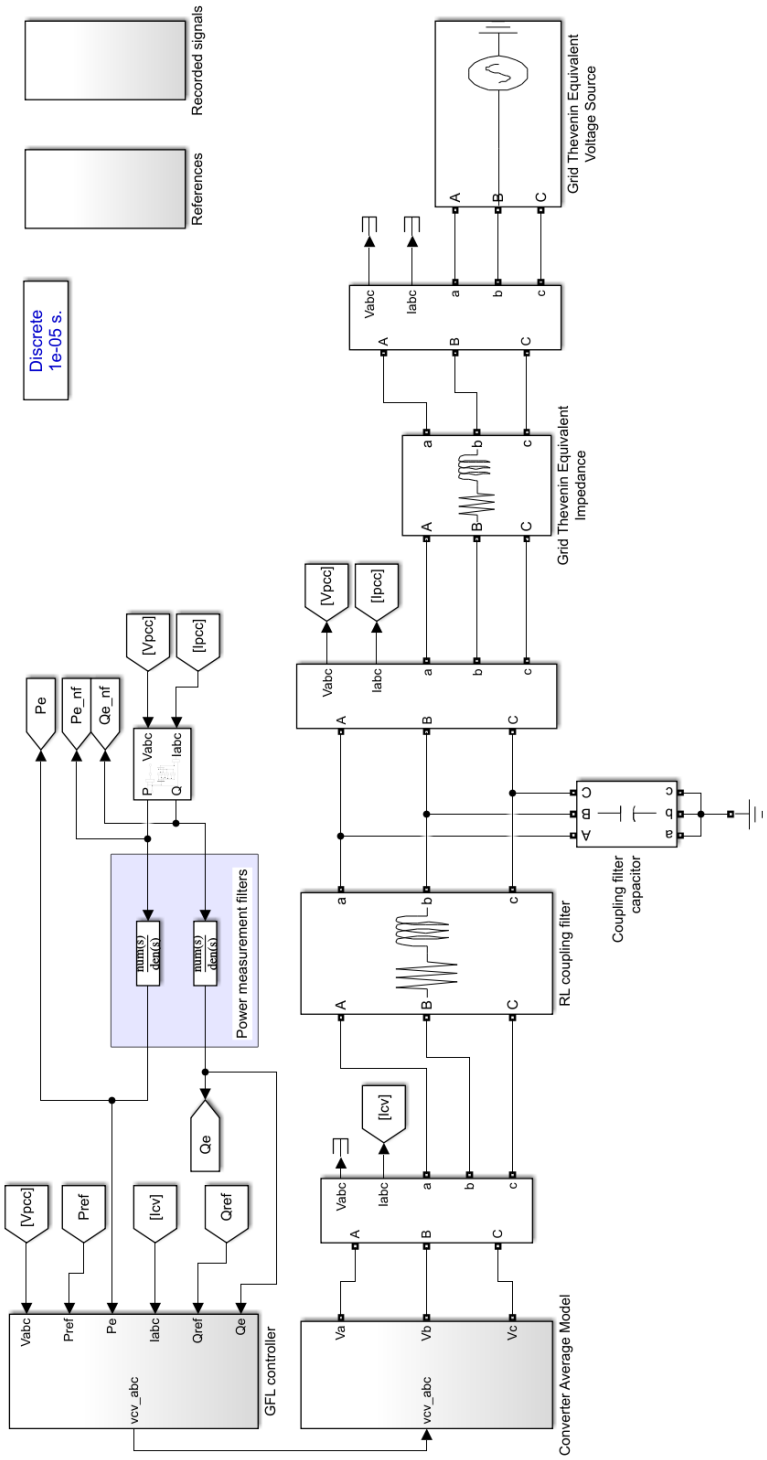

Figure A.6: Upper-level of the Simulink GFL–infinite bus model.

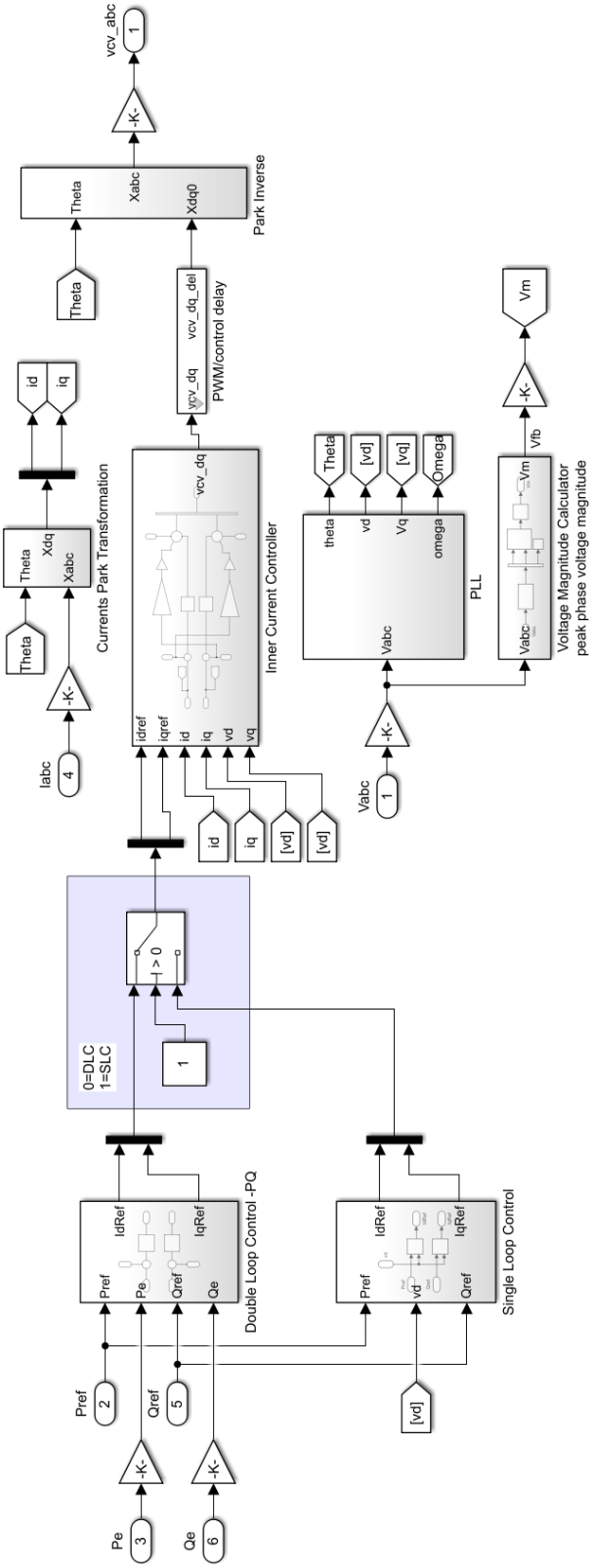

Figure A.7: GFL controller structure Simulink implementation.

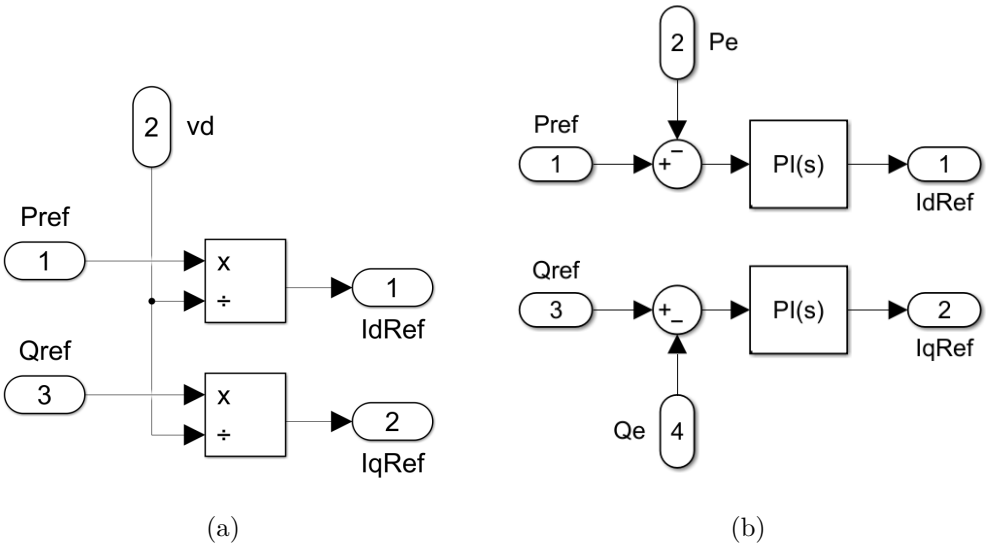

Figure A.8: Simulink implementation of active and reactive power control when using (a) SLC and (b) DLC.

The PLL, as described in Section 2.5.3, is implemented as displayed in Fig. A.9. Note, the "`1/s`" block is an integrator.

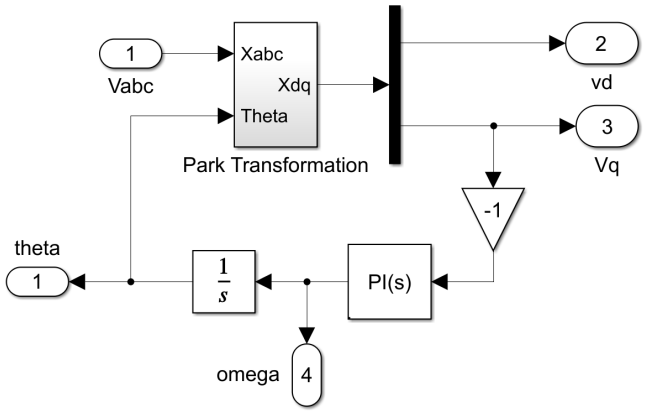

Figure A.9: PLL Simulink implementation.

System Parameters

The system parameters used in the validation tests are summarised in Table A.1. Note, all per unit parameters are on the system base power and voltage.

Table A.1: System parameters used for validation of the GFL small-signal model implementation.

Parameter	Symbol	Value
Simulation time step	τ_{step}	10 μs
System base power	S_{base}	100 MVA
System base voltage (RMS line-to-line)	V_{base}	230 kV
System base frequency	f_{sys}	50 Hz
GFL initial active power reference	P_{ref}	0.5 pu
GFL initial reactive power reference	Q_{ref}	0 pu
Thévenin grid equivalent SCR	SCR	5
Thévenin grid resistance	R_g	0.02 pu
Thévenin grid inductive reactance	$X_{l,g}$	0.2 pu
Output filter resistance	R_f	0.03 pu
Output filter inductive reactance	$X_{l,f}$	0.08 pu
Output filter capacitive reactance	$X_{c,f}$	1/0.074 pu
Power measurement filter cut-off frequency	f_c	5 Hz
Switching frequency	f_s	10 kHz
PWM/control time delay	τ_{pwm}	$1.5/f_s$ s
ICC closed-loop damping ratio, 5% settling time	$\zeta_{icc}, \tau_{st,icc}$	$0.7, 5$ ms
ICC proportional gain, integral gain	$K_{p,icc}, K_{i,icc}$	$\{0.2756, 187.0883\}$ $\mathrm{V_{pu}/A_{pu}}$
ICC voltage feed-forward gain	$K_{ff,v}$	1
PLL proportional gain, integral gain	$K_{p,pll}, K_{i,pll}$	$\{60, 1400\}$ $\mathrm{rad/s/A_{pu}}$
APC proportional gain, integral gain	$K_{p,apc}, K_{i,apc}$	$\{0.25, 25\}$ $\mathrm{A_{pu}/MW_{pu}}$
RPC proportional gain, integral gain	$K_{p,rpc}, K_{i,rpc}$	$\{0.05, 5\}$ $\mathrm{A_{pu}/MVAr_{pu}}$

A.2.1 Validation When Using Single Loop Control

When using SLC, the small-signal model and non-linear Simulink model responses of the active power output, P_e, and the PLL speed measurement, ω_{PLL}, to a 0.1 pu step of active power reference are displayed in Fig. A.10a and Fig. A.10b, respectively.

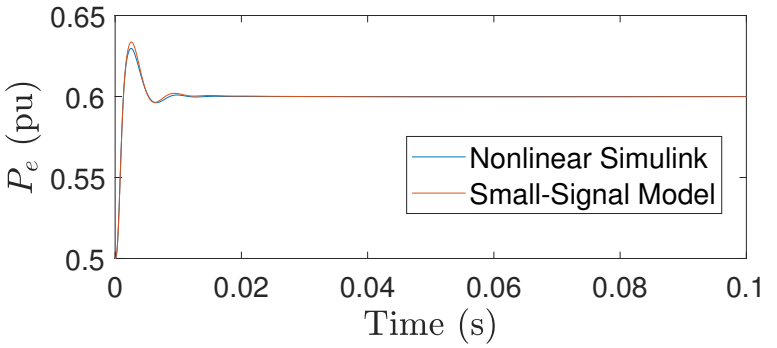

(a)

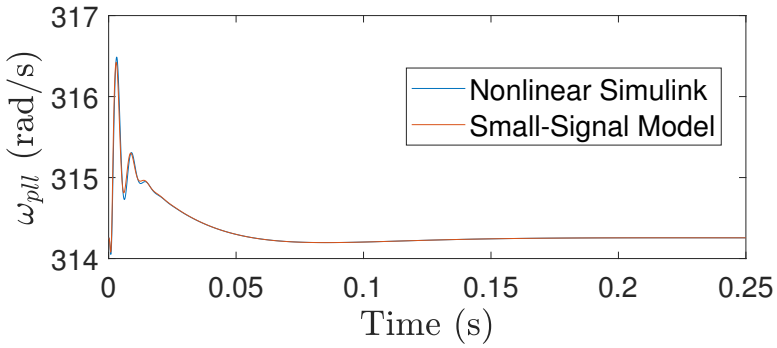

(b)

Figure A.10: Comparison of small-signal model and corresponding non-linear Simulink model of the GFL when adopting SLC when subjected to a step change of 0.1 pu active power reference. Time domain responses for (a) the active power output, P_e, and (b) the PLL speed measurement, ω_{PLL}.

Similarly, when using SLC, the responses of the voltage magnitude (at the output filter capacitor), $|\boldsymbol{v_m}|$, and the reactive power output, Q_e, to a 0.1 pu step of reactive power reference are displayed in Fig. A.11a and Fig. A.11b, respectively.

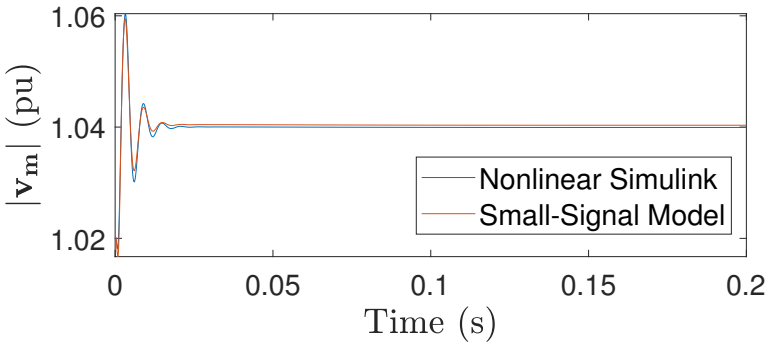

(a)

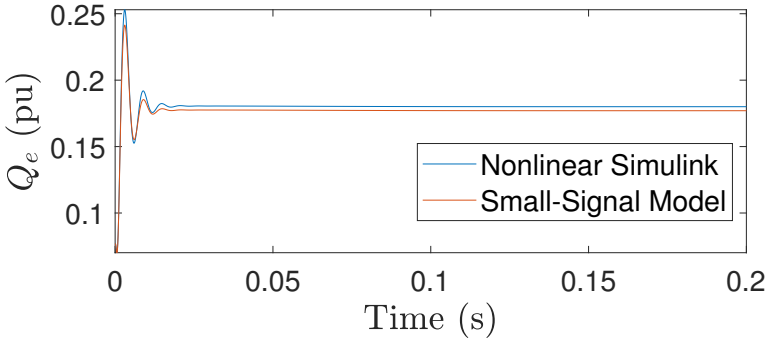

(b)

Figure A.11: Comparison of small-signal model and corresponding non-linear Simulink model of the GFL when adopting SLC when subjected to a step change of 0.1 pu reactive power reference. Time domain responses for (a) the voltage magnitude of the output filter capacitor, $|\boldsymbol{v_m}|$, and (b) the reactive power output, Q_e.

A.2.2 Validation When Using Double Loop Control

When using DLC, the small-signal model and non-linear Simulink model responses of the active power output, P_e, and the PLL speed measurement, ω_{PLL}, to a 0.1 pu step of active power reference are displayed in Fig. A.12a and Fig. A.12b, respectively.

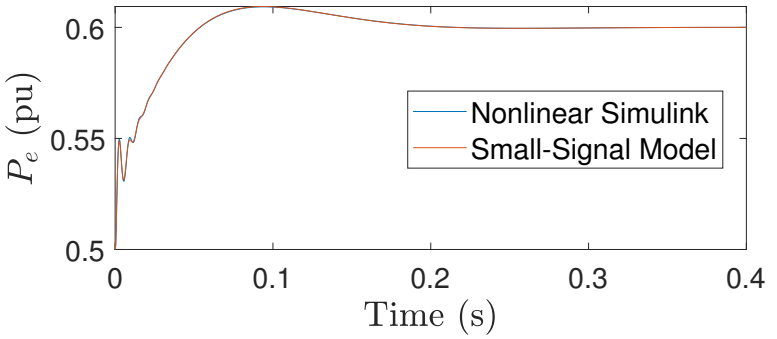

(a)

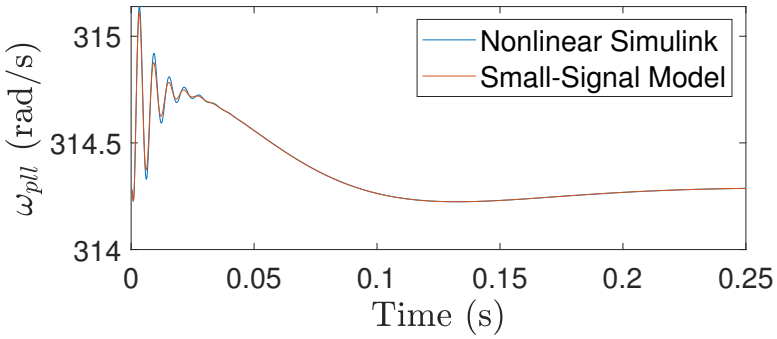

(b)

Figure A.12: Comparison of small-signal model and corresponding non-linear Simulink model of the GFL when adopting DLC when subjected to a step change of 0.1 pu active power reference. Time domain responses for (a) the active power output, P_e, and (b) the PLL speed measurement, ω_{PLL}.

Similarly, when using DLC, the responses of the voltage magnitude (at the output filter capacitor), $|\boldsymbol{v_m}|$, and the reactive power output, Q_e, to a 0.1 pu step of reactive power reference are displayed in Fig. A.13a and Fig. A.13b, respectively.

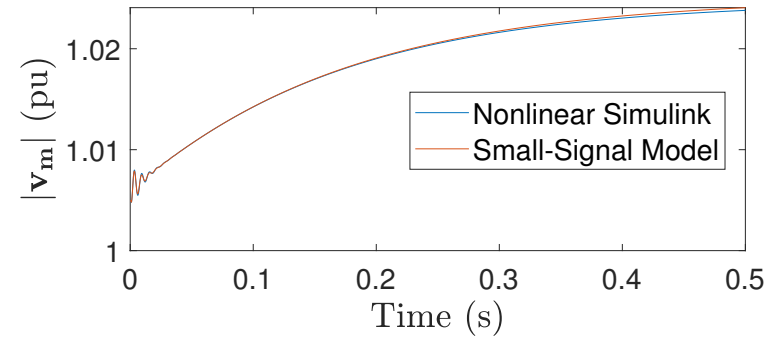

(a)

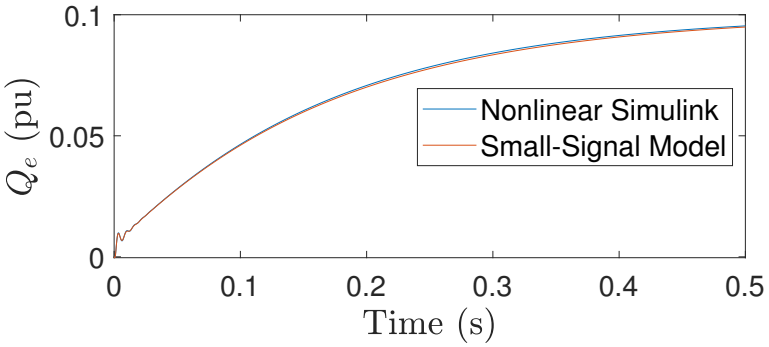

(b)

Figure A.13: Comparison of small-signal model and corresponding non-linear Simulink model of the GFL when adopting DLC when subjected to a step change of 0.1 pu reactive power reference. Time domain responses for (a) the voltage magnitude of the output filter capacitor, $|\boldsymbol{v_m}|$, and (b) the reactive power output, Q_e.

A.3 Grid-Forming Converter–Infinite Bus

Simulink Model

The upper level of the GFM–infinite bus Simulink model, displaying the Simscape Electrical Specialized Power Systems electrical system, the current and voltage measurement locations, the active and reactive power measurement LPFs, and the signal interconnections is displayed in Fig. A.14.

The GFM controller structure is displayed in Fig. A.15. Several of the subsystems of the controller have been detailed already, including the Park and inverse Park transforms (Fig. A.1a and Fig. A.1b), the PWM/control delay (Fig. A.3b), the voltage magnitude calculation (Fig. A.4), and the ICC (Fig. A.5). Further to this, depending on whether SILC or DILC is used, there is a static current reference calculation or an IVC, respectively, as displayed in Fig. A.16 and Fig. A.17. Note, the parameters in the current reference calculation are given names of Rvi2 and Xlvi2 because it can be considered a virtual impedance, although when used in the main body of the thesis, it is used solely to compensate for the output coupling filter (as discussed further in Section 2.5.5). In the IVC Simulink implementation, the previously undefined parameters of Ccv and Kffi represent the filter capacitance (in farads) and feedforward gain of the measured grid output current, respectively. As previously, the gain with value of -K- is a conversion to per unit.

The GFM approach used for the validation is that of droop control, as displayed in Fig. A.18. This incorporates both an active power-frequency and reactive power-voltage droop, with droop gains of mp and mq, respectively. The implementation of the virtual impedance subsystem is displayed in Fig. A.19, where Rvi and Xvi are the virtual resistance and virtual inductive reactance parameters. Note, this virtual impedance is effectively bypassed by setting Rvi and Xvi to zero.

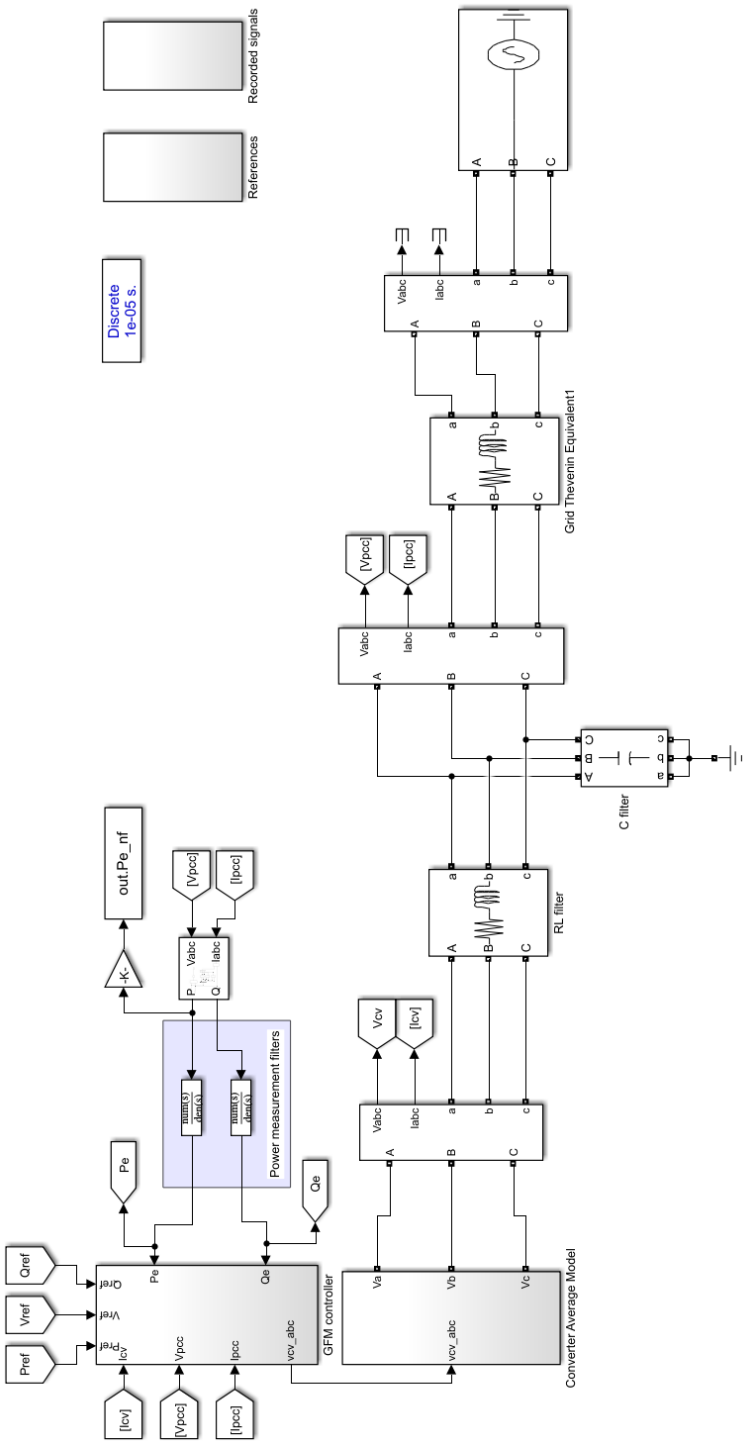

Figure A.14: Upper-level of the Simulink GFM–infinite bus model.

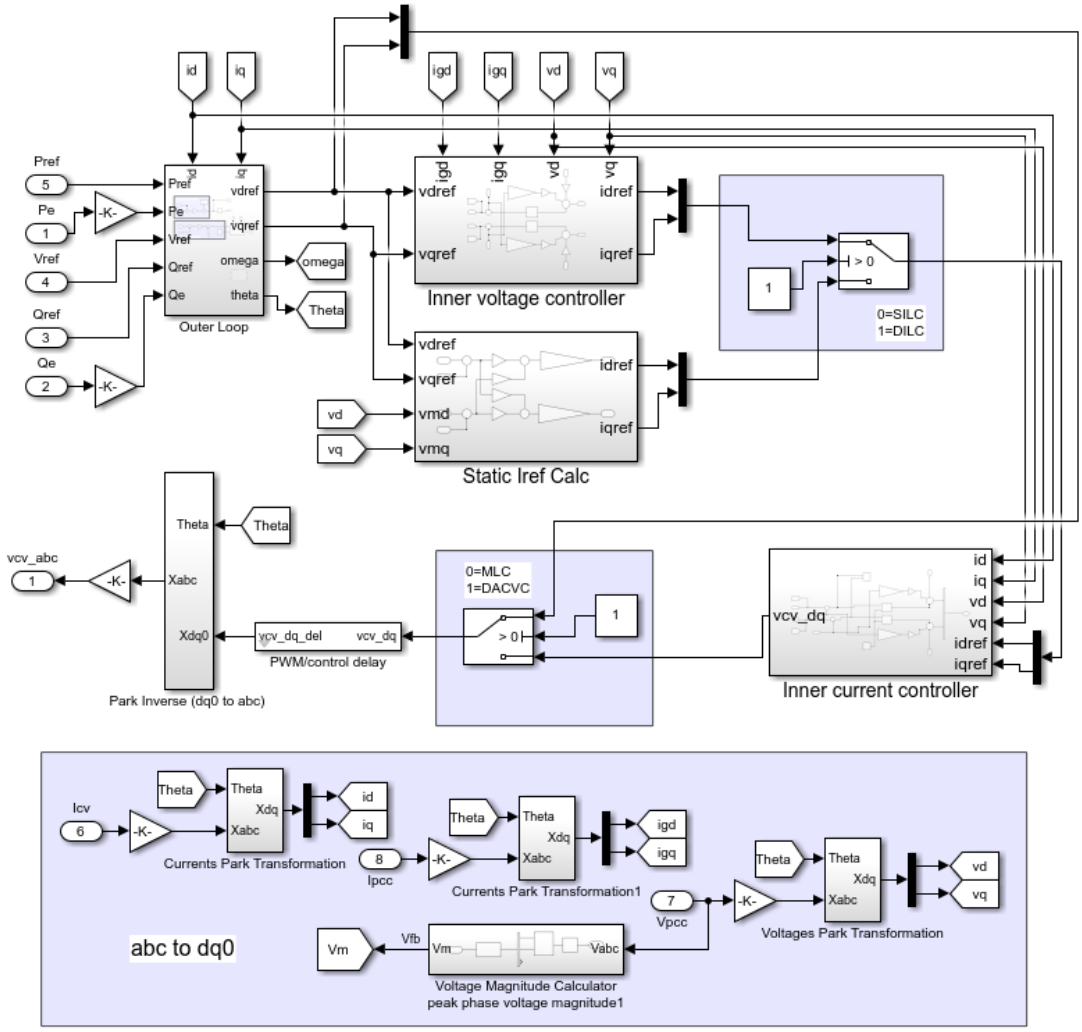

Figure A.15: GFM controller structure Simulink implementation.

System Parameters

The system parameters used in the validation tests are summarised in Table A.2. Note, all per unit parameters are on the system base power and voltage.

A.3.1 Validation When Using Direct AC Voltage Control

When using DACVC, the small-signal model and non-linear Simulink model responses of the active power output, P_e, and the "virtual rotor" speed, ω_{GFM}, to a 0.1 pu step

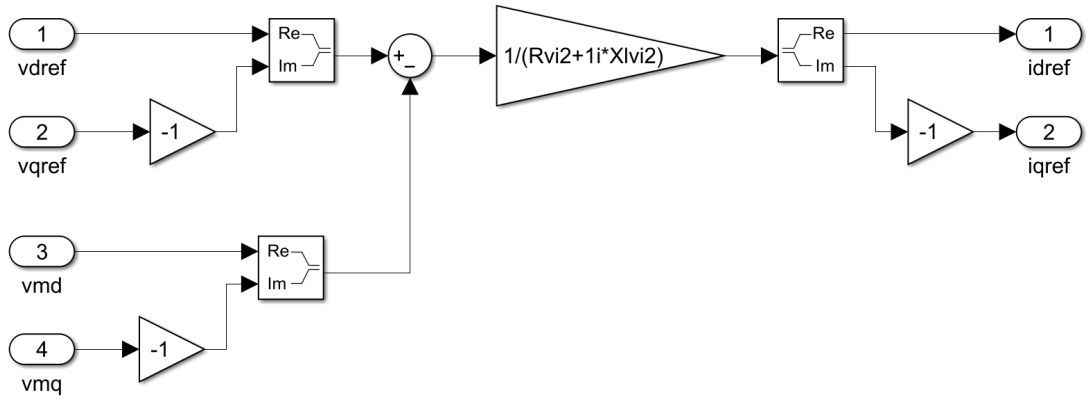

Figure A.16: Simulink implementation of current reference calculation when using SILC.

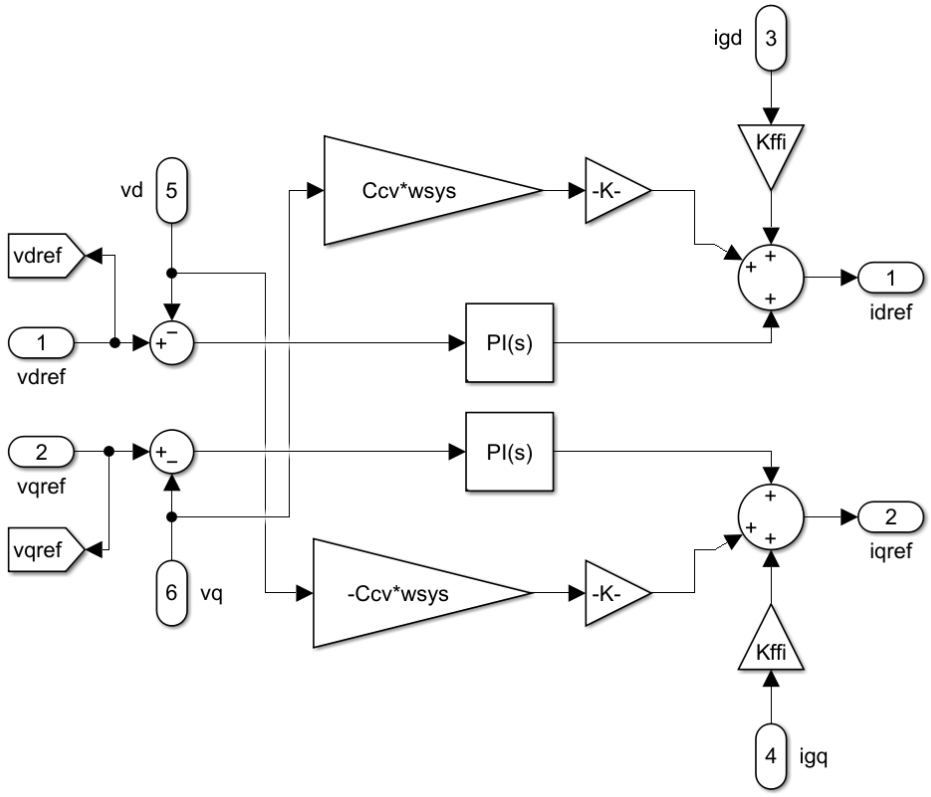

Figure A.17: Simulink implementation of IVC.

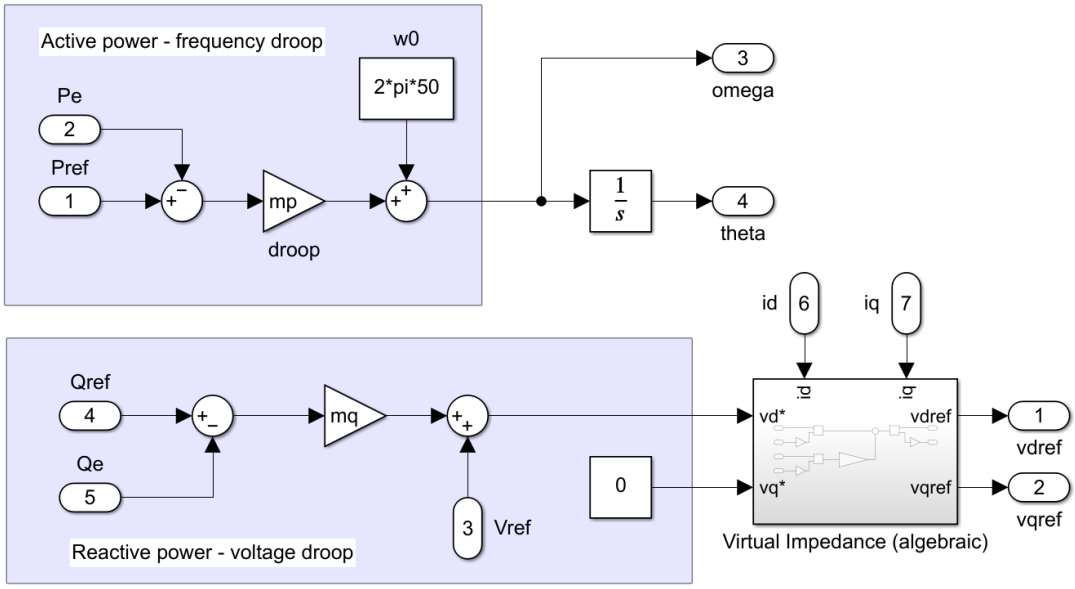

Figure A.18: Simulink implementation of droop control outer controllers. This includes active power-frequency droop, reactive power-voltage droop, and a virtual impedance.

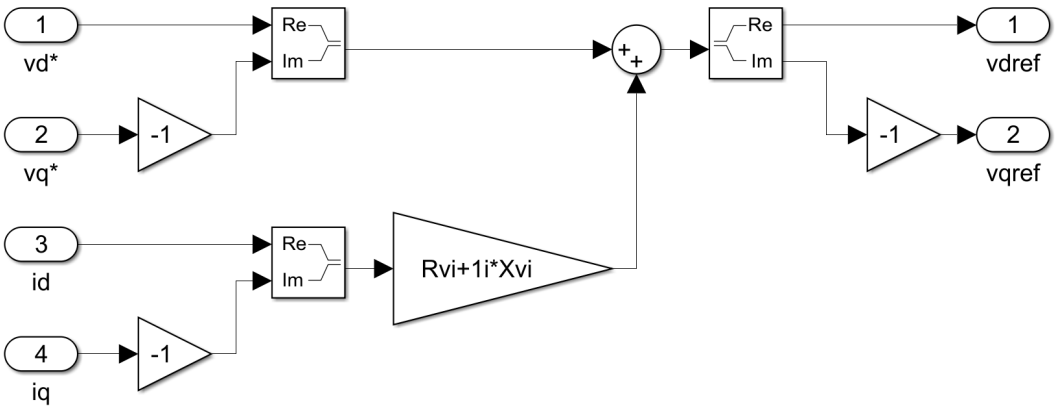

Figure A.19: Simulink implementation of outer controller virtual impedance.

Table A.2: System parameters used for validation of the GFM small-signal model implementation.

Parameter	Symbol	Value
Simulation time step	τ_{step}	10 μs
System base power	S_{base}	100 MVA
System base voltage (RMS line-to-line)	V_{base}	230 kV
System base frequency	f_{sys}	50 Hz
GFL initial active power reference	P_{ref}	0.5 pu
GFL initial reactive power reference	Q_{ref}	0 pu
Thévenin grid equivalent SCR	SCR	5
Thévenin grid resistance	R_g	0.02 pu
Thévenin grid inductive reactance	$X_{l,g}$	0.2 pu
Output filter resistance	R_f	0.03 pu
Output filter inductive reactance	$X_{l,f}$	0.08 pu
Output filter capacitive reactance	$X_{c,f}$	1/0.074 pu
Power measurement filter cut-off frequency	f_c	3.1831 Hz
Switching frequency	f_s	10 kHz
PWM/control time delay	τ_{pwm}	$1.5/f_s$ s
ICC closed-loop damping ratio, 5% settling time	$\zeta_{icc}, \tau_{st,icc}$	$0.7, 1.5$ ms
ICC proportional gain, integral gain	$K_{p,icc}, K_{i,icc}$	$\{0.9886, 2078.8\}$ $\mathrm{V_{pu}/A_{pu}}$
ICC voltage feed-forward gain	$K_{ff,v}$	1
IVC closed-loop damping ratio, 5% settling time	$\zeta_{ivc}, \tau_{st,ivc}$	$0.7, 45$ ms
IVC proportional gain, integral gain	$K_{p,ivc}, K_{i,ivc}$	$\{0.0314, 2.1365\}$ $\mathrm{A_{pu}/V_{pu}}$
IVC current feed-forward gain	$K_{ff,i}$	1
APC droop gain	m_p	$0.0125 \times 2\pi f_{sys}$ $\mathrm{rad/s/MW_{pu}}$
RPC droop gain	m_q	0.001 $\mathrm{V_{pu}/MVAr_{pu}}$
Virtual impedance resistance	R_{vi}	0 pu
Virtual impedance inductive reactance	$X_{l,vi}$	0.05 pu

of active power reference are displayed in Fig. A.20a and Fig. A.20b, respectively.

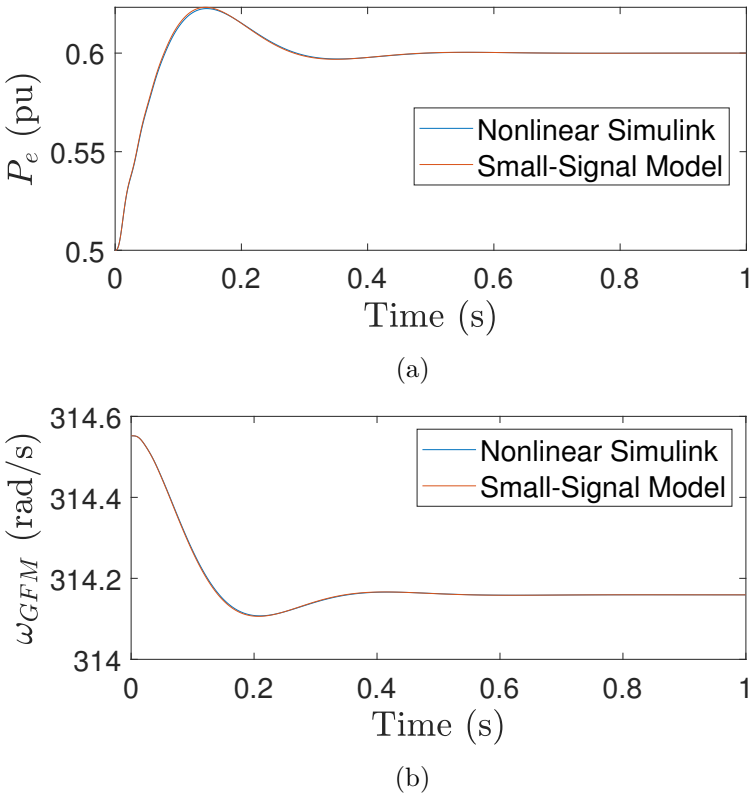

Figure A.20: Comparison of small-signal model and corresponding non-linear Simulink model of the GFM when adopting DACVC when subjected to a step change of 0.1 pu active power reference. Time domain responses for (a) the active power output, P_e, and (b) the "virtual rotor" speed, ω_{GFM}.

Similarly, when using DACVC, the responses of the voltage magnitude (at the output filter capacitor), $|\boldsymbol{v_m}|$, and the reactive power output, Q_e, to a 0.1 pu step of voltage magnitude reference are displayed in Fig. A.21a and Fig. A.21b, respectively.

A.3.2 Validation When Using Single Inner Loop Control

For the validation of the SILC case, the current reference calculation, which can be considered another virtual impedance, is set to compensate for the output filter impedance as per Section 2.5.5.

Note, in this specific case with system parameters as outlined in Table A.2, the system is unstable. Since optimal tuning is not the target of this appendix, we simply

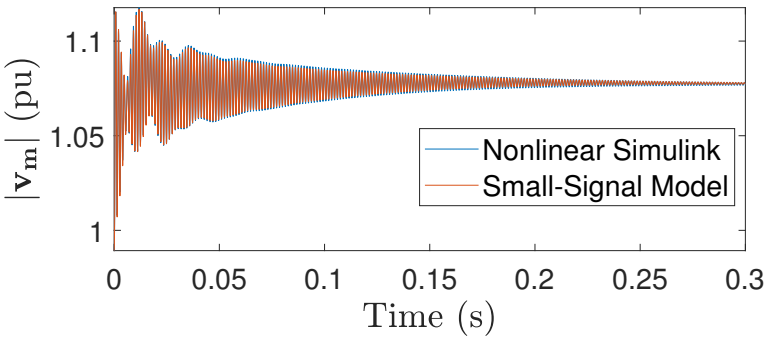

(a)

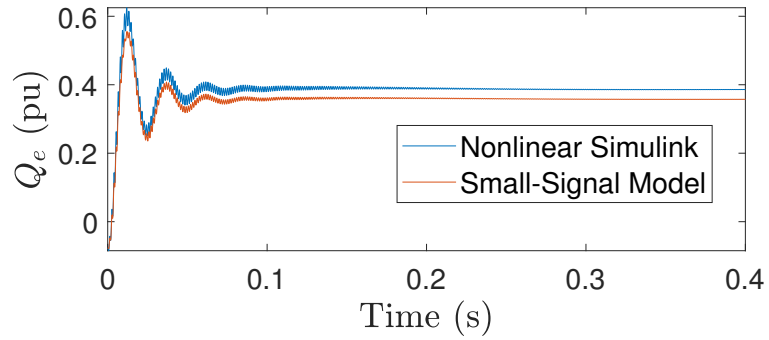

(b)

Figure A.21: Comparison of small-signal model and corresponding non-linear Simulink model of the GFM when adopting DACVC when subjected to a step change of 0.1 pu voltage magnitude reference. Time domain responses for (a) the voltage magnitude of the output filter capacitor, $|\boldsymbol{v_m}|$, and (b) the reactive power output, Q_e.

induce stability by removing the virtual impedance (i.e., setting $X_{l,vi}$ from Table A.2 to 0 pu), and increasing the switching frequency to an unrealistically high value of 1000 kHz. Note, increasing the switching frequency in this case results in a reduction of the PWM/control delay, in addition to the ICC 5% settling time (which is set to be 10× slower than the PWM/control delay). In order to accommodate the resultant faster timescales, the simulation time step is reduced to 0.1 μs.

When using SILC, the small-signal model and non-linear Simulink model responses of the active power output, P_e, and the "virtual rotor" speed, ω_{GFM}, to a 0.1 pu step of active power reference are displayed in Fig. A.22a and Fig. A.22b, respectively.

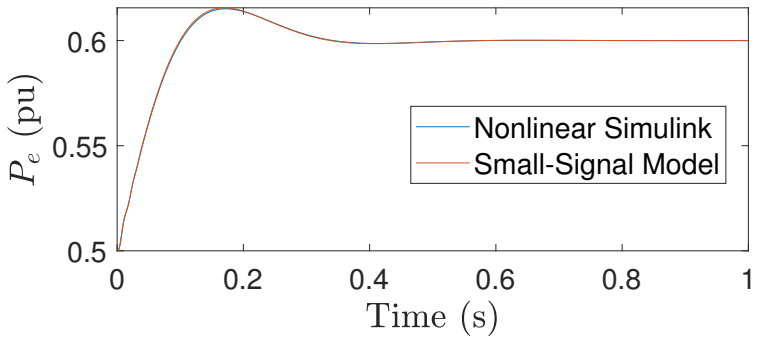

(a)

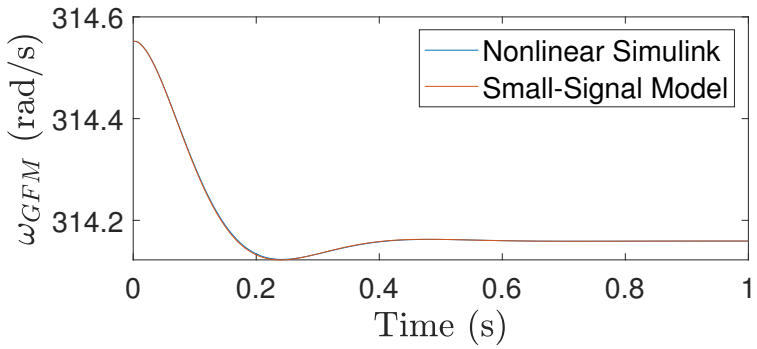

(b)

Figure A.22: Comparison of small-signal model and corresponding non-linear Simulink model of the GFM when adopting SILC when subjected to a step change of 0.1 pu active power reference. Time domain responses for (a) the active power output, P_e, and (b) the "virtual rotor" speed, ω_{GFM}.

Similarly, when using SILC, the responses of the voltage magnitude (at the output filter capacitor), $|\boldsymbol{v_m}|$, and the reactive power output, Q_e, to a 0.1 pu step of voltage

magnitude reference are displayed in Fig. A.23a and Fig. A.23b, respectively.

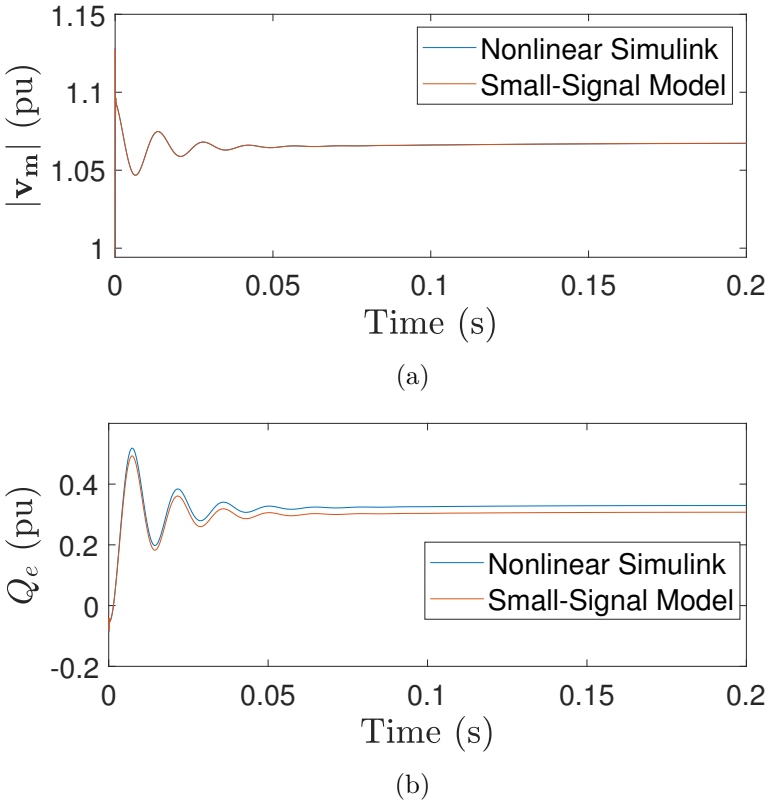

Figure A.23: Comparison of small-signal model and corresponding non-linear Simulink model of the GFM when adopting SILC when subjected to a step change of 0.1 pu voltage magnitude reference. Time domain responses for (a) the voltage magnitude of the output filter capacitor, $|\boldsymbol{v_m}|$, and (b) the reactive power output, Q_e.

A.3.3 Validation When Using Double Inner Loop Control

When using DILC, the small-signal model and non-linear Simulink model responses of the active power output, P_e, and the "virtual rotor" speed, ω_{GFM}, to a 0.1 pu step of active power reference are displayed in Fig. A.24a and Fig. A.24b, respectively.

Similarly, when using DILC, the responses of the voltage magnitude (at the output filter capacitor), $|\boldsymbol{v_m}|$, and the reactive power output, Q_e, to a 0.1 pu step of voltage magnitude reference are displayed in Fig. A.25a and Fig. A.25b, respectively.

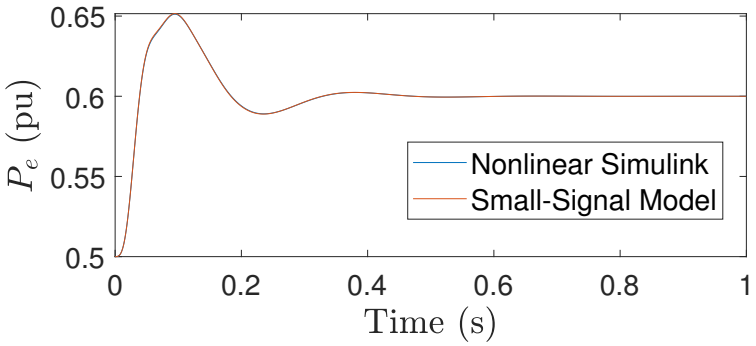

(a)

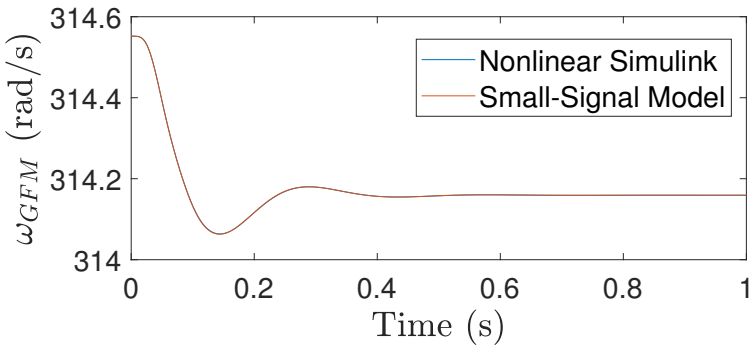

(b)

Figure A.24: Comparison of small-signal model and corresponding non-linear Simulink model of the GFM when adopting DILC when subjected to a step change of 0.1 pu active power reference. Time domain responses for (a) the active power output, P_e, and (b) the "virtual rotor" speed, ω_{GFM}.

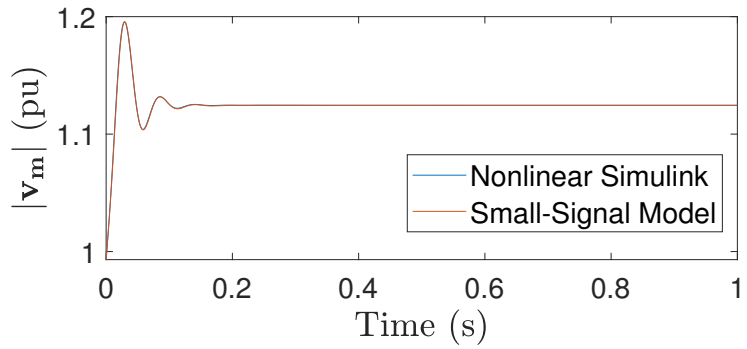

(a)

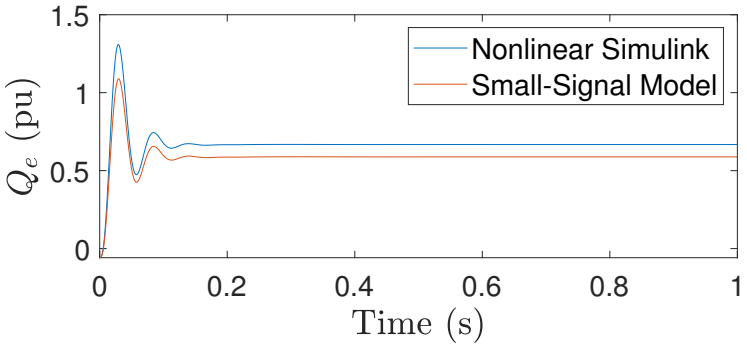

(b)

Figure A.25: Comparison of small-signal model and corresponding non-linear Simulink model of the GFM when adopting DILC when subjected to a step change of 0.1 pu voltage magnitude reference. Time domain responses for (a) the voltage magnitude of the output filter capacitor, $|\boldsymbol{v_m}|$, and (b) the reactive power output, Q_e.

A.4 Multi-Machine System

Since the modelling was completed using a tool created by the author of this thesis [108], the overall system small-signal model requires validation to ensure all processes (i.e., power flow, initialisation, small-signal model creation, module combinations, etc.) are free from errors.

Due to difficulties with initialisation of Simscape Electrical models in multi-machine systems[1], the Julia [111] open-source Sienna modelling framework by National Renewable Energy Laboratory (NREL) is used. In particular, the `PowerSystems.jl` and `PowerSimulationsDynamics.jl` [112] packages are utilised. These approach power system modelling in a similar way to that of [108], whereby a power flow analysis is used to determine the initial operating point before calculating the internal initial states of each system element. Furthermore, they generate the models modularly. Due to the similarities, it is possible to initialise the Sienna power system model at the exact same operating point, i.e., without any initial transients, as would be the case in Simulink, which may cause the system to settle at a different operating point. Furthermore, the Sienna modelling framework enables small-signal analysis through the use of automatic differentiation. This means that the eigenvalues can be used for direct validation of the small-signal model.

To validate the automatic and modular initialisation and compilation procedures, a simple 2-machine system is adopted with both machines being a SG. This is the same system utilised in Chapter 4 whereby the SGs are implemented with constant excitation and constant mechanical torque input. Furthermore, the `PowerSimulationsDynamics.jl` package includes the Sauer and Pai 6^{th} order linear magnetic SG model which is similar to the 8^{th} order model used in this thesis but with stator transients neglected. This same assumption is applied to the MATLAB small-signal model implementation (i.e., the stator impedance is modelled algebraically rather than dynamically, although the network elements are still modelled dynamically)

[1]For the previous OMIB system validations, the Simulink model was run until initialised before extracting the power flow conditions to be manually fed to the initialisation and compilation procedure of the small-signal models.

for better comparison. Therefore, the multi-machine validation here also doubles as validation of the SG model implementation.

The eigenvalues are obtained from both the model developed with the Sienna modelling framework using `PowerSimulationsDynamics.jl` (hereafter referred to as the Julia model) and the model developed using the MATLAB small-signal modelling tool developed and used in this thesis (hereafter referred to as the MATLAB model). The eigenvalues are displayed in Fig. A.26. The only discrepancy is the zero eigenvalue present in the MATLAB model but not the Julia model which can be observed most clearly in Fig. A.26c. It is removed from the analysis by the PowerSimulationsDynamics.jl package because this is a redundant eigenvalue related to the modelling approach whereby the reference frame of a chosen machine is taken as the reference frame of the system (i.e, for the reference machine we have a redundant state in the form of the angle between the reference frames of the machine and the system). This is further described in [10–12]. As such, the two models are seen to have equivalent eigenvalue-described linear dynamics, thereby validating the multi-machine initialisation and compilation procedure developed and utilised in this thesis, as well as the implementation of the Sauer and Pai SG model [11].

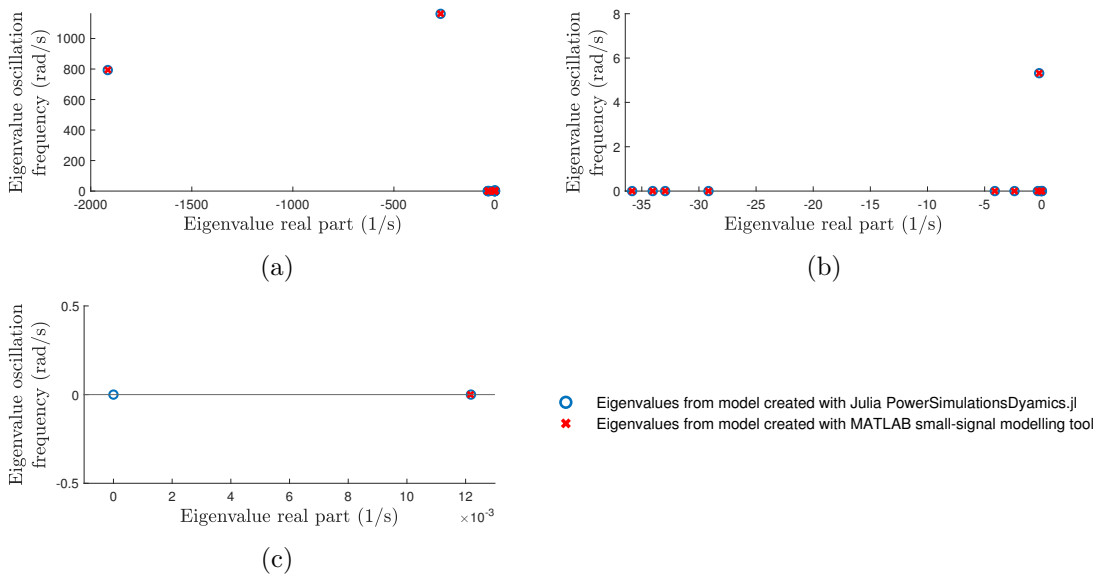

Figure A.26: Comparison of the eigenvalues as obtained form the model developed with (blue circle) `PowerSimulationsDynamics.jl` Julia package and (red 'x') the MATLAB small-signal modelling tool developed and used in this thesis. The subfigures display different eigenvalues from the same system where (c) is a zoomed version of (b) which is a zoomed version of (a).

Appendix B

Electromechanical Interactions Between Synchronous Generators and Grid-Forming Converters

B.1 Introduction

From the literature outlined in the introduction of Chapter 3 as well as the discussions in Section 1.2, it can be determined that with the inclusion of GFMs, further consideration to dynamic interactions needs to be given, since new instability mechanisms might appear in a complex power system. Furthermore, considering power systems will most probably involve SGs for years to come, the interactions between CIGs and SGs should be well understood. Additionally, with GFMs being recognised as a potential solution for maintaining stability, interactions specifically between SGs and GFMs, as well as between multiple GFMs, should be studied carefully.

The fact that GFMs control active power through the voltage angle, and have a resultant inherent frequency synchronisation, suggests the possibility of electromechanical interactions between multiple machines [246]. Therefore, an initial investigation into interactions between a GFM and an SG as well as between two GFMs is performed using eigenvalue analysis. Moreover, the impact of GFM control gains and transmission line lengths on such oscillatory modes and interactions between SGs and

GFMs is also investigated.

Although this investigation is focused on electromechanical modes (e.g., a relatively simple low-order SG model is used), the dynamics of the network elements (transmission lines and constant impedance loads) are included because high frequency phenomena have been proven to be significant in the stability of systems with substantial levels of CIGs [59, 119, 247] (see the discussion in Section 1.2.3 for more detail on this). Subsequently, a series of high frequency oscillatory modes closely associated with transmission line dynamics are also identified, one of which is found to be of interest in terms of stability limits (and influenced by GFM controller parameters). Such results need to be considered with care due to the otherwise low-order nature of the models. However, this investigation is performed as a preliminary step applied on a small system to more easily identify and investigate such interactions.

The remainder of the electromechanical interaction-focused investigation in this appendix is structured as follows: Section B.2 describes the modelling of the network components and Section B.3 details the case studies performed including the network layouts; Section B.4 and Section B.5 discuss the results of the SG-GFM and GFM-GFM system eigenvalue analyses, respectively. Section B.6 details the parametric sweep sensitivity analyses, and Section B.7 provides the conclusions.

The work in this appendix was published as part of the PowerTech2021 conference proceedings [248].

B.2 Component Modelling

The component models included in this investigation are a SG, a GFM, RL branch transmission lines and a static constant impedance RL load.

B.2.1 Synchronous Generator

The SG model comprises the swing equation along with an RL impedance but neglects rotor circuit dynamics as in this study we are focusing on identifying oscillatory modes in the electromechanical range. The swing equation captures the relationship between

the SG rotor speed (and hence angle) and the difference between the input mechanical and output electrical power. This relationship can be written as,

$$\dot{\omega_r} = \frac{1}{2H}\left(P_m - P_e - K_D\Delta\omega - K_{gov}\Delta\omega\right) \tag{B.1}$$

$$\dot{\delta_r} = \omega_r \tag{B.2}$$

where ω_r and δ_r are the rotor speed and angle, respectively. The damping coefficient is termed K_D and the inertia constant, H. Finally, the mechanical and electrical powers are denoted by P_m and P_e, respectively. A speed governor has been included which has been simplified to a proportional gain, K_{gov}, acting on a change of rotor speed, $\Delta\omega$, to augment the mechanical input power.

The electrical part of the SG model consists of the resistance and inductance resulting from the armature coils in addition to the inductance attributed to the armature reaction. The combined impedance is termed the synchronous impedance, $Z_s = R_s + jX_s$, with R_s being the armature resistance and X_s combining the effects of the armature leakage inductance and armature reaction. The transformation from the SG dq0-frame to the common dq0-frame is performed behind the synchronous impedance. However, there is a possible alternative whereby the transformation is performed at the SG terminals (after the synchronous impedance). This synchronous impedance is modelled dynamically, in accordance with (2.21).

B.2.2 Grid-Forming Converter

The VSC section of the GFM is represented with an averaged model which neglects switching effects and the time delay usually associated with the employment of PWM. There is also a harmonic filter containing a series RL impedance followed by a parallel capacitance at the GFM output terminal, as per Fig. 2.4.

The control structure of the GFM contains two main loops. The first is the power loop which manipulates the virtual rotor speed, and hence angle, with a PI controller acting on the difference between the reference power P_{ref} and the measured (or feedback) power P_{fb}. This is the same principle as the SG swing equation and

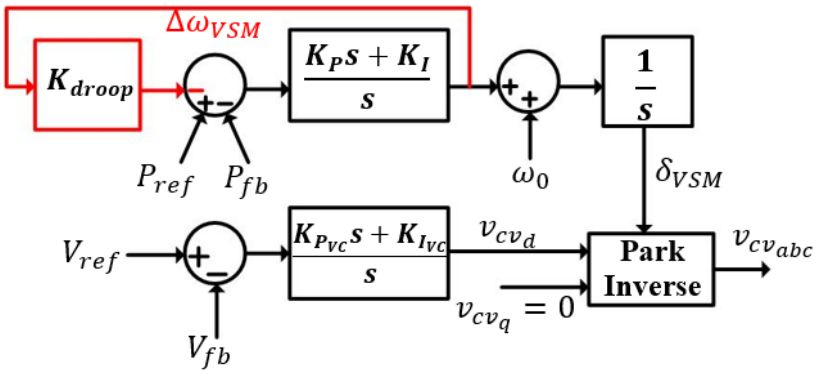

Figure B.1: GFM control scheme block diagram for the electromechanical-focused investigation.

the two systems can be directly compared in their second order dynamic responses by looking at the characteristic equation of their transfer functions. This allows for the equivalent inertia and damping values to be described in terms of the PI controller gains, K_I and K_P. From this, it can be determined that K_I impacts inertia while both K_I and K_P impact damping. However, it can be noted that there are differences in the steady state response since the PI controller acts to bring the output power exactly to its reference, that is there is no damping feedback term acting on the change of rotor speed as there is in the swing equation (although the red droop branch in Fig. B.1 essentially solves this). The second loop is the voltage loop, acting as an AVR by maintaining the voltage magnitude at the filtering capacitor, V_{fb}, to the reference value, V_{ref}.

In the test case with only GFMs, described later, one of the machines is also equipped with frequency droop control to balance the active power in the system. The block diagram for the GFM control structure is displayed in Fig. B.1. Note, the frequency droop branch (displayed in red) is only present for one of the machines in the only-GFM test case, for better equivalence to the SG-GFM test case.

B.2.3 Constant Impedance Load

The load is modelled as a constant series RL impedance. The values of the resistance and inductance are calculated with

$$R_{load} = \frac{V_n^2}{P_{load}} \tag{B.3}$$

$$L_{load} = \frac{V_n^2}{\omega_0 \times Q_{load}} \tag{B.4}$$

where V_n is the base voltage and ω_0 is the base electrical frequency. The desired load active and reactive powers are denoted by P_{load} and Q_{load}, respectively.

B.3 Systems Under Study

Two networks with the layout in Fig. B.2 are analysed in this work. The 'swing' machine being the SG in one test case and the droop-augmented GFM in the other. Further signals within the machines include $i_{cv_{dq}}$ which is the current through the RL section of the GFM output filter and $i_{sg_{dq}}$ which is simply equivalent to $i_{tl1_{dq}}$ in this case. Additionally, $v_{cv_{dq}}$ is the voltage behind the filter impedance in the GFM and E_{dq} is the internal generated voltage of the SG. In the GFM-GFM network, all GFM specific parameters or signals are given a subscript of '1' if related to the left machine or '2' if related to the right.

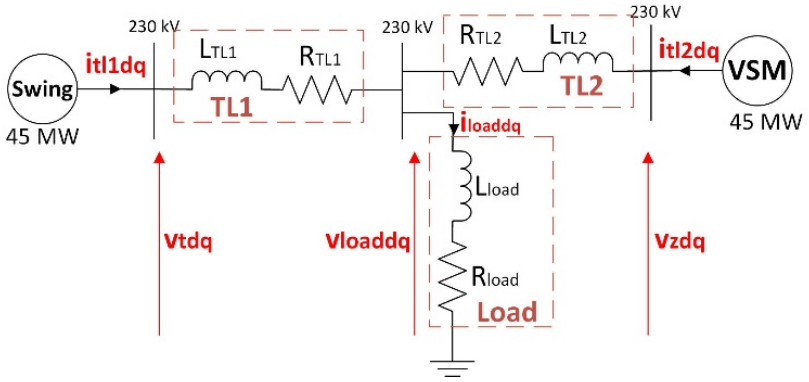

Figure B.2: Final network layout single line diagram for the electromechanical-focused investigation.

Appendix B. Electromechanical Interactions Between Synchronous Generators and Grid-Forming Converters

For both network configurations being tested, small-signal analysis utilising eigenvalues is performed. The use of eigenvalue analysis [10] offers insight into the oscillatory modes that might be excited after a disturbance such as a load increase. With this, potential electromechanical modes can be identified by calculating the frequency of the modes and extracting those in the proximity of up to 3 Hz. Typically, with SGs, local modes are in the range of 1 to 3 Hz and inter-area modes are less than 1 Hz [11]. The eigenvalues and associated frequency and damping ratio are obtained as in [10]. The next step is to calculate the PF of each state for each mode, as per Section 2.1.2. This gives an idea of which states are the most involved in specific oscillatory modes and is especially useful in identifying interactions between two machines.

Finally, parametric sweeps are performed to determine the impact on the small-signal stability of different network elements such as transmission line lengths or GFM controls. The parameters associated with each test case are displayed in Table B.1. The GFM parameters are common to both machines in the only-GFM network with the swing machine also having a droop parameter of $K_{droop} = 0.5\,(100 \times 10^6)$.

Table B.1: Model parameters for electromechanical-focused investigation.

SM *Parameter*	***Value***	***GFM Parameter***	***Value***
H	*4*	K_P	$9{\times}10^{-9}$
$K_D{+}K_{gov}$	*≅10*	K_I	$4{\times}10^{-8}$
R_S	*10.58 Ω*	$K_{P_{VC}}$	*0.1*
L_S	*0.5052 H*	$K_{I_{VC}}$	*50*
P_m	*50 MW*	R_f	*5.29 Ω*
V_{ref}	*230 kV*	L_f	*0.1347 H*
Network Parameter	***Value***	C_f	*1 μF*
$R_{TL1}{=}R_{TL2}$	*35.688 Ω*	P_{ref}	*50 MW*
$L_{TL1}{=}L_{TL2}$	*0.1272 H*	V_{ref}	*230 kV*

B.4 SG-GFM Network Eigenvalue Analysis

The procedure explained above is performed for the network containing the SG and GFM combination. The eigenvalues are presented in Table B.2. This table also includes the frequency of the mode and the corresponding damping ratio. Using this information, the electromechanical mode is identified as λ_9 & λ_{10}. Following this, the PFs representing the contribution of each state to each oscillatory mode were calculated and those with significant contribution (> 10 %) were added to the table.

Table B.2: SG-GFM-load system eigenvalues.

Eigenvalues	***Value***	***Frequency***	***Damping Ratio***	***Contributing States***
λ_1 & λ_2	$-9.56 \cdot 10^3 \pm j8.42 \cdot 10^4$	13.396 kHz	11.28 %	$i_{sm_{dq}}$, $i_{tl2_{dq}}$
λ_3 & λ_4	$-77.07 \pm j3843$	612 Hz	2.01 %	$v_{z_{dq}}$, $i_{cv_{dq}}$
λ_5 & λ_6	$-52.38 \pm j3043$	484 Hz	1.72 %	$v_{z_{dq}}$, $i_{cv_{dq}}$
λ_7 & λ_8	$-216.15 \pm j722.71$	115 Hz	28.65 %	$i_{cv_{dq}}$, $i_{sm_{dq}}$, $i_{tl2_{dq}}$
λ_9 & λ_{10}	$-1.5661 \pm j10.57$	1.68 Hz	14.65 %	ω_r, δ_{GFM}

The most significant states in contributing to the electromechanical mode are ω_r and δ_{GFM}. This clearly suggests an interaction between the SG and GFM, confirming the expected behaviour.

Techniques previously used to address interactions between SGs will likely need to be considered as GFM-coupled RESs are integrated.

High frequency oscillatory modes are also present, the most interesting being λ_3 to λ_6 which are seen to have very low damping. Despite the low damping ratio associated with some of these modes, they are damped very quickly in time. The damping ratio represents attenuation of the mode per cycle and with high frequency, the oscillation does not last long in time. Through parametric sweeps (excess to those in the scope of this appendix), the eigenvalues of λ_3 to λ_6 were affected by the GFM voltage loop controls as well as the transmission line lengths, as expected from the contributing

states which includes a small participation from the voltage loop integrator state, V_{int}, of 0.19% for λ_3 & λ_4 and 0.27% for λ_5 & λ_6.

The very fast oscillatory mode of 13.396 kHz was only found to be affected by the transmission line length and not by any of the GFM control parameters. Also, the remaining mode of 115 Hz is discussed later in regard to the K_P parametric sweep.

B.5 GFM-GFM Network Eigenvalue Analysis

In a similar manner, the eigenvalues and corresponding attributes for the GFM-GFM network are presented in Table B.3. The electromechanical mode is this time identified to be λ_{13} & λ_{14}. Again, the PFs are calculated and contributing states of each mode are shown in Table B.3. The states with the highest contribution to the electromechanical modes are found to be P_{int_1}, P_{int_1}, and δ_{GFM_2}. These states are associated with the active power loops of the GFMs and suggest an electromechanical interaction. High frequency modes are also present in this network with analysis being equivalent to those in the SG-GFM network but with the addition of two oscillatory modes denoted in this network by λ_7 to λ_{10}. These are found to have similar characteristics to λ_3 to λ_6 for both networks.

Table B.3: GFM-GFM-load system eigenvalues.

Eigenvalues	***Value***	***Frequency***	***Damping Ratio***	***Contributing States***
λ_1 & λ_2	$-9.51\cdot10^3 \pm j8.36\cdot10^4$	13.303 kHz	11.31 %	$i_{tl1_{dq}}$, $i_{tl2_{dq}}$
λ_3 & λ_4	$-73.7\pm j4271$	680 Hz	1.73 %	$v_{z1_{dq}}$,$v_{z2_{dq}}$
λ_5 & λ_6	$-75\pm j3636$	579 Hz	2.06 %	$v_{z1_{dq}}$,$v_{z2_{dq}}$
λ_7 & λ_8	$-12.46\pm j3065$	488 Hz	0.41 %	v_{z1_d}, i_{cv1_d} v_{z2_d}, i_{cv2_d}
λ_9 & λ_{10}	$-14.52\pm j2514$	400 Hz	0.58 %	v_{z1_q}, i_{cv1_q} v_{z2_q}, i_{cv2_q}
λ_{11} & λ_{12}	$-155.1\pm j316.5$	50.4 Hz	44 %	$i_{tl1_{dq}}$, $i_{tl2_{dq}}$
λ_{13} & λ_{14}	$-2.8\pm j3.7$	0.589 Hz	60.4 %	P_{int_1}, P_{int_2},δ_{VSM_2}

B.6 Parametric Sweeps

To further the contribution of this work, parametric sweeps were performed for several different network and control parameters to determine their impact on the oscillatory modes.

The eigenvalues of interest are displayed with non-essential modes being omitted. The first investigation increased the lengths of the transmission lines. The resistance and reactance per kilometre of both lines are chosen by calculating the required rated current and selecting from the relevant table of cable sizes [249]. Fig. B.3a displays the result of varying the TL1 and TL2 lengths from 40 to 120 km simultaneously. The next two investigations are performed for the GFM power loop PI controller gains. The plots for the proportional gain, K_P, and integral gain, K_I, are displayed in Fig. B.3b to B.3c and Fig. B.3d, respectively. K_P was swept from 0 to 1×10^{-6} and K_I was swept from 1×10^{-12} to 1×10^{-5}. The same sweeps are performed in the GFM-GFM case and similar trends are observed; therefore, these have not been presented here. Additionally, the PI gains of the power loop for the droop-augmented-GFM were swept with the same range as in the other GFM. These sweeps are displayed in Fig. B.3e and Fig. B.3f. Finally, the impact of the frequency droop gain, K_{droop}, is investigated. This parametric sweep is displayed in Fig. B.3g and ranges from 0 to 10 (100×10^6).

B.6.1 SG-GFM Network Parametric Sweep Results

When analysing Fig. B.3a, it is seen that with an increasing length, the damping ratio of the electromechanical mode decreases from 16.84% to 12.88%. In this test case the mode remains stable but in a different system, the impact of transmission line length might be more critical.

Altering the controller gains shows significant impact on the electromechanical mode in Fig. B.3c and Fig. B.3d. The gain K_I is seen to cause small-signal instability of the electromechanical mode as it is increased whereas K_P can fully damp the interaction, however the oscillation at 115 Hz, seemingly related to network current dynamics, is brought towards the unstable region, as seen in Fig. B.3b.

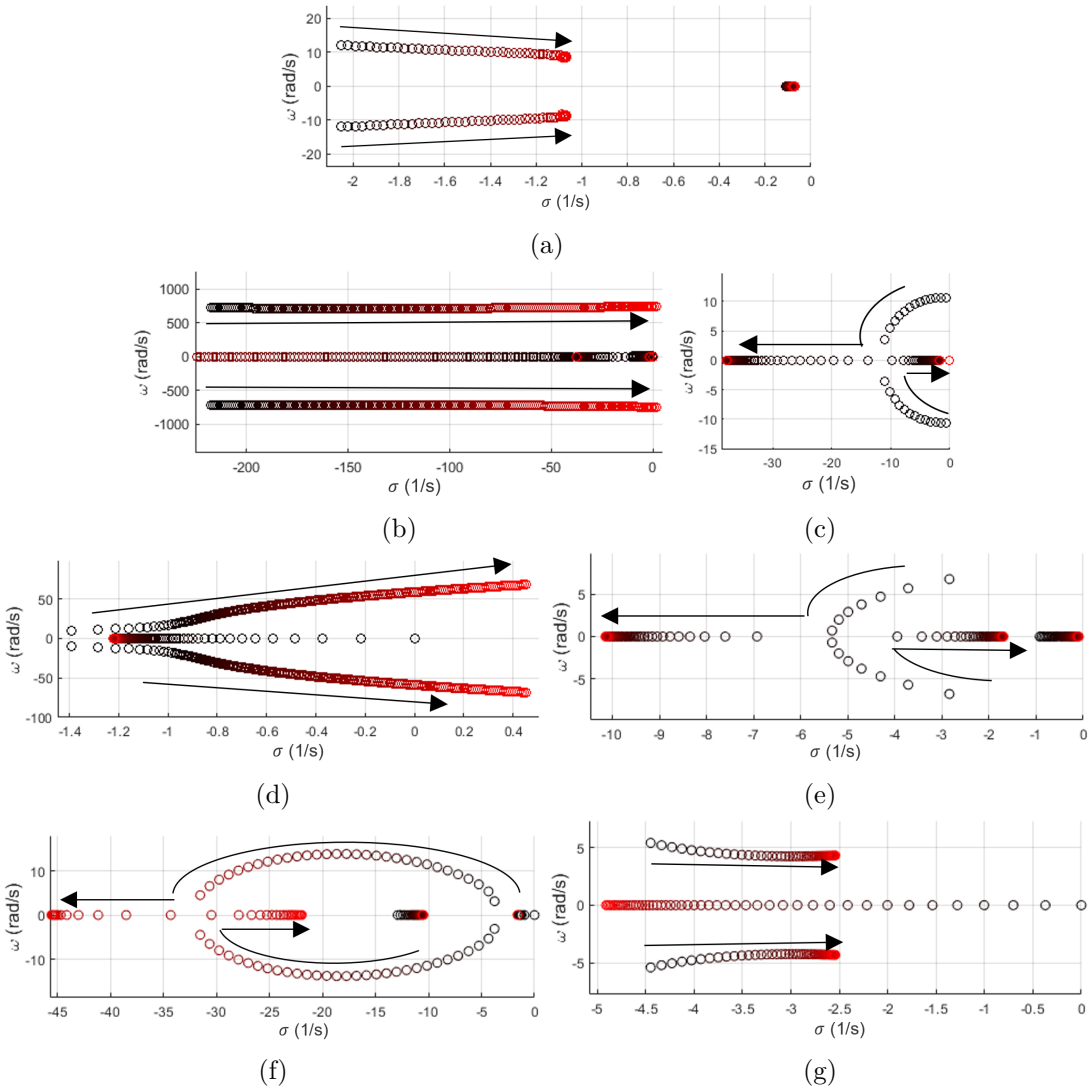

Figure B.3: Eigenvalues of interest for parametric sweep of the SG-GFM-load network for (a) TL1 & TL2, (b) K_P, (c) zoomed K_P, (d) K_I and of the GFM-GFM-load network for (e) K_{P_1} , (f) K_{I_1} and (g) K_{droop}.

B.6.2 GFM-GFM Network Parametric Sweep Results

The increase of the proportional and integral gains, K_{P_1} and K_{I_1}, are seen to fully damp the electromechanical interaction and this time no adverse effect is found on any higher frequency modes. The droop gain sweep in Fig. B.3g provides evidence of another highly impactful control parameter associated with the GFM, allowing for higher controllability of the electromechanical mode dynamics. Like the transmission line length sweep, it is seen that the electromechanical mode is brought towards the unstable region, potentially causing instability if this mode was initially closer to the y-axis.

B.7 Conclusions

This appendix presents a preliminary investigation into interactions between SGs and GFMs with a focus on electromechanical modes. This is achieved with modular small-signal modelling, followed by eigenvalue analysis. The states corresponding to the electromechanical mode in the SG-GFM system were found to be those associated with the power loop of the GFM and the swing equation of the SG, thereby confirming the presence of electromechanical interactions, similarly between two GFMs. Finally, a series of parametric sweeps are performed, offering an insight into the impact and flexibility that the GFM control provides for manipulating the electromechanical mode.

Small-signal instability is found to occur from high values of K_I as the electromechanical mode traverses into the unstable region. In the case of K_P, this mode can be fully damped but doing so will bring a higher frequency oscillation towards instability. Additionally, for the GFM-GFM network, it was found that the PI control gains of the droop-augmented GFM provided the potential to fully damp the electromechanical interaction with no significant effect on any higher frequency oscillations. However, increasing the frequency droop gain brought the electromechanical mode closer to the unstable region, similar to increasing the transmission line lengths.